

Copyright

by

David Stevens Stoker

2006

The Dissertation Committee for David Stevens Stoker
certifies that this is the approved version of the following dissertation:

**Ultrafast third-harmonic generation from
nanostructured optical thin films and interfaces**

Committee:

John W. Keto, Supervisor

Michael F. Becker

Michael C. Downer

Manfred Fink

Boris Breizman

**Ultrafast third-harmonic generation from
nanostructured optical thin films and interfaces**

by

David Stevens Stoker, B.S.

Dissertation

Presented to the Faculty of the Graduate School of

The University of Texas at Austin

in Partial Fulfillment

of the Requirements

for the Degree of

Doctor of Philosophy

The University of Texas at Austin

May 2006

To my family

Acknowledgments

The greatest aid to me in this grand endeavor was my advisor, John Keto, whose genuine curiosity and fervor provided constant forward motion through the countless obstacles that were encountered during my work in his laboratory. No less important to my success was the encouragement and wisdom of Kay Hoffmann, and the spiritual support of Craig McCluskey, who as mentors made a strong impact on my character as a scientist. I am indebted to the technical staff of the UT Department of Physics, Allan Schroeder, Lanny Sandefur, and Ed Baez, who sustain an unwavering commitment to the graduate students. But my most loyal benefactor was Jack Clifford, whose personal attention I could always count on.

If it weren't for the inspired lectures of Michael Downer, I would never have discovered the field of nonlinear optics. My sincere gratitude is given to Michael Becker, for providing your optics expertise and financial support for my travels. Desi Kovar, Dr. Zhou, Andre Albert, James Ma, and Claudia Torres: your willingness to share your ceramics experience and processing equipment was a blessing.

John McDowell was instrumental in developing of our FROG system. Nathan Erickson, you helped me 'big time' with the photoluminescence lifetime measurements. Thank you, Jonghoon, for your stewardship over the pulsed laser deposition apparatus. Iganacio, I always benefited from your refreshing point of view, even if it was from a hand-held tape recorder.

There are people to thank, but then there are my wife and parents, whose presence and love make everything possible.

Finally, I am grateful for the financial support from the National Science Foundation's grant DMI-0304031, as well as partial support from the Robert A. Welch Foundation, and SPRING.

DAVID STEVENS STOKER

The University of Texas at Austin

May 2006

Ultrafast third-harmonic generation from nanostructured optical thin films and interfaces

Publication No. _____

David Stevens Stoker, Ph.D.

The University of Texas at Austin, 2006

Supervisor: John W. Keto

Optical harmonic generation from nanostructured thin films and interfaces was investigated experimentally and theoretically. Sample materials were large band gap optical semiconductors (AlN/GaN), rare earth oxides (NdAlO_3), and noble metals (Ag). They were examined as solids, nanoparticles, and as hybrid nanocomposites. The goal of the project was to create and characterize high susceptibility, third-order (third-harmonic) materials that relied on nanostructure for an enhanced response. Laser ablation of a microparticle aerosol (LAMA) was used to produce these materials. Two routes to nanostructured materials were investigated. In the first method, a microparticle aerosol, composed of a small concentration of metal or semiconductor, and a larger amount of glass microparticles, was ablated by a

focused excimer laser, and the resultant nanoparticle aerosol was supersonically deposited and sintered. In the second method, a monolayer of silver nanoparticles was deposited by LAMA, and this film was further processed by pulsed laser deposition (PLD) of either a passive glass or active matrix material. Better optical quality was found in the hybrid LAMA/PLD materials. Many optical properties were required for characterization: linear transmission and absorption spectroscopy of plasmon resonances, second-harmonic generation (SHG) for field-enhancement analysis, and fluorescence spectroscopy and fluorescence lifetime experiments provided preliminary data for third-harmonic generation studies. The third-harmonic generation experiments were performed using an ultrafast laser system, and modeling the ultrafast dynamics of harmonic generation showed that pulse breakup occurs in the third-harmonic field. Interfaces were found to produce the harmonics, through cooperative group-velocity and phase mismatching. This uniquely ultrafast effect allowed for z-scan measurements to be simplified and for focusing effects to be eliminated. Using frequency-domain interferometry allowed for the measurement of the absolute phase of a third-harmonic pulse, and for an accurate determination of the third-order susceptibility of AlN. Finally, enhancement of second- and third-harmonic generation in PLD-coated Ag nanoparticle films was found to depend both on the material microstructure and the fundamental laser intensity.

Contents

| | |
|--|------------|
| Acknowledgments | v |
| Abstract | vii |
| Chapter 1 The Manufacture of Optical Nanomaterials Using Laser Ablation | 1 |
| 1.1 Method I. co-ablation of microparticles | 1 |
| 1.1.1 aerosol laser ablation | 2 |
| 1.1.2 controlling deposition through gas dynamics | 3 |
| 1.2 Aerosol ablation results | 8 |
| 1.2.1 film quality prior to sintering | 9 |
| 1.2.2 sintered nanoparticle films | 11 |
| 1.2.3 film quality after sintering | 17 |
| 1.2.4 conclusion: direct deposit nanocomposites | 22 |
| 1.3 Method II. LAM/PLD approach | 23 |
| 1.3.1 experimental overview | 23 |
| 1.3.2 LAM/PLD results | 26 |
| 1.4 Summary | 27 |
| Chapter 2 Linear Optical Characteristics | 31 |
| 2.1 Optical quality of sintered silica and glass nanocomposites | 31 |

| | | |
|---|---|-----------|
| 2.1.1 | x-scanning optical transmission setup | 32 |
| 2.1.2 | sintered nanocomposites | 33 |
| 2.1.3 | ADN fumed silica | 33 |
| 2.1.4 | ablated, deposited and sintered silica microspheres | 35 |
| 2.1.5 | x-scan of sintered glass:silicon nanocomposites | 37 |
| 2.2 | PLD optical films | 39 |
| 2.2.1 | aluminum nitride on sapphire | 39 |
| 2.2.2 | neodymium-aluminum oxide PLD sample | 42 |
| 2.2.3 | neodymium-aluminum oxide PLD / silver nanocomposite sam- ple | 43 |
| 2.3 | Surface plasmon resonance | 45 |
| 2.3.1 | theory/background | 45 |
| 2.3.2 | experiment | 47 |
| 2.3.3 | simulation | 47 |
| 2.4 | Field enhancement | 50 |
| 2.5 | Conclusions | 52 |
| Chapter 3 Second-Order Nonlinear Effects | | 54 |
| 3.1 | Second-harmonic generation in PLD aluminum nitride | 54 |
| 3.1.1 | rotational measurements | 55 |
| 3.1.2 | observation of crystal texture | 57 |
| 3.2 | Field-enhanced SHG in Ag nanoparticle films | 59 |
| 3.2.1 | symmetry considerations | 61 |
| 3.2.2 | local-field coupling in second-order effects | 63 |
| 3.3 | Two-photon induced fluorescence | 64 |
| 3.3.1 | models of noble metal fluorescence | 65 |
| 3.3.2 | lifetime measurements of silver nanocomposites | 69 |
| 3.4 | Conclusions | 80 |

| | | |
|------------------|---|------------|
| Chapter 4 | Ultrafast Laser Physics and Interface THG | 83 |
| 4.1 | Ultrashort-pulsed laser source | 83 |
| 4.1.1 | principle of operation of the mode-locked Ti:sapphire | 83 |
| 4.1.2 | pulse characterization through autocorrelation | 86 |
| 4.1.3 | phase-sensitive pulse characterization with FROG | 88 |
| 4.2 | Pulse propagation | 89 |
| 4.3 | THG with group-velocity mismatch | 94 |
| 4.4 | THG from simple optical elements using a focused laser | 96 |
| 4.4.1 | experiment | 98 |
| 4.4.2 | results | 101 |
| 4.4.3 | discussion | 105 |
| 4.5 | Conclusions | 107 |
| Chapter 5 | Quantifying Ultrafast Third-harmonic Generation from Thin Films | 108 |
| 5.1 | Introduction | 108 |
| 5.2 | THG from PLD aluminum nitride | 110 |
| 5.2.1 | THG from aluminum nitride/sapphire interfaces | 112 |
| 5.3 | THG z-scan measurements of interfaces | 123 |
| 5.3.1 | model | 124 |
| 5.3.2 | application to thin film $\chi^{(3)}$ measurements | 125 |
| 5.3.3 | THG spectrum | 131 |
| 5.3.4 | Fourier analysis | 133 |
| 5.3.5 | non-paraxial Effects | 135 |
| 5.4 | Summary of aluminum nitride measurements | 138 |
| Chapter 6 | Harmonic Generation from Enhanced $\chi^{(3)}$ Nanocomposites | 141 |

| | | |
|---|---|------------|
| 6.1 | Introduction | 141 |
| 6.2 | Cross sectional nonlinear measurements of resonant nanocomposites | 145 |
| 6.2.1 | intensity-dependent cross sectional measurements | 147 |
| 6.3 | Z-scan saturation analysis | 152 |
| 6.3.1 | intensity-dependent z-scan measurements | 157 |
| 6.4 | Third-harmonic saturation | 159 |
| 6.4.1 | intensity-dependent effects in field-enhanced nanocomposite materials | 160 |
| 6.4.2 | discussion: quartic power dependence and saturation in field-enhanced THG | 163 |
| 6.5 | Measurement of third-harmonic phase | 164 |
| 6.6 | Conclusions | 171 |
| Appendix A Operation Manual for the Femtosoft FROG Apparatus | | 174 |
| A.1 | Introduction | 174 |
| A.2 | Collecting data with ak_spectrographfrog.vi | 174 |
| A.3 | Managing the Frog routine through the Femtosoft executable | 177 |
| A.4 | Manipulating the Frog3.exe output | 180 |
| Appendix B CAD Drawings of the Pyrolytic Boron Nitride Vacuum Furnace Assembly | | 182 |
| Bibliography | | 192 |
| Vita | | 198 |

Chapter 1

The Manufacture of Optical Nanomaterials Using Laser Ablation

1.1 Method I. co-ablation of microparticles

Thick coatings of glass nanoparticles, doped with semiconducting nanoparticles, were manufactured in a controlled nanoparticle writing process. The deposition conditions determined the film quality. We used gas jet dynamics to control the average pore size and density of the films, and exhibit the results with high resolution SEM measurements of the films. Following deposition, heat was added to sinter the films, because these materials as initially written are not fully dense. Knowing how the starting film properties related to deposition conditions allowed us to optimize conditions prior to sintering. We find the most important variables to be surface roughness and gas velocity, and the best model for low energy aerosol impaction of nanoparticles must include effects for material compression during deposition, as well as the eroding force of the aerosol jet on the substrate. Deposition and

sintering pure glass or SiO_2 showed better optical quality than materials doped with semiconductors.

1.1.1 aerosol laser ablation

Laser Ablation of Microparticle Aerosols(LAMA) offers the possibility to create a variety of new functional optical materials [1]. Fundamental to any optical application is the ability to write materials which are dense enough to eliminate optical scattering. If the films are intended to be used as a THG medium for nonlinear optics, they must transmit in the ultraviolet, so high purity SiO_2 was chosen as the primary ablation material. Spherical particles, average particulate size (APS) 20 μm , of fused silica (KOBO products) were entrained in an aerosol, and served as the primary target for producing nanoparticles.

The microparticle aerosol is then fed into the focus of an Kr:F excimer laser, where laser fluence is in excess of 2 J/cm². The gas-flow velocity is tuned to the 200 Hz repetition rate of the laser, and so leaving the focal region is a monodisperse nanoparticle aerosol, with absolute particle size of 5-10 nm.

Microparticle ablation occurs when laser energy is high enough to ionize the material, and initiate efficient absorption of the laser energy. The laser is rapidly absorbed, and a shockwave travels through molten material. The hot, plasma material expands, and cools adiabatically, nucleating spherical nanoparticles as the temperature drops below the melting point of the material. A schematic of laser ablation of a glass microparticle is shown in Fig. 1.1.

The ablated nanoparticle aerosol is fed through a supersonic nozzle, into a high vacuum chamber, where it is deposited onto a sapphire substrate through a cylindrical nozzle with a length L of 250 μm and a diameter D of 250 μm . The ultimate velocity of the particle is a fraction of the gas-jet velocity, but is understood primarily as a function of the value L/D . Based on calculations of nanoparticle

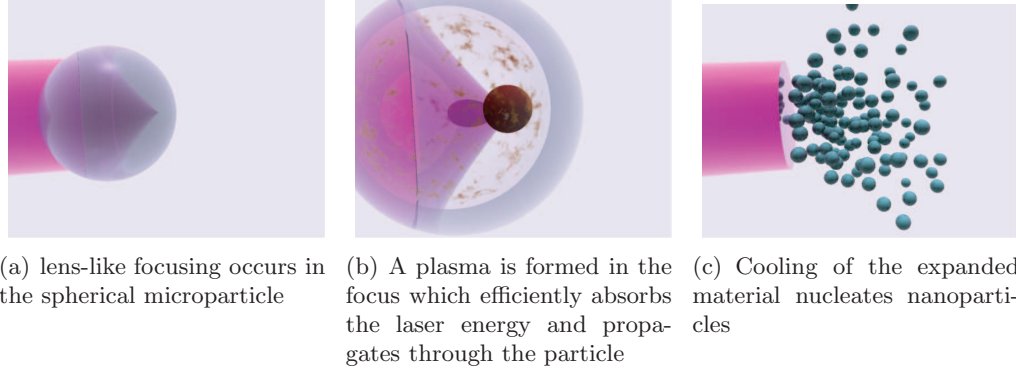


Figure 1.1: Schematic of microparticle ablation

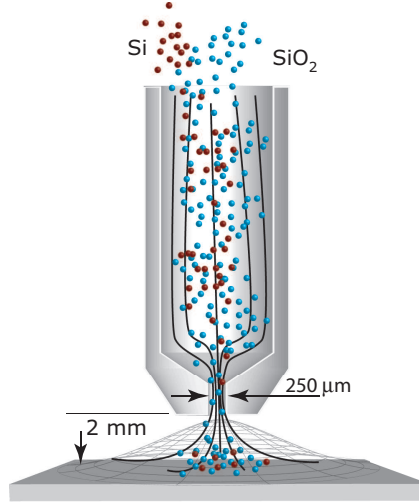
acceleration in the gas jet, some slowing occurs in the bow shock just above the substrate, but the nanoparticles will still impact with enough energy to be partially sintered. A schematic of the deposition is shown in Fig. 1.2.

1.1.2 controlling deposition through gas dynamics

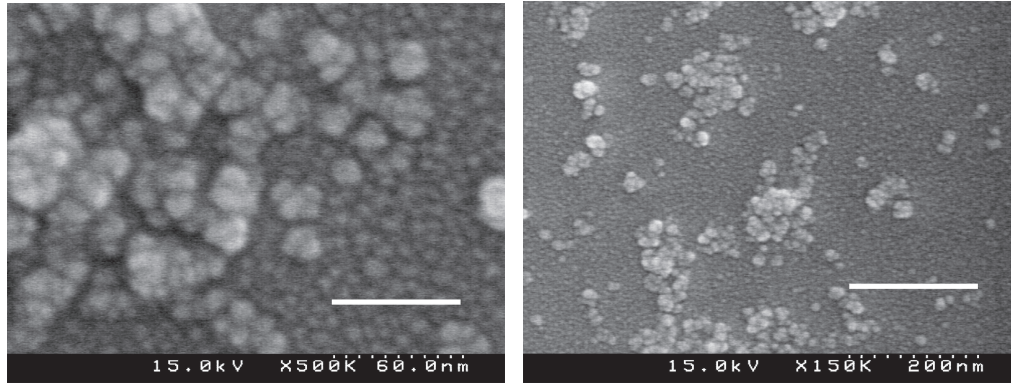
During deposition the nanoparticles in the aerosol are sympathetically controlled by the carrier gas. Gas dynamics in the nozzle are largely governed by the Mach number M_e , which is determined by the ratio of the nozzle throat area A_t to the A_e the exit nozzle area. In our setup, the nozzle to throat ratio is approximately equal to 1 (flat plate design). The Mach number is determined graphically, from the equation

$$A_e = A_t [(\gamma + 1)/2]^{-(\gamma+1)/(\gamma-1)/2} \frac{[1 + M_e^2 * (\gamma - 1)/2]^{[(\gamma+1)/(\gamma-1)/2]}}{M_e}. \quad (1.1)$$

Where γ is the ratio of the specific heat at constant volume to the specific heat at constant pressure $\frac{C_p}{C_v}$. For an ideal gas, the ratio γ for helium and argon is 1.667. For air or nitrogen, $\gamma = 1.405$. A plot of the RHS of Eq. 1.1 for each of these cases is shown in Fig. 1.3. The nozzle geometry indicates the flow is 'choked', meaning



(a) schematic of supersonic deposition of a bidisperse nanoparticle aerosol. A 1 mm long, 250 μm diameter nozzle accelerates a mixture of silicon and silica nanoparticles to near the 1000 m/s gas velocity. The nanoparticles, after exiting the nozzle into a vacuum chamber, are decelerated in a bow shock, which exists just above the substrate and attenuates with decreasing distance from the nozzle.



(b) The local surface modification for initial film growth. Scale bar is 60 nm. Smaller, uniformly distributed particles are Au/Pd (c) Scale bar is 200 nm. Same area at lower magnification shows the particle distribution over a larger area.

Figure 1.2: Ablated SiO_2 microparticles begin to cover the Al_2O_3 surface as clusters of nanoparticles. As material is randomly deposited onto the substrate the exposed gaps on the surface are filled. The silica nanoparticles do not deform significantly when they impact.

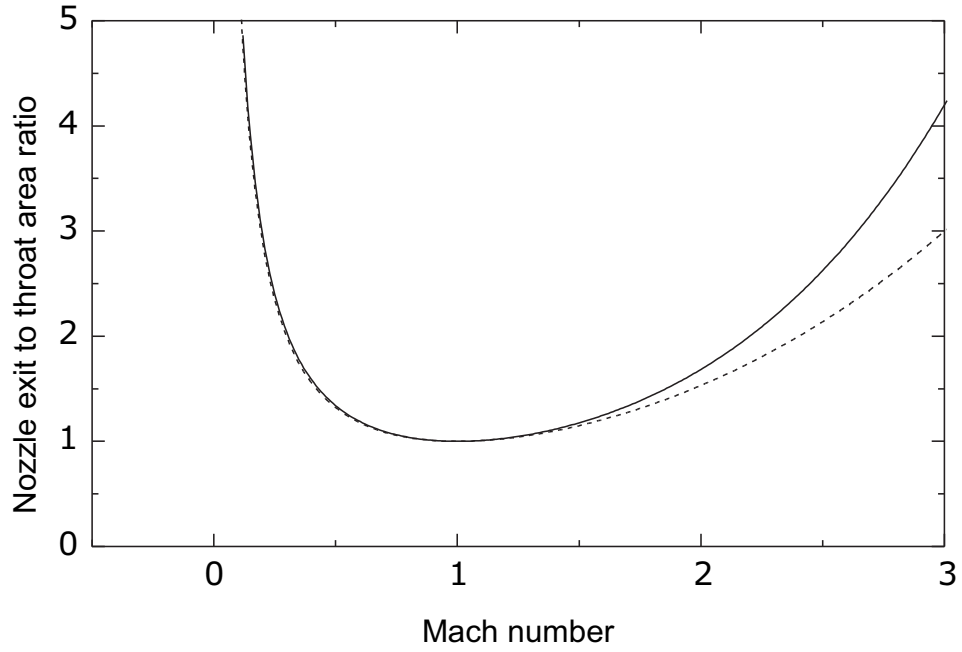


Figure 1.3: Plotting the RHS of Eq. 1.1 shows the Mach number for the unexpanded nozzle, or flat plate is 1 for both the inert gases (solid), as well as nitrogen (dashed).

that $M_e=1$. The Mach number determines the gas temperature at the nozzle exit as

$$T_e = T_0[1 + M_e^2(\gamma - 1)/2]^{-1}. \quad (1.2)$$

Similarly, the pressure at the nozzle throat is

$$P_e = P_0[1 + M_e^2(\gamma - 1)/2]^{-[\gamma/(\gamma-1)]}. \quad (1.3)$$

where P_0 is the pressure in the ablation cell (1.5 atmosphere) and P_e is the pressure at the exit of the nozzle throat. The exit velocity is given by

$$v_e = M_e \sqrt{\gamma R T_e}, \quad (1.4)$$

where R is the gas constant, 8314 J/(Kg-Kelvin). These values are listed for the simple, flat-plate nozzle in Table 1.1.

Table 1.1: Calculated gas parameters (Assumes $P_0=1140$ Torr and $T_0=298$ Kelvin)

| material | P_e | T_t | v_e |
|----------|----------------|------------------|---------------|
| He/Ar | 555.29 (Torr) | 247.817 (Kelvin) | 1759.89 (m/s) |
| N_2 | 601.283 (Torr) | 223.472 (Kelvin) | 1701.41 (m/s) |

Acceleration of the nanoparticles is impeded by hydrodynamic slipping in the gas flow. Calculations of the final velocity of the particles can be calculated by including the Cunningham slip factor, and has been considered elsewhere [2]. The gas-flow velocity also determines the amount of force applied to the substrate through

$$F = \dot{m}v_e + (P_e - P_a)A, \quad (1.5)$$

where A is the nozzle area ($4.91 \times 10^{-8} \text{m}^2$). The exit nozzle pressure is given in Table 1.1 for each of the gases used, and converted to SI units (N/m^2). The ambient pressure in the deposition chamber P_a is 39.985 N/m^2 (300 mTorr) in the experiments conducted. The mass flow rate \dot{m} is understood simply from dimensional analysis as

$$\begin{aligned} \dot{m} &= \left(\frac{\text{mass}}{\text{volume}}\right) \times \left(\frac{\text{volume}}{\text{time}}\right) \\ &= \rho \nu. \end{aligned} \quad (1.6)$$

The gas density ρ and the volumetric flow rate (typically about 100 sccm) determine the overall mass flow rate. Substituting appropriate values into Eq. 1.5, indicates that changing the gas will change the amount of force applied to the substrate. More important is the force per unit area, which is more appropriate for determining how the deposit will respond to the gas jet. The downward pressure of the gas jet on the

deposit is 1.0×10^6 N/m² for helium, and 0.4×10^6 N/m² for argon and nitrogen.

Microparticles which have been impacted directly are known to produce solid-density films of optical quality. In these high-velocity fields, the microparticles will accelerate and impact the surface inelastically. The resultant high density is only partly enabled by the high microparticle velocity achieved by acceleration in the nozzle; more important is the differential compression across a microparticle when it impacts the substrate. Differential compression will cause it to crush as it impacts the surface. Akedo *et al.* observed visible light emission from the film, which he attributed to plasma breakdown of the carrier gas as the microparticle ionized during collision with the substrate [3, 4]. Once that film is deposited, because it is solid, it is no longer susceptible to damage by the gas jet. Supersonic deposition of nanoparticles occurs differently. The smaller particles can reach gas velocities more rapidly, because of their lower inertia. But they will decelerate with equal ease in the bow shock just above the deposition region, as shown in Fig. 1.2. The density of the resulting film is inversely proportional to the size and density of the aerosol nanoparticles. Deceleration occurring in the bow shock was previously estimated by Nichols [5].

In our technique, the ablated aerosol material deposits the substrate at a velocity which is determined by gas conditions and nozzle geometry. The effect of carrier gas on deposition has been observed in previous experiments [1]. Helium minimizes the deceleration within a bow shock region above the substrate, which increases the impaction energy, and hence the density of the film. The bow shock reduces the impact energy of the nanoparticles, but the velocity-reducing potential depends on the density of the nanoparticle. Glass nanoparticles, have a particularly low inertia, due to their low density and are more susceptible to deceleration. We found that the glass films were neither as dense as the microparticle-deposited films of Akedo, nor as dense as silver nanoparticle films of laser ablated silver micropar-

ticles. It was only by adding heat after deposition that we were able to densify the glass films.

Even though densification was achieved by addition of heat, gas dynamics continued to play a dominant role in the final film quality. The low initial film density makes the film susceptible to damage by the high gas pressure coming from the nozzle. The force of the gas jet is less important if the film is completely dense, but lower density films are easily damaged. Films damaged prior to sintering are much lower in optical quality than uniformly porous starting materials. For these reasons, proper deposition is achieved by balancing extremes: the jet must be powerful enough to densify the nanoparticle film, but not so powerful that it erodes the film.

1.2 Aerosol ablation results

Though in theory, many metallic nanoparticle films are expected to be very dense when deposited in helium and under close nozzle to substrate conditions, in practice the films are only 50-70 % dense. The situation exacerbated when glass, with 1/5 the density of silver, is used. Size is important because the small particles fail to melt as easily when impacting the surface, because there is no differential compression of the particle when it hits. When particles are so small, and light in the case of SiO_2 they can efficiently decelerated in the bow shock on the substrate. In that case, the material achieves a very high density, but the granularity is still representative of the particle size.

A glass nanoparticle film was examined as a function of position under the nozzle after being deposited in a helium gas jet. Directly underneath the nozzle, we observed the poorest film quality. Though the film appeared denser in the center, large pieces would break away, and would be accelerated by the gases exiting from the jet. There, the average pore size was large, and varied from several hundred

nanometers to several microns.

Far away from the nozzle, we observed a different type of deposition. There, the glass grew more slowly, and the average pore size was small and uniform. However, the low energy of deposition did not make the film very dense.

1.2.1 film quality prior to sintering

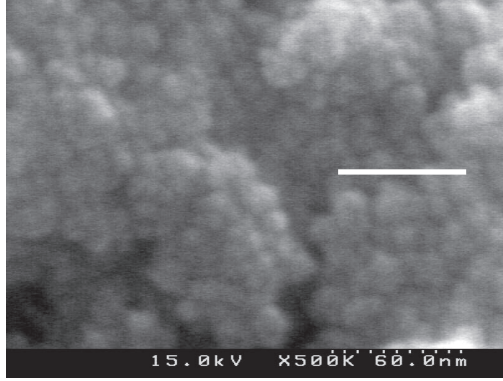
As in the firing of bulk ceramic material, the microstructure of thin films is important for controlling the quality of the final product. If the material is not uniformly porous, then differential shrinking will occur during sintering. If large pores exist, there is then the possibility that the final product will not be a single coherent mass. In direct writing of nanoparticles, we aim for the highest green density (meaning smallest average pore size), and the highest uniformity of porosity. It is well-known that these are the ideal starting conditions in a bulk material that sinters by grain boundary diffusion. However, aerogels which sinter viscously can have green densities as low as 10 %, and yet they will sinter to above 99 % dense.

Microscopically, deposition occurs in discrete packets of nanoparticles, because the feedstock is made of isolated microparticles. Gas flow conditions also affected the morphology of the deposition. We observed several ways the gas influences the deposition, but for glass, which appears not to self-sinter, the most important was the downward force of the gas on the film.

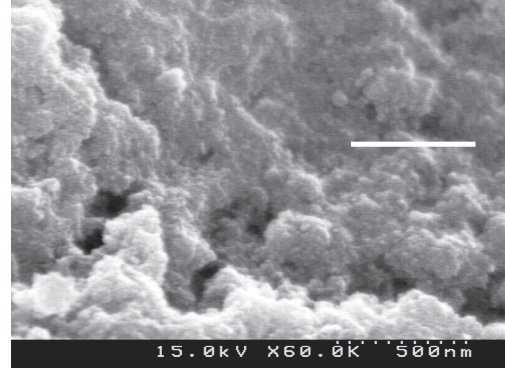
Directly under nozzle

Film growth directly underneath the nozzle is the most rapid, and will have locally high densities, as shown in Fig. 1.4(a). But the highly compressive gas from the nozzle will erode the material. Some areas underneath the nozzle are very dense, but these can fracture into pieces several microns in size as shown in Fig. 1.4(c). Eroded pits are subsequently covered, but leave behind voids that do not sinter to

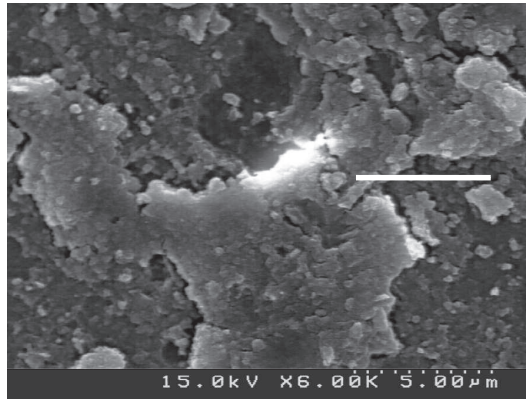
fully dense.



(a) Scale bar is 60 nm. Locally, the film appears to be very dense.



(b) Same area. Lower magnification. Scale bar is 500 nm.



(c) Same area. Lower magnification. Though locally dense, structure is irregular and porous at the microscale.

Figure 1.4: Film deposition underneath the jet is subject to erosion by the force of the gas.

Under high magnification, the film directly underneath the nozzle shows some areas with extremely high density, and no visible porosity. The high density is due to the large impact velocity of the particles, and large compressive forces of the jet. But lower magnification shows very uneven growth. Particles deposited directly underneath the nozzle have velocities in excess of several hundred m/s. The

energetic deposition of highly accelerated nanoparticles can produce a film that is very dense, given the ideal condition that the particle velocity is large enough to melt at the surface. Unfortunately, there is a tendency for the film to erode underneath the supersonic nozzle. When pieces break off underneath the nozzle, they accelerate in the velocity field of the gas jet. The smallest particles are the least damaging, and mostly stick to the first thing they can find. The largest particles are either too heavy to move anywhere, or easily become stuck. However, micron-sized particles are readily found many nozzle diameters away from the center of the film, having been accelerated in the tangential gas flow.

Tangential deposition (far from nozzle)

Spreading of the gas and conservation of volumetric flow causes the velocity of the gas flow to decrease as $\frac{1}{r}$ from the nozzle. The structure of the film one nozzle diameter away from the deposition axis is shown in Fig. 1.5, the film grows more slowly and with a higher porosity because of the lower impact kinetic energy.

Deposition in the tangential gas flow far from underneath the nozzle occurs differently than just underneath the nozzle. The forces that contribute to film erosion are smaller, and the impact energy is lower. These forces cause a more uniformly porous, and smoother film growth. SEM images of the silica film grown far from the nozzle opening are shown in Fig. 1.5.

1.2.2 sintered nanoparticle films

Glass films sinter viscously. So, to sinter a glass film, heat is added until the viscosity of the material lowers enough that it will deform, and flow together. The critical parameter for viscous sintering is the glass-formation temperature, which can change drastically from one material to the next. A list of several glasses, and the corresponding T_g are listed in Table 1.2

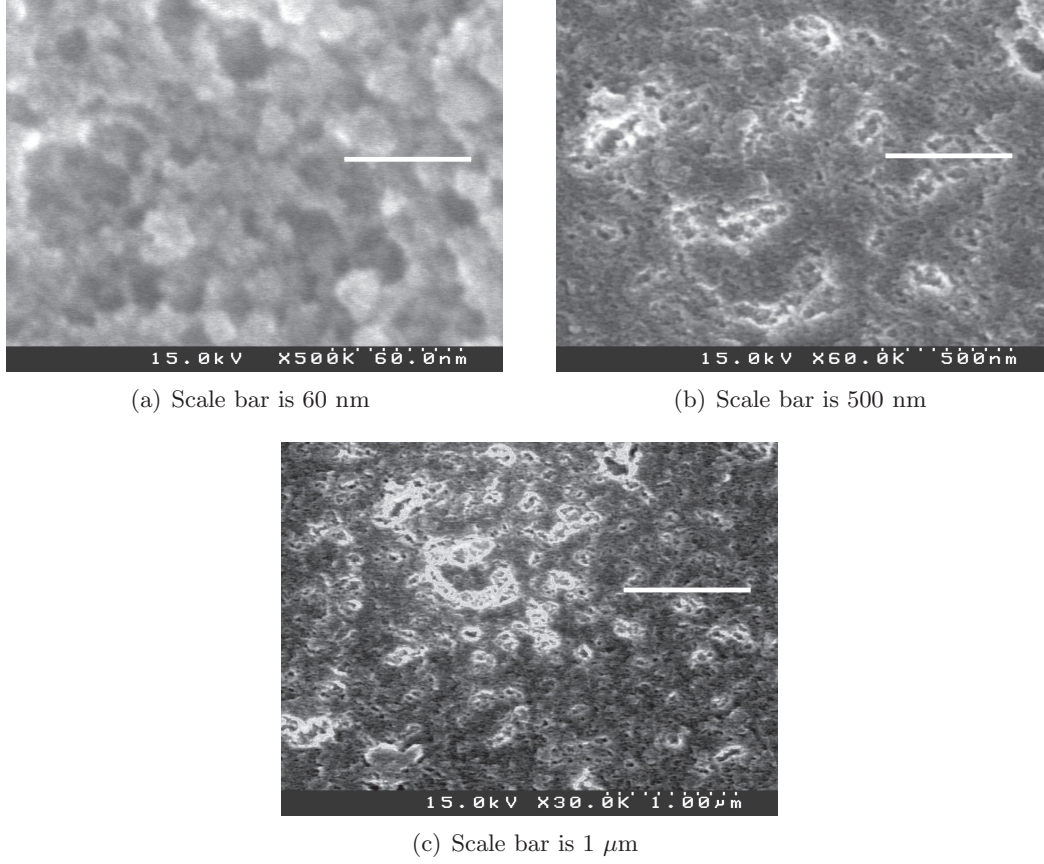


Figure 1.5: Far from the deposition axis (under nozzle), the film appears much less affected by downward thrust of the gases, and grows more uniformly. Though it is more porous, the average pore size remains small.

Table 1.2: Glass transition temperatures of various glasses

| material | T_g |
|--------------------------|---------|
| SiO_2 | 1450 °C |
| Al_2O_3 | N/A |
| soda lime | 750 °C |
| fumed silica (60-100 nm) | 1250 °C |

Sintering on a rigid substrate differs from bulk viscous sintering [6, 7, 8]. In the case of viscous sintering, the substrate reduces the mobility of the flowing material, in a no-slip condition, which is identical mathematically to describing viscous flow of liquids near a wall. For thin, glassy films, the sintering dynamics cause initially low-density deposits to form islands of uniformly dense material. Fig. 1.6 demonstrates island-formation in soda lime glass (Duke Scientific - diameter is $8.5\ \mu\text{m}$), after sintering spherical microparticles at $800\ ^\circ\text{C}$ for 90 minutes, with ramp rates of $5\ ^\circ\text{C}$ per minute.

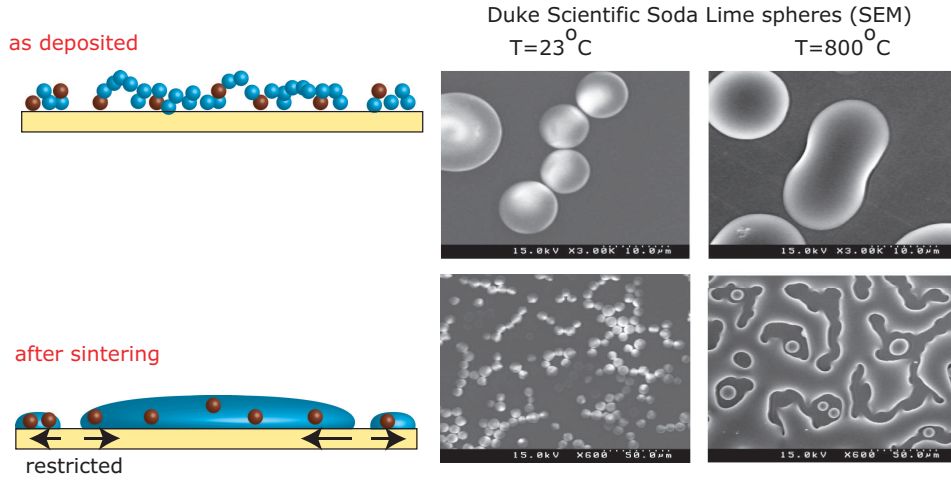


Figure 1.6: Viscous flow is hindered by the low dimensionality of the substrate. So, a reduction of free energy (surface area) occurs more rapidly for surfaces not bound to the substrate.

Most of the supersonically deposited films were sintered in a box furnace (Thermolyne, model 46100), which is exposed to air, so any active nanoparticle constituents, like Si or Ag, were oxidized, or dissolved into the matrix glass. The box furnace was adequate for studying sintering kinetics of the matrix glass, by itself. To sinter pure silica nanocomposite materials requires a combination of controlled atmosphere and high temperature.

High temperature vacuum furnace

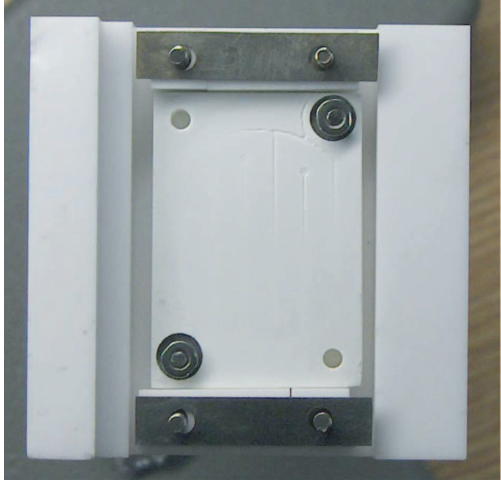
To address the two-fold need of high temperature and atmosphere control, a vacuum sintering unit was designed and added to the supersonic deposition chamber. The vacuum furnace was developed by shaping bisque-fired alumina (Aremco, Inc.) and molybdenum. The bisque fired alumina was then fully fired at 1650 °C (see Appendix I. for detailed drawings). During firing, the bisque alumina decreased in size by about 13 % in each dimension. Built into the heating unit is a pyrolytic boron nitride heating element (PBN - HTR1001, GE Advanced Ceramics Division), which is capable of sustaining surface temperatures in excess of 1700 °C. It was added to the sample deposition chamber, and designed to hold the a molybdenum substrate holder, upon which the LAMA-produced nanoparticles are supersonically deposited. Basic tests and photos of it prior to and after installation are shown in Fig. 1.7.

Sintering of jet-written films of fumed silica was initially performed under high 1×10^{-7} Torr vacuum. However, due to malfunction of the furnace, films made primarily from ablated silica (3N purity) were sintered in the atmospheric box furnace, which reached temperatures high-enough to sinter the films.

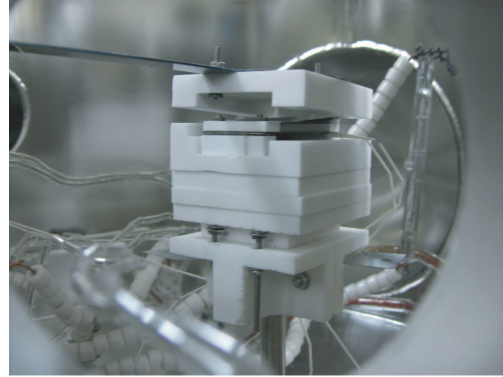
We annealed three samples at 1000-1500 °C. Although Fig. 1.8 indicates that 1250 °C is sufficient to achieve densification, optical quality of the material was still low at that temperature, and pure silica films benefited from slightly higher temperatures.

Box furnace sintering

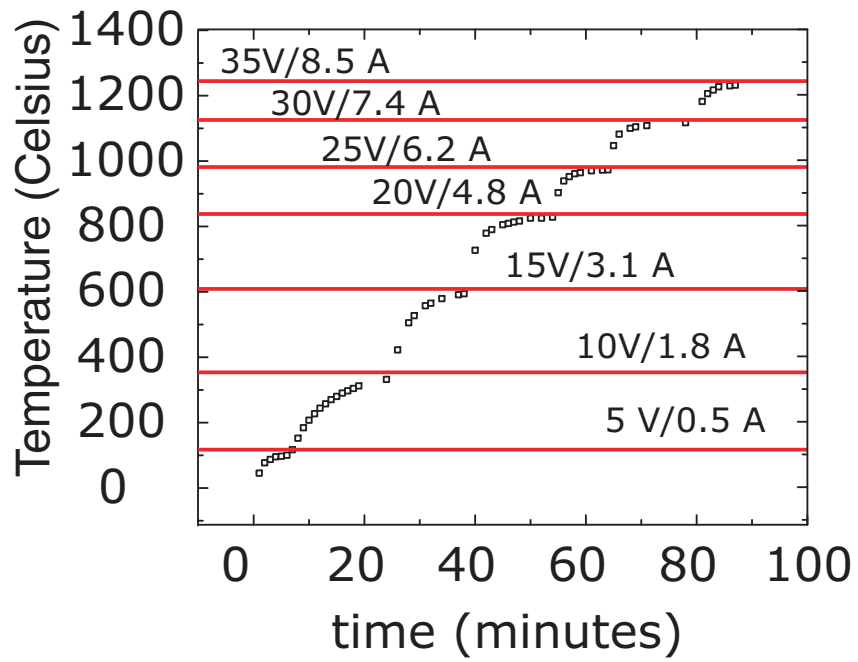
Several pure silica films were sintered in the box furnace. In these experiments, we were able to determine that nanoparticle sintering occurs at lower temperature, compared to large particles. Box furnace results after sintering fumed silica (DeGussa Aerosil 10- to 100-nm diameter) for 2 hours at 5 °C/min at three temperatures are shown in Fig. 1.8. The fumed silica sintering results confirmed the inverse depen-



(a) Top-view of pbn element, in the bisque alumina furnace assembly.



(b) Entire assembly shown in the vacuum chamber.



(c) Heater test shows measured temperature as a function of time (\square). The applied voltage (and current) was changed in increments over 1 hour.

Figure 1.7: PBN vacuum substrate heater and tests

dence of sintering temperature on particle size (typically bulk SiO_2 softens closer to 1450 °C). LAMA-produced nanoparticle films also showed softening at 1250 °C.

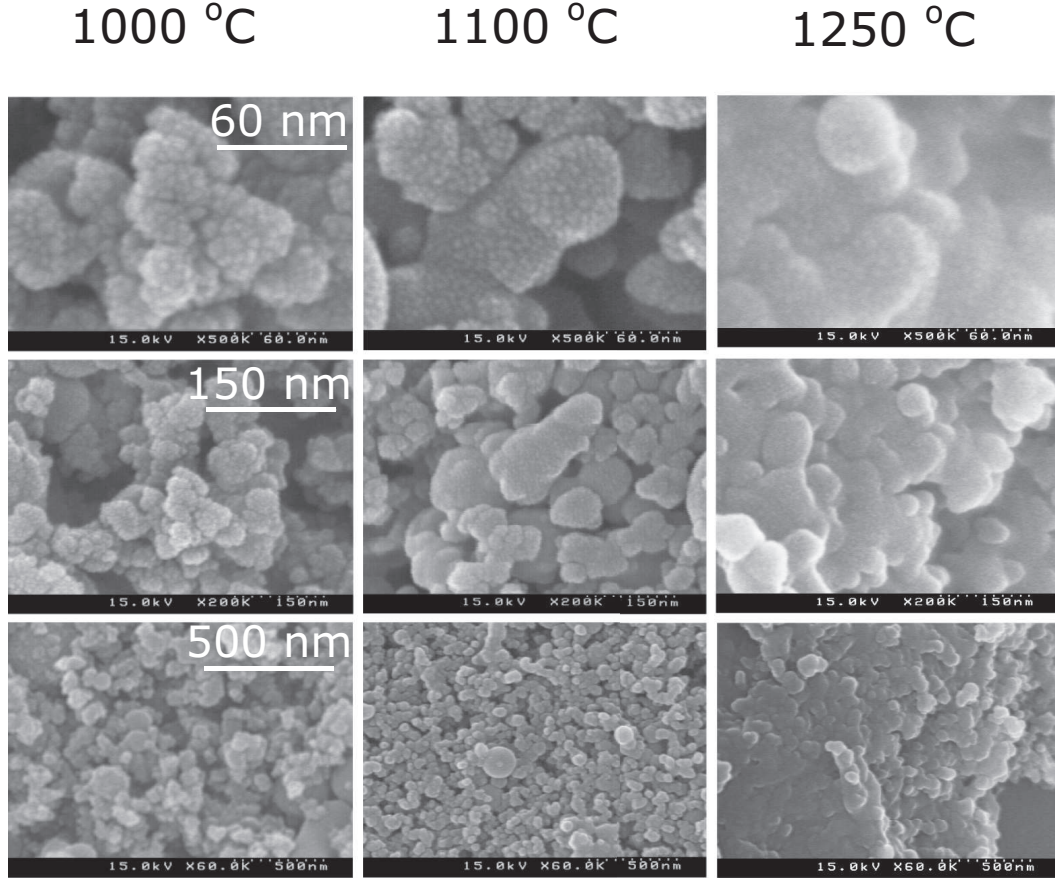


Figure 1.8: Densification of sub-100-nm silica particles occurs readily at 1250 °C. For comparison, other temperatures, 1000 and 1100 °C, are shown.

Low temperature tube furnace

Sintering of glass films with rigid inclusions has been examined [9]. Because soda-lime glass has a low glass transition temperature, and low temperature tube furnaces were readily available, we could readily examine the sintering kinetics of

soda-lime:silicon nanocomposite films. These experiments were carried out in an Ar atmosphere, or in a low concentration Hydrogen in a N₂ atmosphere.

The glass spheres and silicon micropowder were mixed in a 10:1 volume ratio, fed into the excimer laser focus, and supersonically deposited onto a sapphire substrate. Several resulting samples were sintered at different temperatures. The optimal temperature for soda-lime glass sintering was 750 °C. In the controlled atmosphere, the silicon inclusions would not oxidize. Diffusion of silicon into silicon dioxide is not thermodynamically favorable; the phase diagram of silica and silicon indicates the two materials are immiscible.

Densification of the composite materials was reduced by the presence of silicon, and potentially by the lower wetting coefficient of soda lime on the sapphire substrate. Because the controlled atmosphere furnace could not reach 1250 °C, other nanocomposites such as Si:silica were not sintered.

1.2.3 film quality after sintering

We found the silica films would densify, but achieving a uniform film thickness was difficult. The initial low density, combined with restricted motion at the substrate meant films were not always uniform. However, we were able to achieve the best uniformity under two conditions: aerosol depositing 60-nm nanoparticles in He, with the nozzle far from the substrate (more than 5 mm), and LAM of 20 micron silica spheres in an argon atmosphere, with the nozzle close to the substrate. Though the films were not completely uniform over all areas, in each experiment, either the area under the nozzle or the area at the edge appeared to be fully dense, and mostly uniform.

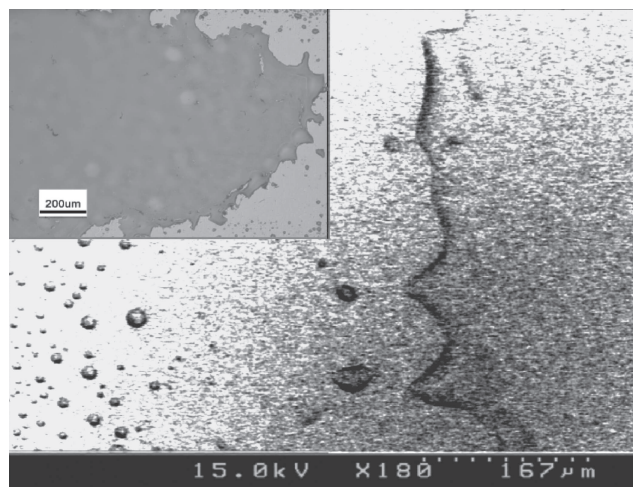
Pure silica films

We deposited directly fumed silica (60 nm APS, Degussa) onto a sapphire substrate. The larger particle size relative to the LAM silica nanoparticles meant that the average material density was high enough that voids would not form as easily. Here, the edge of the film after firing at 1450 °C was completely dense and uniform, as shown in Fig. 1.9.

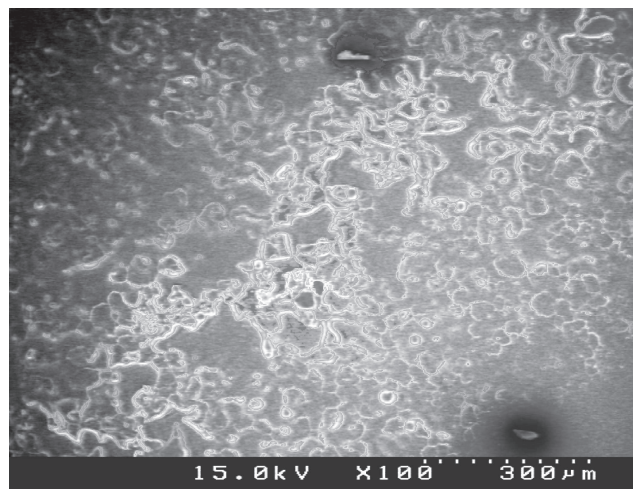
The sintered, LAM-deposited silica films were lower in quality at the edges, because the starting density of the LAM silica films was much lower. The smaller particle size puts the initial density at closer to 10%, which is quite close to an Aerogel. Sintering densifies the film, but the reduced flow at the surface causes the formation of beads, all throughout the edge of the film. Because helium jets had such a high thrust, and tended to erode the center of the film, argon was substituted, and the nozzle substrate distance was reduced. Sintered films produced in the Ar atmosphere were much more smooth in the center, and near to entirely uniform, except for the beaded edges. These results are shown in Fig. 1.10.

soda-lime nanocomposites

The sintered soda-lime glass and silicon nanocomposites showed poor densification after firing, either due to the presence of the rigid silicon nanoparticles or poor wetting to the sapphire substrate. Optical microscope images of the resulting material are shown in Fig. 1.11. Scattering is strongest from the large morphological variations. Under the jet, 50-100 μm islands form. Far from the jet, smaller 500-nm agglomerates were found. These smaller agglomerates cause the edge of the film scatter less light, compared to the larger islands, and so appear less dark in the image.

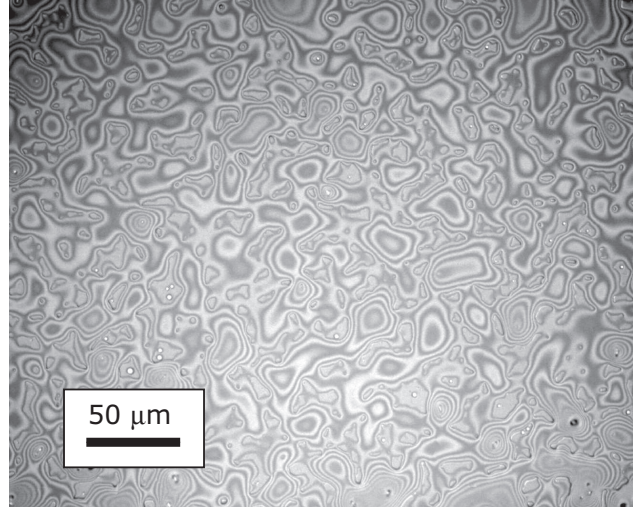


(a) SEM image of the edge of the film. The inset is an optical image of the same area, with a 200 micron scale-bar.

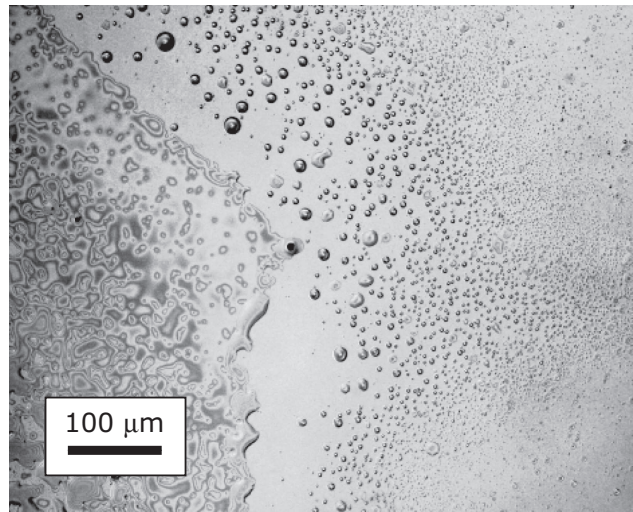


(b) The film center is highly irregular after firing, and low quality.

Figure 1.9: Sintered fumed silica films with starting average nanoparticle size of 60 nm. The edge is much higher quality, compared to the center.



(a) Optical image of the center of the film.



(b) Far-view of the edge. Notice the sample primarily beads far away from the center.

Figure 1.10: Sintered LAM-produced glass nanoparticle (5- to 10-nm particles) films. These optical photos were taken using a polarization microscope. The fringes are continuous for a constant height.

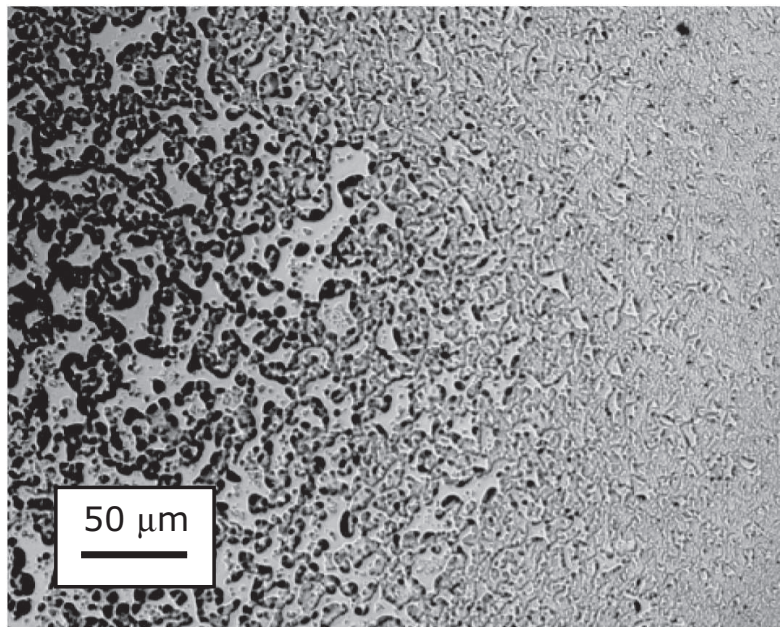


Figure 1.11: Sintered LAM-produced soda-lime:silicon nanocomposite films. Agglomerates exist throughout all regions of the sample. Underneath the nozzle, agglomerates are largest (20-100 μm). Farther from the nozzle, agglomerates are uniform, and small ($< 1 \mu\text{m}$).

1.2.4 conclusion: direct deposit nanocomposites

The film quality of glass nanocomposite is dominated by the glass material. So, controlling the supersonic deposition of silica or glass is essential for controlling the overall quality.

The quality of a sintered bulk material is controlled by the initial pore size and initial density of material. However, film sintering must also account for the substrate. The substrate reduces the mobility of the surface atoms, so thinner, films tend to be less uniform after one heating cycle. The decreased uniformity after sintering was observed in TiO_2 films, by Scherrer *et al.* and they solved this problem by repeating the deposition to fill-in the empty spaces on the film [6].

Cyclical heating and deposition is not a realistic approach for LAM-deposited films, which use tube furnaces to sinter the material. However, the use of a vacuum substrate heater improves the prospects of such an approach. Ideally, samples could be heated and voids filled by repeated deposition cycles. This should produce very thick and smooth films. The latter method required operating the vacuum heater continuously at temperatures in excess of 1250 °C for extended periods, and would require some modification of the current vacuum substrate heater.

Though several of the aerosol-deposited nanoparticle films exhibited a locally full-density after sintering, none exhibited uniform, solid density throughout the entire film. As an example, the edge of helium-deposited fumed silica (DeGussa Aerosil 60-nm average diameter) sintered to full density at 1400 °C, but the center of the film contained pits and pores, and was not of optical quality. Depositing LAM-generated silica nanoparticles through a nozzle in argon, using an increased nozzle-substrate distance of about 1 cm lowered the tendency for the film to erode underneath the nozzle. So, the quality of the film just beneath the nozzle was better, and higher density than the edge regions of the sample. The center of those samples, when sintered, was as uniform and dense as the edge of the Degussa sample.

1.3 Method II. LAM/PLD approach

Because making optical quality materials solely with LAM had problems, we sought to control the glass using a controllable technique: PLD.

An additional benefit is that heating the sample is not required for achieving a dense sample, which allows the possibility of including a metal in a glass matrix is possible. We coated silver (Ag) with both sapphire and a rare earth perovskite, NdAlO_3 . AlN films were also made by PLD and characterized, but were not used in any nanocomposites.

1.3.1 experimental overview

The materials were made LAM of Ag, followed by vacuum transfer to a PLD chamber. In the PLD chamber, the same Kr:F 248-nm laser was focused onto a solid target in a reactive atmosphere. Oxide materials made by PLD tend to be O_2 deficient, unless the deposition is carried-out in O_2 , so both NdAlO_3 and sapphire target ablations were done in a 10^{-5} Torr flowing oxygen atmosphere [10].

The laser was brought to a focus at the surface of the target, at an incident 45 degree angle. The focusing lens was translated in a small circle, which caused the focus to move in a circle in the focal plane. Because the incident angle of the laser was large, the laser moved in and out of focus in the plane of the target surface. The slightly asymmetric motion caused the samples to be slightly wedged, but other properties, like density and surface roughness were excellent compared to evaporation-based methods.

PLD Target preparation

In some circumstances we had to make our own PLD targets for these studies. Many targets are commercially available, like the AlN target, but others were not available commercially. In the latter case, manufacturing a target required the dry-pressing

a ceramic green body which was fired at high temperature to sinter it.

While the alumina powder was purchased (Alcoa / Sumitomo, Inc.), it was not even possible to purchase the NdAlO_3 starting powder. The target powder was made by reacting 1 part by mole of alumina powder and 1 part of Nd_2O_3 powder (Sigma Aldrich). Though the Nd_2O_3 has the proper (3+) oxidation level of the neodymium atom, neodymia will absorb water readily, and a target made from Nd_2O_3 will absorb water in the atmosphere, crack, and expand. However, NdAlO_3 is stable in atmosphere. It has a stable, though complicated, crystal structure: perovskite. Perovskites made from transition metal atoms have unique transport properties and have been used as substrates for growing superconductors, because they lattice-match many of the cupric-based, high T_c materials.

The reaction of alumina and neodymia were carried out at a sequence of high temperatures. Here is the recipe for making NdAlO_3 : First fire Nd_2O_3 in the box furnace at 900°C , for at least 9 hours to drive off water. Next, weight out equal amounts (by mole) of Nd_2O_3 and Al_2O_3 . Mix these thoroughly by hand and press into a pellet. The solid-state reaction is more efficient if pressed. First, fire at 1100°C . Fire for 12 hours, with ramp rate of 5 degrees/minute. Remove target. Crush by hand in a mortar. Grinding is very tedious, and can take several hours to do properly. I found that repeatedly tapping pieces of the target will eventually break it, and reduce it to a smaller sized powder. Press into a pellet again. Fire at 1300°C , again for 12 hours. Remove, and crush, and press a new target. Fire at 1400°C for 12 hours. Remove and crush and press again. Fire at 1450°C for 12 hours. Remove and crush into a powder. When the reaction has finished, the target should have made the transition to a violet-gray color, indicating formation of single-phase NdAlO_3 . We verified the transformation using powder x-ray diffraction. The final firing must be done at 1650°C for at least 12 hours. Pellet formation of the target is most important before the final firing. If the final target cracks, it

cannot be re-crushed and repeated, because the sintering is not as effective. At lower temperatures the diffusion is enhanced by material concentration gradients and chemical reactions (primarily the latter).

Any powder can be dry pressed, but it will not necessarily hold together during the firing. Many variables affect the difficulty of the process for a given material. Particle size and moisture level are two of the most potentially troublesome. Typically the NdAlO_3 powder is more and more difficult to press after successive firings. If a powder is very dry, as is after being fired at high temperature, it will not stick together very well, so a small amount of starch, about 5% (by mass) improves results.

Pressing the dry target was done in an iron die that has been lubricated by graphite powder. The basic shape is a rectangular collar, that is very closely shaped to two rectangular pistons, as shown in Fig. 1.12(a). The target powder, about 50 grams in total, was dumped into the dye, with the lower piston half-way inserted. If the top piston is put in, and immediately pressed, small variations in the powder surface will cause extreme differential compression of the target, and when the pellet is removed from the dye, it will break. To avoid fracturing the green body, carefully control the flatness of the powder, prior to pressing. Press the bottom piston upwards, until the surface of the powder is just above the collar. Then, drag a straight-edge across the surface of the powder to make a surface that is uniform and parallel with the surface of the collar, as shown in Fig. 1.12(b). Finally, raise the collar so the surface of the powder is at the half-way point in the collar. Then, slowly add the top piston, and compress in a hydraulic press to 20,000 lbs (about 3,000 lbs/in²). Removal of the pellet follows: Use the hydraulic press with some metal blocks to push the collar down (it may be lodged after pressing) until the top of the powder is barely exposed. Remove the top piston then carefully remove the lower assembly from the hydraulic press. Then gently push down the collar until

the top surface of the collar is parallel to the bottom surface of the pellet. Then carefully slide the pellet across the surface of the collar onto an alumina plate, also parallel to the surface of the collar. The pellet is ready for firing.

Firing the pellet was done in a box furnace. The alumina target was fired at 1600 °C for 2 hours. The NdAlO_3 target was fired at 1650 °C for 12 hours. The heating ramped at 5 °C/min until reaching the sintering temperature, where the temperature was held.

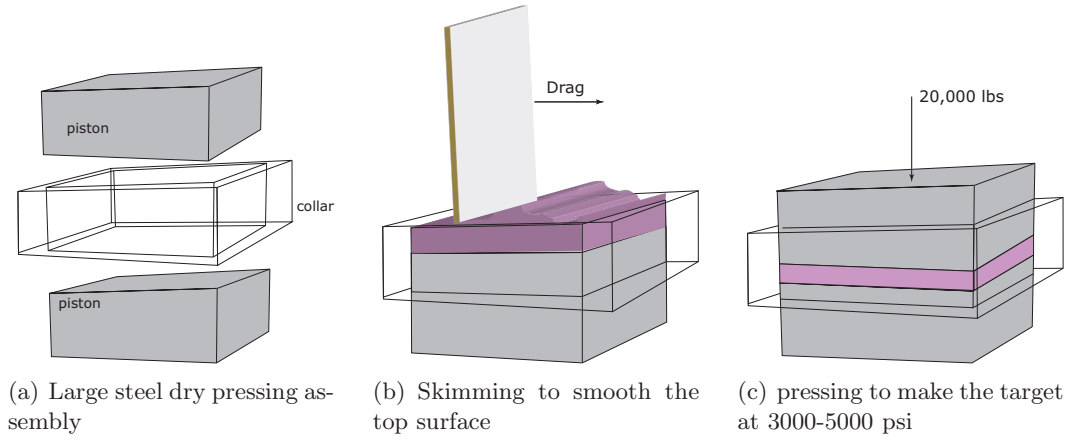


Figure 1.12: The quality of a dry-pressed PLD target correlates with the uniformity of the starting shape. Smoothing the powder surface allows for the most uniformly dense green body formation.

1.3.2 LAM/PLD results

The Ag films were deposited with the nozzle at least 5 mm from the substrate surface. The deposits were also made quite thick just beneath the nozzle. Beneath the nozzle, the film was far too thick for use in an optical experiment, but we found that the edges of the deposit, far from underneath the nozzle were essentially monolayers of Ag nanoparticles, which extended over several hundreds of microns. The film quality of the silver material, at the edge of the deposit is shown in Fig.

1.13.

The silver spreads out, uniformly, on the sapphire substrate. A step-edge visible in Fig. 1.13(a). The coverage is highly uniform over several hundred microns, and is the region of interest for optical studies.

The Ag nanoparticle size is much larger than the SiO_2 particle produced by LAM. The smallest visible Ag particles are about 20 nm, and form larger clusters up to 100 nm due to the high surface energy of the the silver nanoparticles combined with collisions induced by surface diffusion underneath the gas jet.

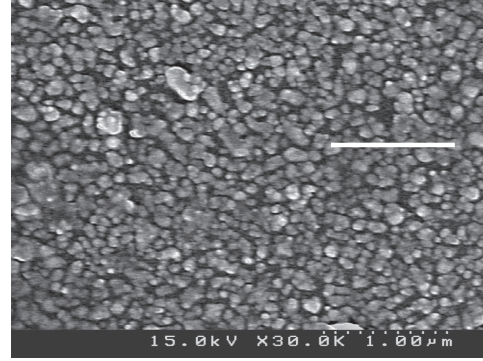
The silver nanoparticles were coated by a layer of PLD-deposited oxide glass, with thickness between 0.5 and 1.0 microns. Both sapphire coatings, as well as NdAlO_3 were made. In order to maintain the silver nanostructure, coatings were made below 300 °C. Fractured surface SEM images reveal how well-coated the nanoparticles are by the PLD layer. Images are shown in Fig. 1.14.

1.4 Summary

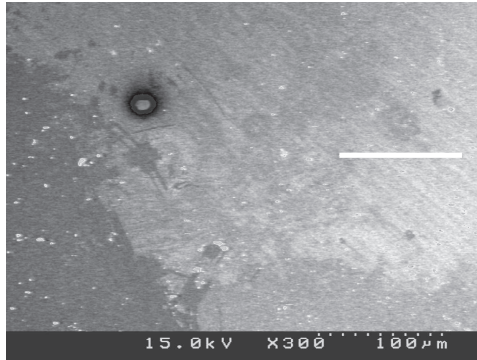
To make optically transparent films using LAM, there are two approaches. One approach is to use hard impacts of mixed, ablated glass and semiconductor particles. In that case, additional heat was required to sinter LAM glass NP films. Two deposition energy regimes were identified, based on differential impaction energy beneath the nozzle. Directly underneath the nozzle, the downward thrust of the gases tended to destroy (erode) the film. Erosion had a large effect on the quality of the glass films, because the nanoparticles are only weakly bonded to each other. By moving the nozzle away from the substrate, the gas pressure on the film was lower and the tendency to erode the films was reduced. The second regime was found near the edge of the film, where the particles deposited with lower energy because of the lower jet velocity and downward pressure. Uniform, low porosity films were produced near the edge.



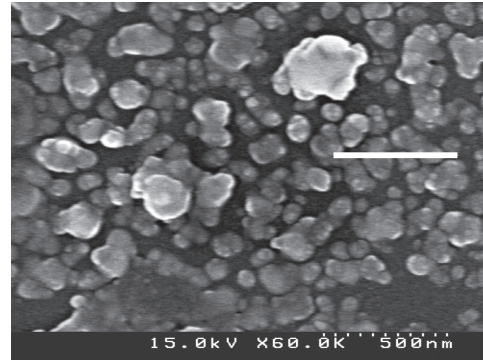
(a) Scale bar is 200 μm . Step edge is visible.



(b) Scale bar is 1 μm .



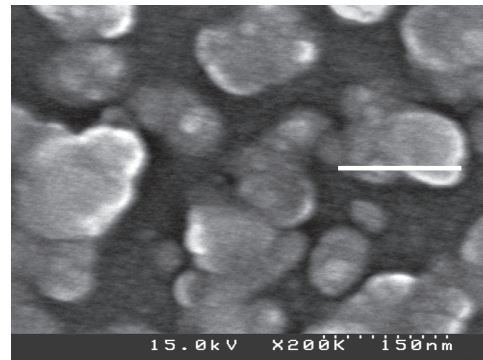
(c) Scale bar is 100 μm .



(d) Scale bar is 500 nm

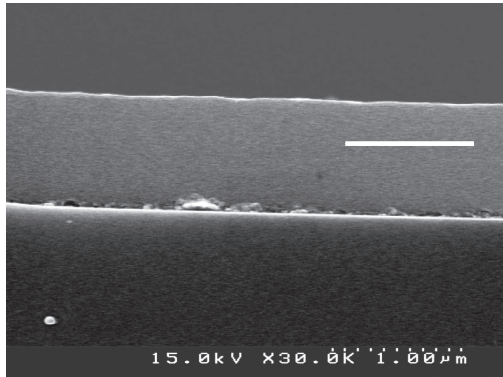


(e) Scale bar is 5 μm .

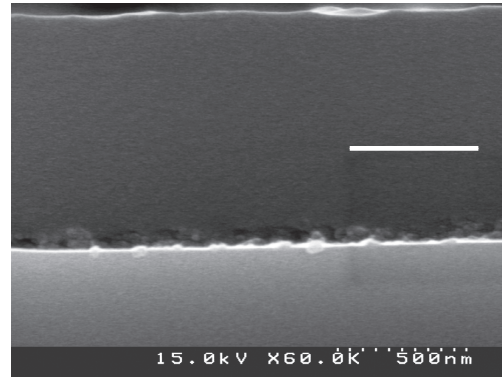


(f) Scale bar is 150 nm

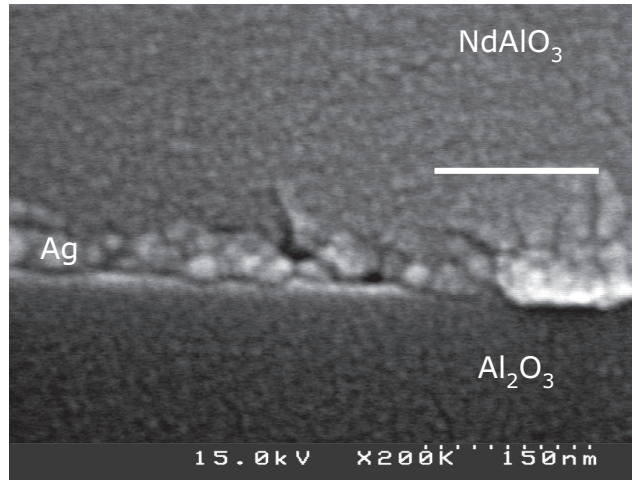
Figure 1.13: Plane-view images of the LAM-produce Ag films at different magnifications far from underneath the nozzle. These films have larger average particle size than the SiO_2 films made under the same conditions.



(a) NdAlO_3 (upper), coating Ag NPs, on a sapphire substrate (below). Scale bar is 1 μm



(b) Scale bar is 500 nm.



(c) Sub-100-nm Ag nanoparticles are encapsulated by the film and the substrate. Scale bar is 150 nm.

Figure 1.14: Fracture-surface (edge-on) SEM images of Ag nanoparticles, coated with NdAlO_3 , on a sapphire substrate.

Highly uniform silver nanoparticle films were found at the edge of supersonically-deposited silver films. The average particle sizes were much larger compared to glass (50 nm versus 5 nm), because of self-sintering of the silver nanoparticles on the substrate. These films were coated by PLD layers of either sapphire or NdAlO_3 , to make nanocomposite interfaces.

Chapter 2

Linear Optical Characteristics

2.1 Optical quality of sintered silica and glass nanocomposites

The force of the gas jet affects the optical quality of the as-deposited glass samples. By increasing erosion near the center of the sample, porosity increased, and scattering increased in the thickest region of the written material. There the scattering was so high that the optical transmission through the line is nearly zero. Optical scattering was found to depend on the position relative to the nozzle orifice. As apparent in Fig. 2.1(a), the edges of the Si:silica films do not scatter light as much as the center, because the average pore size near the edge is uniform and small compared to the wavelength of light. So, even though the material is not dense, the local optical properties can be quite good, as shown in Fig.2.1(b).

There is a direct correlation between the microstructure of the prefired films, and the optical quality of the sintered product. Chapter 1 described much of the structural details of the films, both before and after sintering. Here, the linear optical transmission is measured in those same films. Because of the spatial variation in the quality of each of the samples, a laser-scanning measurement was employed to

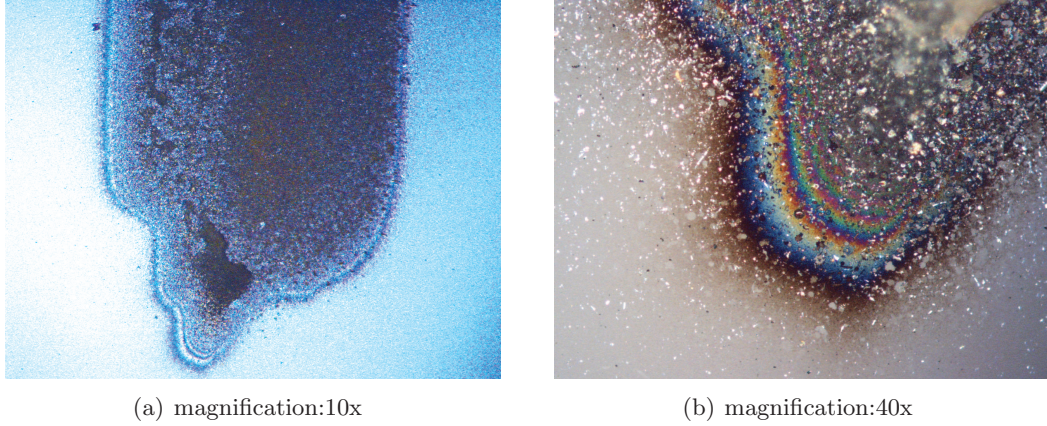


Figure 2.1: Images of an SiO_2 films taken with an optical microscope show how surface modification during the deposition changes the optical quality of the film. Polarization optics enhance the topographic variation of the film.

measure the optical transmission as a function of position in the sintered samples.

2.1.1 x-scanning optical transmission setup

Optical transmission of the materials was performed at 400 nm. The samples were placed in the focal plane of a 2 cm f.l. (focal length) lens, and the sample was stepped through the laser focus, while measuring the transmitted light. The amount of transmitted light is determined by scattering in the film, since the band edge of silica is closer to 200 nm. Consequently, the laser-scanning measurement maps the scattering in the sample, with a spatial resolution given by the focal diameter of incident light, which 7 microns. A schematic is shown in Fig. 2.2.

The x-scanning transmission experiment was performed with a modified mode-locked Ti:sapph oscillator. A thin BBO (Beta-Barium Borate - 100 μm , Eksma Inc.) was inserted into the unfocused beam, to created a weak blue beam, which was focused at the sample surface. The sample is mounted on a linear actuator, with resolution of about 0.1 micron. In practice, a larger x-step size of several

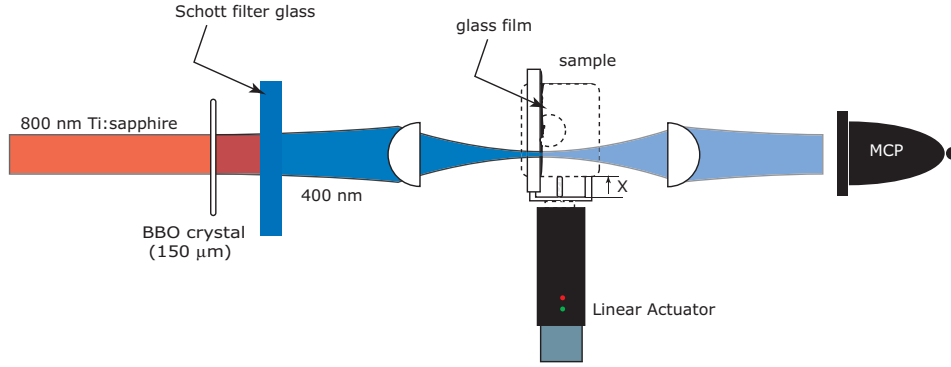


Figure 2.2: Schematic of x-scanning linear optical transmission measurement. The optical source was the frequency doubled output of an 800-nm Ti:sapphire laser.

focal diameters was used, anywhere from 20 microns, to 50 microns.

2.1.2 sintered nanocomposites

The x-scan allowed us to measure the spatially-dependent optical transmission of several of the sintered nanocomposites. Sintered fumed silica, deposited directly onto the substrate in He, without laser ablation was measured first. The ablated and deposited silica (Kobo products 20 microns 99.9 %), from an Ar atmosphere, sintered at 1250 °C followed. Finally, transmission through the sintered soda-lime glass: silicon sample was measured, to compare the optical quality of a LAM-produced nanocomposite to pure glass samples.

2.1.3 ADN fumed silica

Silica nanoparticles were deposited from commercial-brand fumed silica. The average particle size is about 60 nm, and the fumed silica as purchase from the manufacturer is highly agglomerated, so acceleration supersonic nozzle is not well-known. There is reason to believe that the acceleration of agglomerates is affected by their large surface area, so in the velocity field of the gas flow, thermalization is rapid.

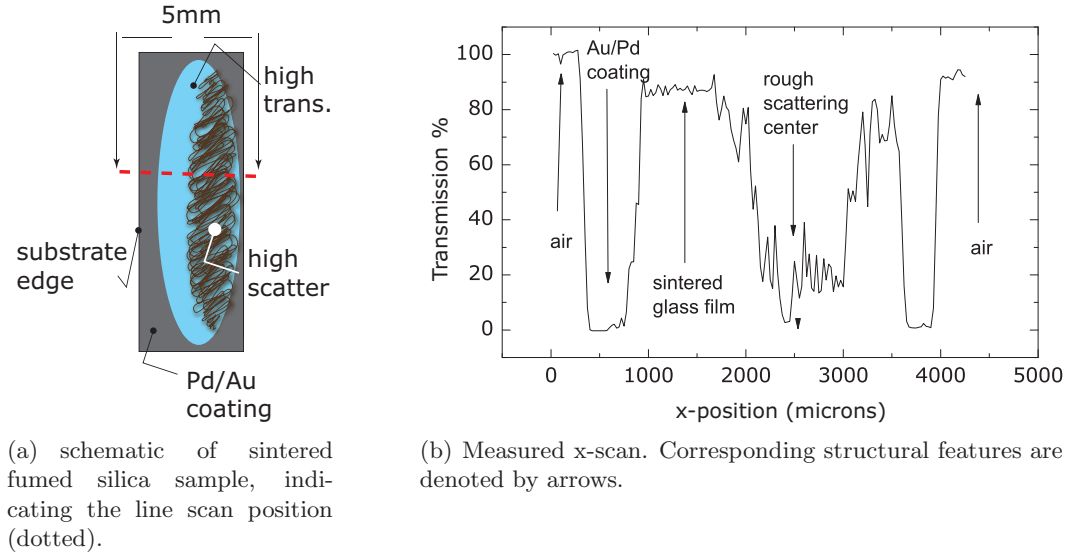


Figure 2.3: Transmission of sintered Degussa fumed silica. The edge of the sample is high-transmission.

Consequently, agglomerates will accelerate to the high gas velocities in the nozzle, but will have a larger deceleration in the bow shock, compared to individual nanoparticles.

Lower deposition energy of fumed silica nanoparticles causes an enhancement of differential deposition. The low deposition velocity, means the initial density of the sample beneath the laser is very low, but the high flow rates easily tear off sections of the weakly bound material, and the downward force compresses the rest of the film. In the center of the sample, large voids develop next to compact structures. However, at the edge of the sample, the situation is different; the lower gas flow rates, introduces a lower tendency to erode the material and a lower compression of the film. Near the edge, the thinner material does not have the eroded pockets, nor does it have the packing density fluctuations found underneath the gas jet.

The initial morphology of the films determines their optical quality after sintering. The x-scan of the sintered fumed silica is shown in Fig. 2.3. The sintered

sample was coated with a thin evaporated layer of Au/Pd (an artifact of previous SEM studies), which had to be removed before prior to the optical measurements. The Au/Pd coating rubbed away in the center of the sample, but it could not be completely removed near the edges, so the x-scan is affected by the presence of the coating. In the measurement, the laser focus begins just off the supporting sapphire substrate, and translates onto the sample edge at 250 microns. The laser encounters the coating and is reflected. When the focus reaches the sintered edge of the deposit, transmission improves for several hundred microns, until reaching the damaged, central part of the deposit, which scatters strongly because of the randomly sized pores. The transmission picks up again at about 3500, but drops again as the focus leaves the sample, returning to the left-over Au/Pd coating. Finally, when the focus completely leaves the substrate, transmission returns to 100 %.

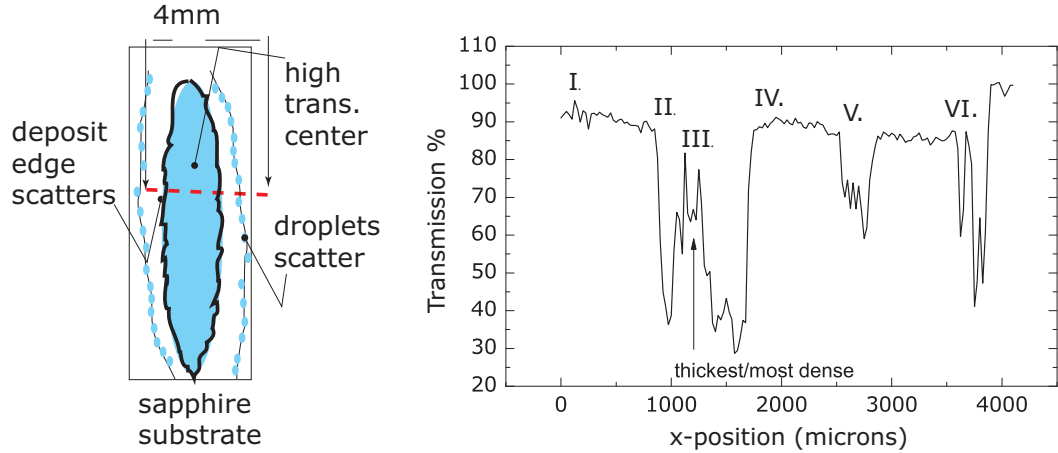
2.1.4 ablated, deposited and sintered silica microspheres

The sintered LAM-produced samples that were produced from laser ablation were different from the fumed silica samples. The LAM-sample is shown in Fig. 2.4

There are several reasons for the different result. First, the ablated nanoparticles are much smaller (5 nm compared to 50-75 nm). The smaller particles impact with less energy, so particle impacts erode the surface less. However, the lower momentum deposit, combined with the smaller particle size, means that the initial (prior to sintering) density of the material is lower. Because of the reduction of viscous flow at the interface, and the low initial density, the edge of the deposit will bead into small spheres on the surface after sintering. But the center of the film, owing to the downward compressive force of the gas jet, is dense enough that sintering produces a more transparent film.

The position-dependent transmission response of the sintered LAM silica sample is shown in Fig. 2.4. In the experiment, the laser was initially focused at

the bare glass surface. After sintering, portions of the substrate previously coated by nanoparticles became exposed as the film reduced in size. A small amount of glass remained at the edge of the initial deposit region. In the transmission scan, the origin (I.) was between the outer edge, and the center of the line, just where the substrate is exposed. Then, the laser was drawn in, towards the center of the line. First, the outer edge of the deposit (II.) at about 900 microns, which is rough, scatters the laser. Then, in the thickest, densest part of the sample (III.), the transmission increases to just below 80 percent. Continuing on, the focus passes through the other edge of the thick deposit (IV.) at 1500 microns, and through one of the outer (beaded) deposit remnants (V.) at 2500 microns, and then off the edge of the substrate (scattering a small amount in the process) at 4000 microns.



(a) schematic of sintered silica nanoparticle sample. Dotted line indicates the line scan position (dotted). (b) Measured x-scan. Corresponding structural features are denoted by arrows.

Figure 2.4: Transmission of sintered Kobo silica nanoparticles. As a consequence of sintering, the center of the sample has a higher transmission than the edges.

2.1.5 x-scan of sintered glass:silicon nanocomposites

In addition to the purely silica samples, the transmission of the soda-lime glass:silicon also measured. Contrary to both large and small silica nanoparticle films, the glass:silicon nanocomposite displayed no region of improved optical quality after sintering. As mentioned in chapter 1, the low quality of the soda lime nanocomposite material is likely due to two things: poor wettability of the soda lime to the sapphire substrate, and the presence of rigid inclusions, which reduced the effectiveness of sintering. Though the concentration of silicon nanoparticles is quite low, other reports indicate they greatly reduce the viscous flow during the sintering process at small concentrations [9].

The x-scan of the nanocomposite is shown in Fig. 2.5. The results of the

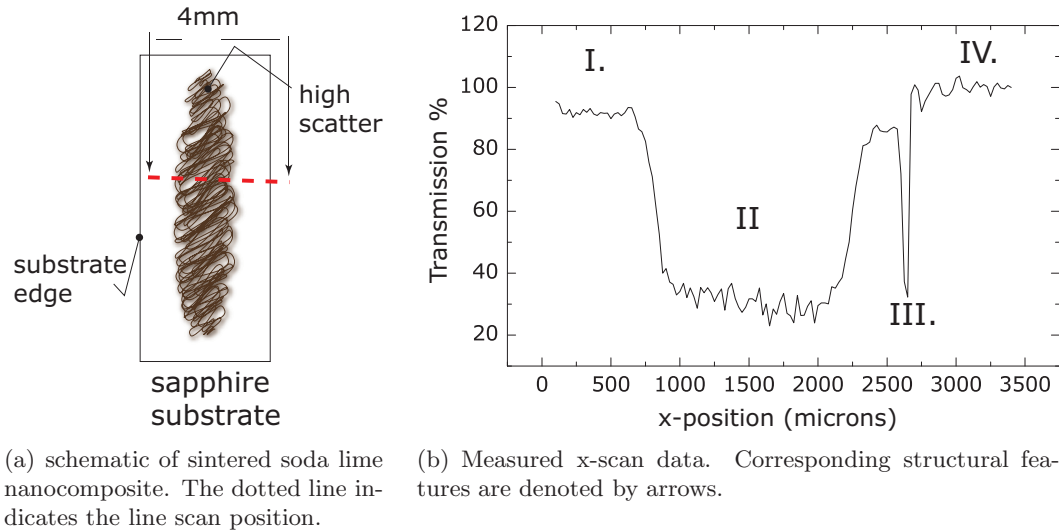


Figure 2.5: Transmission of sintered LAM-made soda lime glass:silicon nanocomposite. The sample is translucent, but sintering had little effect.

silicon are straight-forward ¹. There is not a region of the sample that benefited

¹Note that nano silicon may be absorptive at 400 nm. Repeating the transmission measurement at 800 nm may produce a slightly different result.

from the sintering step. In the measurement the laser focus was scanned, starting in an unexposed part of the substrate (I.), towards the center of the substrate (II.), where the transmission dropped to about 30 %. An additional dip in transmission was observed as the laser focus scattered on the edge of the substrate (III.), just before reaching the highest transmission - in air (IV.).

The work of Scherer *et al.* indicates that the sintering step may be improved if more time were given. Though the presence of the inclusions may slow the viscous flow and subsequent consolidation, it does not completely inhibit the sintering step. In future experiments, longer time spent at the sintering temperature may improve the result, even more so than merely by using a wettable substrate.

It is clear from Figs. 2.3, 2.4, and 2.5 that controlling the scattering due film morphology is most important for improving optical transmission in LAM-produced optical films. Because of the unavoidable problems of erosion during deposition, and of beading during the sintering stage, it will be impossible to completely remove scattering without further modification of the growth method. My suggestion for achieving the lowest optical scattering is as follows: The deposition must be carried with simultaneous heat treatment. The substrate must be heated so that surface temperatures of the nanoparticles can achieve up to 1400 °C C. Even if the electrical connections to the heater were more rigid, heat must propagate through the back of the sample to get to the film, which is very inefficient. A better solution is one which allows for surface temperatures to reach up to 1300 °C C either during deposition, or between multiple depositions. Multiple depositions of nanoparticles and heat are required to obtain a uniform film. With each subsequent deposition, nanoparticles will bead into larger and larger islands until reaching a threshold point at which it no longer scatters light. Sintering the film continually (at least with punctuated heat intervals) during deposition is the only way to avoid void formation in final film.

The current vacuum furnace heater must be modified to reach these temperatures. First of all, the electrical connections to the PBN heater must be made more secure. Because the furnace is mounted on a flexible shaft, inserting and removing samples from the furnace assembly caused the delicate graphite washers to crack. Either the furnace assembly must be made in a single piece or the assembly must be designed so it does not flex when samples are inserted in/out. To improve heat transport to the glass film the molybdenum conducting plate that contacts the PBN heater should be bored through, along with the molybdenum sample holder. Then, heat is radiantly transported to the glass film from the PBN heater. The sample could be returned to an upright position for further deposition after that point. As an alternative, a Kaufman ion source could be installed to sinter the sample between depositions. One drawback of the ion source is that it could not be used during deposition, and evacuation must take place between heating and deposition steps. Additionally, ion sources are known to produce higher defect densities.

2.2 PLD optical films

Because of the difficulty in preparing optical nanocomposites by sintering, PLD films were substituted. PLD films have a very high optical quality. The films primarily used were sapphire, AlN, and NdAlO₃. Preliminary linear optical analysis determined phase matching parameters, group delay parameters and inherent reflection losses. Because the PLD technique produced films with a wedge shape, the measurements were done on just a small, $\approx 1 \text{ mm}^2$ total area, to improve accuracy.

2.2.1 aluminum nitride on sapphire

The linear transmission of sapphire and AlN films and sapphire were measured and the result is shown in Fig. 2.6. We treat the analysis of these together, since they both have a large band gap near. The transmission of the sapphire coating does

not display interference fringes, since it is index-matched to the substrate. The

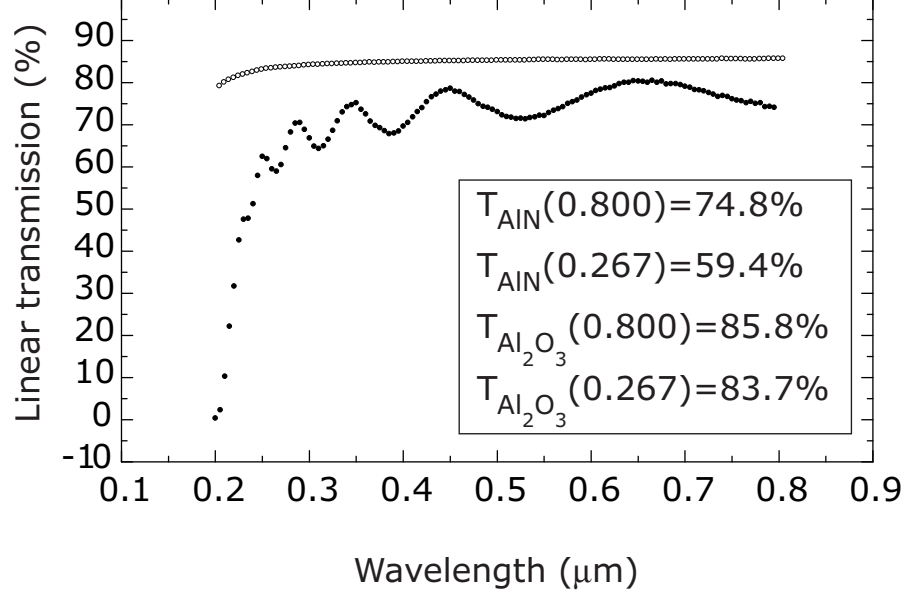


Figure 2.6: Linear optical transmission through the sapphire PLD film on Al_2O_3 [0001] substrate (○) and the AlN/substrate sample (●).

interference fringes in the linear transmission of AlN determine the linear index, absorptivity, and film thickness [11]. The calculated index of refraction is shown in Fig. 2.7, and was fit by an analytical Sellmeier equation,

$$n(\lambda) = \sqrt{a + \frac{b\lambda^2}{(\lambda^2 - c^2)}}, \quad (2.1)$$

The fitted parameters for both the AlN and sapphire films are shown in Table 2.1².

Individual reflection losses at each interface can be distinguished from the total loss of the film and substrate material. For instance, the total optical transmission of the pump field is determined by the product of the Fresnel transmission

²note the stated errors are 1- σ standard deviations. The sapphire index error is negligibly small, and not stated. Digits in parentheses indicate the error in the last digit $1.4(2) \equiv 1.4 \pm 0.2$

Table 2.1: Sellmeier fit parameters

| material | a | b | c |
|--------------------------------|--------|--------|----------|
| Al ₂ O ₃ | 0.898 | 2.172 | 0.092 |
| AlN | 1.4(2) | 2.7(2) | 0.135(4) |

factors in the bulk and the thin film,

$$\mathcal{F}_1^T = \mathcal{F}_1^B \mathcal{F}_1^{\text{TF}}. \quad (2.2)$$

The field transmission factor \mathcal{F}_i^B defines the i^{th} field's transmission through a bulk-like interface. The field transmission factor $\mathcal{F}_i^{\text{TF}}$ defines transmission at the thin film, Al₂O₃ /AlN interface. Each of these contributes separately to the nonlinear thin film equations, which will be discussed in subsequent chapters. They are assumed to be constants, since both the third-harmonic and fundamental are far from the band edge.

Individual, bulk interface Fresnel coefficients were calculated from the index of refraction, and the thin film coefficients, due to multiple reflections, were inferred from the linear transmission measurement. At zero degree incidence of the i^{th} field, from a bulk material n to bulk material n' , the Fresnel field transmission factor is

$$\mathcal{F}_i^B(\lambda) = \sqrt{1 - R(\lambda)}, \quad (2.3)$$

where

$$R(\lambda) = \frac{(n(\lambda) - n'(\lambda))^2}{(n(\lambda) + n'(\lambda))^2} \quad (2.4)$$

is the reflected intensity at the n/n' interface. The important Fresnel factors are summarized in Table 2.2. We made use of the linear transmission to easily account for thin film interference.

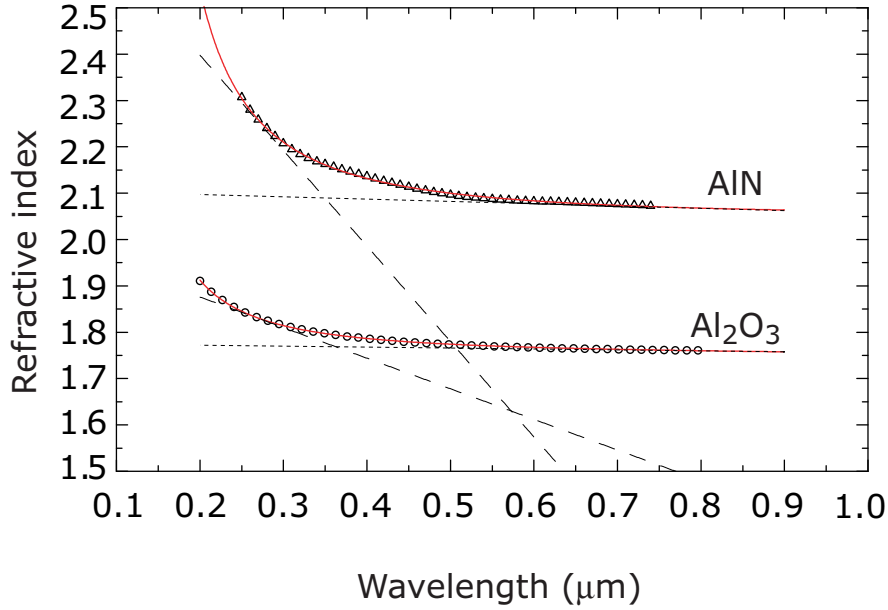


Figure 2.7: A thin film algorithm was used to extract the linear index of AlN(Δ), which was fitted by the Sellmeier equation in Eq. 2.1. Published linear data for sapphire(\circ) were fitted to the same Sellmeier form, and used to describe dispersion in the substrate. Data from the fits are shown in Table 2.1. The dashed lines are the tangents at both the third-harmonic and pump wavelengths, calculated from the fitted curve. The differences in slopes indicate that a large group-velocity mismatch exists between the fundamental (short dashes) and third-harmonic (long dash) pulses.

2.2.2 neodymium-aluminum oxide PLD sample

A nice feature observed in the NdAlO₃ system is that it index-matches to sapphire. The relative difference between the indices of refraction is less than 5% [10]. When the NdAlO₃ samples were prepared on the sapphire substrates, and subsequently analyzed in a uv-vis spectrometer, they show no interference fringes. NdAlO₃ is also highly transparent into the ultraviolet. As shown in Fig. 2.8, just the atomic resonances of the Nd³⁺ ion are visible. The resonances of the neodymium ion are used in many solid state photonic devices, most notably in the Nd:YAG laser system.

Table 2.2: Fresnel factors

| $\mathcal{F}_i^j(\omega)$ | value | description | method |
|-----------------------------|----------|------------------------------------|--|
| \mathcal{F}_1^B | 0.961(1) | pump transmission air/sapphire | $\sqrt{1 - \frac{(1-n(\lambda_0))^2}{(1+n(\lambda_0))^2}}$ |
| \mathcal{F}_3^B | 0.956(1) | TH transmission air/sapphire | $\sqrt{1 - \frac{(1-n(\lambda_0/3))^2}{(1+n(\lambda_0/3))^2}}$ |
| $\mathcal{F}_1^{\text{TF}}$ | 0.899(3) | pump transmission through AlN film | $\frac{\mathcal{F}_1^T}{\mathcal{F}_1^B}$ |
| $\mathcal{F}_3^{\text{TF}}$ | 0.806(3) | TH transmission through AlN film | $\frac{\mathcal{F}_3^T}{\mathcal{F}_3^B}$ |

When pumped at either of these resonances, the neodymium ion will fluoresce at several visible and IR wavelengths. The exact wavelength of the photon depends on the crystal field in the neighborhood of the neodymium ion. In this sample, the 810-nm pump laser coincides with the $^4I_{9/2} \rightarrow ^4F_{5/2}$ transition in the neodymium ion [12]. When excited at 800 nm, fluorescence at 1150 nm was observed.

2.2.3 neodymium-aluminum oxide PLD / silver nanocomposite sample

When Ag nanoparticle were deposited onto the sapphire substrate prior to depositing the glass, the uv-vis spectra of the composite sample changed. Because of the presence of the silver in between, the interface between the NdAlO₃ thin film and the sapphire substrate no longer index-matched. The silver-coated interface caused the NdAlO₃ to act like a low Q cavity, which displays interference fringes, once again, as shown in Fig. 2.9.

As discussed in the context of the optical quality of the LAM films, the downward gas pressure during deposition causes the transmission to drop in the region of the sample deposited underneath the supersonic nozzle. Because of that, the transmission measurement shown in Fig. 2.9 was taken from the edge of the sample. In addition to the interference fringes in the spectra, the silver nanoparticles absorb between 400-600 nm. Still visible is the neodymium ion's atomic absorption

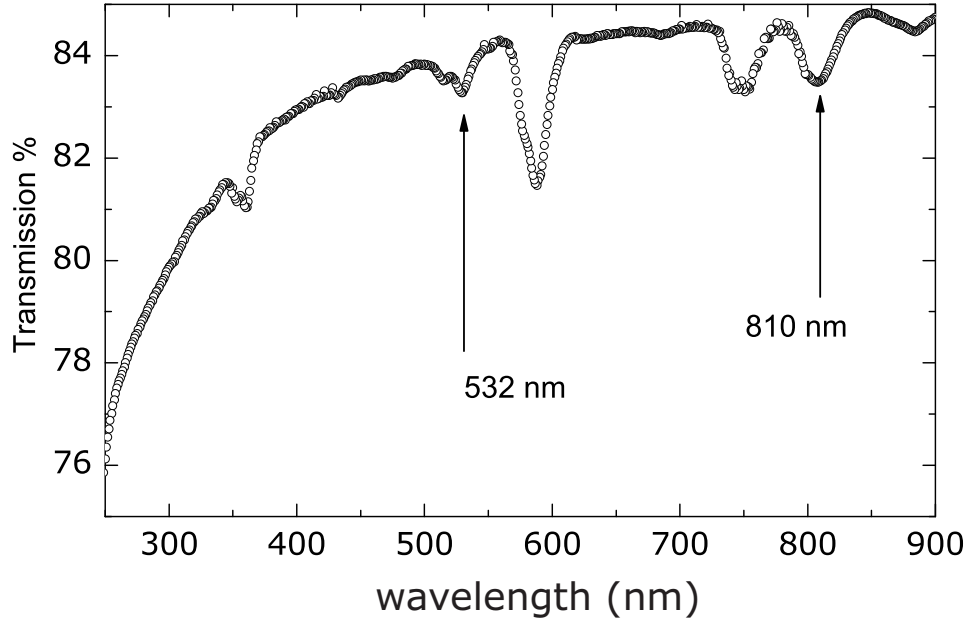


Figure 2.8: The linear transmission of NdAlO_3 displays two of the prominent atomic resonances of the Nd^{3+} ion, one at 532 nm, and another at 810 nm. Though the film is grown on sapphire, no interference in the film indicates the film and substrate have nearly identical indices of refraction.

at 810 nm. Both of these optical resonances are important to the development of the nanostructured material's nonlinear properties.

The macroscopic transmission suggests that the microscopic dielectric constant of the nanoparticle/matrix composite can be modeled by an effective dielectric, which has some properties of each separate component. Indeed, an effective dielectric is appropriate and the formalism for such a material has been provided by J.C. Maxwell-Garnett. In this case, for some volume fraction d of nanoparticles the effective dielectric

$$\epsilon_{\text{eff}} = \tilde{\epsilon}_{\text{m}} \left\{ 1 + 3d \frac{(\tilde{\epsilon}_{\text{m}} - \epsilon_{\text{n.p.}})}{(\tilde{\epsilon}_{\text{m}} + 2\epsilon_{\text{n.p.}})} \right\}, \quad (2.5)$$

is written in terms of the complex matrix dielectric $\tilde{\epsilon}_{\text{m}}$ and the real part of the nanoparticle $\epsilon_{\text{n.p.}}$ [13, 14, 15].

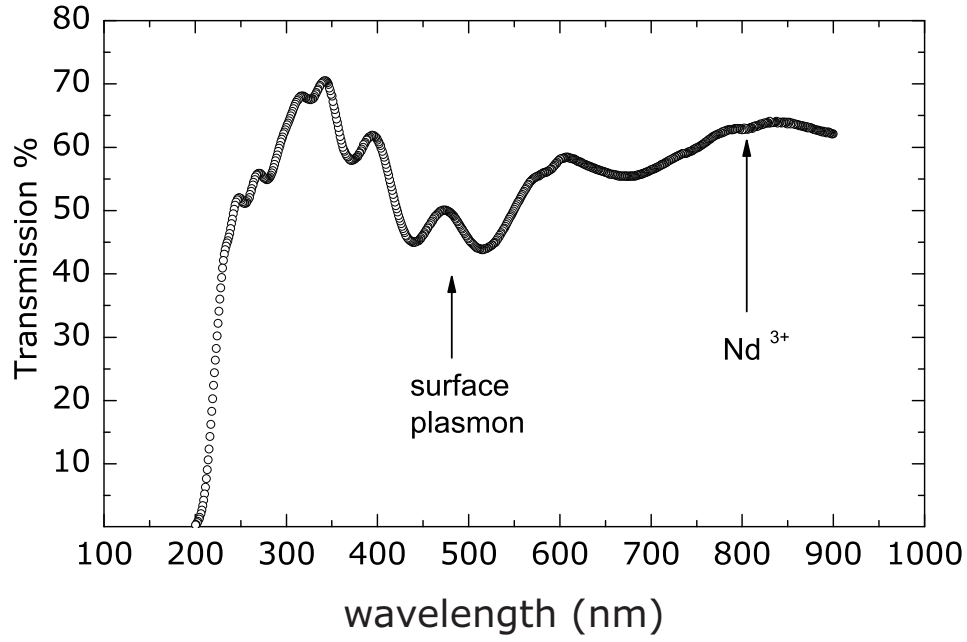


Figure 2.9: The linear transmission of the edge of the Ag/NdAlO₃-coated sample displays two of the prominent resonance of each system: the atomic resonances of the Nd³⁺ ion, at 810 nm, and the silver surface plasmon at 400 nm. The periodic modulation of the spectrum is caused by the silver, which breaks the index matching between the film and the substrate.

2.3 Surface plasmon resonance

2.3.1 theory/background

A flat, conducting surface has an electromagnetic resonance called a surface plasmon (SP), whose frequency and parallel momentum obey the dispersion relation

$$k_{\parallel}^2(\omega) = (\omega/c)^2 \text{Re}[\epsilon_m \epsilon(\omega) (\epsilon_m + \epsilon(\omega))^{-1}], \quad (2.6)$$

where $\epsilon(\omega)$ is the dielectric function of the metal, and ϵ_m is the surrounding medium [16]. These excitations are not radiative, and the excitations quickly dissipate into the bulk of the material as heat. These waves are evanescent in nature, because

momentum at the surface is greater than that of an vacuum wave at the same frequency [17].

In bulk solids, the absorption into these surface modes were first seen by electron-loss spectroscopy, and subsequently by optical-loss [18, 19]. But it was unclear why radiation was not emitted. It was soon recognized that radiation was only visible from gratings and roughened surfaces [20]. These observations have spurred countless investigations of the relationship between micro-structure and optical properties of metallic surfaces.

Nano-roughened surfaces have the advantage of being SP active, but due to the small particle size, are optically translucent. For a particulate material, there is a resonance in the optical absorption with energy $\hbar\omega_R$, found from the condition $\text{Re}[\epsilon(\omega_R)] = -2\epsilon_m$, which is the dipole resonating term. Higher-order terms can also be excited, but they do not radiate [21].

The optical absorption corresponds to surface charge density oscillations similar to traditional plasma oscillations. The free electrons in a metal move against the ionic lattice. The stabilizing force in the motion of free electrons about the ion lattice is *Quasi neutrality*, which states that stabilization occurs by forcing the net electric charge in the material toward zero. Perturbations about neutral charge equilibrium condition sets up a restoring potential, which solved roughly as the wave equation, and shows wave-like solutions. Solving the system in three dimensions describes the bulk plasmon. In two dimensions, the solution is a surface plasmon.

Since in a metal, charge is perturbed by optical excitation, surface plasmon excitations will contribute to the medium's dielectric $\epsilon_{\text{eff}}(\omega)$. The solution of Maxwell's equations states that charge density is altered at the boundary of two dielectrics. These conditions describe the Clausius-Mosotti solution for a dielectric material embedded in another. The solution to the Clausius-Mosotti equations shows that the energy of the surface plasmon is affected by the surrounding dielec-

tric.

2.3.2 experiment

Surface plasmon resonances were observed via optical extinction in temperature-activate suspensions of LAM-generated Ag nanoparticles [22]. In those experiments, prior to temperature activation, the particles agglomerated, Rayleigh scattering dominated, and the liquid samples were entirely opaque. When Ag is ablated, and collected onto a bare sapphire substrate, force of impact causes the nanoparticles to sinter into a near solid-density material, which again is opaque. However, on portions of the substrate far from just beneath the supersonic jet, impacts are less frequent, and produce a lower density film, which is highly plasmon active. The silver nanoparticle film varies from one to two monolayer thick, and is yellow in appearance. UV/VIS measurements of the silver monolayers were carried out (CARY 5000). The transmission results are shown in Fig. 2.10. The plasmon absorption in the bare silver sample peaks at about 436 nm and has a FWHM of 80 nm. The NdAlO₃-coated sample peaks at approximately the same position, and is more broadened. The sapphire-coated sample does not display a strong absorptive peak, and appears to be blue-shifted with respect to the other samples. Always accompanying the absorptive maxima in silver is a transmission maxima, which peaks at 320 nm, and is due to a bulk inter-band transition in the solid.

2.3.3 simulation

There is a granular film simulator that is free for download, written by Ingve Simonsen and R. Lazarri called *Granfilm*. It takes into consideration particle-particle interactions as well as quadrupolar interaction terms. It has the capability of simulating the response of an island monolayer, for different substrate conditions as well as different material coatings. Since the code takes into consideration all the

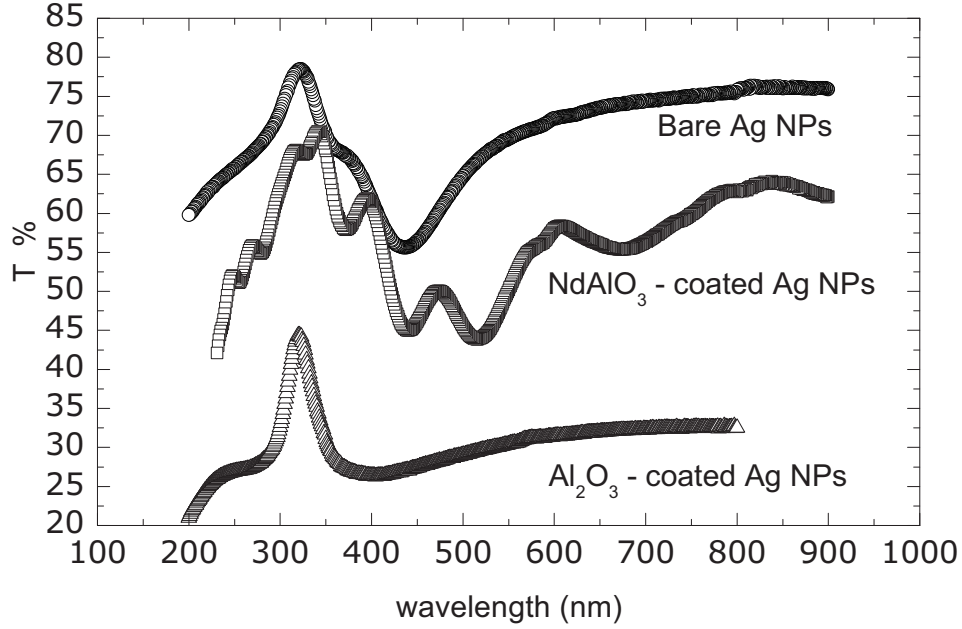


Figure 2.10: Transmission data of Ag nanoparticles on a 500 μm substrate. The bare Ag sample (\circ) and NdAlO_3 -coated sample (\square) are compared with a sapphire-coated sample (\triangle).

features in the silver materials shown in Chapter 1, the *Granfilm* code was used to simulate the absorption of both the bare and coated silver samples, including higher-order terms. However, injudiciously including higher-order multipole and interparticle coupling terms caused the simulated optical response to deviate from observed values. The results of the simulation are shown in Fig. 2.11.

In the simulation plotted in Fig. 2.11, inter-particle effects were ignored, and only the lowest 2 multipolar terms were included. The main result of the simulation is to show that the wavelength of the resonance is significantly altered from the particle in vacuum response when resting on a substrate. Aside from the exaggerated absorbance of the simulation, a comparison of the simulation and the experimental data shows qualitative agreement. It is interesting to note that low-

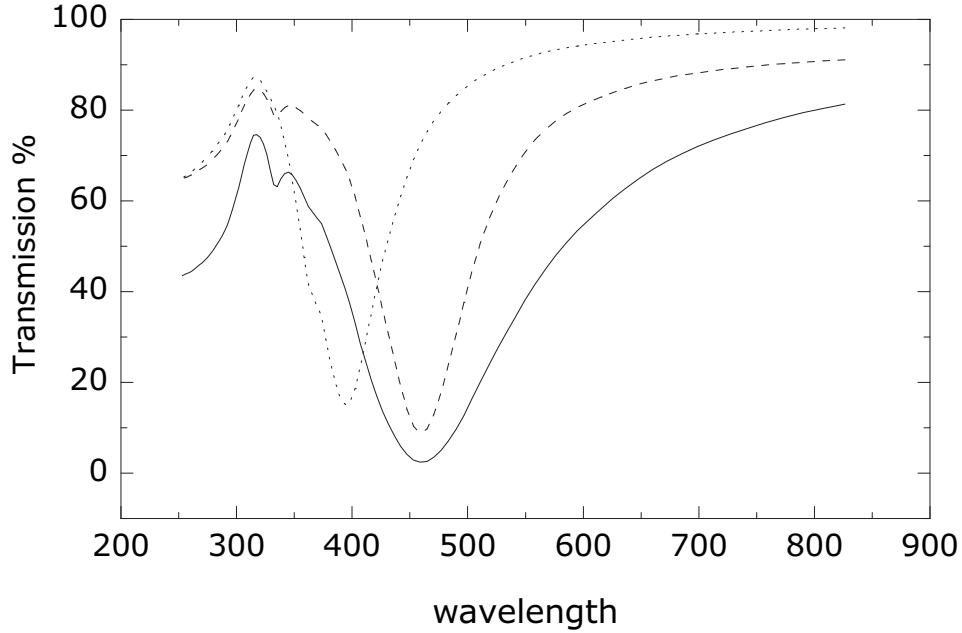


Figure 2.11: *Granfilm* simulations of the optical transmission of 35(dash) and 70-nm-diameter(solid) Ag nanoparticles resting on sapphire. As a comparison, the simulated optical response of 35-nm particles in vacuum is shown (dotted).

order *Granfilm* simulations of coated particles do not significantly differ from those of bare particles on a substrate. However, the NdAlO_3 PLD layer does not fully penetrate the particles, causing a bare regions between the silver and the sapphire substrate. The presence of these small voids lowers the symmetry of the optical response further, necessitating the inclusion of higher-order expansion terms in the simulation. The calculation showed that these voids cause the plasmon resonance to shift 0.25 eV lower in energy from 460 nm to 506 nm. This red shift may be the reason for the slightly red-shifted SP in the NdAlO_3 -coated sample. However, even with the addition of the higher-order terms, only weak qualitative agreement with the measured transmission spectra in Fig. 2.10 was found. For instance, the lack of a distinct SP in the sapphire-coated sample is unclear. The lack of interference fringes in the sapphire-coated sample indicates the sapphire PLD coating was thinner than

the NdAlO₃ coating. It likely the case that non-spherical particle shapes, multipole effects, and the atomic resonances of the neodymium ion will add further corrections to the calculated extinction spectrum. Such additional corrections may be required to accurately describe the data in Fig. 2.10.

2.4 Field enhancement

Field enhancement is a fundamental aspect of plasmonic systems, and is one of the primary reasons why plasmonic systems are technologically utilized. If either the excitation or emission field is resonant with the plasmon the polarization of the material is enhanced, producing a higher photon production efficiency. By increasing the local field of either the input or output field, the local dipole moment increases. In some sense, surface roughness is the origin, because it increases local material curvature. For that reason, smaller nanoparticles have been argued to provide bigger enhancement. Many early calculations of the optical response of metal nanoparticles indicated small (5-nm) diameters exhibit field enhancement in excess of 3 orders of magnitude greater than large (50-nm) nanoparticles. However, it was later found that size-dependent effects based on image charges do not agree with experimental results. Consequently, models that account for size-dependent lattice changes, conductivities, and multiparticle (agglomerate) effects are desired [21].

The inherent, local field-enhancement factor for spherical particles

$$g = (\epsilon - \epsilon_m)/(\epsilon + 2\epsilon_m). \quad (2.7)$$

indicates a resonance occurs when ω is chosen to satisfy $\epsilon(\omega) + 2\epsilon_m(\omega) = 0$. The factor g is known as the Lorentz local field factor, and the resonance is tuned by changing the dielectric constant of the surrounding medium ϵ_m . The dependence

on the surrounding dielectric is derived from boundary conditions on Maxwell's equations, which change the charge density of surface-bound electrons. The factor g is plotted for several different surrounding media in Fig. 2.12.

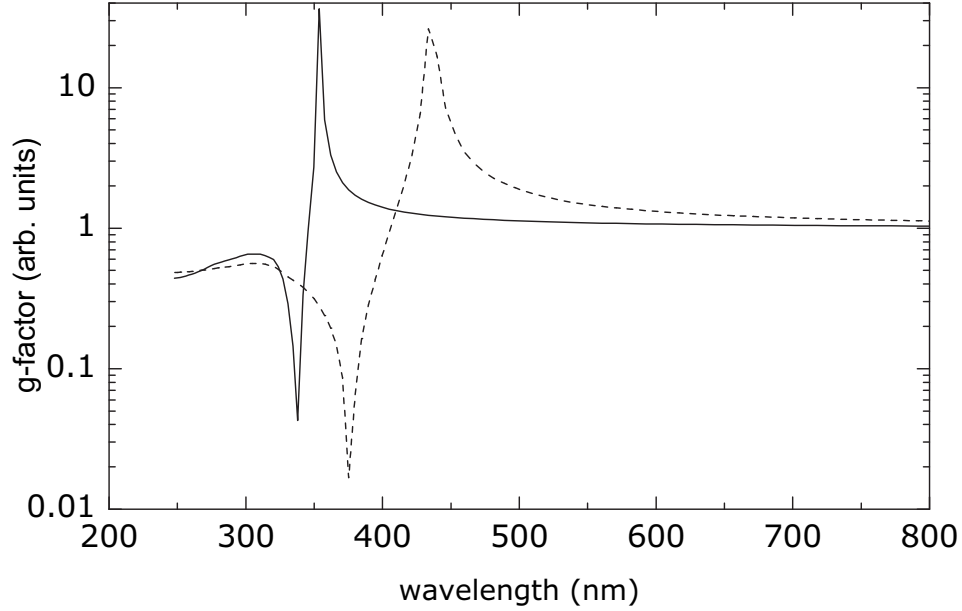


Figure 2.12: The wavelength dependence of the local field-enhancement factor in Eq. 2.7 is plotted for a silver nanoparticle in vacuum (solid) and for a silver nanoparticle in sapphire (dashed).

Field enhancement has been utilized in SERS (Surface-enhanced Raman spectroscopy). Because of it, molecular adsorbates were shown to have Raman signals millions of times larger than unadsorbed molecules. Field enhancement has been used to study Raman, fluorescence, and charge transfer of surface-adsorbed molecules [21].

Work by N. Halas and H. Atwater has shown that microstructure affects local field strength through particle-particle interactions. Both near neighbor and individual particle shapes have been shown to further enhance local field formation. Shape effects have been investigated by in the case of hemispheroids of silver on

a substrate, including damping into the bulk, and found optimal shapes that could create larger fields. They found spheroids that are 10 times as long as they are wide will have field-enhancement factors of 1000. It explained the observed 'lightning rod effects' [23, 24].

In the nanoporous materials formed from LAM, fractal networks of nanoparticles may enhancing fields strongly. 'Lightning rod' effects may be present when two particles adhere. Because the particles are tightly packed, coherence between particles will be important to the optical response even though the average particle separation is larger. The potential in the electrostatic approximation, assuming a the wavelength of the incoming field λ is large compared to the spherical particle, is given by

$$V(r, \theta) = E_0(r - gR^3/r^2) \cos(\theta), \quad (2.8)$$

where R is the sphere radius, r is the distance from the center of the sphere [25]. Because of the non-zero value of the field strength outside of the particle indicated by Eq. 2.8, clusters of particles produce local fields that are stronger than materials composed of isolated particles.

2.5 Conclusions

The optical transmission of sintered glass films produced by supersonic deposition of nanoparticles was analyzed using a cross sectional laser scanning setup. The cross section transmission data correlated with the microstructure of the films, observed in Chapter 1. Both large and small nanoparticle films showed improved optical transmission after sintering. In the case of large particles (60-100 nm) the highest optical quality was observed near the edge of the deposit, where the initial porosity was uniform; the center of these films were mostly eroded, so voids and pits formed in the material after firing produced scattering centers that lowered transmission.

Smaller nanoparticles (5-10 nm) were formed from ablation of 20 μm silica spheres. When deposited in argon, with a nozzle to substrate distance that was larger than 1 mm, the center of the deposits were found to be uniform and without pores. However, because of reduction of diffusion near the surface of the material, and the lower initial density of the films composed of smaller nanoparticles, the final films did not completely cover the substrate.

Deposition of silver nanoparticles followed by PLD of either sapphire or neodymium aluminum oxide produced exhibited a much better optical quality overall. Film quality was uniform enough to allow a straightforward uv-vis analysis of the optical constants of aluminum nitride and sapphire. The monolayers of silver nanoparticles exhibited strong extinction due to surface plasmon oscillation. Atomic resonances were identified in the near solid-density NdAlO_3 films, which index-match to the sapphire substrate. Extinction due to both Ag and Nd^{3+} was observed in the nanocomposites. The location of the plasmonic resonances matched relatively well with model calculations. Some aspects of plasmonic systems, namely field enhancement, were discussed in preparation for following chapters, which show how field enhancement impacts higher-order optical nonlinearities.

Chapter 3

Second-Order Nonlinear Effects

3.1 Second-harmonic generation in PLD aluminum nitride

In the second-order, the general three-wave sum-frequency mixing process is governed by the susceptibility tensor $\chi_{ijk}^{(2)}$. Because these three fields are coupled, the dynamical evolution of any fields can be very difficult to describe. The tensor $\chi_{ijk}^{(2)}(\omega_3, \omega_2, \omega_1)$ describes the probability for the absorption of 1 photon each of ω_1 and ω_2 , producing 1 photon at ω_3 , and has 27 elements. But there are a total of 12 different ways in which these three fields can interact. For instance, the absorption of a photon in field 3 with simultaneous stimulation at field 1, and 2 is described by $\chi_{ijk}^{(2)}(\omega_2, \omega_3, -\omega_1)$. There are twelve different three photon processes in all, and each one has 27 elements because each of i,j, and k can independently be either x,y, or z. The coordinates x,y,z are determined relative to the local crystallographic axes. The tensor component $\chi_{xyy}^{(2)}(\omega_3, \omega_2, \omega_1)$ determines the efficiency that an x-polarized photon at the frequency ω_3 is produced from 2 y-polarized photons at frequency ω_1 and ω_2 , respectively [26].

3.1.1 rotational measurements

Though there are many tensor components, in most cases only the hand-full of independent ones, which are determined by the particular crystal symmetry in the material are important. When two of the fields are identical, as in the case of harmonic generation, the problem is further simplified. Considering only the $(\omega_1, \omega_1) \rightarrow \omega_2$ process, and for the nitride semiconductors, with hexagonal C_{6v} (Shoenflies notation; also seen as C_{6v}^4 or $6mm$) symmetry gives the symmetry class of wurzite AlN. The nonzero tensor elements are

$$\begin{aligned} \chi_{zzz}^{(2)} \\ \chi_{xzx}^{(2)} &= \chi_{yzy}^{(2)} \\ \chi_{xxz}^{(2)} &= \chi_{yyz}^{(2)} \\ \chi_{zxx}^{(2)} &= \chi_{zyy}^{(2)}. \end{aligned} \tag{3.1}$$

The effect of rotating the AlN crystal is determined by tensor rotations of the lab-frame tensor

$$\chi_{ijk}^{(2),lab} = R(\phi)_{i\alpha} R(\phi)_{j\beta} R(\phi)_{k\gamma} \chi_{\alpha\beta\gamma}^{(2),crystal}. \tag{3.2}$$

Where

$$R_z(\alpha) = \begin{pmatrix} \cos(\alpha) & \sin(\alpha) & 0 \\ -\sin(\alpha) & \cos(\alpha) & 0 \\ 0 & 0 & 1 \end{pmatrix}$$

refers to a rotation of α about the z axis in the lab,

$$R_y(\beta) = \begin{pmatrix} \cos(\beta) & 0 & \sin(\beta) \\ 0 & 1 & 0 \\ -\sin(\beta) & 0 & \cos(\beta) \end{pmatrix}$$

refers to a rotation of β about the y axis in the lab, and

$$R_x(\gamma) = \begin{pmatrix} 1 & 0 & 0 \\ 0 & \cos(\gamma) & \sin(\gamma) \\ 0 & -\sin(\gamma) & \cos(\gamma) \end{pmatrix}$$

refers to a rotation of γ about the y axis in the lab. With these rotations, any arbitrary crystal position can be modeled.

The tensor mapping model has been used to analyze the rotational dependence of SHG in thick GaN crystals as well as in thin films grown on crystalline semiconductors [27, 28]. Rotational second-harmonic studies have also been performed on AlN, which has been grown via ion sputtering [29]. The effect of the tensor susceptibility is observed by rotating the crystal relative to the fundamental laser field.

How exactly a rotational measurement is performed can have a large influence on the signal observed. The rotational anisotropy of second-harmonic generation from our aluminum nitride thin film was found by rotating the crystal. Rotating the fundamental laser polarization with a $\lambda/2$ waveplate while maintaining a fixed sample orientation is an equivalent approach. There are problems with rotating the polarization. Our setup incorporated a grating, and because of its polarization dependence, the signal would have to be deconvoluted in a non-trivial way. Also, the $\lambda/2$ waveplate has its own rotational second harmonic signal which is small, but the same order of magnitude as the aluminum nitride signal. Though rotating the sample instead of the optics may cause the laser focus to move relative to the surface of the nonlinear material, the signal is easier to interpret. Another benefit is that the polarization optics do not need to be rotated if the fundamental source has a constant polarization. In our case, measurements were performed using a monochromator, coupled to an Optical Multichannel Analyzer (Princeton Research

model 1420). A schematic of the rotational second harmonic generation apparatus is shown in Fig. 3.1.

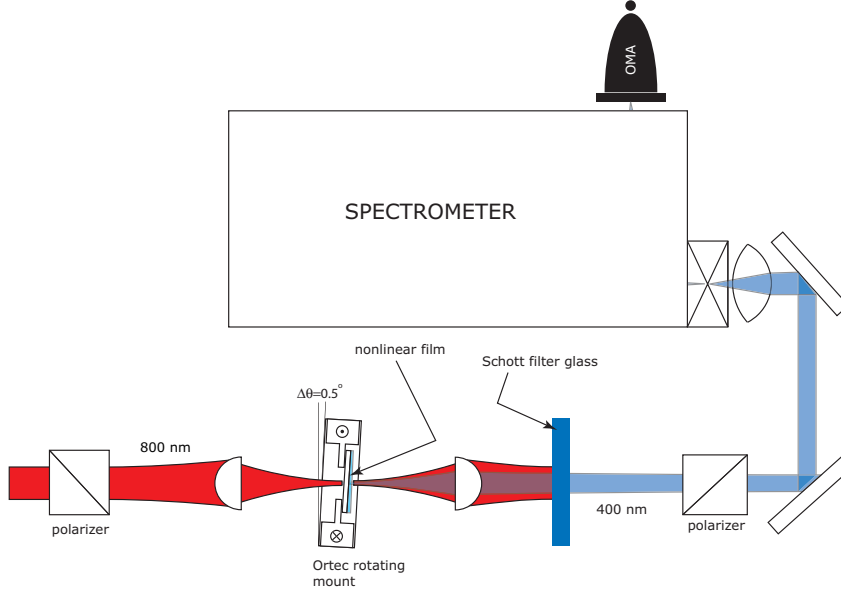


Figure 3.1: Schematic of rotational SHG anisotropy measurement

3.1.2 observation of crystal texture

Though most plasma processed growth of AlN produces an amorphous or highly polycrystalline material that does not show a well-defined crystal axis, PLD grown AlN is known to produce crystal texturing [30, 31, 32]. Attempts to quantify the long-range ordering of the crystal grains using nonlinear optics techniques have been reported [29]. What causes texturing is not fully understood, but is thought to correspond to unique conditions during growth. We confirmed our film is textured by measuring the rotational dependence of second-harmonic generation and by performing x-ray rocking curves. The results of the second-harmonic studies are reported here, but the x-ray work is reported in Jonghoon Baek's thesis [10].

To analyze the AlN texture, the intensity of the second harmonic was recorded

as the sample was rotated about the surface normal vector, which was slightly tilted with respect to the z -propagation axis (≈ 1 deg). The azimuthal SHG measurements are shown in Fig. 3.2(a).

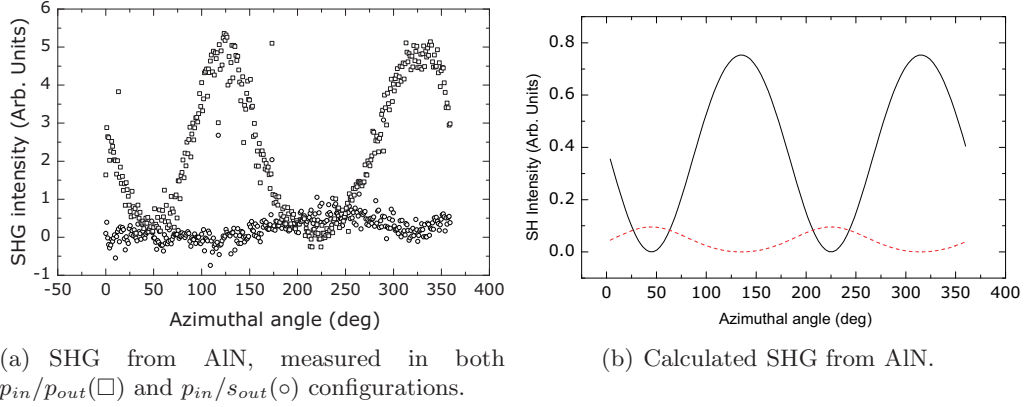


Figure 3.2: The rotational SHG response of AlN is well-fit by convolving several rotations $R_x(\phi_x)$ $R_y(\phi_y)$ $R_z(\phi_z)$.

Since we observe SHG, we know there is some macroscopic ordering to the wurzite microcrystals; the crystals, themselves, are too small to be SHG-active. Aluminum nitride films produced by PLD show a variable grain size as the thickness increases, from a small size near the sapphire interface, up to near 100 nm at the air interface [32]. For materials without a center of inversion, or that are suitably polycrystalline, there should be no SHG emitted. For the SHG case, all the signal originated in the film; the sapphire substrate with (0001) orientation has no SHG response.

Using Eq. 3.2, and considering a very slight tilt of the AlN crystal texture about the y -axis which was less than $\pi/10$ (zero tilt gives identically zero), predicts a rotational anisotropy due to C_{6v}^4 that matched very well with the experimental results. For the tilted crystal-axis orientation, the form of the solution for each of

the x and y – polarized second-harmonic fields are

$$\begin{aligned} I_x(3\omega) &\propto \cos(\delta + \alpha)^2 (\cos(\delta + \alpha)^2 (2 + \cos(2\beta)) + 3 \sin(\delta + \alpha)^2 \sin(\beta)^2) \\ I_y(3\omega) &\propto \sin(\delta + \alpha)^2 (\cos(\delta + \alpha)^2 \cos(2\beta) + \sin(\delta + \alpha)^2 \sin(\beta)^2). \end{aligned} \quad (3.3)$$

To fit the experimental data in Fig. 3.2(a), equation 3.3 was plotted as a function

| <u>Table 3.1: fitted texture orientation</u> | | | |
|--|----------|----------|----------|
| Parameter | α | β | δ |
| Value | (varies) | $\pi/10$ | $\pi/4$ |

of the rotational angle α about the z – axis. To align the data and model, α was shifted by a constant value δ . No rotational anisotropy was observed unless an additional small rotation about either the x – or y – axis was introduced. For the fit a $\beta = \pi/10$ rotation about the y – axis was sufficient. Making β even smaller preserved the shape of the graph, but decreased the magnitude of the x and y field components symmetrically over all z angles α . A summary of the fitted parameters is shown in Table 3.1.

3.2 Field-enhanced SHG in Ag nanoparticle films

Early observations of the optical response of roughened Ag samples indicated an enhanced SH signal [23]. Enhancement was also verified in our Ag samples made via LAM. Due to deposition conditions, SHG was only observed near the edge of the deposits from the LAM-generated silver nanoparticle films.

The SHG measurement was made using a x-scan measurement. The details of the apparatus are shown in Fig. 3.3. The setup is similar to what was used to probe the spatial linear optical quality in Chapter 2. The difference here is that the full intensity of the fundamental beam was used to excite the sample, and only

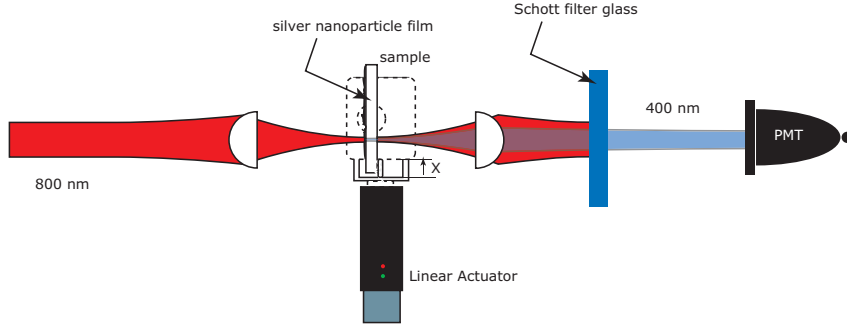


Figure 3.3: Schematic of x-scanning second-harmonic generation optical transmission measurement

the portion of the signal near the second harmonic wavelength was collected. In addition to the second-harmonic, a broadband 'white light' fluorescence emission from the silver samples was observed. The signal was spectrally resolved in the same monochromator used for the rotational anisotropy SHG measurements of the aluminum nitride film.

Measuring the second-harmonic signal as a function of position determined a 'field enhancement' map of the sample, shown in Fig. 3.4. In Fig. 3.4, the SHG x-scan is depicted along with the linear transmission at the SH wavelength (400 nm). No SH signal was measured from the substrate, but in areas with impeded transmission due to the presence of nanoparticles SH was observed. The linear transmission determines the scaling of the x-dependent signal according to

$$\tilde{E}_2(x) \propto \chi^{(2)}(2\omega; \omega, \omega)(\tilde{E}_1 \mathcal{F}_1^T(x))^2, \quad (3.4)$$

where $\mathcal{F}_1^T(x)$ is the linear transmission of the fundamental field through the silver sample, as a function of position. The silver film eroded during nanoparticle deposition, so the transmission increased by a small amount in the center of the deposit. The highest nonlinear efficiency in the sample was found partially-coated areas, with

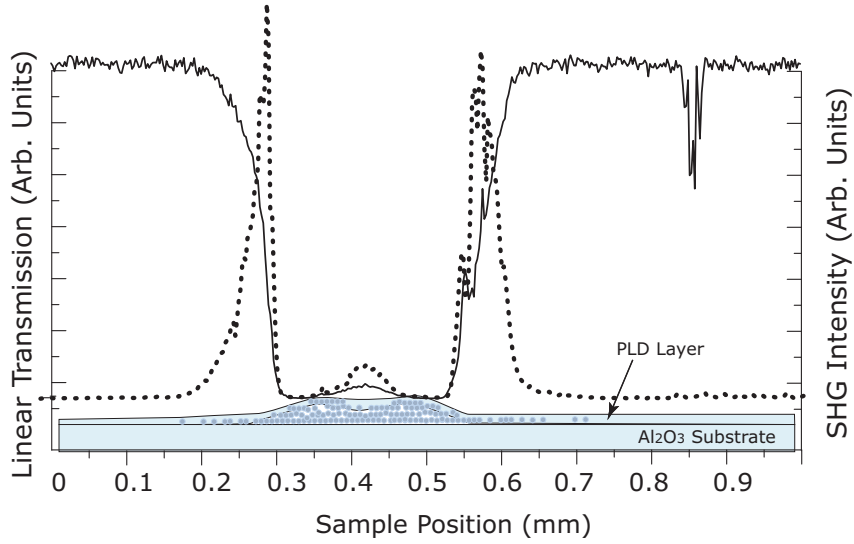


Figure 3.4: SHG data from x-scanning second-harmonic generation measurement from sapphire-coated Ag nanoparticles. The dotted line is the raw second harmonic signal. The solid black line is the linear transmission through the sample.

$\sim 50\%$ transmission.

Roughened surfaces are not required to observe enhanced SHG. Second-harmonic generation in plasmonic systems was identified at about the same time that surface-enhanced Raman Scattering was observed, during the 1970's. However, the earliest experiment showing a connection of nonlinear conversion to plasmons did not make connection to the roughened surface [17]. By showing the angular dependence of SHG, and that the SHG peaked at the same angle where the surface-plasmon coupling peaked, Simon *et al.* showed the participation of the surface plasmon in the second-order process.

3.2.1 symmetry considerations

Just having field enhancement is not enough to generate second harmonic radiation. The selection rules of the three-photon process are not satisfied internally by

the fields. However, if the medium is discontinuous in the bulk dielectric, the centrosymmetry is effectively broken, and the selection rules of SHG may be satisfied. In the nano-roughened Ag material we are investigating, there is reason to believe more may be happening. Higher-order angular modes in individual particles have been shown to be very important in their optical response. Dadap *et al.* showed second harmonic radiation from spheres also has quadrupolar scattering components due to intraparticle coupling between the front and back-side of the particle, which affects both second-harmonic generation as well as second-order Rayleigh scattering [33]. The quadrupolar moments in the excitation patterns distort the radiation far-field pattern, and effective internal-field pattern of the particles. Also, 20 to 100-nm-sized particles are not sufficiently described by the lowest-order Mie scattering terms. These larger particles must include quadrupolar and higher terms in the polarization expansion. The presence of these higher-order modes (either because of internal interference or size effects) allow for rough silver samples to conserve angular momentum in the three-photon process and emit second-harmonic radiation.

In addition to the internal, quadrupolar modes which are present in the silver samples, higher-order polarization components are present in inter-particle coupling of neighboring particles. Work by Simonsen and Wißmann showed these higher-order particle-particle interactions will shift the surface plasmon resonance energies further into the infrared [34, 35]. According to their results, inter-particle effects will shift the metal surface plasmon resonance by as much as tens of nanometers in wavelength. Interparticle coupling may increase conversion efficiency of second-order processes by lowering the symmetry of the light-matter interaction in clusters of nanoparticles, which improves angular momentum conservation in frequency-doubling from our roughened silver samples.

3.2.2 local-field coupling in second-order effects

The Lorentz local field enters into the nonlinear polarization in the same way as linear Fresnel coefficients. Since the Lorentz field is linearly proportional to both fundamental and harmonic, the overall nonlinear signal can be enhanced by many orders of magnitude, if the fundamental field is enhanced just by one order of magnitude.

Coupling of harmonic radiation to surface plasmons was demonstrated experimentally and modeled for the case of roughened silver films by G.T. Boyd and J. Gersten [24, 23]. In the case that Boyd modeled, the surface was assumed to contain at least some ellipsoidal particles, which act independently from others. Because of observations of 'Lightning Rod' effects, there was a belief that particle shape has a strong affect on the nonlinear response. Their model found that for certain geometries, when at the plasmon resonance, the linear field enhancement was even greater, and close to 1000 times that of simple hemispheres. In that case, the local-field correction factor L was composed of two parts: the plasmon-field correction $L_p(\omega)$ (Lorentz correction) and the lightning rod correction L_{LR} . The total local-field correction L is the product of these $L = L_p(\omega)L_{LR}$. In these results, they found that geometry greatly affected the plasmon resonance condition; elongated hemispheres resonated at lower wavelengths than the spherical ones, and could cause enhancement of the fundamental, infrared field.

Near-field enhancement on the nonlinear response is found by keeping track of the enhancement of the fields around individual particles. In general notation, the second-harmonic polarization field $P(2\omega)$ from a rough surface,

$$P_{roughsurface} \propto |L(2\omega)L^2(\omega)|^2 E^4(\omega), \quad (3.5)$$

shows how enhancement has the tendency to enter at very high orders.

Further field enhancement caused by interactions between neighboring particles can be strong, so the most accurate description of a local-field response should account for particle-particle interactions. However, the statement is irrelevant if the individual particle response is not well-known. Contrary to the plasmonic approach, some researchers have proposed models that rely less on individual particle effects, and more on bulk effects. In an experiment by L. E. Brus *et al.*, the response of single Rhodamine 6G molecules adsorbed to the surface of Ag nanoparticles showed that size and shape effects in rough silver may be even more complicated [36]. In his view, tunnelling of ballistically travelling electrons may play a role in understanding the local-field response of metal particles. In his work, the fluorescence and SERS spectra of the adsorbed molecules was correlated to the size and structure of the nanoparticles. The field enhancement from clusters of nanoparticles and larger nanoparticles by far exceeded that of individual ones, indicating that a single particle model may not be applicable at all. Quasi bulk effects, tunnelling between particles and from surface states, and wall-collisions were all discussed as possible mechanisms ¹.

3.3 Two-photon induced fluorescence

To better understand the nonlinear optical response of metal islands, L. E. Brus correlated the fluorescence and Raman spectra of surface-bound Rhodamine molecules. But early second-order surface enhancement studies by Chen *et al.* also reported that these noble metal films will fluoresce. We also observe fluorescence in the silver samples produced by LAM. By exploring the fluorescence of the silver nanoparticles, we aimed to better understand the complementary effect of field enhancement.

The fluorescence from the silver samples we observed spanned just over two

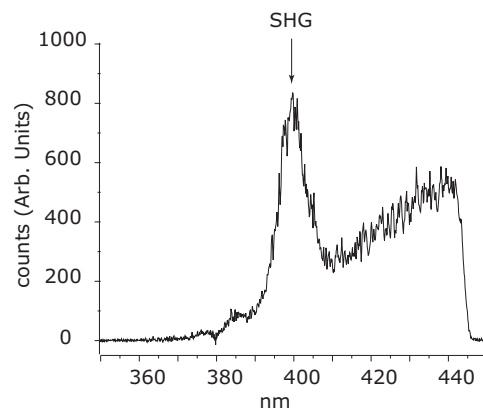
¹Though the arguments of Brus are compelling, there is doubt that many of the proposed 'mysterious' interparticle effects arise from mechanisms beyond currently-utilized SERS models.

hundred nanometers in the visible spectrum. The peak was about 510 nm, and turned on sharply at energies slightly lower than the second-harmonic energy. A plot of the emission spectrum is shown in Fig. 3.5.

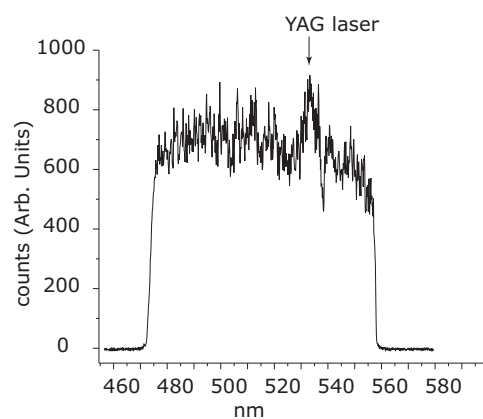
3.3.1 models of noble metal fluorescence

In the past thirty-seven years, several different models of metallic photoluminescence have been proposed (see Fig. 3.6). The earliest model was proposed by Mooradian [37]. Because the fluorescence was observed to be broad and wavelength-independent, he argued the photoluminescence is due to recombination of conduction band electrons with holes created by electron photoexcitation from the d-band. Subsequent to the excitation, holes scatter toward the high symmetry points in the d-band. Recombination probability is related to the increasing population of electrons below the Fermi energy, as observed in the slow rise in the emission spectra relative to the excitation photon energy.

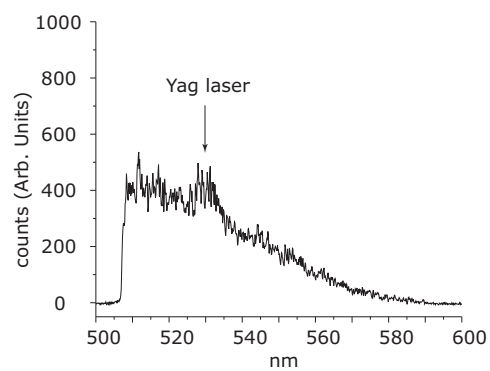
There are problems with Mooradian's theory, for silver. Direct band excitation is only observed in silver at wavelengths smaller than about 300 nm, which is much larger in energy than the observed two-photon excitation we observe. Silver also allows a two-photon excitation using 1050 nm, as confirmed in earlier studies by G. T. Boyd *et al.* on roughened silver surfaces [23]. Even with the allowed excitation, band symmetries still restrict direct recombination. To explain the photoluminescence, they argued in favor not of recombination, but of a qualitatively different fluorescence mechanism: direct radiation of the silver nanoparticles. Their hypothesis seemed compelling, because no fluorescence from smooth silver surfaces was observed. Because of their size, small nanoparticles have a dipolar polarization, and can radiate. In G. T. Boyd's model, the size of the silver particles also changes the plasmon energy, and the spectral spreading of plasmon resonances due to morphology is responsible for the spread in fluorescence energy. Comparing the



(a) SHG and high energy fluorescence

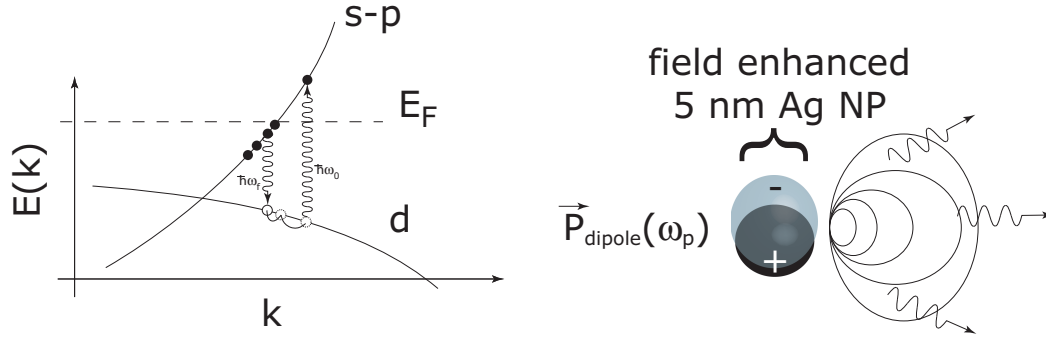


(b) 'green' fluorescence. Also visible is a small amount of Yag laser scattering into the detector.



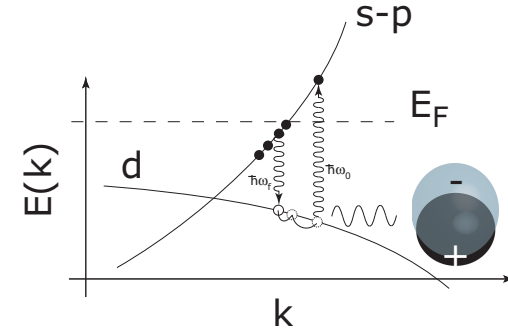
(c) Tail of the spectrum ends at just below 600 nm. Longer wavelengths may be present, but were attenuated by the glass filter.

Figure 3.5: Fluorescence spectra of Ag nanocomposites



(a) In Mooradian's theory of d-band recombination (1969), a single photon of energy $\hbar\omega_0$ excites a d-band electron into the s-p conduction band. Scattering and diffusion of the resultant hole allows for it to recombine with a lower energy conduction band electron below the Fermi energy.

(b) In G. T. Boyd's theory (1984), excited plasmons on roughened surfaces have dipolar polarizations which directly radiate.



(c) Varnavski's hybrid, field-enhanced d-band recombination model (2005) assumes that electrons and holes undergo driven diffusion in the presence of local fields, and that radiation occurs more efficiently under the presence of strong local fields.

Figure 3.6: Several models of metallic photoluminescence

bare silver plasmon resonance width to the width of the fluorescence in the LAM-generated silver samples shows close agreement ².

Varnavski *et al.* performed up-conversion lifetime studies of the silver fluorescence, and showed the time-scale of the fluorescence decay is similar to that of the plasmon [38]. Knowing of no other effect that could cause such a fast relaxation of the fluorescence, the conclusion of the study was that the plasmon was coupled to the interband system. Though the time-dependence of the fluorescence shows a decay similar to the surface plasmon, it does not necessarily indicate that the plasmon, itself, is the radiation source. In SERS, the local-field enhancement which is due to the plasmon resonance, will cause nearby fluorescing molecules to fluoresce more brightly while the plasmon is excited. Once the plasmon decays, the fluorescence decays, even though the adsorbed molecule may have an inherently longer lifetime. In the experiments performed by Varnavski, adsorbed molecules on Ag nanoparticles showed a picosecond decay that was much faster than for unadsorbed molecules.

One observable unexplored by Varnavski is the wavelength dependence of the pure metallic fluorescence. In a recent article by Beversluice *et al.*, the infrared tail of the fluorescence spectrum of gold STM tips was shown to have a different physical origin than the primarily observed visible spectrum [39]. Though the lifetime measurements of the tail made with a streak camera indicated the emission decays faster than a few picoseconds, Varnavski's measurements show there may be a long time-scale component to the Ag fluorescence. That fact, in addition to the wavelength dependence demonstrated by Beversluice, indicated a more thorough lifetime measurement of silver is required.

²nitrogen deficient aluminum nitride contains aluminum nanoparticles, which do not exhibit any resonant surface plasmon, but fluorescence at nearly identical wavelengths when excited by the same source.

3.3.2 lifetime measurements of silver nanocomposites

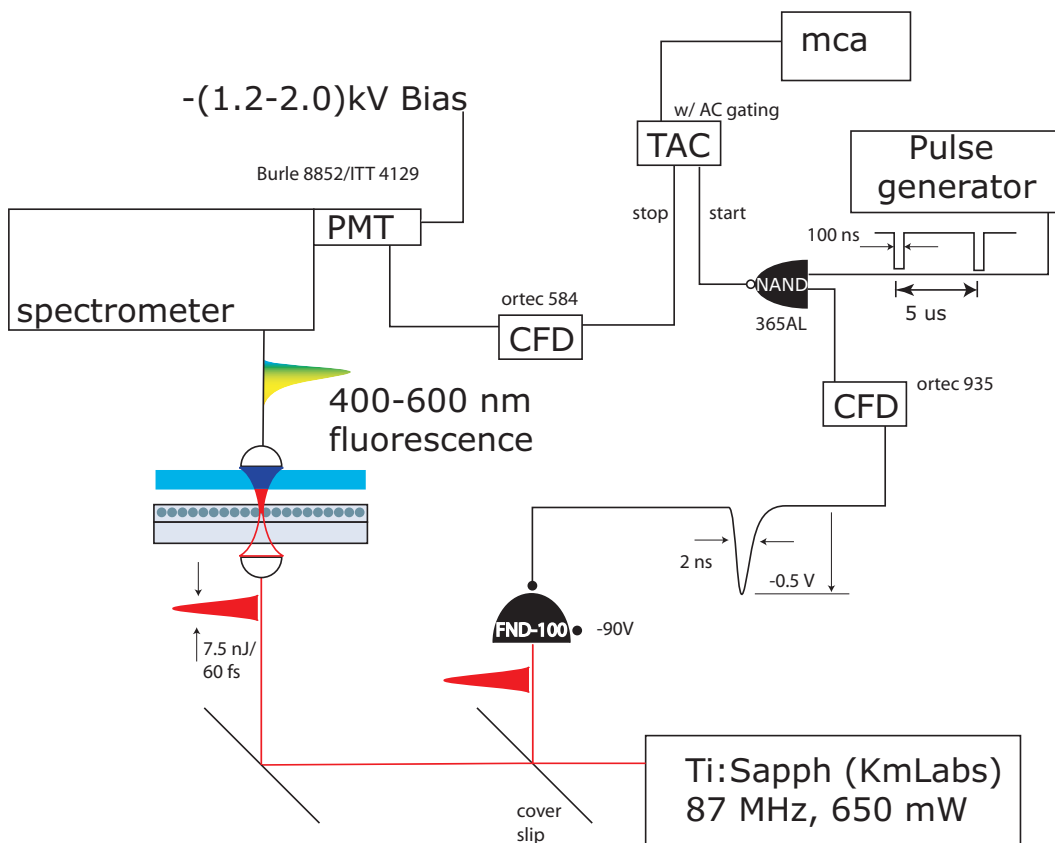


Figure 3.7: Schematic of high repetition rate time-correlated single photon counting experiment

Since the work by G. T. Boyd showed the absence of direct excitation and recombination in silver, we expect certain decay routes leading to fluorescence from our roughened silver samples will have time-scales long enough to measure with a traditional time-correlated single photon counting (tc-spc) apparatus. We performed these measurements using the same excitation as the x-scanning SHG measurements in Fig. 3.3. However, instead of measuring the fluorescence with the OMA, we used a photodetector in connection to several pieces of photon counting equipment.

The layout of the photon counting apparatus is shown in Fig. 3.7. In single photon counting measurements, the duration between the excitation (start pulse) and the fluorescence (stop pulse) is measured electronically. The mechanism used to count the time is the TAC (time to amplitude converter). The start pulse is taken from the sequence of pulses coming from the Ti:sapph oscillator cavity. These pulses are measured by a FND-100 photodiode, and connected to a constant fraction discriminator. The constant fraction discriminator (CFD) reduces time-walk due to fluctuations in the pulse amplitude of the input. Because the repetition rate of the stop pulse is so high, the output of the CFD is digitally multiplied, to eliminate saturation of the TAC input. Our setup is not a traditional TCSPC setup, and was engineered specifically to avoid saturating many of the electronics due to the high rep-rate of the detector. Though in theory reverse-mode TCSPC (in which the fluorescence pulse could be used as a gate for the start pulse) is possible, we found the gating electronics were unreliable due to the high repetition rate. Reducing the start rate to a short sequence of pulses, spaced by several microseconds allowed for clean pulse timing. The quality of the signal is primarily determined by the quality of the constant fraction discriminator. Because of the uncertainty in the CFD setup, I have included a scope trace of the ideal output from the CFD monitor channel in Fig. 3.8

lifetime measurements with the Burle 8852 photomultiplier

When properly set-up, constant fraction discriminators (CFD) will reduce the electronic time-walk to less than 50 ps. The CFD uncertainty is much lower than the uncertainty in the detector. The detector uncertainty is given by jitter in the cathode to dynode transit time. Because the signal occurs via an electron avalanche in the dynode chain, the transit time-for-flight of the electron from the photocathode to the first dynode determines the time the pulse leaves the detector. The jitter in

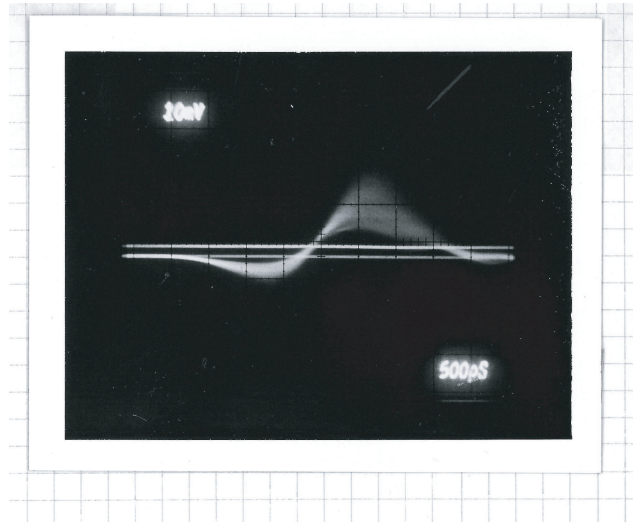
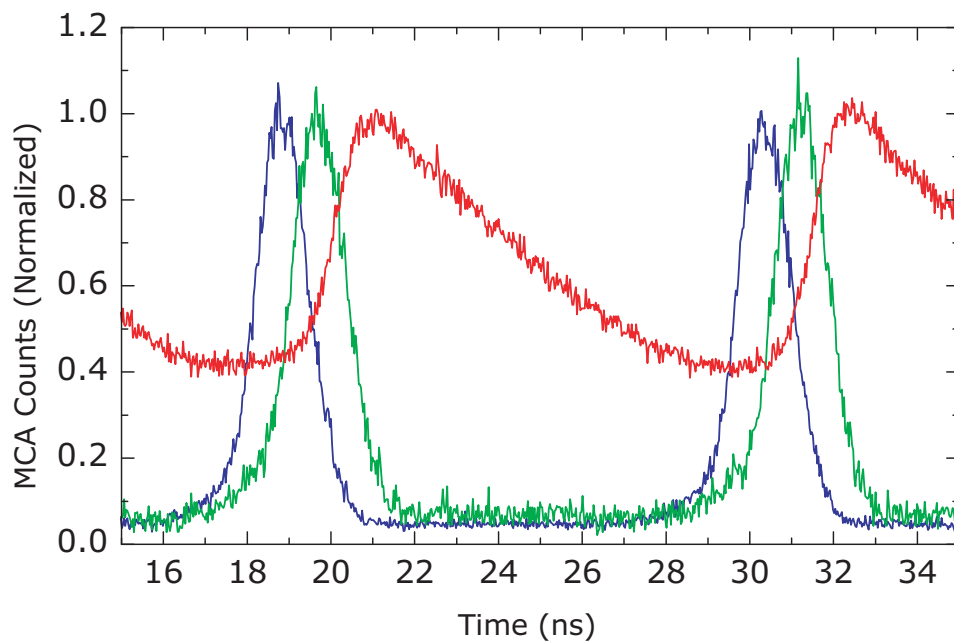


Figure 3.8: CFD output used in the single photon counting experiments.

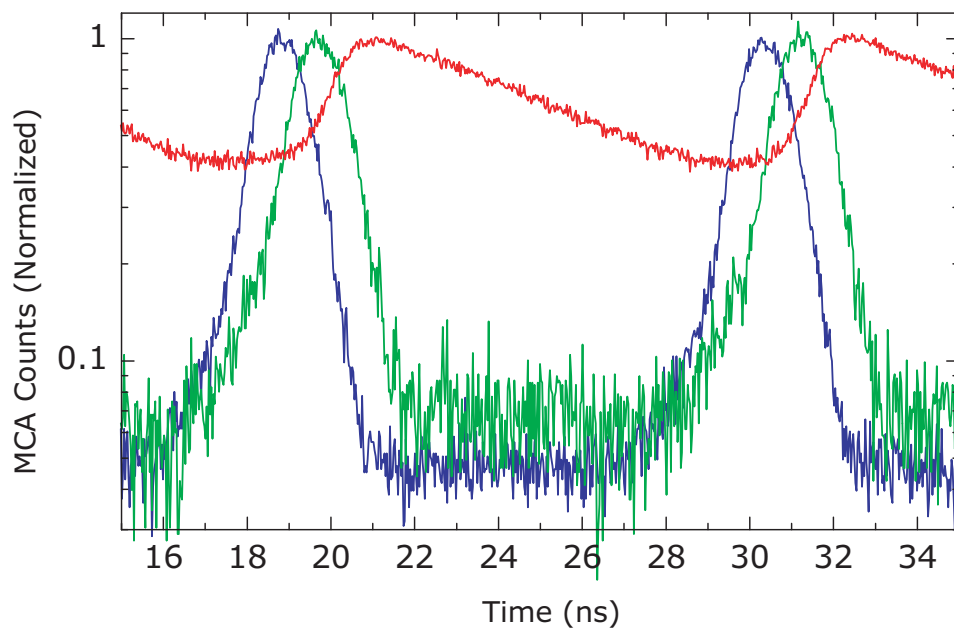
the Burle 8852 detector is relatively large, about 2 ns.

We calibrated the apparatus by measuring a Rhodamine dye, by replacing the silver sample with a cuvette. Then we measured the lifetime of the the second-harmonic of the fundamental pulse, obtained by replacing the cuvette with a 100 micron BBO crystal. Finally, we measured the lifetime of the silver sample. These measurements are shown in Fig. 3.9. There are several consequences of the electronic configuration. The combination of the high repetition rate of the mode-locked Ti:Sapphire with the low count rate of the detection system means that not every start pulse is followed by a photon that corresponds to that pump pulse. After the start pulse reaches the TAC, the first detected photon may not be from that same laser event, and may be from one of the earlier pulses. Since these other pulses are equally spaced in time, what is observed after counting for an extended period is the sequence of the photoluminescence pulses emitted by the pump pulse train. Data from each of the different test materials in Fig. 3.9.

As a consequence of the close spacing of the pump pulses, the longer decay



(a) linear-linear



(b) log-linear

Figure 3.9: Fluorescence decay measured by the Burle 8852 photodetector. Rhodamine 6G (red, upper), near the centroid of Ag fluorescence at 510 nm (green, middle), and the system response (blue, lowest) are shown.

of the Rhodamine dye decays from sequential decays overlapped. The longer decay is visualized as a vertical baseline offset. Apart from the baseline shift of the Rhodamine curve, the peak position and fluorescence onset time are different in each sample. Many photodetectors have a cathode-response function that changes as a function of wavelength, and may cause some of the difference in the onset time of each curve. However the cathode response times are usually less than 500 ps. What is observed in Fig. 3.9 is partially electronic in origin.

Aside from the peak position, the onset time in these curves has significance. For instance, the Rhodamine dye solution begins to fluoresce more slowly than the other curves, as noticed in the reduced upward slope (going from left to right). The reason for the slow onset time of the fluorescence is the slow population of the

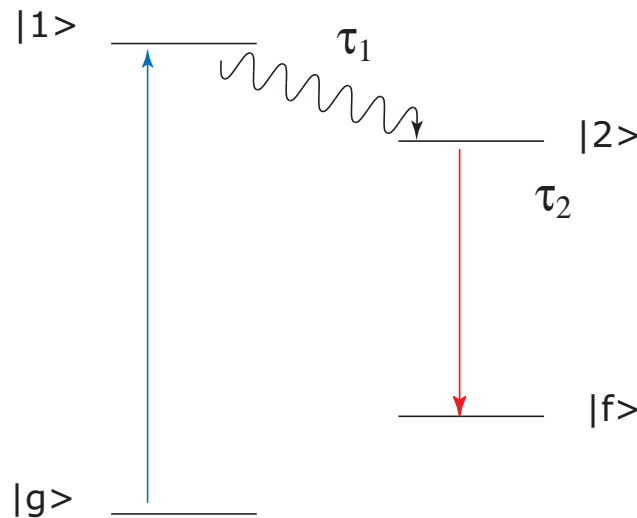


Figure 3.10: Schematic Rhodamine decay pathway, indicating the phonon-assisted electron population of the upper fluorescent state.

upper fluorescent level in Rhodamine. Between absorption and fluorescence, there is a large delay as the electron slowly decays before emitting the 615-nm photon. A schematical representation energy cascade is shown in Fig. 3.10. The same may

be true of the silver fluorescence, but using the 8852 photodetector did not resolve the onset time of the silver fluorescence. The observed lifetime of the silver sample, aside from the different peak position, was identical to the measured decay of the system response curve. After all of the electronics setup, using the Burle 8852 we found we could not resolve any differences between the Ag fluorescence and the system response.

lifetime measurements with the ITT 4129 photomultiplier

Using a multichannel plate detector allowed a better time resolution than the 8852, because of the smaller spread in the cathode to channel plate transit time. Measuring with the ITT 4129 requires the floating of two power supplies to float the the cathode voltage relative to the electron accelerating grid. The multichannel plate detector has an improved timing response compared to the 8852. A comparison of the system response decay for each detector is shown in Fig. 3.11.

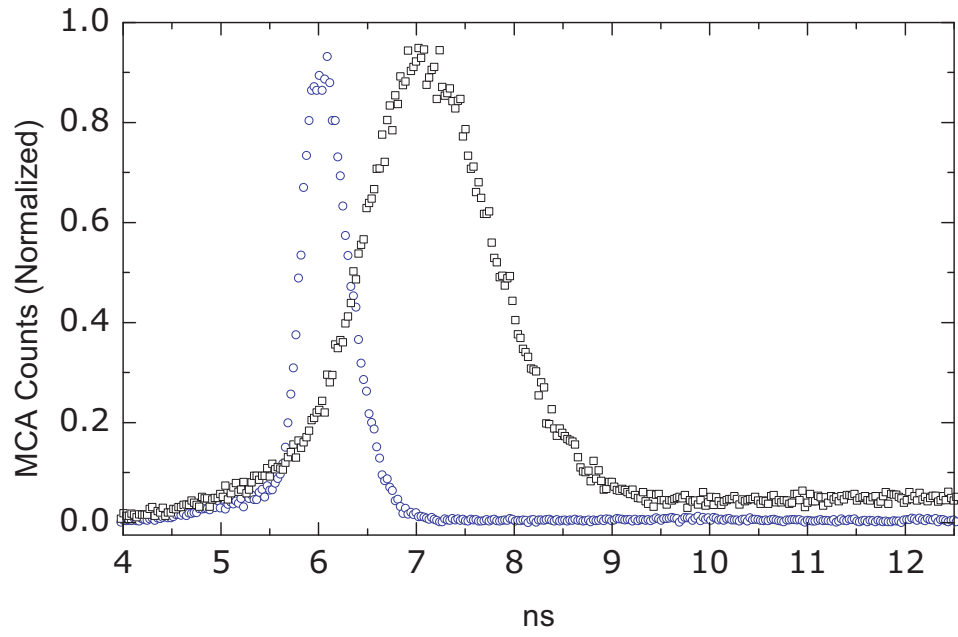
The observed response of the photodetectors was fit to a convolution of the exponential fluorescence decay function with a Gaussian detector response

$$F_L(t) = \int_{-\infty}^t a e^{-bx^2} e^{-c(t-x)} dx. \quad (3.6)$$

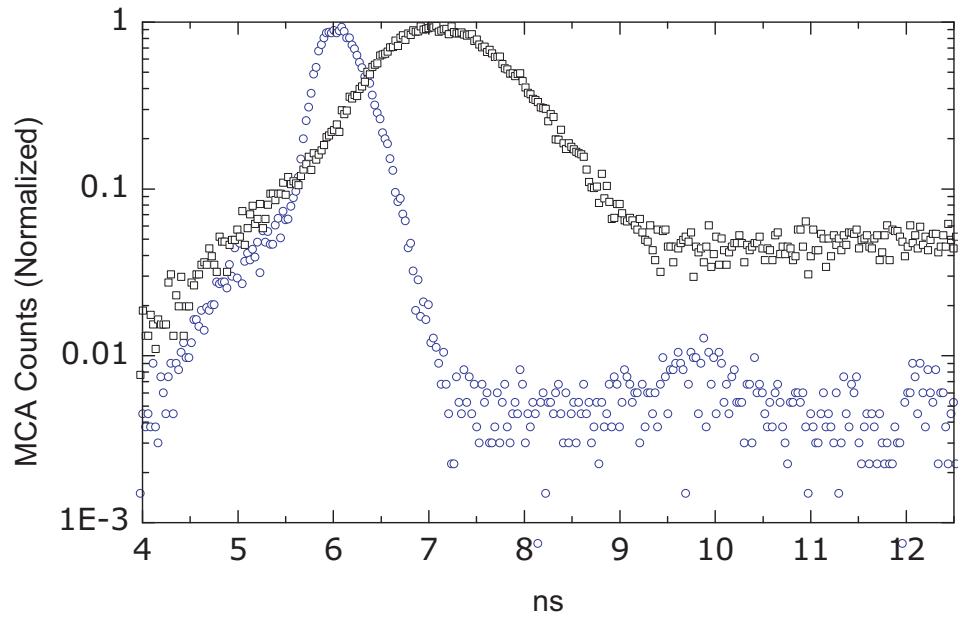
The integral is analytically solved as

$$F_L(t) = \frac{a\sqrt{\pi} e^{\frac{1-4b\tau t}{4b\tau^2}} \left[1 + \text{Erf} \left[\left(t - \sqrt{b} \frac{1}{2b\tau} \right) \right] \right]}{2\sqrt{b}} \quad (3.7)$$

Equation 3.7 was used to fit the system response curve of the ITT 4129 MCP. The fit worked well-enough to conclude the MCP has an inherent time-response of 160 ps. The shorter instrument response allowed for some differences between the measured decay of an ideal, short pulse and the silver fluorescence to be resolved. As in the case of rhodamine, we observed a delay in the onset time.



(a) Linear-Linear



(b) Log-Linear

Figure 3.11: Comparison of the Burle 8852 (\square) and ITT 4129 (\circ) system response

The larger onset time of Ag photoluminescence delays the peak of the fluorescence by 350 ps. The delay could be attributed to collisions in the nanostructured thin film. Because the excitation is two-photon, the initial decay of the populated s-p hybrid conduction electrons is not possible, though it is possible in gold nanoparticles [40]. There must be some angular momentum changing contribution of the rough surface, or other collisions that allow the decay into the lower levels.

hole cascade model

The decay of the excited holes can be roughly modeled as a phonon-assisted electron cascade, by calculating the contribution of another exponential decay with decay constant $\tau_{1,nr}$, prior to the final, fluorescence-emitting decay to the the ground state with time constant $\tau_{2,rad}$. A schematic of the hole cascade model is shown in Fig. 3.12³.

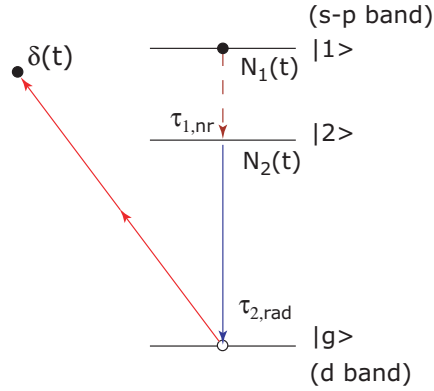


Figure 3.12: Bloch schematic of the de-excitation. At $t=0$, the laser populates the ground state with a hole, which recombines via an intermediate state with a $s - p$ conduction band electron.

The cascade model of silver is identical to electron de-excitation mechanisms in molecules. The difference is that at $t=0$, a delta function population of holes is

³Fig. 3.12 depicts a parity changing collision of the excited electron. An equivalent description incorporates a parity changing collision of the hole, which then recombines with the excited electron.

created in the ground state d-band. Because direct recombination is not available in Ag, there must be at least one additional collision which alters the symmetry of either the hole or a conduction band electron, which makes the final, radiative transition possible.

Initially, the upper N_1 state is occupied by with a density of N_0 , and decays according to

$$\frac{dN_1}{dt} = N_0\delta(t) - \frac{N_1}{\tau_1}. \quad (3.8)$$

The decay is exponential and given by

$$N_1(t) = N_0 e^{-\frac{t}{\tau_1}}. \quad (3.9)$$

The population in the N_2 state increases due to decay from N_1 and decreases by recombination with the hole in the ground state. The N_1 dynamics are represented as

$$\begin{aligned} \frac{dN_2}{dt} &= \frac{N_1(t)}{\tau_1} - \frac{N_2}{\tau_2}, \\ &= \frac{N_0 e^{-\frac{t}{\tau_1}}}{\tau_1} - \frac{N_2}{\tau_2}. \end{aligned} \quad (3.10)$$

Equation 3.10 was solved using a Laplace transform method. Transforming variables from t to s allowed us to write the s coordinate dynamics as

$$N_2(s) = \frac{N_0}{\tau_1} \left(\frac{1}{s + \frac{1}{\tau_1}} \right) \left(\frac{1}{s + \frac{1}{\tau_2}} \right). \quad (3.11)$$

In the derivation, we used the fact that the Laplace transform of $N_i(t)$ is $N_i(s)$, the Laplace transform of e^{at} is $1/(s - a)$, and that the Laplace transform of $dN_i(t)/dt$ is $sN_i(s)$. Solving for the dynamics in the t -coordinate is done by computing the

inverse Laplace transform of Eq. 3.11, which is of the form

$$\mathfrak{L}^{-1} \left\{ \frac{1}{(s-a)(s-b)} \right\} = \left(\frac{1}{(a-b)} \right) (e^{at} - e^{bt}). \quad (3.12)$$

The result is, in the time-domain coordinate,

$$N_2(t) = \left[\frac{\tau_2 N_0}{\tau_1 - \tau_2} \left(e^{-\frac{t}{\tau_1}} - e^{-\frac{t}{\tau_2}} \right) \right] \quad (3.13)$$

Using the result for the decay of the N_2 state allowed for the expected Ag fluorescence decay curve to be calculated by convolving the exponential in Eq. 3.13 with the same Gaussian used to find the system response. The result of the calculation predicts the decay of the fluorescent state follows the form

$$F_{cascade}(t) = \frac{a_2 \sqrt{\pi}}{2\sqrt{b}} \frac{\tau_2}{\tau_2 - \tau_1} \times \left\{ e^{\frac{1-4b\tau_1}{4b\tau_1^2} t} \left[1 + \text{Erf} \left[\left((t - t_0) - \frac{1}{2\sqrt{b}\tau_1} \right) \right] \right] \right. \\ \left. - e^{\frac{1-4b\tau_2}{4b\tau_2^2} t} \left[1 + \text{Erf} \left[\left((t - t_0) - \frac{1}{2\sqrt{b}\tau_2} \right) \right] \right] \right\} \quad (3.14)$$

shown in Fig. 3.13. The fit shows that the onset system response is well-fit to a Gaussian convolved with a single exponential decay. However, the fluorescence required an additional exponential to fit the delayed fluorescence onset, which indicates the model on Fig. 3.12 is appropriate for describing the silver decay. The fit is not as good near the peak of the fluorescence decay curve; the data dips below the fitting function. Results of Chapter 6 indicate the deviation may be due to saturation of the nonlinear transition. Aside from the shape distortion, both the rise and decay were both well-described by either a one-level, or two-level decay. The fitted parameters are listed in Table 3.2.

The fits to the data in Fig. 3.13 determined that the decay of the silver excited state is at least as rapid as what can be measured by the multichannel plate detection system, which is 170 ps. Though the decay is at least that rapid, we could

Table 3.2: Fitted lifetime parameters

| Parameter | a_1 | a_2 | b | τ_1 | τ_2 | t_0 |
|-----------|----------|----------|---------------------|------------|------------|-------------|
| Value | 100(1)E2 | 150(1)E2 | 12 ns ⁻² | 0.16(1) ns | 0.17(1) ns | 40.55(1) ns |

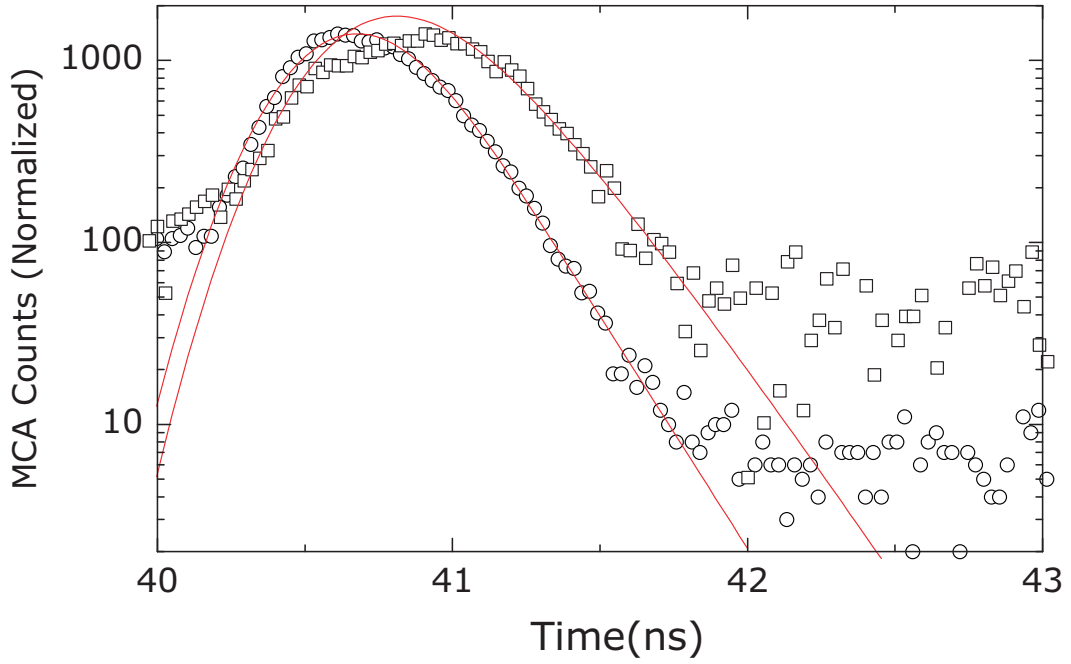


Figure 3.13: MCP lifetime data for the system response (\circ) and fluorescence near 520 nm (\square) including the effect of an intermediate decay state in Ag. The shift in the Ag decay is caused by the lifetime of the intermediate transition.

measure a difference in the onset of the decay of about 165 ps. The fluorescence was measured around 510 nm, which is significantly far away from the 2-photon excitation energy at 400 nm. There is some time required for the excited electrons (or holes) to scatter and reduce their energy, which is why there is a time delay between the system response function and the measured fluorescence lifetime.

To more accurately understand the dynamics of the excited silver nanoparticles shorter time resolution is required. Because electronic gating systems are comparatively slow, an all-optical gating system is required to improve the resolution of the excited dynamics. We have begun construction of a fluorescence upconversion apparatus, which functions by measuring an autocorrelation between a reference pulse of 100-fs duration and the fluorescence decay. The signal is found in an equivalent manner to the photodetector method described, except the instrument response is given by the femtosecond optical width, not the Gaussian spread of electrons in Eq. 3.7. The difference is that instead of binning time-delayed coincidence counts, the physical delay between the fluorescence signal and time-gate is controlled. The product of the fluorescence and the gate pulse is measured by overlapping them in an angle tunable BBO crystal.

3.4 Conclusions

The second-order optical properties of the films produced by laser ablation are quite broad. In the case of the PLD-produced AlN, texturing of the microcrystallites exhibited a long-range order. Rotating the sample in the focus of the fundamental beam resolved the symmetry of the long-range structure of the crystals. Silver also showed an interesting second-harmonic response. Generally, the signal levels were comparable to those of AlN. Because the LAM-produced samples are not uniform, we measured SHG cross-sectionally through the samples to see how the signal correlates with the microstructure.

The laser scanning measurements showed that the signal peaks at the edges of the deposit, where there are only one or two monolayers of silver nanoparticles. In addition to the SHG, we observed a broad fluorescence background that extended across most of the visible spectrum. Though the origin of the SHG-enhancement is believed to be caused by field enhancement and coupling to the surface plasmon, the strong fluorescence in Ag indicates that interband processes may be particularly strong players in the nonlinear regime. Our lifetime measurements indicate there may be a sequence of very short-lived decay states of either the excited electrons or holes. However, because the measurements were performed at the limits of our experimental equipment, repeating these measurements in an apparatus with improved time resolution would provide unambiguous data to support the cascade model.

It is interesting to note that electron-hole recombination is not the only means by which noble metals can emit broadband photoluminescence. Using longer (8 ps) pulses at much lower energy, Dieter Pohl observed white light supercontinuum (WLSC) generation from the nm-sized gap between two 100-nm-dipole antennas [41]. The photoluminescence Pohl observed is unrelated to the broadband emission we observe, because WLSC requires at least several picoseconds of pulse duration and our experiments used pulses less than 100 fs. Actually the emission spectrum of the WLSC is difficult to distinguish from the interband fluorescence, so Pohl showed the difference through the power dependence; the WLSC followed a quartic law, while the fluorescence was quadratic. In a separate experiment, performed much earlier in 1962, R. H. Ritchie observed broadband optical emission from foils when bombarded with multi- KeV electrons [42]. The effect Ritchie observed is Bremsstrahlung, which is caused by relativistically energetic electrons unavailable in our laser-excited samples. Much of the emission was due bulk plasma oscillations of the metal.

In most of the early studies of the nonlinear optical response of nano-rough silver, multiphoton absorption via interband transitions was ignored. As indicated by D. Pohl's work, the pulse duration of the excitation field will fundamentally change the power-dependence of the optical response. Some of the ultrafast response has been modeled by Knorren in a recent review paper on the ultrafast nonlinear excitation dynamics of silver [43]. In that work, ballistic loss of electrons from the excitation region, due to diffusion at the Fermi velocity ($\sim 10^6$ m/s), was found to change the optical response of very short pulses. However, diffusion plays more of a role at 300 K and higher. Knorren also argues that ballistic loss of electrons is inhibited when the metal is a thin film. Though not described in that review paper, nanoparticles will also confine these energetic electrons within the laser focus (because of confinement of the nanoparticles). Because of the small dimensions in the nanoparticle, energetic electrons photoexcited from the d-band scatter into the wall, where they lose their energy to the surface-bound conduction band electrons. Whether these wall collisions play a role on the decay dynamics of ultrafast photo-excited nanoparticles is a topic of current investigation.

Chapter 4

Ultrafast Laser Physics and Interface THG

4.1 Ultrashort-pulsed laser source

The excitation laser source used in all of the nonlinear optical studies is a mode-locked Ti:sapphire oscillator. It can deliver relatively high intensities by condensing the energy in the optical cavity into a sequence of sub 100-fs pulses. The repetition rate of the pulses depends on the size of the laser cavity. The output repetition rate was 85-87 MHz, measured on an oscilloscope using a fast photodiode (FND-100). The primary advantage of the ultrafast setup is two-fold: first, nonlinear effects are easily observed in the high instantaneous intensities, and second, short time-scale events can be measured. Additionally, the wide bandwidth can be used to perform single-shot spectral measurements covering nearly 100 nm in the near infra-red (IR).

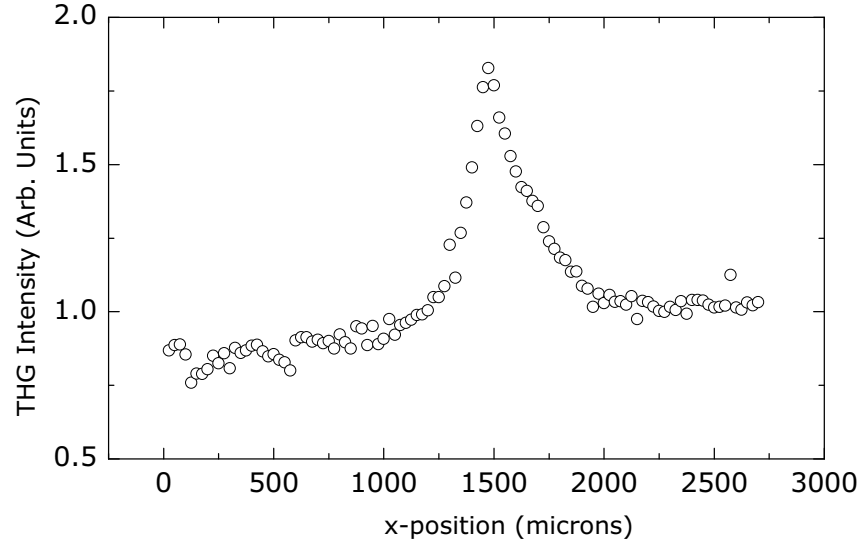
4.1.1 principle of operation of the mode-locked Ti:sapphire

The Ti:sapphire laser was assembled from a kit, with specifications for optimum layout given by the manufacturer (KMLabs). After assembly, configuration and

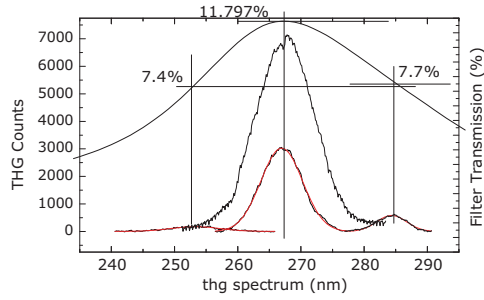
tuning of the laser cavity is required in order to achieve good operation. Different configuration of the cavity allows for either continuous-wave operation, or pulsed (mode-locked) operation. The average power output for cw operation is a little higher than that when mode-locked.

Because there are two possible configurations of the cavity, the cavity is set up on a translational stage, allowing for the adjustment of the position of the second cavity mirror. We used the cavity in the mode-locked operation, which is found by moving the second cavity mirror to the *outer edge of the inner stability zone*. To find the mode-locking cavity position, first decrease the cavity size until the output power in cw operation is a maximum (almost 1 Watt). Then increase the cavity size in steps, maximizing the output power by adjusting the cavity end mirrors (output coupler and high reflector) along the way, until the cw laser output is about 50-60 % of the maximum. 1.29 inches is the approximate position of the second cavity mirror required for mode-locking.

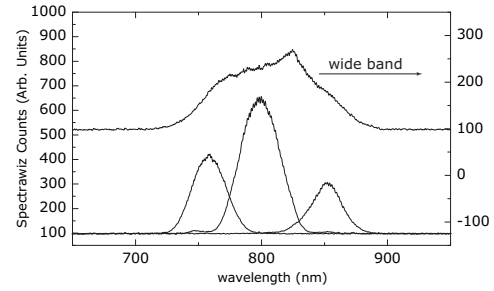
Inside of the cavity is a prism pair. Mode-locking the laser is accomplished by observing the power spectrum while issuing a small movement to the prism closest to the high reflector. The bandwidth of the output will increase dramatically when mode-locked, and depend on the insertion distance of the prisms. Using the wide bandwidth, we performed THG spectroscopy by tuning the centroid of the output laser. In a GaN nanoparticle deposit, we sought to resonate either the second harmonic or the third harmonic of the fundamental frequency at 800 nm. Because the particles may have their resonance frequency-shifted by quantum confinement, we expected the resonance to differ from the bulk band gap. The THG spectroscopy measurements are shown in Fig. 4.1. The wavelength dependence depicted in Fig. 4.1(b) is due to a frequency-dependent transmission coefficient of the third-harmonic field through the 267-nm band-pass filter (CVI). Also contributing to the frequency dependence of the signal is the gain function of the laser cavity. When configured to



(a) cross sectional THG measurement (X-scan) of a line of aerosol-deposited GaN nanoparticles. The peak indicates the location of the deposit maximum. The nonzero background is the TH response of the sapphire substrate.



(b) TH spectra for four different bandwidth configurations



(c) Corresponding fundamental laser bandwidths for the TH spectra in (b).

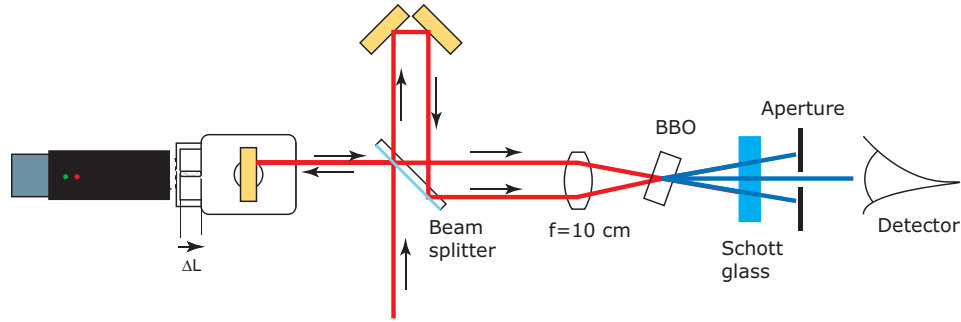
Figure 4.1: THG spectroscopy of GaN, accomplished by frequency-tuning the Ti:Sapphire cavity.

operate closer to 750 nm, or 850 nm the power output is much lower. The reflectivity of the cavity high reflecting mirror and output coupler are more restrictive than the inherent gain of the Ti:sapphire crystal. As a consequence, the already narrow spectral range in THG spectroscopy is even more limited.

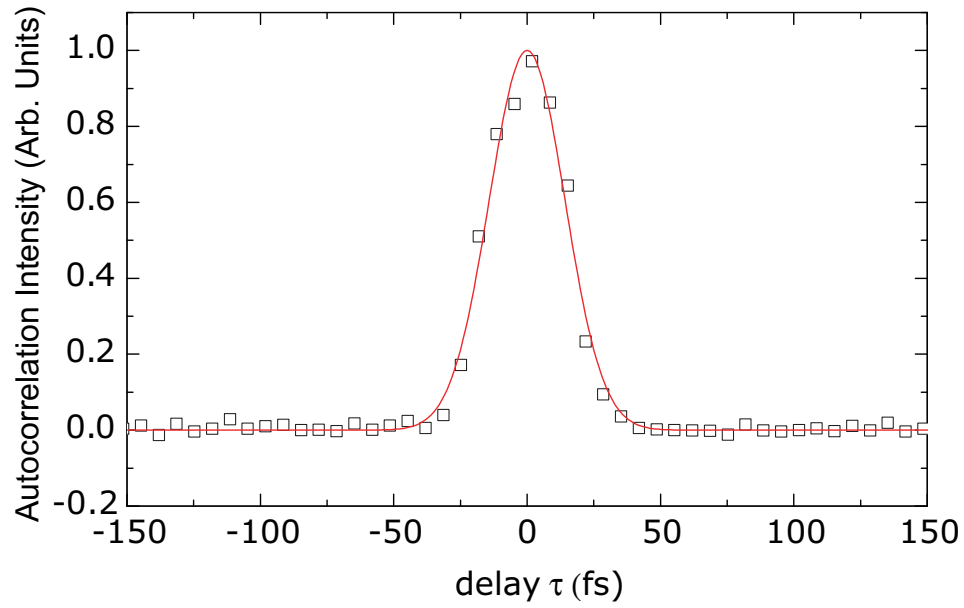
The prism pair inside of the cavity compensates for group-velocity dispersion (GVD) in half of a cavity cycle. However, when the pulse exits the cavity, its temporal width increases, because of GVD in the second half of the crystal and the output-coupling optic. To further compensate for GVD, an external prism pair is introduced after the cavity. The external prism pair can be tuned by changing the prism separation length to give the shortest pulse. A separation of 70 cm was found to be optimal for the current cavity layout. Pushing the laser to operate in the largest bandwidth lowered the overall intensity of the lasing, so most measurements requiring high intensities (such as THG) were performed with a narrower bandwidth. Nevertheless, wide band operation clearly produced the shortest pulses. 80-nm-bandwidth pulses were routinely measured to be less than 20 fs at several external prism spacings between 60 and 70 cm.

4.1.2 pulse characterization through autocorrelation

The duration of the pulses coming from the oscillator cavity were measured using the autocorrelation setup shown in Fig. 4.2(a). In an autocorrelation experiment, the pulse to be measured is split, and one of the copies of the pulse is delayed by some amount $\Delta t = \Delta L/c$. The other copy is spatially separated and timed equally with the pulse from the other arm of an interferometer, and both are sent through a focusing lens. In the focal plane is a frequency doubling crystal which creates three output beams, each corresponding to phase matching 2 photons from beam 1, 2 photons from beam 2, or one photon each from either beam. The last case produces



(a) schematic setup for performing pulse duration experiments



(b) measured autocorrelation data (\square), compared to a Gaussian fit, with FWHM=28.3(4) fs.

Figure 4.2: Apparatus used to measure pulse duration (a) and corresponding data (b)

a beam in the forward direction with an observed intensity I_2 given by

$$I_2(\tau) \propto |\chi^{(2)}(E_1(t)E_1(t+\tau))|^2 \quad (4.1)$$

Computing a value for the SH signal intensity as a function of delay is done by computing the absolute value of the right-hand side of Eq. 4.1. The absolute value of some time-dependent field $E(t)$ is determined from the integral $\int E(t)E^*(\tau-t)dt$. Integration over all time reduces Eq. 4.1 to a function of the delay between the pulses τ . For the output fields, Eq. 4.1 accounts for just the cross-terms of the frequency-doubled field, which is in the forward direction. The geometry in the background-free autocorrelation in Fig. 4.2(a) prevents interference of the fundamental fields, so the Michelson fringes observed in collinear experiments aren't observed in the crossed beam setup. The result of an autocorrelation of a 60-nm-bandwidth fundamental pulse using the crossed-beam method is shown in Fig. 4.2(b).

4.1.3 phase-sensitive pulse characterization with FROG

The autocorrelation measurement does not fully characterized the pulse exiting the oscillator cavity. To completely know the pulse being used, one likes to measure the time-dependent phase, as well as the time-dependent amplitude. (Having both parameters is necessary for describing any field.)

In measuring the time of a field using amplitude methods, alone, one often finds that the pulse length is longer than expected based on bandwidth considerations. Only when a pulse is transform-limited, it will have the shortest length. A transform limited pulse is achieved when the time-dependent phase of the pulse is constant. In general, the duration $\tau(\lambda)$ of a transform limited pulse has a well-defined relationship to its bandwidth. The time-bandwidth relationship also depends on the spectral and temporal shape. For a Gaussian pulse, the pulse time is

related to the bandwidth through

$$\tau_p(\lambda) = \frac{0.441\lambda^2}{c\Delta\lambda(\lambda)}. \quad (4.2)$$

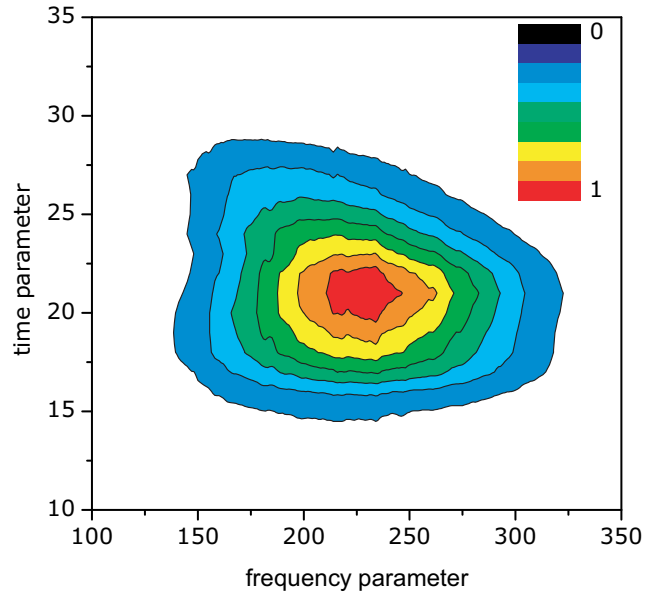
The relationship in Eq. 4.2 can be used to describe the propagation of a transform-limited Gaussian pulse using the coefficient $\Gamma = 2\ln(2)/\tau_p^2(\lambda)$ as the exponential parameter.

In general situations, in which the time-bandwidth coordinates are not transform-limited, the time-dependent phase of a pulse must be measured. One way find the time-dependent phase is to use frequency-resolved optical gating (FROG) [44]. In that case, a spectrometer is used as a detector in Fig. 4.2(a)(instead of a photodiode), and at each delay position of the interferometer, the emitted SH pulse is spectrally-resolved. The power spectra are then accumulated into an array, sequential with the delay times. The array is fed into a numerical subroutine (FROG algorithm), which computes the time-dependent amplitude and phase. The FROG algorithm computes the time-dependant field amplitude and phase. We characterized the oscillator pulses from the cavity using such an algorithm (see Appendix A for details).

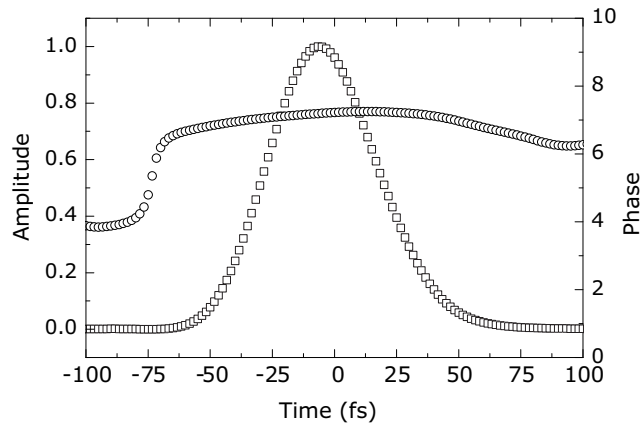
In the example shown in Fig. 4.3, a pulse of approximately 60-nm bandwidth returned a pulse measurement of about 50 fs, and relatively little phase distortion. Generally, phase distortion is rapidly increased as more prism glass is inserted into the beam path. Also, cavity stability decreased when operating in the widest bandwidth configuration.

4.2 Pulse propagation

As previously mentioned, a temporal pulse parameter is used to describe the propagation of a Gaussian-pulsed laser. Including higher-order dispersion in the propaga-



(a) Femtosecond Frog program input data is a time-frequency matrix.



(b) Amplitude(\square) and phase(\circ) of the field, recovered by using the FROG algorithm and the data from (a)

Figure 4.3: Representative analysis of short pulse measurements using FROG.

tion formulas is essential to describe the propagation of a general femtosecond laser pulse. Eq. 4.2 showed that the timewidth of Fourier transform-limited pulse has a well-defined relation to the bandwidth, but generally, this relationship is not valid, as exhibited through the observations of temporally-broadened, wide-bandwidth pulses following exit from the oscillator cavity. Pulse broadening is the time-analog of Gaussian beam diffraction. So, in the same way as a tightly-focused beam diffracts greatly, a broad-bandwidth pulse will greatly broaden in time. Just as putting a lens introduces a spatially-varying phase-front on a plane wave that causes the wave to focus, introducing a time-dependent phase in a pulse causes it to broaden.

The space-time analog is a useful way to understand the dynamic evolution of a laser pulse. A Gaussian beam (cw) is described by the complex Gaussian beam parameter, $\tilde{q}(z)$. The beam parameter describes the phase-front curvature and waist size of a pulse at a location z . Once some instantaneous value is known, the future propagation of a pulse can be calculated exactly. The Gaussian beam parameter is given by

$$\frac{1}{\tilde{q}(z)} = \frac{1}{R(z)} - i \frac{\lambda_0}{\pi \omega^2(z)}, \quad (4.3)$$

where $\omega(z)$ refers to the cross-sectional radius of the beam at a distance z from the beam waist. The Rayleigh parameter z_R defines the distance over which the waist (radius) increases by a factor of $\sqrt{2}$, relative to the beam waist radius ω_0 through

$$z_R = \frac{\pi n \omega_0^2}{\lambda_0}. \quad (4.4)$$

Typically in Gaussian beam analysis, one wishes to know extreme conditions for some initial beam parameter \tilde{q}_0 . To find the laser focus position, the beam parameter is taken to be purely imaginary, and then solved for z , which is the position of the focus. Substitution of the instantaneous value into the waist function will determine the laser waist at the laser focal plane. The other commonly encountered scenario

is propagation through a medium of index n , followed by propagation through a new media n' . One need not worry about the affect on the curvature, or the waist. Just propagate using the ABCD matrix for free space propagation, assuming $z/n \rightarrow z/n'$. The transverse field-dependence of a laser is then found by incorporating the beam parameter into the exponential

$$\tilde{u}_1(x_1) = e^{-i \frac{\pi x_1^2}{\tilde{q}_1(z)\lambda}}, \quad (4.5)$$

which is a factor describing the z -dependent variation of the field in the transverse coordinate x_1 . The transverse factor u_1 multiplies the overall field strength $\tilde{E}(x_1, x_2, z) \propto \tilde{u}_1(x_1, z) \tilde{u}_2(x_2, z)$.

The temporal propagation of a laser beam follows an analysis similar to that of a spatial beam parameter \tilde{q} . To describe the temporal evolution of a pulse, the time-analog (Γ) of the spatial Gaussian beam parameter is used. The parameter was previous mentioned in the discussion of Eq. 4.2, but in that case there was no z -dependence, which implies the temporal shape of the pulse remains constant. (This is the time-analog of a plane wave.) But, adding some linear temporal dispersion (chirp) to the pulse is also possible, which is equivalent to adding some spatial phase (not curvature) to a Gaussian beam. In that case, Γ , now rewritten as Γ_0 , is

$$\Gamma_0 = \frac{2 \ln(2)}{\tau_p^2} + ib. \quad (4.6)$$

The imaginary coefficient b has units of rad/s^2 , and describes the degree to which the linear carrier frequency of the pulse changes over the duration of the pulse. If b is nonzero, the pulse is said to be chirped. Chirp is a linear distortion of the time-dependent phase of the pulse. Just as linear phase distortion of the spatial phase of a beam does not cause diffraction, chirp does not cause a pulse to broaden. The time-analog of diffraction, pulse broadening, is affected through yet another

term, which is proportional to the second-order dispersion β'' . In the latter case, the complex time parameter is written

$$\frac{1}{\Gamma(z)} = \frac{1}{\Gamma_0} + 2i\beta'', \quad (4.7)$$

which has a form similar to Eq. 4.3.

Pulses will not change when they propagate through vacuum, but they will change upon propagating through a medium with even a slight amount of quadratic dispersion β'' . Visualizing how a pulse will propagate through an amount z of material is found by computing the field

$$\tilde{E}(z, t) = \exp \left[i\omega \left(t - \frac{z}{v_\phi(\omega)} \right) \right] \times \exp \left[-\Gamma(z) \times \left(t - \frac{z}{v_g(\omega)} \right) \right] \quad (4.8)$$

and plotting the result as a function of time. The material dependence of Eq. 4.8 occurs through the phase velocity $v_\phi(\omega_0) = \omega/\beta(\omega_0)$, the group velocity $v_g(\omega_0) = 1/\beta'$, and the group-velocity dispersion which is proportional to the second derivative of β . Actually, β is the total function for the wavenumber k , expanded in ω about the carrier frequency ω_0 . The terms of the expansion of β have the following meaning

$$\begin{aligned} \beta &\equiv \beta(\omega)|_{\omega=\omega_0} &= \frac{\omega_0}{v_\phi(\omega_0)} &\equiv \frac{\omega_0}{\text{phase velocity}} \\ \beta' &\equiv \frac{d\beta}{d\omega} \Big|_{\omega=\omega_0} &= \frac{1}{v_g(\omega_0)} &\equiv \frac{1}{\text{group velocity}} \\ \beta'' &\equiv \frac{d^2\beta}{d\omega^2} \Big|_{\omega=\omega_0} &= \frac{d}{d\omega} \left(\frac{1}{v_g(\omega_0)} \right) &\equiv \text{“group-velocity dispersion”} \end{aligned} \quad (4.9)$$

Treatment of pulse propagation using these parameters is a common feature in ultrafast laser design, and is commonly found in professional literature. Much of the previous analysis is covered in Siegman’s optical engineering text book, *LASERS*

[45].

Because much of the following analysis will depend on differences in material properties, we opted to calculate the phase and group velocity and group-velocity dispersion using wavelength derivatives instead of the theoretically favorable ω derivatives. Working in terms of wavelength enabled a direct calculation of dispersive properties from the commonly-cited Sellmeier equations, which describe the wavelength-dependent index of refraction $n(\lambda)$. Since much of the following analysis relies on frequency-dependence of the wave number k , we used that value instead of the phase-velocity parameter. In that case the beta parameters are

$$\begin{aligned}
\beta &= k(\lambda_0) &= \frac{2\pi n(\lambda_0)}{\lambda_0} \\
\beta' &= \left. \frac{dk}{d\lambda} \frac{d\lambda}{d\omega} \right|_{\lambda=\lambda_0} &= \frac{n(\lambda_0) - \lambda_0 \frac{dn}{d\lambda} \Big|_{\lambda=\lambda_0}}{c} \\
\beta'' &= \left. \frac{d^2 k}{d\lambda^2} \left(\frac{d\lambda}{d\omega} \right)^2 \right|_{\lambda=\lambda_0} + \left. \frac{dk}{d\lambda} \frac{d^2 \lambda}{d\omega^2} \right|_{\lambda=\lambda_0} &= \left. \frac{\lambda^3 n''(\lambda)}{2c^2 \pi} \right|_{\lambda=\lambda_0}
\end{aligned} \tag{4.10}$$

4.3 THG with group-velocity mismatch

The relevant equations are derived by including pulse dispersion into the nonlinear wave equation¹. Analysis of THG with group-velocity mismatch (GVM) was recently reported by Tasgal *et al.* [46]. For details, we encourage the reader to consult their article, which includes both transverse and longitudinal effects. The main result is derived briefly here.

The laser pulses propagate along the z -axis, and the propagation is assumed to be independent of x, y . Effects of focusing a Gaussian beam are described in Sec. 5.3. Therefore, the basic starting point is the one dimensional wave equation with

¹Reprinted text with permission from D. S. Stoker, J. Baek, W. Wang, D. Kovar, M. F. Becker, J. W. Keto, Physical Review A, Vol. 73, 002605 2006. Copyright (2006) by the American Physical Society

linear and nonlinear driving terms,

$$\frac{\partial^2}{\partial t^2} \tilde{E}_i(z, t) - \frac{1}{c^2} \frac{\partial^2}{\partial z^2} \tilde{E}_i(z, t) = \frac{-4\pi}{c^2} \frac{\partial^2 \tilde{P}_i}{\partial t^2} \quad (4.11a)$$

$$\tilde{P}_i = \tilde{P}_i^{\text{NL}} + \tilde{P}_i^{(1)}. \quad (4.11b)$$

Energy transfer between the fundamental and harmonic fields occurs through the nonlinear polarization \tilde{P}_i^{NL} , while the linear polarization $\tilde{P}_i^{(1)}$ determines how each pulse propagates. Growth of each of the nonlinear polarization components occurs with an efficiency determined by the product of the third-order nonlinear susceptibility and a triple product of the propagating fields,

$$\tilde{P}_3^{\text{NL}} = \chi^{(3)} \tilde{E}_1 \tilde{E}_1 \tilde{E}_1, \quad (4.12a)$$

$$\tilde{P}_1^{\text{NL}} = 3 \chi^{(3)} \tilde{E}_3 \tilde{E}_1^* \tilde{E}_1^*. \quad (4.12b)$$

In our approach, we neglected higher-order contributions to the TH polarization.

Computing the Fourier transform of $\tilde{P}_i^{(1)}$, in accordance with the derivation of the parabolic wave equation, leaves dispersion of the ω_i field described by $\omega^2 \chi^{(1)}(\omega)$ [45]. When expanded, it becomes

$$\omega^2 \chi(\omega) \approx \omega_i^2 \chi(\omega_i) + \frac{d}{d\omega} [\omega^2 \chi(\omega)]|_{\omega=\omega_i} \times (\omega - \omega_i) + \dots \quad (4.13)$$

The linear susceptibility $\chi^{(1)}$ can be rewritten in terms of the propagation constant $k(\omega) = k(\omega_i) + [\frac{dk}{d\omega}]|_{\omega=\omega_i} \times (\omega - \omega_i) + \dots$, where ω_i refers to the fundamental or harmonic field. The result, using the relationship $k^2(\omega) = (\omega^2/c^2)[1 + \chi(\omega)]$, and assuming the envelope of the pulse is slowly varying, implies the ω_i field freely propagates according to

$$\frac{\partial \tilde{E}_i(z, t)}{\partial z} + \frac{1}{v_{g,i}} \frac{\partial \tilde{E}_i(z, t)}{\partial t} = \frac{-4\pi}{c^2} \frac{\partial^2 \tilde{P}_i^{\text{NL}}(z, t)}{\partial t^2}. \quad (4.14)$$

Equation 4.14 can be rewritten in terms of reduced time with a change of variables $\eta_i \equiv t - z/v_{g,i}$ and $z' \equiv z$, resulting in the simplified form,

$$\frac{\partial \tilde{E}_i(z', \eta_i)}{\partial z'} = \frac{-4\pi}{c^2} \frac{\partial^2 \tilde{P}_i^{\text{NL}}(z', \eta_i)}{\partial \eta_i^2}. \quad (4.15)$$

Equation 4.15 describes third-harmonic generation in the rest-frame of the TH pulse. In the TH reference-frame, the nonlinear polarization moves with the group velocity of the ω_1 pulse $v_{g,1}$, which is faster by $\frac{1}{\Delta\beta}$. We assumed the fields do not attenuate, and there are no resonances near the fundamental, or third-harmonic wavelengths, so we considered only the real value of the linear susceptibility. We also assumed $\chi^{(3)}$ is isotropic, unless noted otherwise.

Group-velocity effects have been used to treat picosecond SHG, but pulse walk-off was assumed not to occur [47]. In femtosecond SHG pulse walk-off does occur [27]. Recent work has shown THG is more susceptible to walk-off, because of larger dispersion and shorter pulse lengths [48, 46, 49]. Additionally, for a given group-velocity mismatch, the pulse length τ_p of the TH is shorter, causing walk-off to occur more rapidly for THG. In typical optical materials, when using a near-infrared (NIR) pump, the third-harmonic of the fundamental wavelength $\frac{\lambda_0}{3}$ is at the band edge, where $\frac{dn}{d\lambda}$ is large.

4.4 THG from simple optical elements using a focused laser

We modeled a typical ultrashort-pulsed, Gaussian-focused beam, including both group-velocity mismatch and phase mismatch of the fundamental and harmonic fields ². Competition between group-velocity mismatch and phase mismatch leads

²Reprinted text with permission from D. S. Stoker, M. F. Becker, J. W. Keto, Physical Review A, Vol. 71, 061802(R) 2005. Copyright (2005) by the American Physical Society

to third-harmonic generation that is sensitive only to interfaces. THG of modern femtosecond lasers in optical solids is a bulk process, without a surface susceptibility, but bears the signature of a surface enhancement effect in z-scan measurements. We demonstrate the accuracy of the model, by showing the agreement between the predicted spectral intensity and the measured third-harmonic spectrum from a thin sapphire crystal.

Third-harmonic generation (THG) in thin, transparent materials has been interpreted in a variety of ways [50, 51, 52, 53, 54]. Some have attributed it to a surface effect or surface-enhanced effect, and others stated that their measurements are consistent with traditional models of bulk nonresonant harmonic generation. Common among all of these experiments is the use of ultrashort laser pulses to achieve the required high intensities, but none model the time-dependence of third-harmonic production.

It is important to understand third-harmonic production in transparent dielectrics, because they are typical substrates for the manufacturing of more advanced materials and devices. To measure nonlinear optical properties of a film, it must be isolated from any background, requiring precise knowledge of how the substrate contributes to the signal. Tsang *et al.* state that third-harmonic generation in typical glasses has a surface enhancement effect [52]. Trebino used frequency-resolved optical gating (FROG) to study surface THG, and attributed the observed, minimal phase distortion to the surface effect [55]. Barad, *et al.* claim their measurements are consistent with the Gaussian harmonic treatment and disagree with the surface enhancement explanation [51, 56]. We show here that the results measured by Tsang and Trebino are compatible with a bulk susceptibility when a full time-dependence is included in the model. We also show that the observed harmonic signal is only generated close to the interface. This apparent third-harmonic source is significantly shorter than previously reported [51, 53].

4.4.1 experiment

Our measurements and model are based on the z-scan THG technique that has been introduced elsewhere [52, 51, 53]. Our laser pump source was an unamplified Ti:Sapphire oscillator(KMLabs), with 800-nm central frequency, λ_0 . The pulses are 40 fs, 30 nm (FWHM), 7.5 nJ with an 85-MHz-repetition rate. A piece of sapphire was translated through the focus of the laser at $z = 0$, and the THG spectrum was measured for each position, z , using a monochrometer connected to an optical multichannel analyzer. We focused the laser using a 2 cm f.l. lens to a measured waist radius, $\omega_1 = 4.4\mu m$, from a measured input waist, $\omega_0 = 600\mu m$. We measured the depth of focus, z_r , to be $75\mu m$ in air, somewhat smaller than the calculated value. We correct for the index of refraction of sapphire, $n(\lambda_0) = 1.76$, through $z_r = \frac{\pi\omega_1^2 n(\lambda)}{\lambda}$. The quantity, $I_{3\omega}(z)$, determines the intensity at the third-harmonic produced by the material, as a function of position, z . Phase matching in the Gaussian beam geometry has been formalized for continuous-wave (cw) beams as

$$I_{\lambda/3}(z, \lambda) \propto |\chi^{(3)}(\lambda/3; \lambda, \lambda, \lambda)J_p(z)|^2 \quad (4.16a)$$

$$J_p(z, \lambda) = \int_{z-\frac{L}{2}}^{z+\frac{L}{2}} \frac{e^{i\Delta k(\lambda)z'}}{(1 + i(\frac{z'}{z_r}))^2} dz', \quad (4.16b)$$

where J_p is the phase matching integral [56]. The material thickness is L , and the limits of integration track the input and output surface of the nonlinear medium for a fixed laser focus at $z = 0$. $\Delta k = 3k_\omega - k_{3\omega}$. Eq. 4.16a is explicitly wavelength dependent through $k = \frac{2\pi n(\lambda)}{\lambda}$.

Z-scan THG measurements cannot easily distinguish between surface and bulk effects. As such, interpretations of z-scan measurements have not given a clear impression of the harmonic generation mechanism [51, 50, 52]. To illustrate this point, Fig. 4.4 compares a surface generation model, approximated as thin nonlinear material at each interface, and a bulk cw generation model for THG from a thin,

sapphire (Al_2O_3) crystal. They are qualitatively similar. Both exhibit a peak in the signal when the laser focus is placed at the interface, but THG efficiency decreases when the laser focus is placed in the center of the sample.

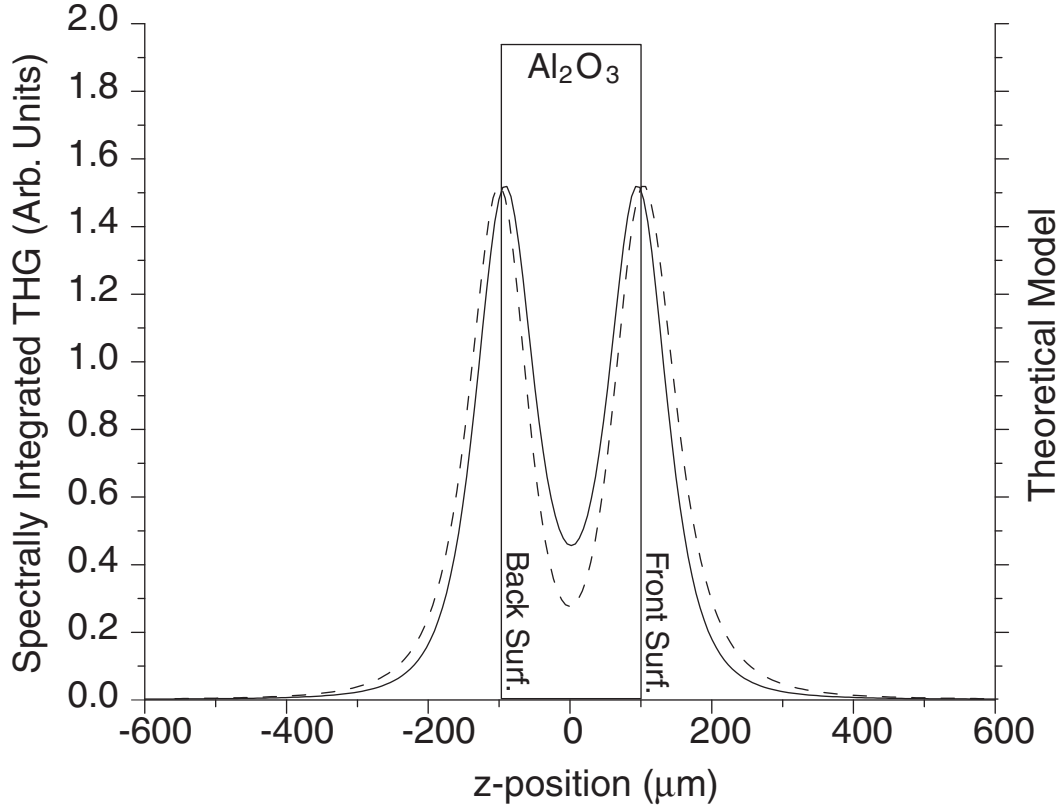


Figure 4.4: Comparison of surface and bulk models of THG in transparent media. Solid line shows theoretical surface effect. Dashed line shows theoretical bulk effect of Eq. 4.16a and integrates the contributions of all modes within the bandwidth. Distances have been scaled by 1.76, the index of refraction of Al_2O_3 at the pump wavelength.

A close inspection of Fig. 4.4 shows differences. Continuous-wave lasers generate third-harmonic less efficiently when focused in the bulk of the sample, because the photons generated after the focus are out of phase with those generated prior to it [57, 56]. However, ultrashort-pulsed lasers suffering from group-velocity mismatch of the harmonic and the fundamental do not spatially overlap through the entire

focus. As a result, a z-scan measurement done with ultrashort laser pulses will appear as a surface effect. We will show how this apparent surface effect is obtained through a bulk susceptibility if group-velocity mismatch is included. This requires modifying Eq. 4.16a to account for the time-dependence of third-harmonic generation. Not accounting for the full time-dependence of THG will lead to erroneous interpretations of z-scan measurements.

Although the time-average of Gaussian pulse propagation is equivalent to Gaussian cw beam propagation, harmonic generation using ultrashort pulses exhibits important differences. For pulses, coherent transfer of energy between the fundamental and harmonic fields can not occur for all times, because of group-velocity walk-off. Accurate models for group-velocity mismatch in second-harmonic production are known [47, 58, 59, 60]. However, the effect is relatively unexplored in the case of third-harmonic generation using ultrashort pulses. Group-velocity mismatch of the harmonic and fundamental laser pulses can be added to Eq. 4.16a. The new phase matching integral can be written as

$$J_p(t, L) \equiv \int_0^L \frac{\tilde{E}^3(t - \tau(z))e^{i\Delta kz}}{\left[1 + i\frac{(z-\xi)}{z_r}\right]^2} dz \quad (4.17a)$$

$$\tau(z) = [\beta_1(\lambda) - \beta_1(\lambda/3)]z, \quad (4.17b)$$

where ξ is the distance from the entrance surface of the nonlinear medium to the laser focus, and the fundamental field is written as

$$\tilde{E}(t) = e^{-\tilde{\Gamma}_0(t)^2}. \quad (4.18)$$

Time, $\tau(z)$, accounts for the separation of the pulses as they propagate some distance, z , through the material in terms of the inverse-group velocity, $\beta_1(\lambda) = \partial k / \partial \omega|_{\lambda_0}$. The length, L , is the total thickness of the nonlinear material, and $\tilde{\Gamma}_0$ is the complex Gaussian beam parameter [45, 61].

4.4.2 results

Changes in the spectral intensity of the third-harmonic signal are used to monitor the time profile of the radiated field. The ability to accomplish this is derived from the phase matching integral for Gaussian beams, J_p , which is proportional to $e^{i\Delta k(\lambda)z}$, shown in Eq. 4.16b. Phase dispersion accumulates rapidly as L increases. Eq. 4.16a predicts spectral modulation will develop within the bandwidth of the laser after just a few coherence lengths. This can be verified by including the dispersion of Al_2O_3 in the calculation of J_p , and so counting the spectral oscillations is a natural gauge for the depth over which a harmonic is produced. However, this method is limited for materials much thicker than the Rayleigh range of the focus. This is because the ability to resolve any spectral modulation decreases, independent of z_r , beyond the resolving limit of instrumentation as L becomes very large.

Eq. 4.17a can be used to predict the time-dependent third-harmonic field radiated from a transparent material. In Fig. 4.5, the radiated fields are computed numerically for various propagation lengths with the laser waist at the input surface as the output surface is placed sequentially further away. The interplay of phase mismatch and group-velocity dispersion causes the third-harmonic pulse to split. As the nonlinear material increases in thickness, the harmonic pulse produced by the fundamental beam steadily declines over the Rayleigh length of the laser focus, so that for the case of an infinitely long medium, the output pulse is just what was created at the input surface. The effect on the spectral intensity due to this is consistent with the previous discussion of phase-mismatched THG over large distances. We measured the third-harmonic spectrum in this limiting case, from a sapphire crystal with $L = 3$ mm, and observed a smooth spectral intensity.

It is interesting to consider this effect in the context of the measurement done by Trebino and Tsang, who saw that surface third-harmonic generation displays minimal phase distortion in FROG [55]. Our analysis predicts this to occur, not

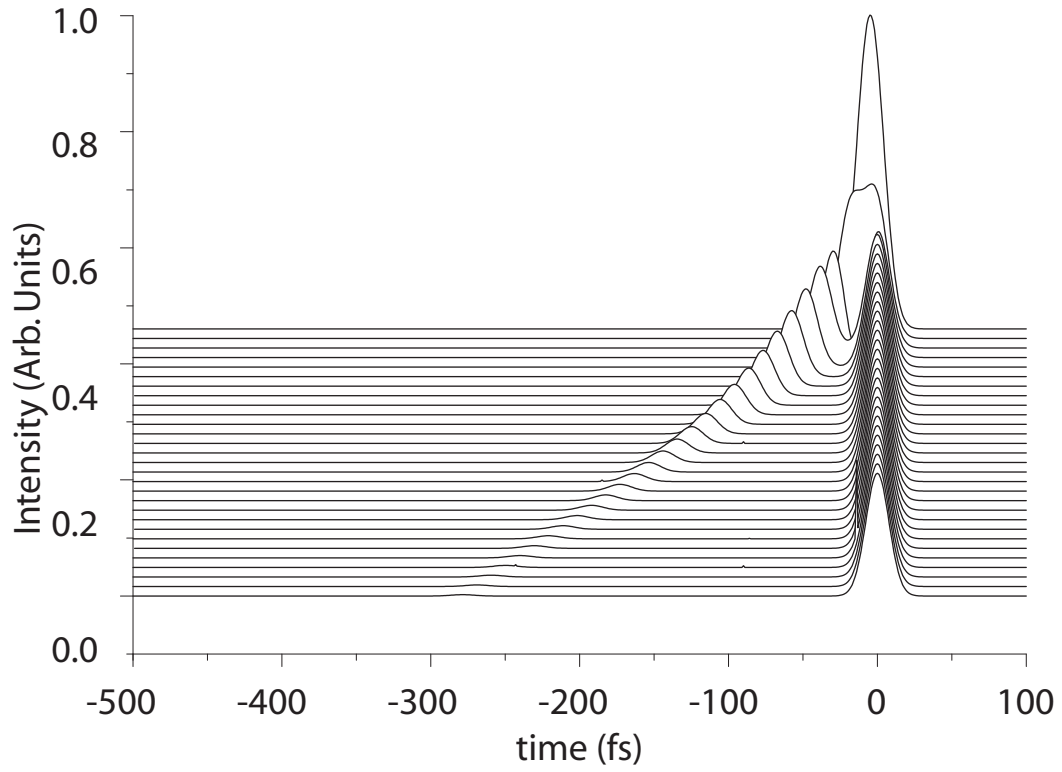


Figure 4.5: Time-dependent third-harmonic field radiated from Al_2O_3 of various thickness ranging from $0.1z_r$ in the highest curve to $3z_r$ in the lowest curve in steps of $0.1z_r$. The signal is plotted in the rest-frame of the harmonic pulse, relative to the time of detection.

because the harmonic generation is due to any $\chi_{surface}^{(3)}$, but because the active region of the crystal is small compared to the interaction length required to modulate the spectral intensity. Fig. 4.5 shows how temporally, and as well spatially, the large phase mismatch and considerable group-velocity mismatch cause the harmonic pulse to remain short. The very short distance over which the interaction occurs leaves the phase of the pulse undistorted. We emphasize that this is not really an ‘enhancement’, because the $\chi^{(3)}$ value is not changing in a fundamental way at the surface. The amplitude of the radiated third-harmonic grows solely through a coherent process.

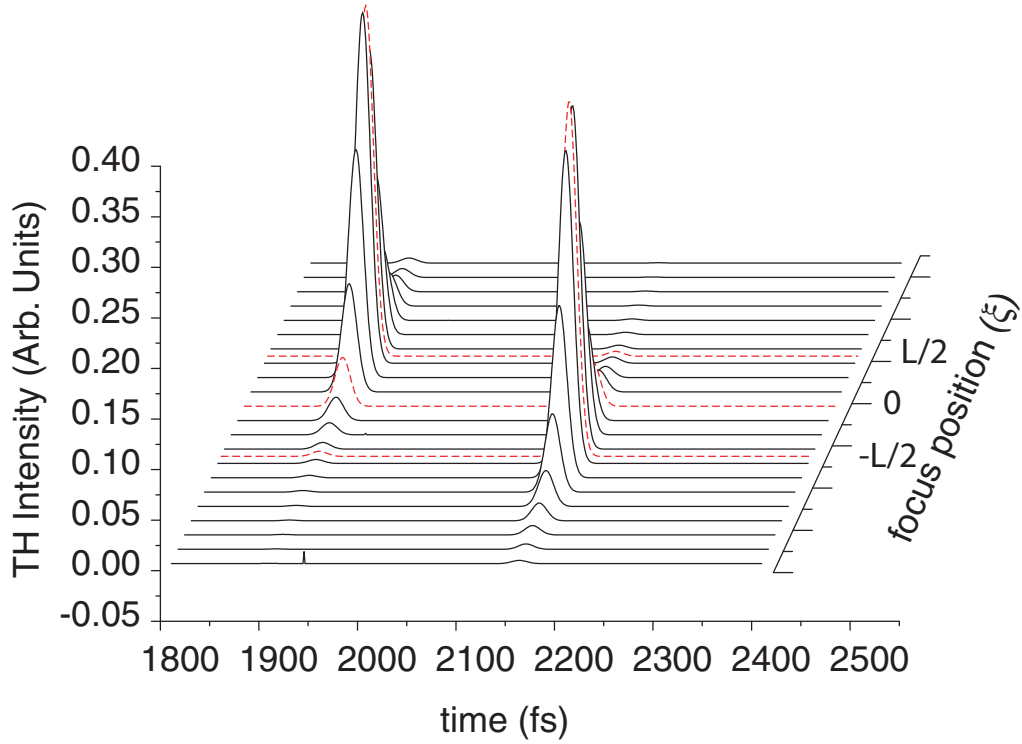


Figure 4.6: Time-dependent harmonic field radiated from 330- μm -thick Al_2O_3 as a function of the focal position, ξ . Dashed curves emphasize THG for focusing at either surface, as well as in the center.

Using Eq. 4.17a it is possible to calculate the time-dependent, radiated fields when the focus is placed at an arbitrary position, ξ , relative to the original beam waist. We calculate these fields for various focal positions in Fig. 4.6. We find that the radiated field can be approximated as the sum of two Gaussian pulses, where each pulse is generated within one coherence length of each surface, and the pulses are separated in time by $\tau(L) = (\beta_1(\lambda) - \beta_1(\lambda/3))L$. In reality, third-harmonic light is being generated in all regions of the crystal, but phase matching is so poorly satisfied, there is no chance for the field to amplify. In cw Gaussian optics, the Guoy effect manifests itself as a reduction in the efficiency of THG when the fundamental beam is focused in the center of isotropic media [57]. This remains true even when spatio-temporal overlapping is no longer satisfied, but the dominant mechanism for the disappearance of the harmonic field upon focusing at the center of the crystal is not Guoy, which is commonly understood as “light generated prior to the focus destructively interferes with that generated beyond the focus” [50]. Group-velocity mismatch eliminates such a long-range coherent effect, so the z-scan will always resemble a surface effect.

We z-scanned a 330 μm sapphire substrate, shown in Fig. 4.7, spectrally resolving the signal for each position ξ , and obtained a series of spectra which are conjugate to the time-domain fields in Fig. 4.6. Eq. 4.17a predicts the radiated third-harmonic field is approximately a Gaussian pair, separated by τ , with field strengths, $E_{3\omega}(z_{surface}) \propto E_{\omega}(z_{surface})^3$. Using the Fourier transform,

$$|\tilde{E}(\Omega)|^2 = \left| \int_{-\infty}^{\infty} \tilde{E}(t) e^{-i\Omega t} dt \right|^2 \quad (4.19)$$

, and assuming a purely real-valued electric field (for the sake of simplicity)

$$\tilde{E}(t) = e^{-\Gamma_0 t^2} + e^{-\Gamma_0 (t-\tau)^2} \quad (4.20)$$

allowed for the spectrum to be computed. Equation 4.19 is a standard integral which has the solution

$$|\tilde{E}(\Omega)| = \left| \sqrt{\frac{\pi}{\Gamma_0}} e^{\frac{\pi^2 \Omega^2}{\Gamma_0}} (1 + e^{i\tau\Omega}) \right|, \quad (4.21)$$

where the electric field is in the form of equation 4.18. The result is in good agreement with what we observe experimentally in the 330 μm substrate, when the focus is placed at $\xi = 0$. Fig. 4.7 demonstrates how a z-scan experiment cannot be distinguished from a surface enhancement effect. The temporally integrated fields of Fig. 4.6, when plotted as a function of ξ , produce a curve identical to the surface model in Fig. 4.4. This is a result of the third-harmonic's origination from a thin layer near the dielectric interface. The experimental data fit this model well at the first surface. At the second surface the signal is stronger, plausibly resulting from an overcompensation of group-velocity dispersion in our experimental setup.

4.4.3 discussion

Third-harmonic generation in transparent materials is a bulk process. The same $\chi^{(3)}$ which is used for cw measurements applies to measurements done using ultrashort-pulsed lasers. However, there are significant differences in the coherent nature of the harmonic process, due to the group-velocity mismatch of the pump and harmonic, which causes a z-scan measurement to indicate a surface susceptibility, rather than a bulk susceptibility. We have shown how to model the time-dependence of third-harmonic generation to account for this. Since the frequency-domain and time-domain are related by a Fourier transform, the appearance of spectral modulation in a short pulse laser indicates either phase modulation of the pulse, or multiple pulses without phase modulation[61, 62]. We observe spectral modulation due to pulse breakup. The origin of this phenomena is the group-velocity mismatch of the fundamental and harmonic light pulses. This can be understood as follows: as

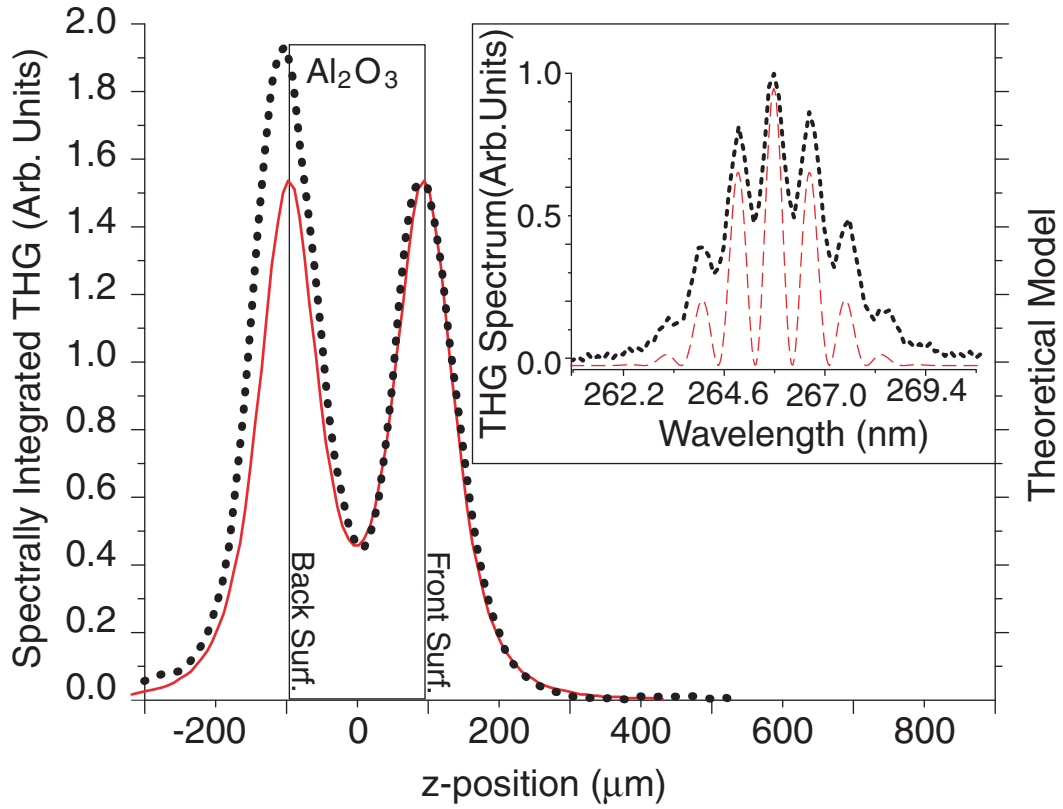


Figure 4.7: Comparison of temporally integrated z-scan calculation of Eq. 4.17a for 330 μm sapphire sample, solid line, and experimental data. Also shown (inset) is the Fourier transform of the calculated time-dependent fields, shown as a dashed line, and the observed spectrum, shown as a solid line.

the harmonic pulse begins to fall behind the fundamental in such a way that in one group-velocity walk-off length of the nonlinear interaction, the initial harmonic pulse is no longer spatially overlapped with the instantaneous harmonic relative to the fundamental, the effect of phase matching is to cut the pulse into two, separate pulses. For a thin optical material, the frequency-domain of the third-harmonic signal can interpret the temporal separation of the signal pulses generated at dielectric interfaces. This temporal separation is directly proportional to the length, L , of the nonlinear medium.

4.5 Conclusions

The propagation of short optical pulses can have dramatic consequences on nonlinear optical processes in materials. To fully understand nonlinear laser matter effects, the propagation of the pulses must be coupled to the equations governing growth of a harmonic field. We examined closely how propagation affected third-harmonic generation, by performing time-domain analysis. We were surprised to find that third-harmonic generation in materials appears as a surface effect when ultrafast lasers are used.

What causes the sensitivity to the interfaces was not fully described using the interface response, other than to say that interfaces are producing the signal. However the identification of an interface-response allows us to better understand the origin of the third harmonic signals that we observed. Using a cw approach was insufficient for modeling the z-scanning measurements on even a simple optical material. We tried it, but the result did not match up to our experiments. Using the ultrafast model well-described the surface response we observed. Having an accurate description of the bulk response was necessary for describing the third-harmonic response of more complicated systems such as films and multilayered nanostructured optical materials.

Chapter 5

Quantifying Ultrafast Third-harmonic Generation from Thin Films

5.1 Introduction

The z-scan is a straightforward and sensitive method for analyzing nonlinear optical materials using a focused laser ¹. Since it measures how a nonlinear signal changes as a function of the input focus position, it is a fairly direct measure of the nonlinear susceptibility. Applied to degenerate four-wave mixing (DFWM), the z-scan has become a useful tool for characterizing optical switches and other nonlinear Kerr effects [63]. The well-developed formalism permits the measurement of both the real and imaginary parts of the nonlinear susceptibility. Recently, the z-scan principle has broadened to include other nonlinear optical effects, and has been introduced to third-harmonic generation in optical solids and thin liquid layers [52, 55, 51, 53,

¹Reprinted text with permission from D. S. Stoker, J. Baek, W. Wang, D. Kovar, M. F. Becker, J. W. Keto, Physical Review A, Vol. 73, 002605 2006. Copyright (2006) by the American Physical Society

54, 49]. In this report, third-harmonic (TH) z-scans of an AlN film were used to determine the film’s third-order susceptibility $\chi^{(3)}$.

Ultrafast lasers have been utilized to perform THG microscopy [64, 65, 66, 51, 53]. These experiments used tightly-focused beams, which have Rayleigh ranges shorter than the group-velocity walk-off length. Their experimental model relies on focusing effects stemming from the Guoy phase shift, and neglects group-velocity mismatch of the fundamental and harmonic pulses [56, 57]. In a recent article, we showed that THG using focused ultrafast lasers, in which the Rayleigh range is longer than the group-velocity walk-off, is not affected by the Guoy phase shift. In that article we identified group-velocity mismatch (GVM) and phase-velocity mismatch as the important parameters responsible for past observations of interface-sensitive THG [49].

Even with the theoretical complications imposed by focusing, work by Petrov and Barille *et al.* showed that tightly-focused lasers can be used to make accurate susceptibility measurements of liquid and solid thin films [67, 53]. Furthermore, a tight focus allows for spatial discrimination of nonlinearities in inhomogeneous materials [51]. Despite the successes in quantifying THG susceptibilities, there are a few notable deficiencies: tight-focusing produces an asymmetric z-scan shape which is not well-modeled by a paraxial beam formula [53, 51]; numerical techniques were required to evaluate the phase matching integrals [67, 53]; and many of the studies were carried-out in untextured or amorphous samples, which did not require consideration of the tensor nature of the susceptibility [53, 67]. In this paper, we demonstrate that using a slightly lower numerical aperture offers at least two important advantages: an accurate representation of the z-scan shape, and an analytical approach to calculating the susceptibility. Furthermore, we supplement the previous reports with a systematic method for dealing with group-velocity walk-off in third-harmonic generation, which when analyzed in the time-domain allows for the

calculation of the time-dependent phase of the radiated TH field. The phase sensitivity is carried throughout our analysis, and we will show it can be measured from the TH spectrum [49].

In the absence of phase matching, THG originates from the boundaries of bulk nonlinear media. At the dielectric boundary, interruption of phase-matching causes an interface-localized growth of the TH field. THG from interfaces is distinct from surface second-harmonic generation (SHG), which is a sensitivity to angular momentum conservation [68]. More applicable is Kleinman and Miller’s description of harmonic generation in isotropic, phase-mismatched media [69]. They described a surface response that is not exclusive to second-order processes, and is applicable to CW THG experiments. However, ultrafast pulses are only overlapped for a distance smaller than the group-velocity walk-off length. Group-velocity walk-off is practically universal when near-infrared (NIR) pulses are used, since the third-harmonic is near the band edge of many optical materials such as quartz, sapphire, fused silica, and LiF. In a recent experiment, 130-nm pulses from the interfaces of a MgF_2 slab were directly observed [70].

5.2 THG from PLD aluminum nitride

We measured and modeled third-harmonic generation (THG) from an AlN thin film on sapphire using a time-domain approach appropriate for ultrafast lasers. Second-harmonic measurements indicated the polycrystalline AlN contains long-range crystal texture. An interface model for third-harmonic generation enabled analytical representation of scanning THG (z-scan) experiments. Using it, and accounting for Fresnel reflections, we measured the AlN/sapphire susceptibility ratio, and estimated the susceptibility for aluminum nitride $\chi_{xxx}^{(3)}(3\omega; \omega, \omega, \omega) = 1.52 \pm 0.25 \times 10^{-13}$ esu. The third-harmonic (TH) spectrum strongly depended on the laser focus position and sample thickness. The amplitude and phase of the frequency-domain

interference were fit to the Fourier transform of the calculated time-domain field to improve the accuracy of several experimental parameters. We verified that the model works well for explaining TH signal amplitudes, and spectral phase. Some anomalous features in the TH spectrum were observed, which we attributed to non-paraxial effects.

AlN is an interesting material, technologically, and is widely utilized in optoelectronic devices [30, 31]. The primary feature of AlN is a large band gap, which makes it amenable to generating a TH field in the ultraviolet (UV) [32, 71]. In bulk crystalline form, it does not have a large susceptibility, but it could serve as a passive matrix material in a nanocomposite, containing an active material with a larger nonlinear coefficient [67]. In that case AlN could serve as a passive matrix in UV and ultrafast light modulators, or in other nonlinear devices requiring short wavelength operation [72, 29]. In a recent report, AlN films generated by pulsed laser deposition (PLD) were shown to contain nanotexturing [73].

Measuring the third-order susceptibility $\chi^{(3)}(3\omega; \omega, \omega, \omega)$ of AlN requires knowing the relative third-harmonic response of the film and substrate, but other factors in addition to susceptibility contribute to a measured third-harmonic signal. Previously, tightly-focused experiments in nearly or exactly index-matched media could neglect reflections, but this is not possible near interfaces with a larger index mismatch, such as an AlN/sapphire interface [53, 51]. We performed independent measurement of reflection losses and phase matching in the film and substrate; rotational (azimuthal) harmonic dependence determined the macroscopic crystal ordering (texture); and we accounted for the coherent interaction of the film and substrate fields. Knowing all these parameters is a requirement for properly estimating the AlN/Al₂O₃ susceptibility ratio [74].

third-order rotational studies in AlN

We used PLD to deposit the AlN thin film. The ablation source was a 248-nm Kr:F excimer laser, pulsed at 30 Hz, at 150 mJ pulse⁻¹. The laser was focused to $\sim 0.03 \text{ cm}^2$ at the AlN target surface, in a 0.58 mTorr N₂ atmosphere. The plasma plume was directed at a nearby (5 cm), 330 μm thick sapphire (0001) substrate, held at 800 °C, which allowed the plasma constituents to recombine and form a film. During the 30 min deposition, the laser focus moved in a circle at 0.5 Hz, to increase film uniformity. Preparing films in this way produced a material with a slightly wedged shape, of average thickness of 306.3 nm, but other material properties such as density and surface roughness are superior to evaporation-based methods [11].

In chapter 2 it was shown that crystal texturing in PLD films caused a high degree of asymmetry in the rotational dependence of the second harmonic response of AlN. It is known that THG is sensitive to material structure, so we repeated the rotational measurement of the AlN/sapphire interface, measuring TH instead [75, 52]. The results are plotted in Fig. 5.1. Rotational THG could not resolve any $\chi^{(3)}$ anisotropy, neither in the bare substrate, nor in the film. The individual $p_{in} \rightarrow p_{out}$ and $p_{in} \rightarrow s_{out}$ components of THG in the AlN film are essentially identical. The azimuthal response of quartz demonstrates THG has structural sensitivity; the overall periodicity matches the greater periodicity expected for THG. The quartz data in Fig. 5.1 indicates a sensitivity to surface defects, demonstrated by the repeatable distortions of the harmonic signal. When the quartz measurements were repeated, the fine details at 55, 120 250 and 300 degrees were duplicated.

5.2.1 THG from aluminum nitride/sapphire interfaces

In chapter 4 it was shown that the interface THG arises from an interplay between group-velocity and phase mismatching [49]. These coherent effects are always accompanied by a large, incoherent discontinuity in $\chi^{(3)}$ which initiates the signal

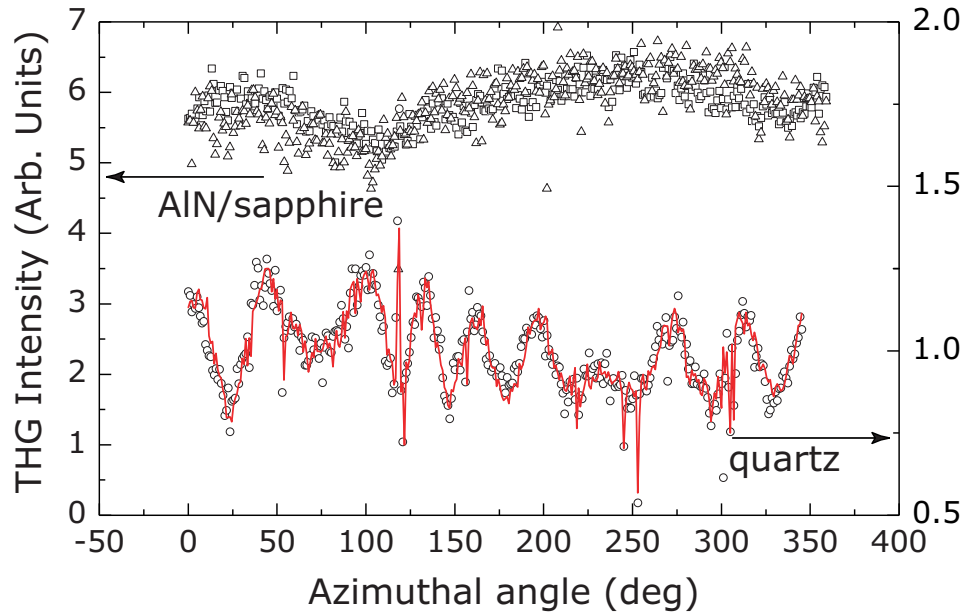


Figure 5.1: THG from AlN, measured in both polarization orientations, $p_{in} \rightarrow p_{out}(\square)$ and $p_{in} \rightarrow s_{out}(\triangle)$. For comparison, the measurement was repeated on a 100- μm -thick piece of z-cut quartz. Two azimuthal measurements of $p_{in} \rightarrow (s+p)_{out}$ THG are shown. The scatter data(\circ) correspond to shorter integration. The line through it is the same measurement, just taken with longer exposure.

growth from a region determined by the coherence length L_c .

Plotting the z -integral of the TH field over a single slab of material as a function of time is a way to characterize the origin of the nonlinear response. The third-harmonic field has temporal dispersion, due to GVM, so a particular time in the third-harmonic output is generated by a particular portion of the nonlinear medium. In the time-domain we calculate two unbroadened pulses will emerge, separated by a time corresponding to the nonlinear medium (slab) thickness, indicating that only the material in the vicinity of the interfaces generates third-harmonic.

First, we treat the interface THG response assuming a Gaussian-pulsed, collimated beam. We begin by deriving an analytical solution for a single slab, which we use later when approximating boundaries as a superposition of two slabs of dissimilar material. Since AlN thin films grown on Al_2O_3 are the interest of this paper, many of the details of that system are provided in this section in parallel with the theoretical description. We also found it is convenient to adopt ultrafast units for the parameters listed in Table 5.1² [27].

Table 5.1: Ultrafast values

| Parameter | Value | Units | Significance |
|-----------------|--------|-----------------------|-------------------------|
| Γ | .00141 | fs^{-2} | Gaussian time parameter |
| c | 0.3 | $\mu\text{m fs}^{-1}$ | vacuum-phase velocity |
| $\Delta\lambda$ | 0.03 | μm | pump bandwidth |
| λ_0 | 0.800 | μm | pump centroid |

The oscillating fundamental field,

$$\tilde{E}_1(z, t) = \tilde{A}_1(z, t)e^{i(\omega t - k_1 z)}, \quad (5.1)$$

is proportional to a slowly varying complex amplitude, $\tilde{A}_1(z, t)$. As written, Eq. 5.1 applies to any space-time pulse type, be it Gaussian, or some arbitrary shape.

²The pump centroid is given as a nominal value. Experimental values varied ± 5 nm

Substituting $\tilde{E}_1(z, t)$ into the paraxial wave equation and canceling common terms gives

$$\frac{d\tilde{A}_3}{dz} = \frac{i2\pi\omega_3^2\chi^{(3)}\tilde{A}_1^3(z, t - \Delta\beta z)e^{i\Delta kz}}{k_3c^2}. \quad (5.2)$$

The group delay term $\Delta\beta z$ in Eq. 5.2 has a minus sign, indicating the nonlinear driving term will continuously travel ahead of the harmonic field. Equation 5.2 must be evaluated numerically for a Gaussian-focused beam, but has an analytical solution for plane-wave pulses.

Phase matching for third-harmonic generation is introduced in Eq. 5.2 as $\Delta k = 3k_1 - k_3$. The phase mismatch Δk is a measure of linear dispersion in an optical material, seen by rewriting it as $\Delta k = 2\pi q\Delta n/\lambda_0$, and accounts for the relative phase of the ω and 3ω fields Δkz as they propagate a distance z through a material. When $\Delta k \neq 0$, there is a coherent transfer of energy between the ω and 3ω fields over a characteristic distance $L_c = 2\pi/\Delta k$.

Equation 5.2 is integrated over the nonlinear material length to find the generated third-harmonic field as a function of time at the exit surface,

$$\tilde{A}_3(t) = \int_{z_i}^{z_f} dz \frac{i2\pi\omega_3^2\chi^{(3)}\tilde{A}_1^3(z, t - \Delta\beta z)e^{i\Delta kz}}{k_3c^2}. \quad (5.3)$$

Taking the limit as $\Delta\beta \rightarrow 0$, $\tilde{A}_3(t)$ reduces to the case describing focusing's effect on THG in gases [57, 56, 76].

If $\Delta k \neq 0$, varying the thickness of a nonlinear medium brings an oscillation of nonlinear signal intensity [77]. Extending this Maker fringe model to ultrafast pulses, Angerer *et al.* showed the SHG loses phase coherence in thick samples, and that the SHG signal deviates from the CW case [27]. Ultrafast THG displays an even more pronounced deviation, because of the larger dispersion between the fundamental and harmonic wavelengths. We integrated Eq. 5.3 for different pulse lengths, assuming an unfocused laser each time, and plotted the TH intensity as a

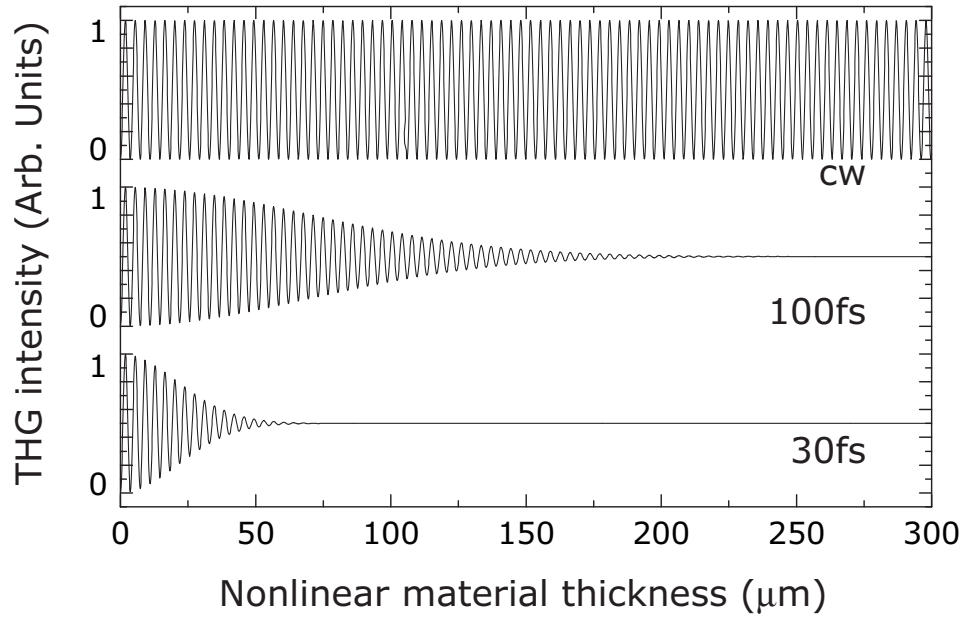


Figure 5.2: Calculated transmitted third-harmonic intensity as a function of Al_2O_3 thickness. Three different laser pulses plotted for reference. The cw laser has the longest $1/e$ damping distance (∞) for the Maker fringes. The 100-fs laser and the 30-fs laser pulses damp over a much shorter distance, because of GVM effects. The high frequency oscillations are spaced by the coherence length $L_c = 3.65 \mu\text{m}$. This calculation assumes an unfocused beam.

function of material thickness in Fig. 5.2.

There is a strong effect of pulse length on THG. Based on Fig. 5.2, two *regimes* are identified. The first, relevant to long pulses, is identified by periodic energy transport over large distances. The short pulse case is easily differentiated in thicker materials, whereby little coherence exists between the harmonic and pump fields. The thinnest optical materials maintain a CW response for any pulse length, because there is not enough material for pulse walk-off to occur.

It appears as though the sensitivity of the TH field to small changes in the thickness of the bulk material disappears in thick materials, when using an ultrafast laser. This is true if only the TH intensity is measured. In fact, the sensitivity to the thickness parameter is not lost: it is maintained by the phase of the TH field. To show how to retain the sensitivity to material thickness, the following analysis includes the phase of the TH pulse.

If the \tilde{A}_1 field is collimated and interacts with a dispersive optical element, it generates a time-dependent harmonic field

$$\tilde{A}_3(t) = \frac{i2\pi\omega_3^2\chi^{(3)}A_1^3}{k_3c^2} \int_{z_i}^{z_f} dz e^{-3\Gamma(t-\Delta\beta z)^2} e^{i\Delta kz}. \quad (5.4)$$

To evaluate the integral we assumed

$$\tilde{A}_1^3(z, t) = A_1^3 e^{-3\Gamma(t-\Delta\beta z)^2}, \quad (5.5)$$

and $\chi^{(3)}$ is spatially non-varying and defined by a stepwise increase in the magnitude, an assumption common to other reports [46, 56, 57, 51]. Eq. 5.4 can be separated

into real and imaginary parts, and integrated. Doing so yields

$$\begin{aligned}
\tilde{A}_3(t) &= \frac{i2\pi\omega_3^2\chi^{(3)}A_1^3\sqrt{\pi}}{k_3c^22\sqrt{3\Gamma}\Delta\beta} \left\{ e^{-\frac{\Delta k(\Delta k - i12t\Gamma\Delta\beta)}{12\Gamma\Delta\beta^2}} \right. \\
&\times \left(-\operatorname{erf}\left[\frac{i\Delta k + 6\Gamma\Delta\beta(t - z_f\Delta\beta)}{2\sqrt{3\Gamma}\Delta\beta}\right] \right. \\
&+ \left. \left. \operatorname{erf}\left[\frac{i\Delta k + 6\Gamma\Delta\beta(t - z_i\Delta\beta)}{2\sqrt{3\Gamma}\Delta\beta}\right] \right) \right\}. \tag{5.6}
\end{aligned}$$

The variables

$$\zeta_k \equiv \frac{\Delta k}{\xi^{\frac{1}{2}}} \tag{5.7a}$$

$$\zeta_t \equiv t\sqrt{3\Gamma} \tag{5.7b}$$

$$\xi \equiv 12\Gamma\Delta\beta^2 \tag{5.7c}$$

simplify the form of Eq. 5.6 to

$$\begin{aligned}
\tilde{A}_3(t) &\propto \sqrt{\frac{\pi}{\xi}} e^{[-\zeta_k^2 + 2i\zeta_k\zeta_t]} \\
&\times \left\{ \operatorname{erf}\left[\zeta_t + \left(i\zeta_k - \frac{z_i\xi^{\frac{1}{2}}}{2}\right)\right] - \operatorname{erf}\left[\zeta_t + \left(i\zeta_k - \frac{z_f\xi^{\frac{1}{2}}}{2}\right)\right] \right\}. \tag{5.8}
\end{aligned}$$

The absolute value of Eq. 5.6 or 5.8 describes the time-dependent TH pulse amplitude, and the angle describes its phase. Each is plotted in Fig. 5.3. The TH field consists of a pair of pulses, which are separated in time. GVM introduces a chirp to each pulse. The jump in the relative phase of the two pulses is a manifestation of sensitivity to material thickness, and is the phase analog of the thickness-dependent intensity oscillations of a cw laser. This temporal description of THG provides clear evidence of the interface response, because temporal dispersion identifies a particular time with a particular point in the material.

The TH response is initiated by a discontinuity in $\chi^{(3)}$, but the magnitude

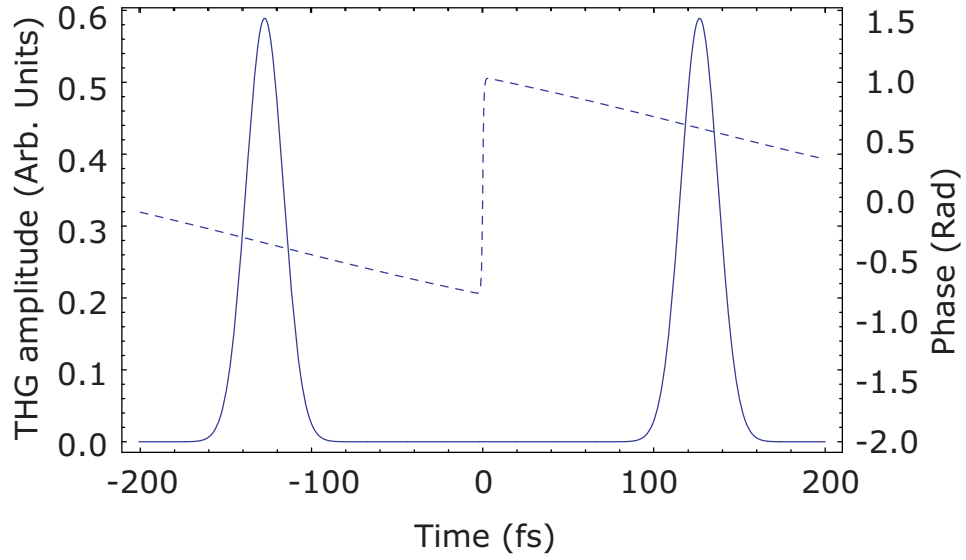


Figure 5.3: Transmitted third-harmonic field strength. Also plotted as a dashed line is the phase, which shows that for an initially unchirped pulse, the harmonic pulse that is generated is linearly chirped. The calculation assumes $330\text{ }\mu\text{m}$ of c-plane sapphire, which corresponds to the substrate thickness in our samples. Calculations for slightly different thicknesses cause the phase jump at $t = 0$ to change, but the amplitude to remain the same.

of the generated field depends on abrupt changes in any of $\Upsilon = \{\Delta k, \Delta\beta, \chi^{(3)}\}$ at an interface. Table 5.2 lists these values for AlN, Al₂O₃, and SiO₂. For multilayer materials, it is important to take care when introducing the inverse group-velocity mismatch, $\Delta\beta$, and phase mismatch, Δk , into the z-integral in Eq. 5.4. Otherwise, the group delay, $\Delta\beta z$ and phase, $\Delta k z$, will be unphysically discontinuous.

Table 5.2: Relevant interface parameters

| Υ | Al ₂ O ₃ | AlN | SiO ₂ | Units |
|---------------|--------------------------------|---------|------------------|-----------------------------|
| Δk | -1.72 | -4.6(6) | -1.288 | μm^{-1} |
| $\Delta\beta$ | 0.79 | 2.3(5) | 0.5774 | $\text{fs}\mu\text{m}^{-1}$ |

To illustrate the effect of changing the Υ parameters in multilayered materials, we calculated the time-dependent TH response of a thick slab of Al₂O₃ adjacent to an equally thick slab of AlN. There are now 3 interfaces: air/sapphire, sapphire/AlN, and AlN/air. The group delay and phase as a function of position in the material are shown in Fig. 5.4. We placed the interface at $z=0$ to prevent discontinuities in the group delay ³.

The TH field generated in the two-slab material was calculated using Eq. 5.8 twice: once for the Al₂O₃ slab and once for the AlN slab. The two solutions overlap at $t=0$ and add coherently. There are now three generated TH pulses. Both the amplitude and phase are plotted in Fig. 5.5. The jump in the phase between the pulses generated at each interface is again visible. Between the pulse from the sapphire/AlN interface and the AlN/air interface, the phase cycles through 2π of phase many times. If a CW field were propagating through the same thickness of AlN, the fundamental and harmonic fields would oscillate in and out of phase as many times the phase cycles through 2π .

As a comparison, the time-dependent third-harmonic field, due solely to

³if a material interface at position z_i is encountered, a change in the inverse group-velocity mismatch $\Delta\beta$ for $z_i \neq 0$ causes an unphysical discontinuity in the group delay $\Delta\beta z_i$

changes in $\Delta\beta$ and Δk was calculated. We assumed the dispersion in Fig. 5.4, using the parameters in Table 5.2, but assumed no change in the nonlinear susceptibility at the sapphire/AlN interface. We calculated no change for the air/sapphire pulse and a decrease by a factor of two of the AlN/air interface. However, the pulse from the sapphire/AlN interface is *larger* by a factor of 2.5. When there is no change in both the susceptibility and Δk , but $\Delta\beta$ was allowed to vary, a smaller pulse by one order-of-magnitude was calculated. Based on the simulations of varying the individual Υ parameters, we conclude that all of them have significant contributions to THG from interfaces.

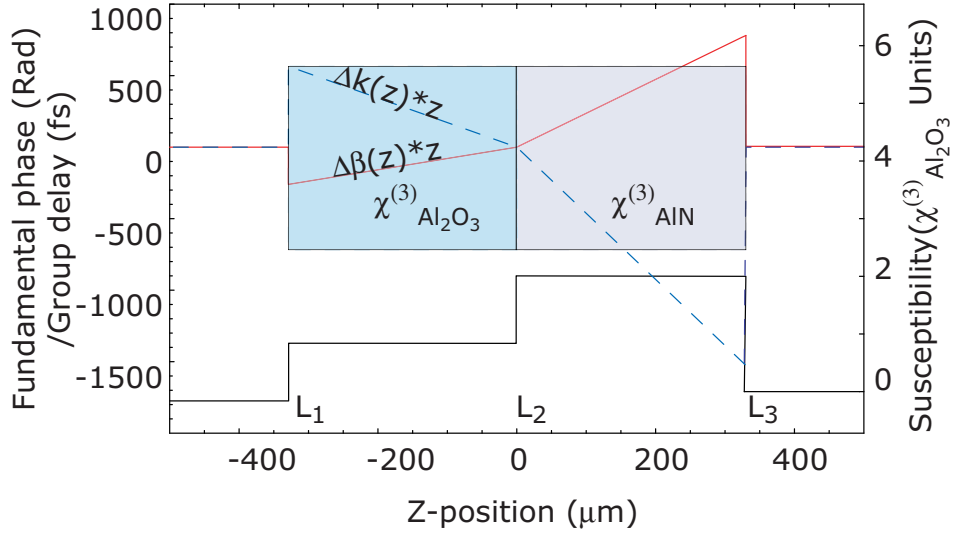


Figure 5.4: Shown here are both the group delay, $\Delta\beta z$, and phase, $\Delta k z$, for the two-slab model. These continuous parameters describe the z -dependence of the entire material's dispersion, and can be inserted into Eq. 5.8, to find the time-dependent radiated harmonic field due to all material interfaces. The interface between the two slabs is placed at $z=0$ to prevent any discontinuities in the group delay $\Delta\beta z$.

Ultrashort pulses generate TH differently, compared to long pulses, whereby long-range effects have dominated, and were noted in earlier articles [57, 76]. The phase mismatch and group-velocity mismatch inhibits the growth of TH radiation

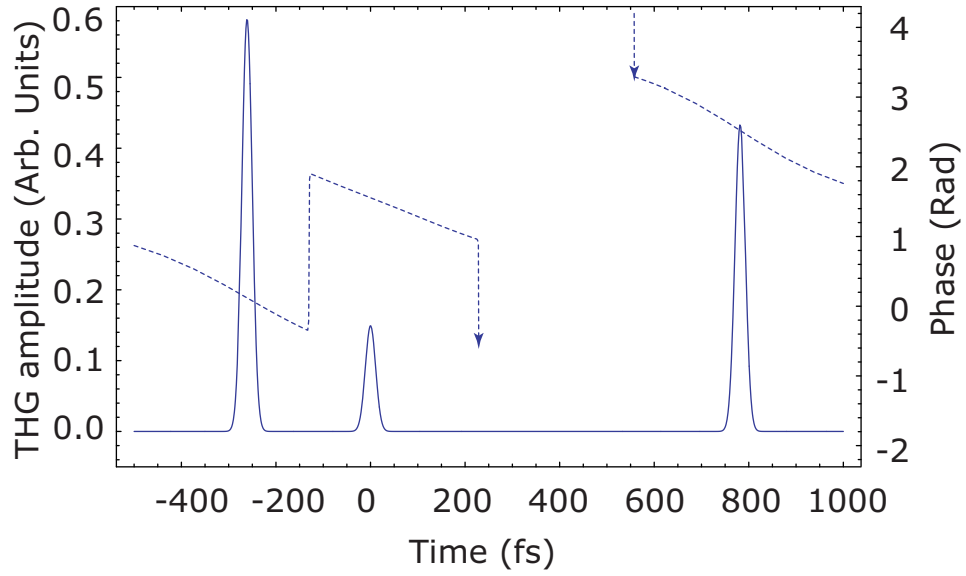


Figure 5.5: Shown here is the calculated time-dependent TH field, radiated from the model system in Fig. 5.4. Adding group delay and phase changes at the dielectric boundary affects both pulse separation and pulse magnitude. At the AlN/Al₂O₃ interface, there is a partial suppression of TH resulting from the vector addition of the amplitude and phase. The time-dependent phase is also plotted. Between $t=225$ and $t=550$ fs, the phase changes rapidly, with a linear slope of ~ -2.0 rad/fs.

from the bulk, but within a coherence length of an abrupt change in the value of the susceptibility a TH field is generated. The magnitude of the fields generated in each material near the interface strongly depends on the phase matching factor Δk . As shown in Fig. 5.2, thin materials display Maker fringes, but thicker bulk optics do not. Thickness information is kept in the relative phase of the pulses generated at the entrance and exit interfaces of a slab of material. The analysis of multilayered materials also indicated the phase of the TH fields strongly impacts how pulses will superimpose. Though the two-slab model assumes the AlN has a thickness comparable to the substrate, the response of the 300-nm film is obtained using the same mathematics. In a film, the pulse located at the $t = 775$ fs in Fig. 5.5 will overlap temporally and interfere with the $t = 0$ pulse. Treating the thin film as a limiting case of a slab provides insight into the TH material response using ultrafast pulses.

5.3 THG z-scan measurements of interfaces

The treatment of Sec. 5.2.1 demonstrated that TH pulses originate from nonlinear material boundaries. In a two-slab material, the pulses at the shared interface add coherently in time to give three pulses. Accordingly, THG from the AlN/sapphire sample is reduced to THG from three interfaces: air/sapphire, sapphire/AlN, and AlN/air. In a slow detector, the sum of the pulses is measured, so there is no information about individual interfaces. In theory, each pulse could be sampled using an ultrafast or pump-probe technique, but the z-scan is a more convenient technique of isolating the pulse from an individual interface. In this section, we show how the interface model of ultrafast THG can be used to model z-scans.

5.3.1 model

The pulsed plane-wave approximation made in Eq. 5.8 is applicable to z-scan measurements that use focused ultrafast pulses. Because growth of the \tilde{E}_3 field turns off immediately after the \tilde{E}_1 field enters the bulk of the material, all the relevant information about the \tilde{E}_1 field is located right at the material interface. Consequently, if a focused laser is scanned through a dielectric interface, the THG signal will scale like the cube of the intensity of the fundamental field at the interface.

The change in the beam diameter varies slowly over the region generating the third-harmonic signal when ultrafast pulses are used. According to the arguments in Sec. 5.2.1, this distance is the coherence length ($\approx 1 \mu\text{m}$), which is much smaller than the Rayleigh range in our experimental setup ($\approx 100 \mu\text{m}$). Consequently, the amplitude of the fundamental field may be removed from the phase matching integral. In the simplest case, if the laser is focused at a single dielectric/air interface at z_f and using the first term in Eq. 5.8, the time-dependent, amplitude-independent phase matching integral $\tilde{J}(t)$ becomes

$$\begin{aligned}\tilde{J}(t) &= \lim_{z_i \rightarrow -\infty} \int_{z_i}^{z_f} dz e^{-3\Gamma(t-\Delta\beta z)^2} e^{i\Delta k z} \\ &= \sqrt{\frac{\pi}{\xi}} e^{(-\zeta_k^2 + 2i\zeta_k \zeta_t)} \\ &\quad \times \text{erf}\left[\zeta_t + \left(i\zeta_k - \frac{z_f \xi^{\frac{1}{2}}}{2}\right)\right].\end{aligned}\tag{5.9}$$

The scaling of the time-dependent radiated TH power (apart from unit factors)

$$\mathcal{P}_3(t) = |\tilde{f}_1^3]_{z_f} \chi^{(3)} \tilde{J}(t)|^2\tag{5.10}$$

is determined by the cube of the fundamental intensity at the interface located at $z = z_f$. Modeling a z-scan becomes simpler, because the integral in Eq. 5.9 is the

same for every focal position, and the interface contribution at $z = z_f$ is stated explicitly.

More generally, the TH response of multiple interfaces can be modeled. In Sec. 5.2.1, the TH response of a plane-wave pulse due to a finite optical element with a beginning and end at z_i and z_f was calculated. The solution, Eq. 5.6, has two terms. Each term describes TH originating at each interface. The sign differs, since the terms arise from an evaluation of the indefinite form of the integral in Eqs. 5.4 and 5.9. The time-dependent TH power for the two interfaces of a single slab on nonlinear material is

$$\begin{aligned} \mathcal{P}_3(t) \propto & |\chi^{(3)} \sqrt{\frac{\pi}{\xi}} e^{(\zeta_k^2 - 2i\zeta_k\zeta_t)}|^2 \\ & \times | \tilde{f}_1^3]_{z_i} \text{erf}[\zeta_t + (i\zeta_k - \frac{z_i \xi^{\frac{1}{2}}}{2})] \\ & - \tilde{f}_1^3]_{z_f} \text{erf}[\zeta_t + (i\zeta_k - \frac{z_f \xi^{\frac{1}{2}}}{2})]|^2. \end{aligned} \quad (5.11)$$

Evaluating the amplitude of the fundamental field \tilde{f}_1 at each interfaces determines the relative contribution of each interface to the measured TH signal. Equation 5.11 can be applied to third-harmonic generation from any sized material, as long as the group walk-off length is much smaller than the Rayleigh range. The mathematical requirement is that $(\Delta\beta z_r \sqrt{\Gamma})^{-1} \gg 1$.

5.3.2 application to thin film $\chi^{(3)}$ measurements

Determining the value of $\chi_{\text{AlN}}^{(3)}$ requires deconvoluting the TH response of the AlN film and the Al_2O_3 substrate. The experimental requirement is manifold. One must measure the TH response of the substrate, the TH response of the AlN-coated substrate, as well as the linear optical parameters of both the film, and the sapphire substrate. The linear optical properties of AlN were determined through the use of an Optical Parameter Extraction (OPE) calculation. The linear thickness was also

Table 5.3: Parameters from Lorentzian fit

| Sample | a_0 (arb.units.) | a_1 (arb.units.) | z_r (μm) | z_0 (μm) | L (μm) |
|---------------|--------------------|--------------------|-------------------------|-------------------------|-----------------------|
| substrate | 64.5(2) | 60.8(2) | 112.5(7) | 534.3(4) | 188.8(6) |
| AlN/substrate | 98.2(3) | 54.2(7) | 110(1) | 544.1(5) | 184(3) |

determined to be 0.31(1) μm . The phase matching and inverse group velocity are listed in Table 5.2, and are the primary variables used for modeling THG in a thin film on a substrate; however, we included the Fresnel coefficients to obtain the most accurate estimate for $\chi^{(3)}$.

Both the bare and coated substrates were measured using the third-harmonic z-scan technique [49]. To satisfy the requirement for the interface model the (vacuum) Rayleigh range of the laser focus was approximately 200 μm , which is greater than the walk-off length in the sapphire substrate ($\approx 25\mu\text{m}$), determined by the damping distance of the Maker fringes in Fig. 5.2. The experimental data are shown in Fig. 5.6. Accounting for each of the air/AlN, and AlN/sapphire interfaces with one phase matching integral allowed the line shape of the z-scan measurements shown in Fig. 5.6 to be described by a sum of cubed Lorentzians

$$\mathcal{P}_{3\omega}(z) = \left[\frac{a_0}{1 + \left(\frac{z-z_0}{z_r} \right)^2} \right]^3 + \left[\frac{a_1}{1 + \left(\frac{z-z_1}{z_r} \right)^2} \right]^3, \quad (5.12)$$

where $z_1 = z_0 + L$. The fitting parameters are listed in Table 5.3.

The data is presented in the laboratory-frame translation units, and the fit allowed us to determine several optical parameters. Taking the average of measurements derived for the coated and bare substrates, we determined the substrate optical thickness L to be 187 μm . Multiplying L by $n_1=1.76$ indicated a physical thickness of 328 μm . The Rayleigh range z_r was also found from the Lorentzian fit. The value, 111 μm , corresponds to the value of z_r within the sapphire, and is consistent with a focal waist diameter of 15 μm .

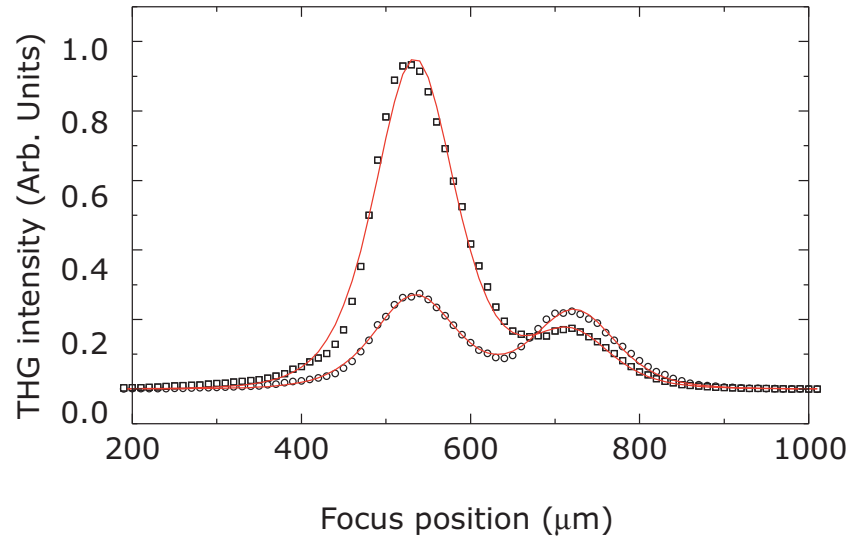


Figure 5.6: Z-scan data from the AlN/sapphire and bare substrate samples, and fitted curves. The top curve (\square) is from the film and substrate, and the lower curve (\circ) is from the bare substrate. I_b and I_m denote the measured substrate and substrate and film intensities at $z_0 = 540 \mu\text{m}$. The horizontal axis is the lab coordinate distance the sample was moved. Within the sapphire, the focus moves across a larger distance, scaled by $n_1=1.76$.

Table 5.4: C_i Parameters from phase matching integrals

| C_i | Definition | Value (arb. units) |
|--|--|--|
| C_1 | $ J_{\text{AlN}} ^2$ | $(\mathcal{F}_1^B \mathcal{F}_1^{\text{TF}})^6 (\mathcal{F}_3^{\text{TF}})^2 \times 1.6(3)$ |
| C_2 | $ J_{\text{Al}_2\text{O}_3} ^2$ (with coating) | $(\mathcal{F}_1^B)^6 (\mathcal{F}_3^{\text{TF}})^2 \times 6.5$ |
| C_3 | $\int_{-\infty}^{\infty} dt (\tilde{J}_{\text{AlN}} \tilde{J}_{\text{Al}_2\text{O}_3}^* + \tilde{J}_{\text{Al}_2\text{O}_3} \tilde{J}_{\text{AlN}}^*)$ | $(\mathcal{F}_1^B)^6 (\mathcal{F}_1^{\text{TF}})^3 (\mathcal{F}_3^{\text{TF}})^2 \times -4.3(6)$ |
| C_4 | $ J_{\text{Al}_2\text{O}_3} ^2$ (bare sapphire) | $(\mathcal{F}_1^B)^6 (\mathcal{F}_3^B)^2 \times 6.5$ |
| $\chi_{\text{AlN}}^{(3)} / \chi_{\text{Al}_2\text{O}_3}^{(3)}$ | Eq. 5.21 (including reflections) | 7.7(8) |

Knowing the relative signals I_b (substrate) and I_m (substrate/film) is required for calculating the film's susceptibility. In the sequential measurements of the coated and bare samples, the signal due to the interface at $710 \mu\text{m}$ is different, because the reflection coefficient at the second interface. The measured values are scaled by the square of the relative Fresnel factors $|\mathcal{F}_3^B / \mathcal{F}_3^{\text{TF}}|^2$ for the TH field propagating from the first interface, through the sample, to the detector. Including the Fresnel factor produces a pump-normalized relative intensity ratio of $I_m / I_b = 3.53(4)$.

The measured energy densities I_m and I_b are related to the calculated fields through an inner product. The energy density of the i^{th} TH field (aside from the factor of $\sqrt{\mu\epsilon}$) is computed with the time integral,

$$I_i = \int_{-\infty}^{\infty} dt \tilde{A}_i(t) \tilde{A}_i^*(t). \quad (5.13)$$

The total field radiated from the $\text{Al}_2\text{O}_3 / \text{AlN}$ interface,

$$\tilde{A}_m(t) = \tilde{A}_f + \tilde{A}_b, \quad (5.14)$$

is the superposition of the substrate-generated field, and the film-generated field. In

which case,

$$\begin{aligned}
I_m &= \int_{-\infty}^{\infty} dt \tilde{A}_b(t) \tilde{A}_b^*(t) + \int_{-\infty}^{\infty} dt \tilde{A}_f(t) \tilde{A}_f^*(t) \\
&+ \int_{-\infty}^{\infty} dt \tilde{A}_b(t) \tilde{A}_f^*(t) + \int_{-\infty}^{\infty} dt \tilde{A}_f(t) \tilde{A}_b^*(t)
\end{aligned} \tag{5.15}$$

and

$$I_b = \int_{-\infty}^{\infty} dt \tilde{A}_b(t) \tilde{A}_b^*(t). \tag{5.16}$$

Each TH field $\tilde{A}_i(t)$ is proportional to a susceptibility $\chi_i^{(3)}$ and phase matching factor $\tilde{J}_i(t)$, with the Fresnel reflection and units constants absorbed into the phase matching integrals. Eq. 5.15 can be rewritten as

$$\begin{aligned}
I_m &= |\chi_{\text{AlN}}^{(3)}|^2 |J_{\text{AlN}}|^2 + |\chi_{\text{Al}_2\text{O}_3}^{(3)}|^2 |J_{\text{Al}_2\text{O}_3}|^2 \\
&\quad + |\chi_{\text{Al}_2\text{O}_3}^{(3)}| |\chi_{\text{AlN}}^{(3)}| \\
&\quad \times \left(\int_{-\infty}^{\infty} dt \tilde{J}_{\text{AlN}}(t) \tilde{J}_{\text{Al}_2\text{O}_3}^*(t) + \tilde{J}_{\text{Al}_2\text{O}_3}(t) \tilde{J}_{\text{AlN}}^*(t) \right).
\end{aligned} \tag{5.17}$$

Both the phase and amplitude information of both the substrate harmonic field $\tilde{A}_b(t)$ and the film-generated field $\tilde{A}_f(t)$ were retained in the calculation. Cross terms were kept and evaluated. The integrals evaluated to four constants, C_1, C_2, C_3 and C_4 and are defined in Table 5.4. Substituting these constants into Eq. 5.17 gives the simplified expression,

$$I_m = |\chi_{\text{AlN}}^{(3)}|^2 C_1 + |\chi_{\text{Al}_2\text{O}_3}^{(3)}|^2 C_2 + |\chi_{\text{Al}_2\text{O}_3}^{(3)}| |\chi_{\text{AlN}}^{(3)}| C_3. \tag{5.18}$$

The arguments of each of the C_i integrals are plotted in Fig. 5.7 to show their relative magnitudes. A high-degree of coherence between the substrate-generated field, and the film-generated field is indicated by the large cross term integral.

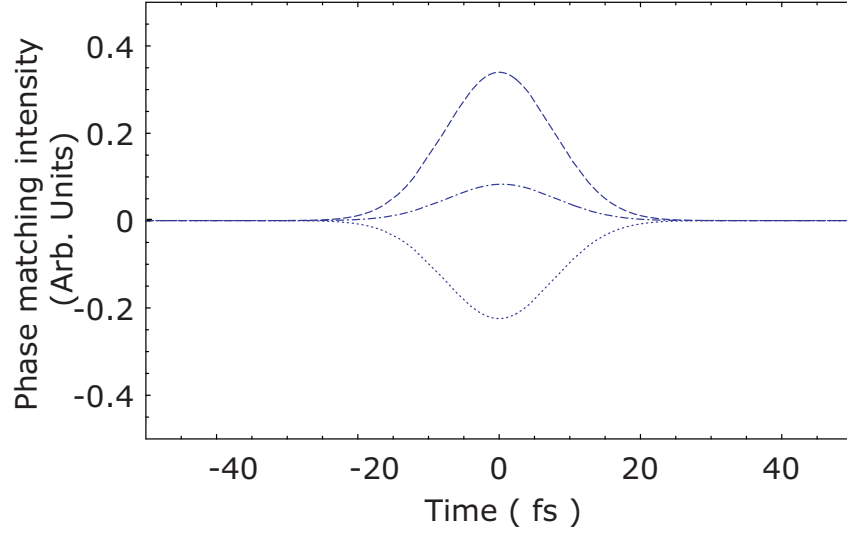


Figure 5.7: Plotted are the time-dependent, real-valued arguments of Eq. 5.17. The dashed line is $|J_{\text{Al}_2\text{O}_3}|^2$. The dot-dashed line is $|J_{\text{AlN}}|^2$. The lower, dotted line is the cross term, $\tilde{J}_{\text{AlN}}(t)\tilde{J}_{\text{Al}_2\text{O}_3}^*(t) + \tilde{J}_{\text{AlN}}^*(t)\tilde{J}_{\text{Al}_2\text{O}_3}(t)$.

Dividing Eq. 5.18 by

$$I_b = |\chi_{\text{Al}_2\text{O}_3}^{(3)}|^2 C_4 \quad (5.19)$$

reduces the problem to solving the quadratic equation,

$$\left(\frac{\chi_{\text{AlN}}^{(3)}}{\chi_{\text{Al}_2\text{O}_3}^{(3)}}\right)^2 \frac{C_1}{C_4} + \left(\frac{\chi_{\text{AlN}}^{(3)}}{\chi_{\text{Al}_2\text{O}_3}^{(3)}}\right) \frac{C_3}{C_4} + \left(\frac{C_2}{C_4} - \frac{I_m}{I_b}\right) = 0. \quad (5.20)$$

It has the solution,

$$\frac{\chi_{\text{AlN}}^{(3)}}{\chi_{\text{Al}_2\text{O}_3}^{(3)}} = \frac{-\frac{C_3}{C_4} \pm \sqrt{\left(\frac{C_3}{C_4}\right)^2 - 4\left(\frac{C_1}{C_4}\right)\left(\frac{C_2}{C_4} - \frac{I_m}{I_b}\right)}}{2\left(\frac{C_1}{C_4}\right)}. \quad (5.21)$$

First, Eq. 5.21 was evaluated assuming no reflective losses, which amounts to using the values in Table 5.4, with the $\mathcal{F}_i^j = 1$. Making the substitutions and taking the positive root indicates the ratio $\chi_{\text{AlN}}^{(3)}/\chi_{\text{Al}_2\text{O}_3}^{(3)}$ is 4.82. Then, we factored

in all the reflections listed in Table 5.4, and found a reflection-corrected value for the susceptibility ratio, 7.7(8).

If the value of the sapphire susceptibility is known, it can be used to estimate the magnitude of $\chi_{\text{AlN}}^{(3)}$. The rotational symmetry of the substrate TH measurement in Fig. 5.1 allows for the film and sapphire tensors to be approximated as isotropic. It can be assumed that for some measured angle, the fundamental field polarization was aligned with the x -axis of the sapphire. At that position, the only nonzero tensor element is $\chi_{xxxx}^{(3)}$. The known value of the tensor component $\chi_{xxxx}^{(3)}$ for sapphire $1.14 \pm 0.15 \times 10^{-14}$ esu was corrected for wavelength, and used to determine the susceptibility of aluminum nitride $1.52 \pm 0.25 \times 10^{-13}$ esu⁴. In computing the error on the film to substrate $\chi^{(3)}$ ratio, we only considered the error in the AlN film C_1 and C_3 parameters.

5.3.3 THG spectrum

For each z-scan focus position, the TH signal propagated through a monochrometer, and the spatially dispersed TH spectrum was imaged on an intensified silicon diode array (Optical Multichannel Analyzer, Princeton Inst. Model 1420). Closing the entrance slit allowed just the forward propagating beam to enter, and produced a TH spectrum containing a significant amount of structure. As mentioned in the context of the disappearance of Maker fringes in ultrafast experiments, the sensitivity to the material thickness is maintained by the relative phase of two pulses generated at the entrance and exit interfaces of the sapphire substrate. This phase is observable when the TH field is spectrally resolved. In the experiments, we ob-

⁴We calculated $\chi_{\text{THG}}^{(3)}$ of sapphire from known DFWM measurement by Levenson. Assuming a sapphire band gap $\lambda' = 150$ nm, the ratio $\lambda/\lambda' = 5.3$ implies the ratio of the susceptibilities $\chi_{\text{THG}}^{(3)}/\chi_{\text{DFWM}}^{(3)} = \lambda^3(1 - 5.3)^3 / [\lambda^3(1 - 5.3)(2 - 5.3)(3 - 5.3)] = 2.41$ at $\lambda = 800$ nm. Similarly, $\chi_{\text{DFWM}}^{(3)}(800\text{nm})/\chi_{\text{DFWM}}^{(3)}(525\text{nm}) = 0.72$. Multiplying the known value 1.14×10^{-14} esu by the previous values determines $\chi_{\text{THG}}^{(3)} = 1.97 \times 10^{-14}$ esu at 800 nm. As a comparison, we repeated the derivation using Millers rule, and found a slightly lower TH susceptibility for sapphire $\chi_{\text{THG}}^{(3)} = 1.37 \times 10^{-14}$ esu [78]

served a relationship between the spectral oscillations and the laser focus position. The spectrally-resolved data are shown in Fig. 5.8. They are displayed separately to eliminate overlapping, and are labeled according to the location of the laser focus.

The spectral modulation is clearest in the data taken while focusing near the air/sapphire interface. There, the centroid is also well-defined and constant over a large range of focus positions. We chose to analyze the spectrum at $z_0 = 680$, because it has the best fringe-to-height contrast, since the TH pulse from the AlN/Al₂O₃ interface and the TH pulse from the air/Al₂O₃ interface are nearly equal in amplitude. The spectral data taken when focusing near the AlN/air interface shows some distortion, because of the angular spread of k-vectors in the beam.

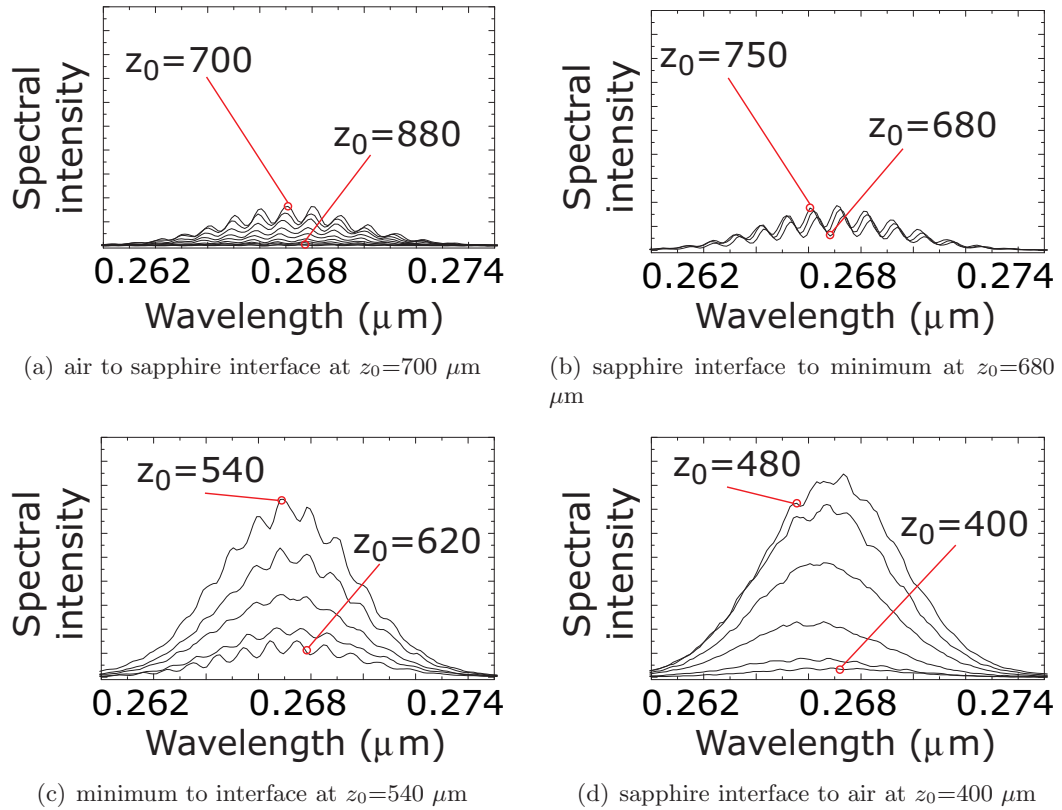


Figure 5.8: spectrally resolved z-scan data of AlN-coated sapphire. Each curve corresponds to a different focus position z_0 .

5.3.4 Fourier analysis

Multiple TH pulses will interfere in the detector if the substrate is substrate if the thickness of the material is comparable to the Rayleigh range of the laser focus [49]. Fig. 5.8 demonstrates this is also the case for the AlN thin films. The interference has several properties which can be used to characterize the material. The spectral intensity

$$|\tilde{A}_3(\omega)|^2 = (2\pi)^{-1} \left| \int_{-\infty}^{\infty} dt \tilde{A}_3(t) e^{i\omega t} \right|^2 \quad (5.22)$$

is the absolute value squared of the Fourier transform of the approximate time-dependent TH field,

$$\tilde{A}_3(t) = (e^{i\Phi_1} e^{-3\Gamma(t-\tau/2)^2} + e^{i\Phi_2} e^{-3\Gamma(t+\tau/2)^2}). \quad (5.23)$$

The analytical evaluation of the integral of Eq. 5.22 gives

$$|\tilde{A}_3(\omega)|^2 = \left| \frac{e^{\frac{-\omega(6i\Gamma\tau+\omega)}{12\Gamma}}}{\sqrt{6\Gamma}} (e^{i\Delta\Phi} + e^{i\tau\omega}) \right|^2, \quad (5.24)$$

or in units of wavelength, it evaluates to

$$|\tilde{A}_3(\lambda)|^2 \propto e^{\frac{2^2 c^2 \pi^2}{6\Gamma} (\frac{1}{\lambda} - \frac{1}{\lambda_0})^2} \cos^2 \left[\left(\frac{\pi c \tau}{\lambda} \right) - \Delta\Phi \right], \quad (5.25)$$

where the TH centroid $\lambda_0 = \frac{2\pi}{\omega_0}$ and the constant phase factor $\Delta\Phi = \Phi_2 - \Phi_1$.

The phase $\Delta\Phi$ was used to fit the constant phase difference between the two pulses. We neglected the linear term, corresponding to a pulse chirp difference, since it is nearly zero, as shown in Fig. 5.5. If included, this linear term will cause the envelope of the power spectrum to shift, because the terms proportional to t can be absorbed into the complex exponential.

The relative phase of the two pulses determines the position of the spectral oscillations. For an unfocused beam, the spectral phase is only related to the

thickness of the nonlinear material, as mentioned in the discussion of Fig. 5.2. However, focusing introduces additional phase. We modeled the focus dependence of $\Delta\Phi$ using the analytical solution in Eq. 5.11 and additional shifts from focusing. We mapped the predicted phase offset as the focus scans through the sample, but found it does not match the observed shift of the phase in Fig. 5.8. The deviation of the experimental data is caused by spatial far-field coherence not included in the paraxial approximation of THG. In addition to the relative phase dependence on focus position, anomalous spectral behavior appeared when the focus was placed near the AlN interface, shown in Fig. 5.8(d), which is not explained by any of the analysis in the previous sections.

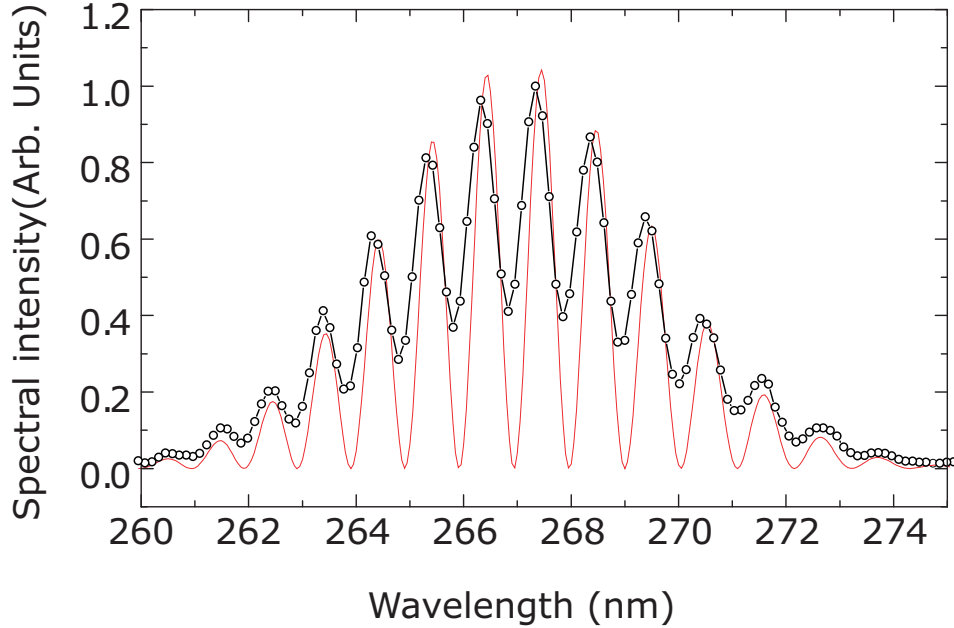


Figure 5.9: Least square fit of TH signal(\circ) fitted using the transform model in Eq. 5.25. The parameters for the fit are shown in Table 5.5. The experimental data correspond to the lowest TH signal in Fig. 5.8(b).

The spectrum was fit using Eq. 5.25 (see Table 5.5) and the result is plotted in Fig. 5.9. The value of Γ determined by the spectral fit (0.00140(6)) agrees well

Table 5.5: Parameters from THG Spectral fit

| Parameter | Value | Units |
|---------------|------------|------------------|
| Γ | 0.00140(6) | fs^{-2} |
| τ | 232.07(3) | fs |
| $\Delta\Phi$ | 1.98(2) | rad |
| $\lambda_0/3$ | 0.26699(5) | μm |

with the expected value in Table 5.1 (0.00141), obtained from measurements of the fundamental bandwidth. The fitted time separation of the pulses, $\tau=232.07$, is more accurate than estimates from published data on sapphire (260 fs). A more accurate value for the inverse group-velocity mismatch $\Delta\beta = L/\tau=0.70(5) \text{ fs}\mu\text{m}^{-1}$ is found by using the measured Γ value along with the substrate thickness data in Table 5.3. But, using this value to correct the calculated film to substrate susceptibility ratio $\chi_{\text{AlN}}^{(3)}/\chi_{\text{Al}_2\text{O}_3}^{(3)}$ produces only a 0.02% correction. On the other hand, a change of equal magnitude (10%) in the the value of Δk for Al_2O_3 , when evaluated with Eq. 5.21, produced a 10% correction.

5.3.5 non-paraxial Effects

Closing the entrance slit to the monochromator was required to reveal the TH spectral oscillations, but produced a significantly different shape of the z-scan curve compared to Fig. 5.6. Z-scan measurements of the same sample measured in section 5.3, except under spectrally-resolving conditions, are shown in Fig. 5.10. In general, the shape of the z-scan data was less symmetric when the slit was closed. We also observed oscillations in the intensity over a small range of focus positions. The new features in the z-scan data observed under spectrally-resolving conditions correlate with the anomalous spectra in Figs. 5.8(c) and 5.8(d).

The origin of the asymmetry in the z-scan is the k-vector spread in the beam focus. This effect is non-paraxial, which is why the interface model did not account

for it. Focus-dependent oscillations in SHG arising from non-paraxial effects and the asymmetry for the case of converging vs. diverging light were described by Kleinman *et al.* [69].

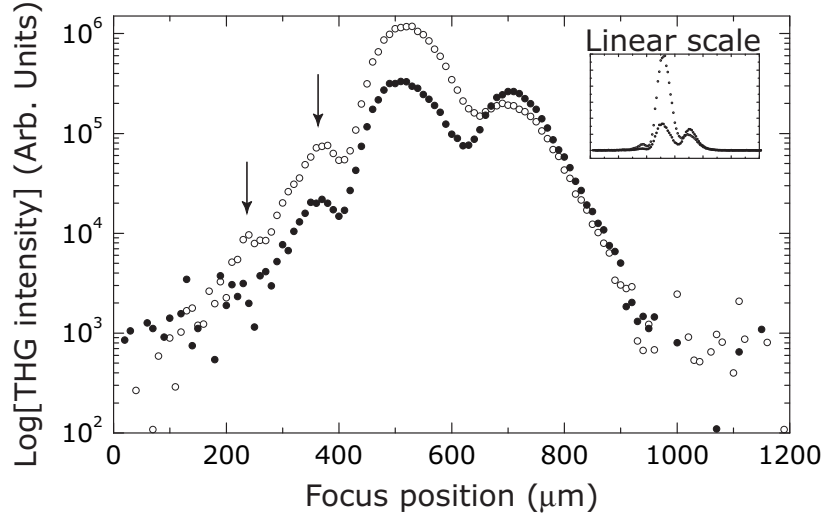


Figure 5.10: A repeat of the measurement shown in Fig. 5.6, except with a nearly closed entrance slit to the spectrometer. An asymmetric line structure is observed and additional peaks (arrows) appear when the focus is placed on the spectrometer side of the sample. Both the sapphire substrate(●) and the AlN-coated sapphire(○) show this effect. In each case, the extra peak intensities scale linearly with the interface signal.

We repeated the THG z-scan experiment using a phase-matched, 150 μm Beta Barium Borate (BBO) crystal. The measured second harmonic z-scan under the tightly closed slit condition is shown in Fig. 5.11. Here, the far-field pattern is observable by eye. The inset depicts the far-field patterns when the sample is placed on the diverging side of the focus, near where the intensity oscillations are observed. The far-field spatial coherence is extremely sensitive to laser astigmatism. Two cases, each for proper and slightly improper laser alignment, show very different far-field patterns.

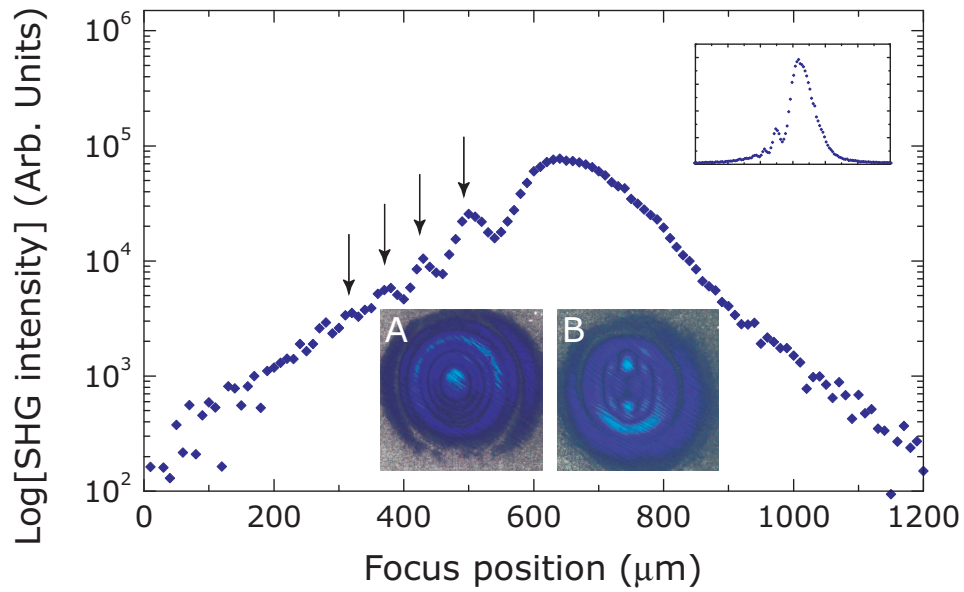


Figure 5.11: A repeat of the measurement shown in Fig. 5.10, again with a nearly closed entrance slit to the spectrometer. SHG is measured as a function of the position of a BBO crystal, relative to the focus. The asymmetric line structure and additional peaks (arrows) are apparent just as in the case of the THG z-scan. Also shown is the far-field pattern for an undistorted beam(A) and a slightly astigmatic beam(B). The far-field pattern only appears when the focus is on the spectrometer side of the sample.

Non-paraxial harmonic generation will affect the far-field pattern in third-harmonic generation [64, 50]. The absolute phase of the TH signal in the z-scan is sensitive to spatial phase when the spectrometer slit is narrowed. To account for non-paraxial THG, a geometric factor that relates the forward generated TH to the spread in k-vectors of the focused pump is required. There is well-developed theory for this in SHG for cw radiation [79].

5.4 Summary of aluminum nitride measurements

We presented several measurements of an AlN film grown on sapphire, which were combined and used to determine the nonlinear susceptibility $\chi^{(3)}$ of the AlN film. A rigorous model for scanning laser (z-scan) third-harmonic generation that relied on ultrafast effects was developed, and was used to model the shape of the z-scan. Interface sensitivity arising from ultrafast effects were exploited to avoid including long-range coherence related to Gaussian focusing. Overall, it afforded a simple, analytical description of interface THG measurements under the generally applicable phase-mismatched condition, as long as the Rayleigh range is long compared to group-velocity walk-off length.

The rotational measurements of the textured AlN film showed a strong second-harmonic dependence, but did not indicate any rotational anisotropy in the third-harmonic. Analysis of the SH rotational anisotropy showed the AlN texture is nearly wurzite, but the z-axis of the film is slightly tilted with respect to the z-axis of the substrate ⁵. We compared the TH rotational measurement of AlN to a z-cut quartz crystal, which displayed the rotational dependence expected from bulk THG. Because neither the thin film, nor the substrate show any rotational anisotropy in THG, it is likely that the spread in k-vectors in a tightly-focused pump laser reduces

⁵The texture fit is insensitive to tilts less than 20 degrees; independent rocking x-ray measurements indicate a tilt of 2 degrees [31]

the resolution of the tensor components. That being the case, more accurate rotational measurements would be available when using a collimated, amplified laser system.

We deconvolved the response of the film from the measured TH from the film on the substrate using the time-domain interference model. Calculations of the time-dependent amplitude and phase of the fields in two adjacent slabs of nonlinear material showed the amplitude of the TH field contains a sequence of pulses, each of which corresponds to a material interface. Using the z-scan technique allowed for the critical thin film interface to be isolated. From our experiments, we determined the film to substrate susceptibility ratio, $\chi_{\text{AlN}}^{(3)}/\chi_{\text{Al}_2\text{O}_3}^{(3)}=7.7(8)$. Using previously published data for sapphire, we concluded that $\chi_{\text{xxxx}}^{(3)}(\text{AlN}) = 1.52 \pm 0.25 \times 10^{-13}$ esu.

The emitted interface pulses also contain information regarding the bulk of the material, but it is contained in the relative phase of each pulse. For ultrashort-pulse measurements in bulk materials which are thicker than the group-velocity walk-off length, measuring the relative phase of the emitted pulse pair is equivalent to measuring Maker fringes in a CW experiment. By spectrally resolving the TH field, we used the ultrafast model to measure the relative phase of the pulses generated at the air/sapphire and sapphire/AlN interfaces, and showed we could retain the information contained in Maker fringes.

Though the time-domain analysis showed that interfaces produce the TH field, it fails to describe why interfaces are so important for generating the harmonics. More insight may be gained by considering harmonic generation and pulse propagation in terms of adiabatic vs. non-adiabatic interactions with a material. In this context, interfaces introduce a non-adiabatic disturbance during pulse propagation, but within the bulk of the material the fundamental pulse propagates adiabatically. Our approximation assumed that the instantaneous bulk TH polarization does not

interact with the interface field, because such a long-range coherence is removed when the group-velocity walk-off length is short compared to the Rayleigh range.

The spectral analysis indicated that ultrafast third-harmonic generation is a promising phase-sensitive diagnostic. To record the spectral phase we used a smaller numerical aperture (NA) lens than has been reported in the THG microscopy literature. A lower NA makes our setup inferior as an imaging system, but affords an interferometric measurement by generating multiple pulses from macroscopically-spaced interfaces in the sample. The previous experiment by Banfi *et al.* showed multiple pulses originate from interfaces in a bulk sample, but chose to separate the pulses for use in timing experiments, rather than allow them to interfere spectrally [70]. If the group-velocity mismatch in the substrate is known accurately, the spectral phase can be used to record small changes in the thickness of a thin film, as well as other phase shifts due to imaginary components of a susceptibility tensor. Even with our choice of a lower NA lens, we observed that the non-paraxial interaction with the samples distorted both the amplitude and phase of the TH field for several laser focus positions. To improve the accuracy of the pulse phase measurement for all focus positions, the effect of a non-paraxial beam should be included.

Chapter 6

Harmonic Generation from Enhanced $\chi^{(3)}$ Nanocomposites

6.1 Introduction

Multiphoton resonant materials were engineered by blending two materials with discrete resonances, Ag and NdAlO_3 , in an optical nanocomposite. A smoothly-varying ($0.5 \text{ nm}/\mu\text{m}$) concentration gradient of Ag nanoparticle was applied to a sapphire substrate using the direct-write process, laser ablation of a microparticle aerosol. As discussed in Chapter 2, the nanoparticles were coated with neodymium aluminum oxide using pulsed laser deposition (PLD). The linear and second-order optical responses of the bare Ag NP coating and NdAlO_3 thin film were discussed in Chapters 2 and 3. In this chapter, the third-harmonic (TH) responses of the bare and coated samples are primarily compared, though a comparison of the second-harmonic response is added. The silver nanoparticle film with and without the coating was analyzed using a cross-sectional laser scanning technique, showing the effect of silver concentration on transmission (always measured at the frequency-doubled wavelength $\lambda_0/2 = 400 \text{ nm}$), second-harmonic generation (SHG) and third-

harmonic generation (THG). Power-dependence measurements showed the TH from bare silver followed a quartic power law vs. the fundamental intensity I_0 , and had a maximum enhancement of 30 (relative to the substrate) at 0.5×10^{11} W/cm² before saturating. The coated sample was less efficient at lower intensities, but followed a cubic power law up to the maximum $I_0 = 1.2 \times 10^{11}$ W/cm², without saturation. At higher intensities, the NdAlO₃-coated sample was more efficient. We compared the cross sectional scans of SHG and THG in each material. Saturation was also clear from depth scanning (z-scan) measurements. Previous models of saturation in THG are contrasted to the saturation observed here, and a qualitative model of saturation in resonant, field-enhanced materials is proposed and discussed.

Many independent nonlinear optical processes are, in general, equally likely in nonresonant materials. By engineering resonances into the material, we aimed to increase the contrast of a particular output state, which for this study is the second-harmonic of our 800 nm fundamental field. The state is made favorable by controlling the material properties, which in this study are material resonances of the Nd³⁺ ions and surface plasmons of the silver nanoparticles. If after the nonlinear interaction, the distribution of total states is peaked around a single one, that more occupied state is said to be *enhanced*. Generally, the term *enhanced* has been used to describe an improved conversion efficiency of a nonlinear process. The efficiency can be improved macroscopically, by phase matching or reduction of saturation or closing of undesired conversion pathways, or microscopically by increasing the material's susceptibility χ to a specific nonlinear effect. In our samples, we will show that for low intensity excitation, the dielectric function of bare silver nanoparticles is modified, leading to a larger conversion efficiency for THG. At higher fundamental intensities ($> 10^{11}$ W/cm²), adding the neodymium matrix suppressed saturation, and allowed for higher conversion efficiency at those intensities. By reducing the saturation in the NdAlO₃-coated sample, we succeeded in increasing the SH yield,

and furthermore the contrast of SHG to THG was increased.

The application of similar enhancement processes has been sought after in nonlinear Kerr media, for use in ultrafast optical switches. By mixing semiconducting nanoparticles into glasses, optical resonances were introduced. Because Mie scattering from sub-10-nm-diameter particles is greatly reduced, thick materials could enhance the value of n_2 (which is proportional to $\chi^{(3)}(-\omega; \omega, \omega, -\omega)$), while minimizing absorptive and scattering losses. There are reasons why manufacturing enhanced Kerr nonlinear media is more straightforward than generating media for other nonlinear processes: first, all multiphoton detunings

$$\Delta = \{\omega_{01} - \omega_1, \omega_{02} - (\omega_1 - \omega_2), \omega_{03} - (\omega_1 - \omega_2 + \omega_3)\} \quad (6.1)$$

are approximately zero in a resonant two-level system, because each virtual energy sublevel $\hbar\omega_{0j}$ coincides with either the upper or lower level when each photon energy satisfies $\hbar\omega_i = \hbar\omega$; second, the nonlinear Kerr process is automatically phase-matched, because dispersion is negligible when the fundamental and signal fields occur at the same energy. Because only a single resonance is required to enhance a Kerr nonlinearity, technical challenges associated with nano-scale engineering are minimized, and many examples have been reported [15]. The use of multiply resonant materials has been reported to enhance THG in alkali metal vapors, because of a fortunate coincidence of several atomic resonances in cesium with the harmonics of a Nd:Yag laser [76]. This dissertation marks the first time resonances have been deliberately engineered into a material for the purpose of enhancing harmonics.

The theoretical switching time of an optical gate is given as a convolution of the optical pulse with the recovery time of the material. In nonresonant media, response-times as short as 100 fs have been reported [80, 81]. A limiting factor of using semiconducting nanoparticles is that the upper excitation level consists of a long-lived exciton state, which can have lifetimes that are on the order of microsec-

onds. It is possible to bleach the samples on smaller time-scales, causing switching times to be limited by the longer, electron-hole recombination time. In our samples, the strong local fields of the silver nanoparticle were utilized, which are mediated by the short-lived plasmon excitation lifetime on the order of 100 fs [82]. Even with the short time-scale dynamics of the plasmon, interactions with the surrounding medium and collisions can dephase the polarization and alter intermediate level populations, and must be considered when the fundamental intensity is large ($>10^{11}$ W/cm²). Studies show that nanoparticle size also determines the response time; though 5- to 10-nm particles equilibrate in just several picoseconds, larger 30-nm particles equilibrate more slowly [83]. The relaxation time of hundreds of picoseconds reported in Chapter 2 are consistent with the previous reports. Understanding the relaxation of the silver nanoparticles in various media is necessary for developing an understanding of the nonlinear optical response of the overall medium.

By bringing neodymium aluminum oxide within a coherence length of the silver particles, we aimed to step off of the single-photon NdAlO₃ resonance, up to the two-photon resonance into the silver conduction band. It is worth noting that the surface plasmon is not directly resonated in this process; the two-photon absorption into the conduction band is used, instead, and has been reported to be significant [23, 84]. With these two resonances we hoped to enhance second harmonic generation. Though some enhancement of SHG was observed, it was found that the proposed mechanism was not correct. The main deficit of our initial model was that it did not include the inverse process: electron loss from the conduction band to the surrounding material.

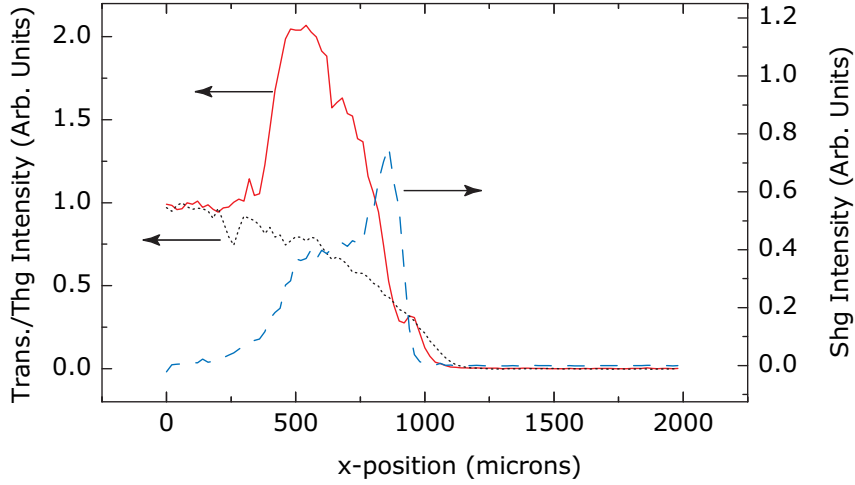


Figure 6.1: SHG (dash) THG (solid) and Transmission (dots) data from a bare Ag nanoparticle film. Silver nanoparticle concentration increases with increasing x .

6.2 Cross sectional nonlinear measurements of resonant nanocomposites

First, cross sectional (x -scan) measurements of the second- and third-harmonic were performed on uncoated (bare) silver nanoparticles deposited on a sapphire substrate. Scanning cross sectionally allowed for the determination of changes in conversion efficiency as a function of changes in material structure due to nanoparticle concentration. The measurements, shown in Fig. 6.1, exhibit a coincident increase in SH and TH signal due to the Ag nanoparticles at low Ag concentration. The maximum observed TH signal did not coincide with the maximum SH signal, and was only about 2 times greater than the sapphire substrate. An additional TH peak was observed near $x=950$ microns, which may also result from coherence between the SH and TH field. Field coupling is also supported by the fact that the maximum SH signal coincides with a local minima of the TH signal at high Ag concentration. The inversely related SH and TH signals in the high Ag concentration area are in

contrast to the low concentration area (for $x < 500$ microns), where the coupling is not observed.

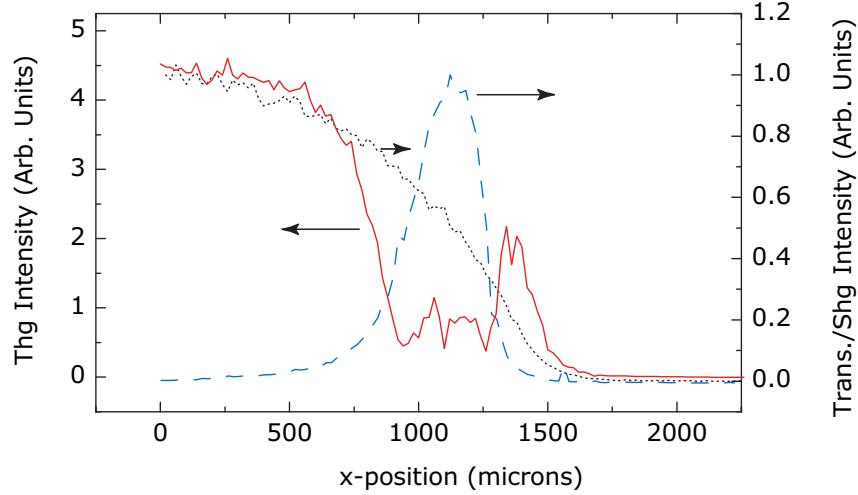


Figure 6.2: SHG (dash) THG (solid) and Transmission (dots) data from a NdAlO_3 -coated Ag nanoparticle film.

The cross-sectional measurement was repeated using the NdAlO_3 -coated Ag sample. The data is shown in Fig. 6.2. There are a few subtle differences from the bare Ag sample. First, in the 100 percent transmission region, the TH signal is dominated by the neodymium aluminum oxide film, which is plotted in units of the bare substrate signal. However, unlike the bare silver sample, there is no region where uncoupled growth occurs; the TH signal immediately decreases as the laser focus scans into the low Ag concentration edge of the sample. Again, as in the bare sample, the drop in the TH signal coincides with a rise in the SH signal. At higher Ag concentration (lower transmission), the SH signal drops, and when it does, the TH signal returns. The amplitude of the maximum TH signal is close to the magnitude of the maximum signal from the bare Ag sample. However, the signal is measured from a region of the film with much lower transmission, which suggests a much larger material susceptibility.

A comparison of SH signals from the bare and NdAlO_3 -coated Ag nanoparticles reveals that the signal strength from the bare sample is slightly lower. The comparison also reveals that the signal increase in the coated sample coincides with a decrease in the TH signal from the same sample, suggesting that the stronger SH signal is attained at the cost of a reduction of THG, via a coherent process. A previous study of resonant multiphoton ionization in gases has demonstrated that higher-order harmonic processes can be shunted via destructive interference to lower-order resonances [85]. In addition to such coherent effects, other phenomena may play a role. Because the two SH cross sectional scans have different efficiencies only in the area of the maximum SH (in the coated sample), it is likely the case that saturation effects are present in the bare Ag sample, but are removed in the coated sample.

6.2.1 intensity-dependent cross sectional measurements

As discussed in Chapter 2, the primary effect of local fields on the overall nonlinear optical signal is enhancement of the fundamental and harmonic field strengths. That being the case, already intense fields which are further enhanced may cause saturation and material damage, so we performed TH cross-sectional scans while varying the fundamental laser intensity. Indeed, we discovered that the TH was saturated under the highest fundamental field strengths. Cross sectional x-scans for a range of fundamental laser intensities are compare in Fig. 6.3.

There are several notable features of Fig. 6.3. First, the largest enhancement does not occur at the highest ($1.2 \times 10^{10} \text{ W/cm}^2$) intensity. Rather, it occurs at about $0.5 \times 10^{11} \text{ W/cm}^2$. Each of the plots is normalized to the signal from the sapphire substrate, which is assumed to have unit signal strength. So, the most enhancement that is observed is approximately 25 times the substrate value. Also, for increasing intensities, the signal maximum shifts from the highest density part of the sample,

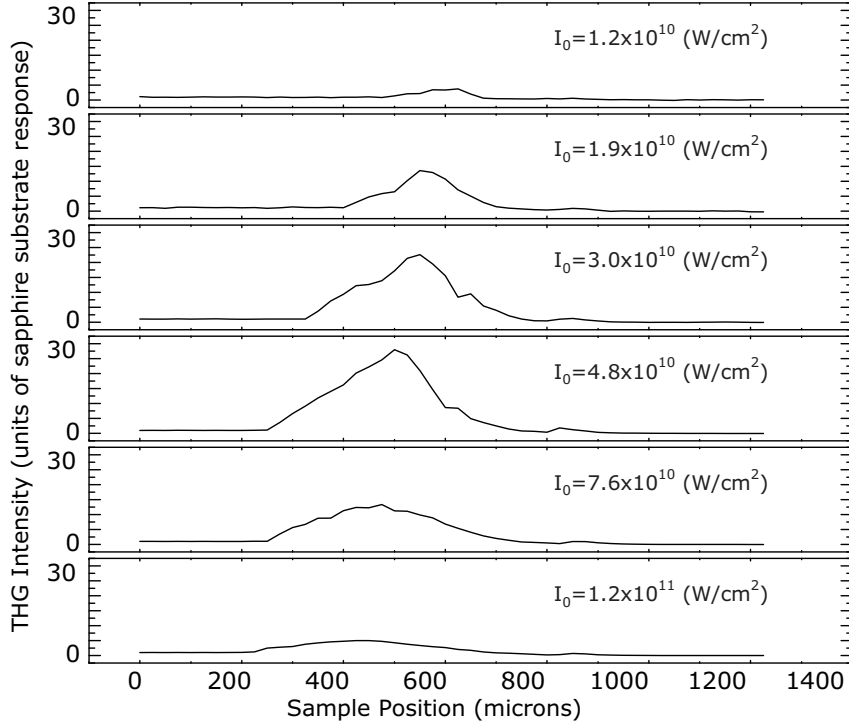


Figure 6.3: x-scans of bare Ag nanoparticle films are shown for increasing fundamental laser intensities. Local fields enhance the signal several times greater than the substrate (left) before attenuation in the dense part of the sample (right).

to the lowest density part of the sample, meaning that saturation occurs at lower field intensities in higher concentrations of silver nanoparticles.

The NdAlO₃-Ag nanocomposite was also cross-sectionally analyzed. Those results are shown in Fig. 6.4. One difference in the NdAlO₃-coated sample is that the saturation intensity threshold at high Ag concentration is slightly higher. When exposed to a laser intensity of $1.2 \times 10^{11} \text{ W/cm}^2$, the coated sample displayed a maximum TH signal two times that of the bare sample. Also, coupling between the SH and TH fields appears to have an intensity-dependence. At low nanoparticle concentration, as the intensity is increased, the TH signal becomes increasingly attenuated. For the largest intensity (and low Ag density), it appears as though the

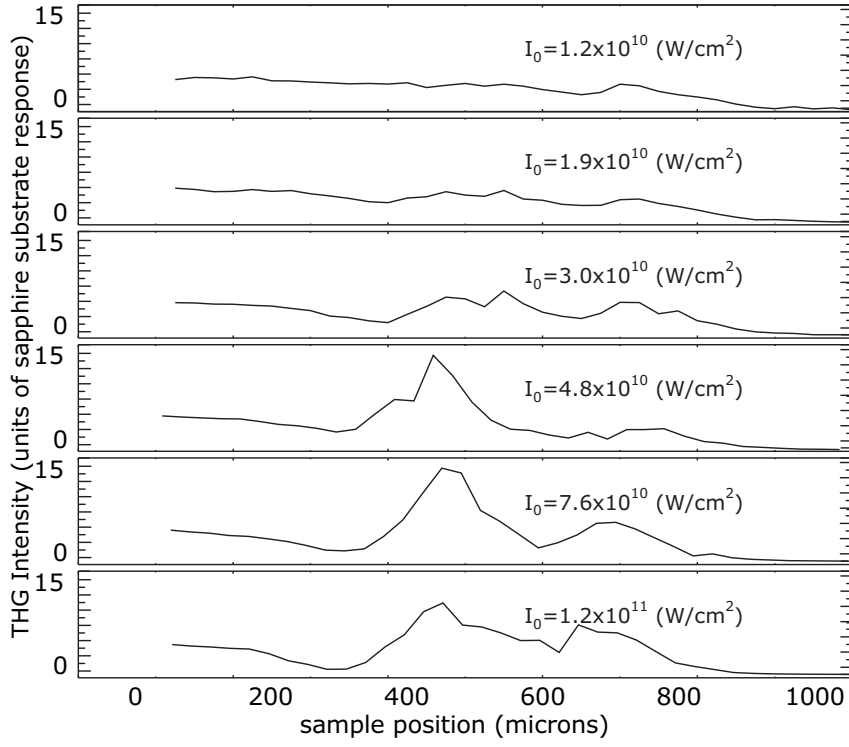


Figure 6.4: x-scans of NdAlO₃-coated Ag nanoporous films are shown for increasing fundamental laser intensities. Local fields enhance the signal several times greater than the just the film (left) before being attenuated in the dense part of the sample (right).

third-harmonic signal has been entirely converted into the second-harmonic field.

The results of the intensity-dependent cross sectional studies are summarized in Fig. 6.5. Based on Fig. 6.5, enhancement of THG in bare Ag nanoparticles is best at low to moderate intensities. However, the overall TH efficiency at high powers is better in the Nd-coated sample. Furthermore, the power dependence of the bare silver sample appears to deviate from the cubic dependence of THG.

One would like to tell the difference between saturation and loss of signal due to conversion to the second-harmonic (a coherent effect). Because the cross sectional scans show large qualitative differences depending on Ag concentration,

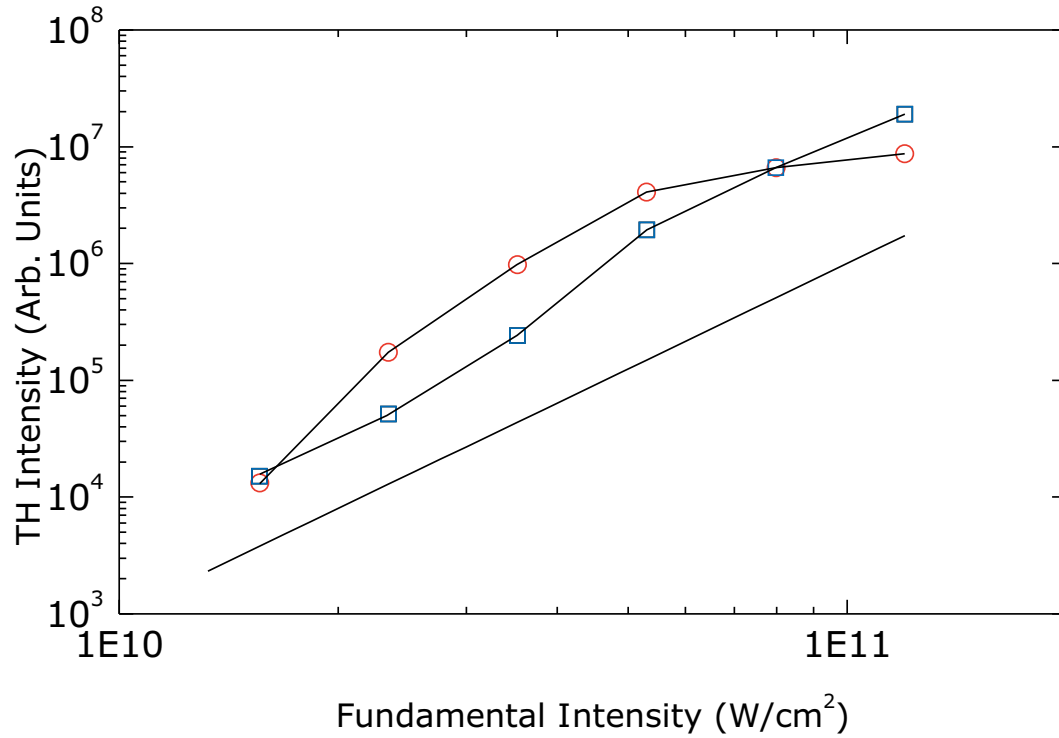


Figure 6.5: The maximum TH signal of each of the bare and coated Ag nanocomposites in Fig. 6.3 (○) and Fig. 6.4(□) is plotted as a function of fundamental laser intensity. Also shown (solid line) is an ideal third-order power dependence. At the highest laser intensity, the maximum signal from the NdAlO₃-Ag nanocomposite is two-times greater than the maximum TH signal measured from the uncoated Ag nanoparticles.

the data Fig. 6.5 provides ambiguous results. Saturation analysis at a single sample position gives a more accurate representation of the intensity-dependence of the nanostructured materials. The intensity-dependent TH signal from Fig. 6.5 was repeated at a single spot in the bare Ag sample, using a slightly better intensity resolution. The results of the measurement are shown in Fig. 6.6. What is apparent

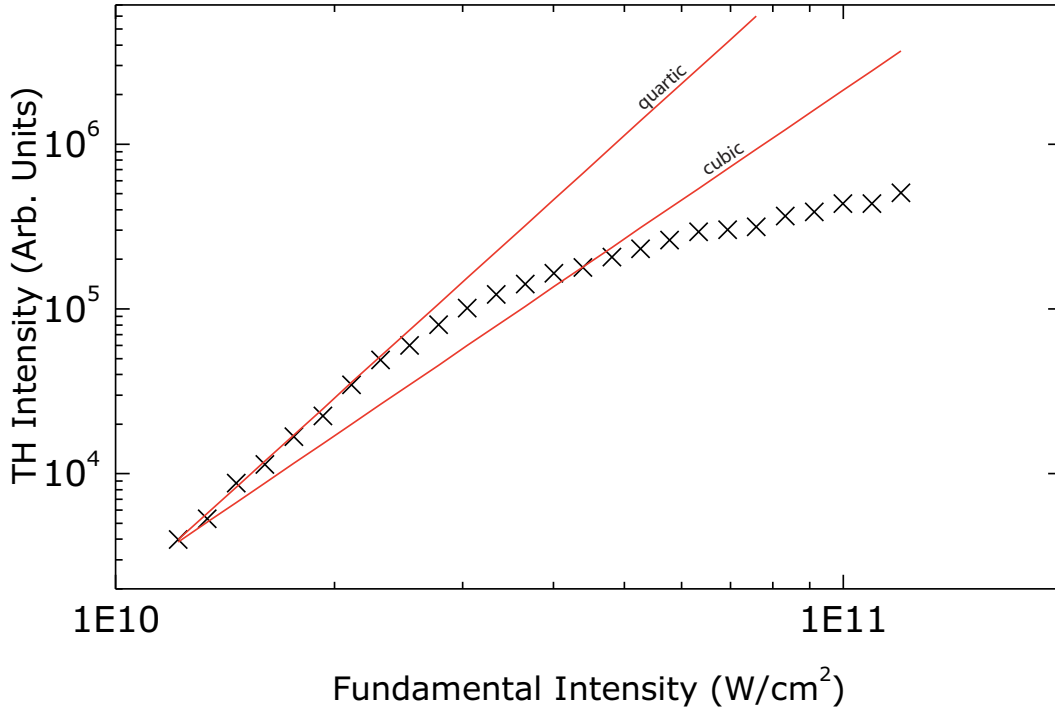


Figure 6.6: Experimental intensity-dependence of the third-harmonic signal from bare Ag nanoparticles on sapphire (\times) is compared to theoretical cubic and quartic power laws (solid lines). The sample was taken from a region with approximately 50 % transmission.

from Fig. 6.6 is that measuring the maximum data point in the intensity-dependent cross section scans overestimated the saturation threshold to be nearly 5.0×10^{10} W/cm², whereas Fig. 6.6 puts the threshold nearer to 3.0×10^{10} W/cm². Because saturation occurs at a lower intensity in the fixed-focus measurements, it is concluded that saturation depends on material microstructure. Still, it is unclear why the TH

in the coated sample saturates at higher intensities.

6.3 Z-scan saturation analysis

The z-scan measurement was used in Chapters 4 and 5 to characterize the TH signal from bare and coated interfaces. Because the z-scan is a mapping of intensity onto the spatial z dimension, it suggests that the z-scan may be a useful tool for characterizing saturation and other intensity-dependent phenomena, particularly what effect of adding different coatings to Ag nanoparticles had on the third-harmonic generation efficiency. Additionally, SHG z-scans were recorded under the same conditions to monitor the effects of coherences, as described in the above discussion.

First, z-scans of the bare silver sample were measured. The overlayed SH, TH and background TH (substrate) data are shown in Fig. 6.7. As was found in

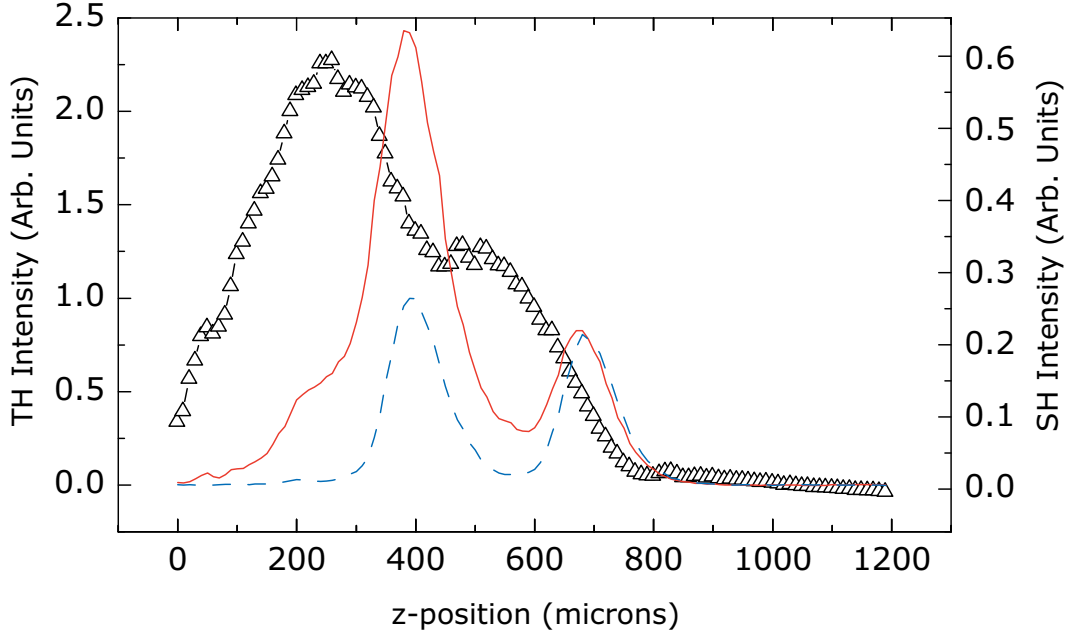


Figure 6.7: SHG (Δ) and THG (solid) z-scans from bare Ag nanoparticles on sapphire, and substrate THG (dashed). $I_0 = 1.2 \times 10^{11} \text{ W/cm}^2$.

the cross sectional scans, nanoparticles increase the signal (relative to sapphire) by a factor of 2 at the maximum intensity, identified by the peak value at $400\text{ }\mu\text{m}$. The corresponding SHG z-scan at the same position is at a local minimum, caused by saturation of the SHG signal. Nonparaxial contributions to harmonic generation cause the SH beam to have a slightly greater signal at lower z -values relative to the saturation. However, saturation alone does not affect the shape of the SHG curve. The dip at $400\text{ }\mu\text{m}$ is also lower, because the level is being depopulated by third-harmonic generation. Near $200\text{ }\mu\text{m}$ is where the onset of saturation is observed in the z-scan of the bare silver sample.

The z-scans of sapphire-coated Ag nanoparticles, shown in Fig. 6.8, indicate a similar yet tempered SH response compared to the bare Ag z-scans. There, saturation again is present in the distorted shape of the SH z-scan. The TH z-scan indicates a small enhancement, but the transmission through the film where the TH was measured was very low such that the overall efficiency was much lower than the measured TH from the bare substrate.

The same z-scan analysis was repeated for the NdAlO_3 -coated sample in Fig. 6.9. The coated sample was analyzed in the (cross sectional) region of depleted third-harmonic, which is at the very edge of the Ag coating, near $x = 1200\text{ }\mu\text{m}$ in Fig. 6.2. In the plot, the TH z-scan from the bare substrate is compared to the z-scan through the nanocomposite film. The equivalent TH signal observed when focusing at the bare sapphire interface at $z = 650\text{ }\mu\text{m}$ provides a basis for calculating the reduction of the TH signal from the nanocomposite (solid line), which is lower by a factor of 4.5. The TH response at $z = 180\text{ }\mu\text{m}$ is interesting, as well, because this small satellite peak (nonparaxial in origin) scales like the amplitude of the interface response of the pure NdAlO_3 film, even though it is depleted in the coated nanocomposite, which indicates that the angular distribution of the wave vectors in the fundamental field affect the coherence between the SH and TH fields. Finally,

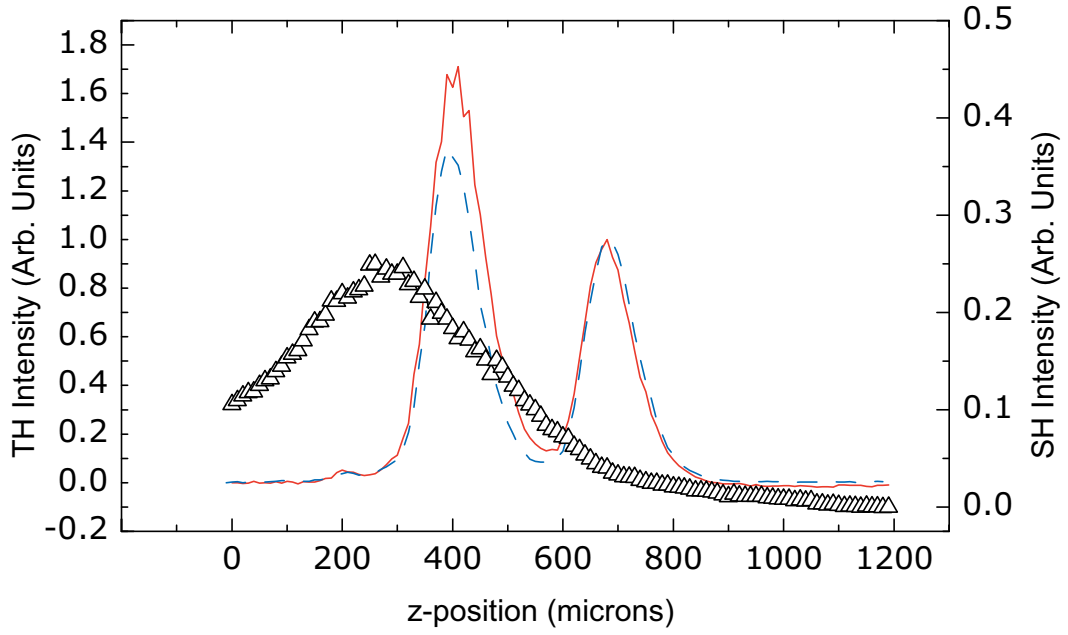


Figure 6.8: SHG (Δ) and THG (solid) z-scans from the Al_2O_3 -coated Ag nanoparticle film on sapphire, and THG z-scan from the bare sapphire substrate (dashed). The magnitude of the THG z-scan from the uncoated sample is actually much larger than that of the NP-coated sapphire, yet is drawn with the same magnitude to emphasize the shape of the curves. $I_0 = 1.2 \times 10^{11} \text{ W/cm}^2$.

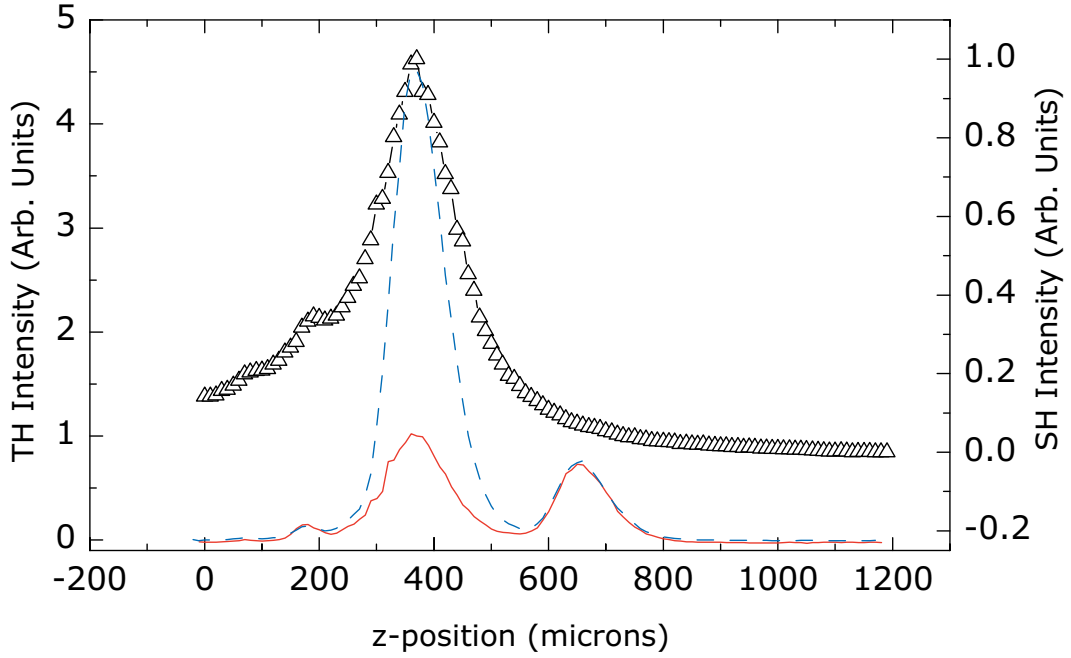


Figure 6.9: SHG (Δ) and THG (solid) z-scans from NdAlO_3 -coated Ag nanoparticles on sapphire, and THG from the NdAlO_3 film on sapphire (dashed). The z-scans were measured at the x-position corresponding to a minima of TH and maxima of SH intensities, near $x = 300 \mu\text{m}$ in Fig. 6.4. $I_0 = 1.2 \times 10^{11} \text{ W/cm}^2$.

the main result here is that the second-harmonic signal is completely unsaturated, and the SH z-scan is undistorted at all intensities (z-values).

The SH z-scan data for the different Ag nanoparticle samples (Figs. 6.7, 6.8, and 6.9) are plotted together in Fig. 6.10. As a result of the suppressed saturation, the NdAlO_3 -coated sample has the largest SH signal of the three when focusing at the coated interface. However, much like the case of THG in these materials, the SH signal from the bare Ag nanoparticles is stronger at lower intensities (or stated equivalently, when not focusing at the coated interface).

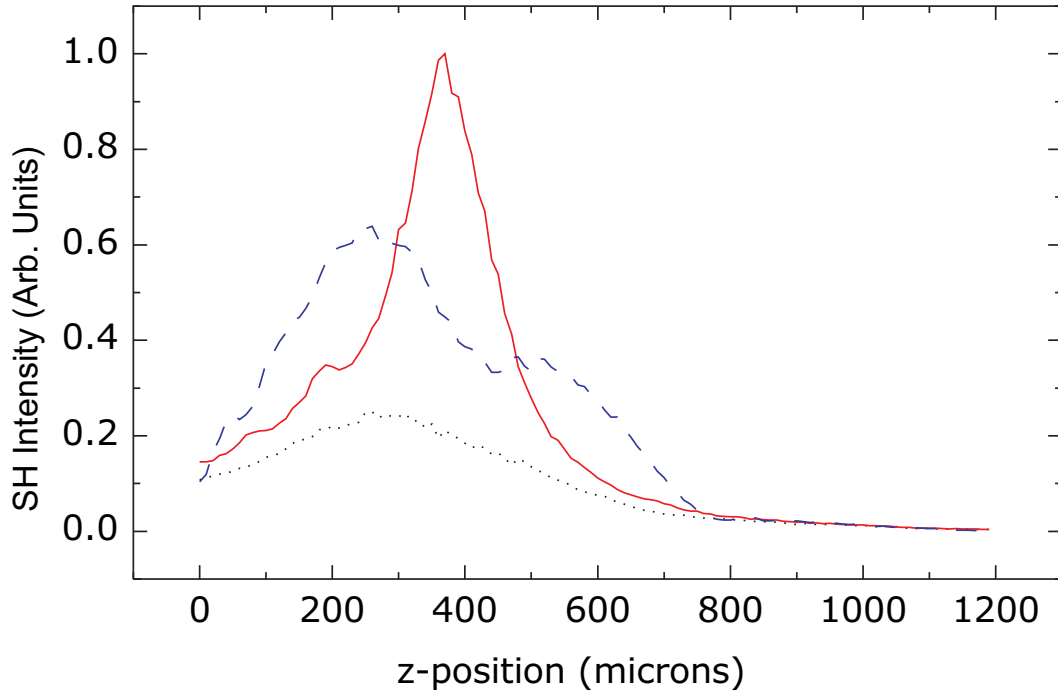


Figure 6.10: SHG z-scans from NdAlO_3 -coated (solid), Al_2O_3 -coated (dotted), and bare Ag nanoparticle (dashed) samples.

6.3.1 intensity-dependent z-scan measurements

We measured z-scans at the maximum TH position in the NdAlO₃-coated sample, in an attempt to unravel coherent effects and any others which may have a role in the sample's intensity-dependent harmonic response. The z-scans were performed in a NdAlO₃ nanocomposite, in an area with a larger Ag concentration, which had a 5 times larger third-harmonic response over bare nanoparticle system. It was expected that if we observed a stronger TH signal, the likelihood of saturating the SH signal would be high, and we may see a z-scan in the NdAlO₃ nanocomposite that is more like what was observed in the other samples. SH z-scans at different intensities at the x-position corresponding to a maxima of TH response in Fig. 6.4 were performed, to see if there is any deviation from the SH z-scan shown in Fig. 6.9.

The SH z-scan was measured at several laser intensities and the results are plotted in Fig. 6.11. The cross sectional position shown in the bottom right plot indicates these SH z-scans are not taken in the depleted TH region, where it was hypothesized that the SH data are not likely to be affected by conversion of TH into the SH field. From these data, it can be concluded that the material coated by NdAlO₃ has a higher saturation threshold than the bare (as well as the sapphire-coated) samples, and this applies to both low and high Ag concentrations. Though the data indicate that there is some energy transfer between the SH and TH fields, coherence may not be the only cause of the higher threshold. Other mechanisms beside field coherence are required to describe the different response of the neodymium-coated sample.

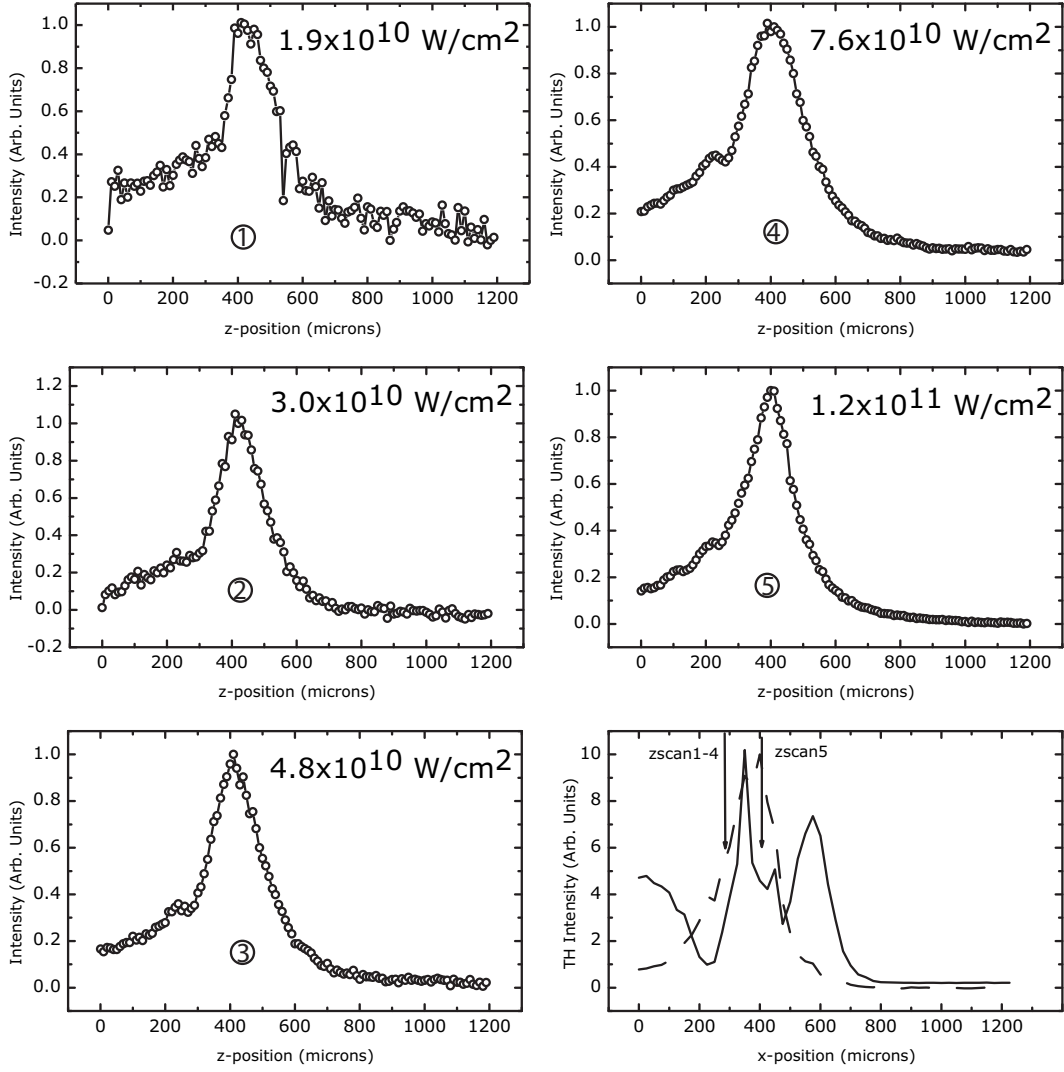


Figure 6.11: Shg z-scans taken at several fundamental field intensities. The corresponding positions are shown in the cross-sectional plot (bottom-right).

6.4 Third-harmonic saturation

The experiments in the first part of this chapter demonstrate that the intensity-dependence of the rare-earth (RE)-field enhanced nanocomposite is different from other nanocomposites without the rare earth doping. The RE-based material has a power-dependence much closer to a cubic law that does not saturate for the measured intensities, making it a less efficient material at low intensities and more efficient material at high intensities. There are reasons why the nanocomposite material responds differently, but first, some background on the origins of saturation in nonlinear signals is important to have.

Saturation of third-harmonic generation in mixtures of resonant atomic gases was analyzed by Vidal *et al.* [86]. Some aspects of that study are less relevant in the case of thin films, but the comparison is important, because the template employed (mixing components with individual resonances to enhance multiphoton efficiencies) is quite similar. Resonant alkali vapors, owing to their large oscillator strengths, have a much lower saturation threshold. Consequently, their use is limited to hundreds of times lower intensity than nonresonant systems. Conversion efficiency was improved by mixing in noble gases, but large index changes due to the Kerr effect (nonlinear refractive index) limited conversion, as well. Nonlinear propagation of the fundamental field was found to destroy long-range coherence, but because the films discussed in this chapter are neither phase-matched, nor very thick, the saturation model developed by Vidal *et al.* has little bearing on the present study.

Puell *et al.* defined some complementary parameters for THG in resonant gases, and showed the importance of two-photon absorption on the overall process [87]. In that case, resonant systems cause a depletion of the fundamental wave via the imaginary part of the third-order susceptibility (as opposed to the real part observed by Vidal). In addition, the AC Stark effect was analyzed and consequently neglected, because the line width of their laser (300 ps) was much larger than the

Stark shift. AC Stark shifts can also be neglected in the present study, because our femtosecond laser has an even broader bandwidth (also the resonance line widths are large). Again, because the present study does not utilize phase matching, Puell's saturation model is of little relevance.

6.4.1 intensity-dependent effects in field-enhanced nanocomposite materials

Since the previous models of TH saturation seem inappropriate for studying field-enhanced materials, some elementary arguments are required to understand their nonlinear optical response at high intensities. Because of our use of short laser pulses, nonequilibrium electron populations are likely to have an impact on the material nonlinearity. Though metallic silver is very inefficient at absorbing the fundamental laser energy, because the 800-nm wavelength is longer than the plasma wavelength, two-photon interband absorptions can more effectively couple energy into the nanoparticle. Two photons of the fundamental laser are not resonant with collective oscillations of the s-p level electrons (assuming the plasmon resonance is dipolar, which is unlikely for large 50-nm particles), but are resonant with interband transition from the d-band, up to the s-p conduction band. The effect of two-photon absorption by silver is depicted schematically in Fig. 6.12. A consequence of the interband transition is that the local fields increase with increasing fundamental laser intensity. More intense fundamental laser drives more electrons into the conduction band which then participate in collective electron oscillations. The result is that the local field correction is not a constant, but will depend on the intensity of the excitation laser.

The electron energies may increase even higher as a result of direct acceleration in the laser field. The kinetic energy of electrons in the combined local fields and laser fields may increase the ionization probability. The TH intensity at

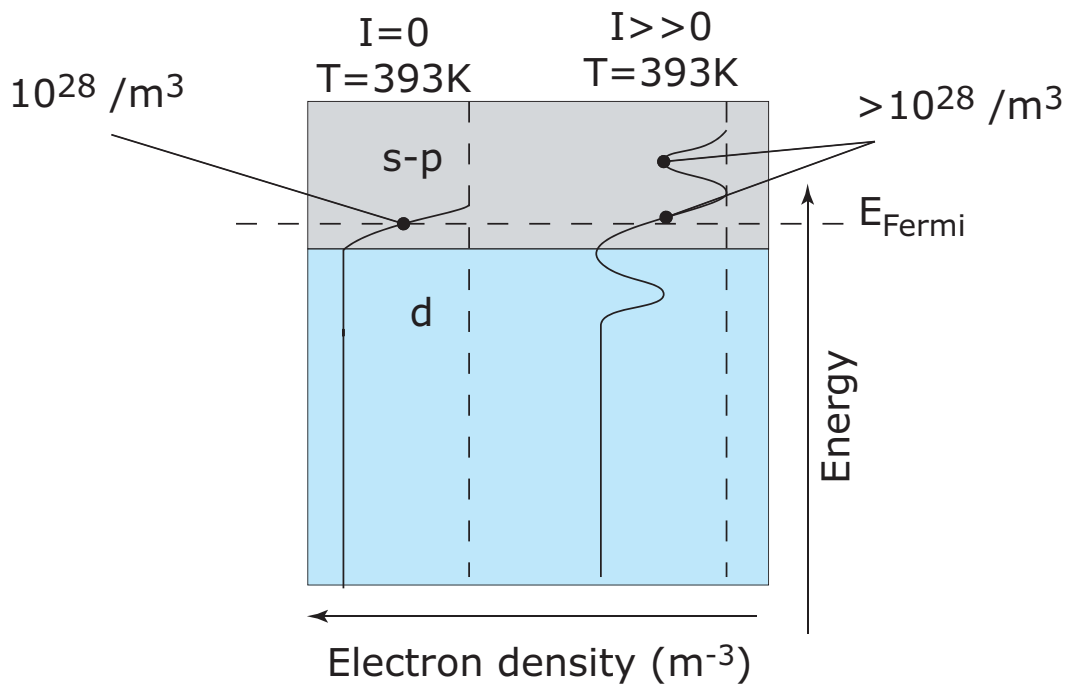


Figure 6.12: While undergoing femtosecond excitation, the density of conduction band electrons in silver is increased from the room temperature value of about 10^{28} m^{-3} to larger values, because of two-photon excitation from the lower d-bands.

0.5×10^{10} was enhanced by a factor of thirty, indicating the fundamental intensity enhancement of $30^{1/3}$. Extrapolation to higher intensities, assuming no saturation, indicates the TH intensity would incur an enhancement of the TH field closer to $1000^{1/3}$. Even with the stronger local fields, the quiver energy of an electron

$$E_{jitter} = \frac{e^2 E(\omega)^2}{m\omega^2} \quad (6.2)$$

is just 0.1 eV, which is very small compared to the work function of bulk silver (4.5 eV). Excitation under these circumstances will not significantly ionize the nanoparticles.

However, the large pulse-rate of the excitation source will increase the temperature of the sample. Heating of the sample can be approximated using Fourier's Law

$$q = -k \left(\frac{dT}{dr} \right), \quad (6.3)$$

using thermal conductivity of sapphire ($k=35 \text{ W m}^{-1}\text{K}^{-1}$), and assuming that 5% of the incident light is absorbed. In thermal equilibrium, heat loss by thermal conduction is balanced by laser absorption

$$-k \left(\frac{dT}{dr} \right) = I_{avg}. \quad (6.4)$$

The time-averaged laser energy absorbed by the material within the focus is $2.175 \times 10^8 \text{ W/m}^2$. Assuming an abrupt temperature rise, with a length-scale given by the focal radius w allows for the calculation of the temperature rise

$$|\Delta T| = \frac{I_{avg.}}{k} \Delta r. \quad (6.5)$$

It is expected that the thermal transport is less than ideal in these materials, so the temperature rise was calculated for a range of thermal conductivities, from 5-35

(W/mK). Such a range of conductivity values indicates thermal increase of 100-700 Kelvin.

Prolonged exposure (greater than 5-10 minutes) of the silver nanoparticle samples under maximum laser fluence resulted in structural changes, such as coarsening and melting. However, neither in the saturation measurements, nor in the laser scanning measurements was the focus held at a single position for more than 1-2 seconds. The fact that structural changes in silver occur for the high fluences indicates a thermal increase on the order of 300-500 °C.

6.4.2 discussion: quartic power dependence and saturation in field-enhanced THG

The quartic power-dependence of THG indicates that that field-enhancement, itself, has a nonlinear response to laser power. Previous studies approximate the response as only linear, meaning nanoparticles have a fixed enhancement factor at all intensities [24, 23]. However, those studies were performed with CW laser systems and do not need to consider nonequilibrium electron populations. The observation of d-band holes through fluorescence (discussed in Chapter 2) is evidence of an increased electron population in the conduction band. Furthermore, our lifetime measurements indicate that there is a delay of several hundred picoseconds during which the excited electrons remain in the conduction band. Though the interband model correctly identifies that the local field response of the particles will deviate from cubic, one expects that the response should be quintic, because the transition is two-photon (the susceptibility is linearly proportional to population). It is possible that other mechanisms such as absorption are playing a role. Recent work by Del Fatti *et al.* has demonstrated highly nonequilibrium populations during ultrafast excitation and provides some insight into this problem [88]. However, those calculations have not been extended to third-harmonic generation.

It is a reasonable assumption that many of the electron-wall collisions happen ballistically; in silver, the mean free path of electrons

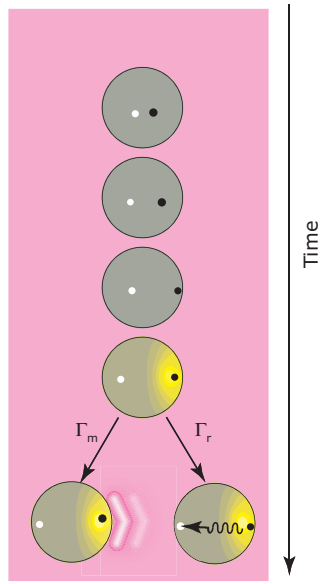
$$l = \frac{(r_s/a_0)^2}{\rho_s} \times 92 \text{ \AA} \quad (6.6)$$

is 52.7 nm, assuming $r_s/a_0 = 3.02$ and $\rho_s = 1.59 \mu\Omega\cdot\text{cm}$ [89]. The mean free path is close to that of the mean diameter of the nanoparticles. At the highest intensities, collisions become important enough that their effect must be considered not just as an enhancing mechanism, but as a source of dephasing. When electrons from the bulk collide with surface states, the phase of the electrons is randomized, causing a reduction of the polarization of the particles.

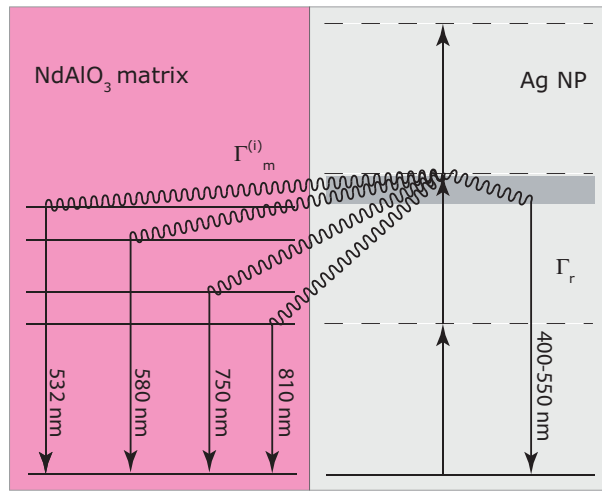
It is interesting to note that wall collisions are particularly important if the matrix material contains some excitable material like Nd^{3+} . In that case, energetic electrons that are gained via the two-photon excitation from the d-band are lost via a transfer to surrounding media. This process is shown schematically in Fig. 6.13(a). As a result of the additional decay mechanism (excitation transfer to the surrounding matrix), the excited electron population in the silver is depleted significantly, compared to the bare or inert glass matrix nanocomposites. The effect described in Fig. 6.13 contributes to the observed suppression of saturation in the RE nanocomposites, described above. Furthermore, the decrease in the concentration of electrons in silver also contributes to the decreased enhancement of the RE nanocomposite at lower intensities, as well as the apparent decrease in TH conversion efficiency at low Ag concentration, shown in Fig. 6.2.

6.5 Measurement of third-harmonic phase

The allowed states of the nanostructured system are those that are coherently accessible to the electrons when coupled to the fundamental driving laser field. Oscillator



(a) When surrounded by a resonant matrix, excited electrons (\bullet) and holes (\circ) in silver nanoparticles decay either by radiation recombination (Γ_r) or by excitation transfer to the surrounding material (Γ_m).



(b) Bloch energy diagram of energy transfer from the Ag nanoparticle (right) to the NdAlO₃ matrix (left). The excited SP level of the nanoparticle decays via broadband photoluminescence (400-550 nm). Several levels of the Nd³⁺ ion are accessible, which decay further by radiation at 532, 580, 750, and 810 nm.

Figure 6.13: Schematic representation of energy transfer at a nanoparticle-RE matrix boundary.

strengths in such a situation are difficult to predict, since the local potential is not well-defined. For this reason experiments may benefit from an ability to determine the degree of coherence in during multiphoton excitation. Furthermore, the enhancing media developed for harmonic generation utilizes spatially separated resonances; electrons may undergo phase-altering collisions while being transported from one material component to another. Consequently, the phase of an electron will be an important measure of the ability of our materials to enhance the overall harmonic.

Using spectral interferometry, it is possible to differentiate materials with resonant nonlinear susceptibilities from nonresonant ones. The radiated TH field from a slab of nonlinear material (depicted schematically in Fig. 6.14) may be approximated as two Gaussian pulses, separated by $\tau(L)$. When these pulses interfere in a frequency-resolving detector, the spectral intensity shows a modulation, with a periodicity determined by the pulse spacing. The effect, frequency-domain interferometry, has been exploited for studying a wide array of materials [62, 90, 91]. So far, only the fundamental and second-harmonics have been used; frequency-domain interferometry using third-harmonic pulses is a new approach, which has some particular advantages for probing nanostructured optical materials.

A simple application of pulse interferometry is to use the phase sensitivity to distinguish between resonant and non-resonant processes. The phase of a THG pulse is determined by the generating material's $\chi^{(3)}$, which is (in general) complex. The third-order susceptibility for nonresonant interactions is real, and does not alter the phase of the fundamental field. Resonant THG susceptibilities have an imaginary component, and do affect the phase of the radiated field. Near a resonance, the TH susceptibility sum reduces to a single term

$$\chi_{res.}^{(3)} \propto \frac{1}{(\omega - \omega_{g1} + i\gamma_{g1})(2\omega - \omega_{g2} + i\gamma_{g2})(3\omega - \omega_{g3} + i\gamma_{g3})}. \quad (6.7)$$

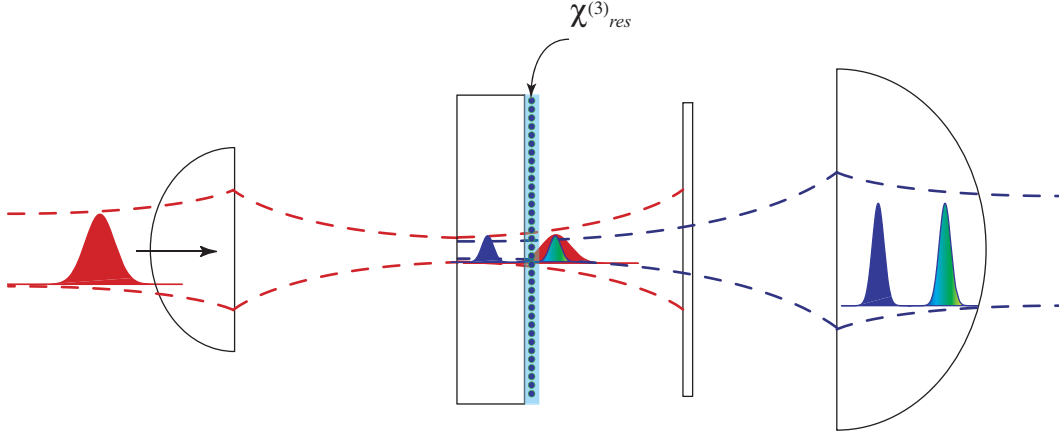
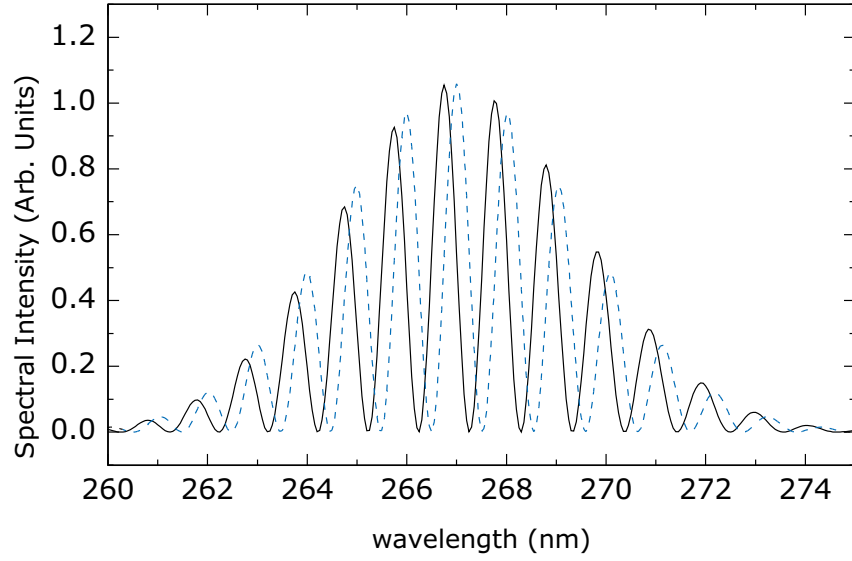


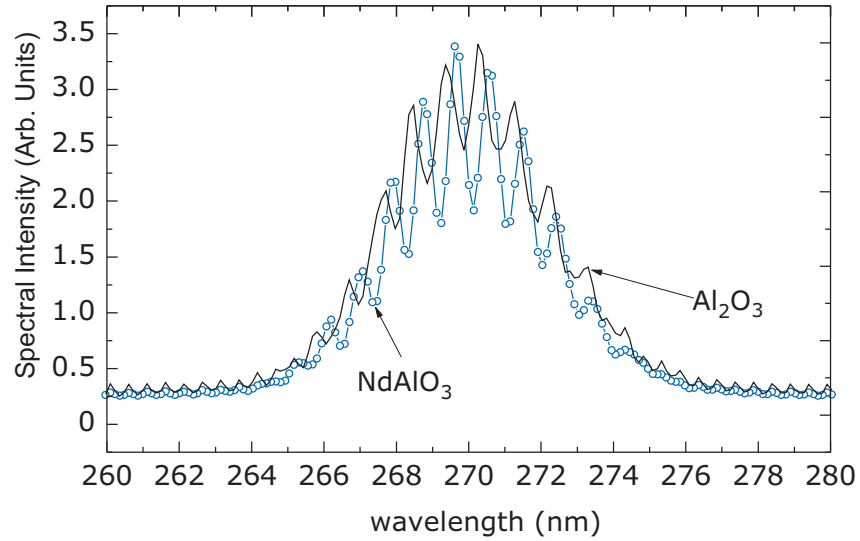
Figure 6.14: If a slab of material has a resonant thin film on one side, the phase of the TH field emitted at that interface will be shifted relative to the phase of the TH pulse emitted from the bare interface. The spatial separation is achieved via group-velocity mismatch of the fundamental and third-harmonic fields in the nonresonant substrate.

If the film at one side of a slab of material has a susceptibility with a non-zero imaginary part, as shown in Eq. 6.7 if $\omega \cong \omega_{g1}$, and if the substrate is thin enough, then the radiated field consists of one Gaussian pulse which is out of phase with a second Gaussian pulse. The interferometric signal originates from the interference between these two pulses when the signal is spectrally resolved in the monochromator. (Chapter 5 offers a discussion for the case of nonresonant materials and thin films.) For a typical thin film, which is not resonant, there is no absolute phase difference between the electric fields generated at the front and back surfaces of the material. However a resonant material like NdAlO_3 exhibits a spectral shift. Fig. 6.15 compares the theoretical and experimental spectra of both resonant and nonresonant materials.

Using the spectral phase to identify material properties is particularly useful for characterizing resonant nanostructured materials. Since the length scale is much shorter than the wavelength of a probing field, coherent transitions between resonant



(a) Theoretical THG spectrum generated in a 330 μm sapphire substrate (solid) is compared to a theoretical spectrum from a resonant thin film grown on the substrate (dashed). (solid).



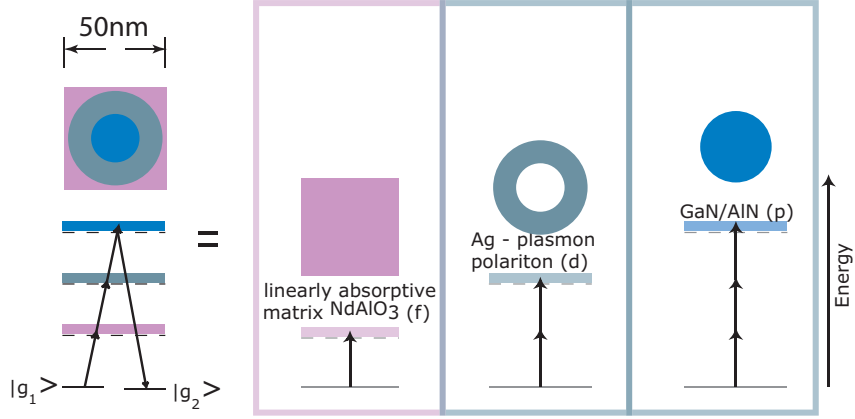
(b) Experimental THG signals are compared for non-resonant (solid line) and resonant (dashed) $\chi^{(3)}$.

Figure 6.15: The third-harmonic spectrum is used to detect the 808-nm resonance of NdAlO_3 (bottom). The resonance is detected through the shift of the spectral fringes. The effect of the resonance in compared to a theoretical model (top).

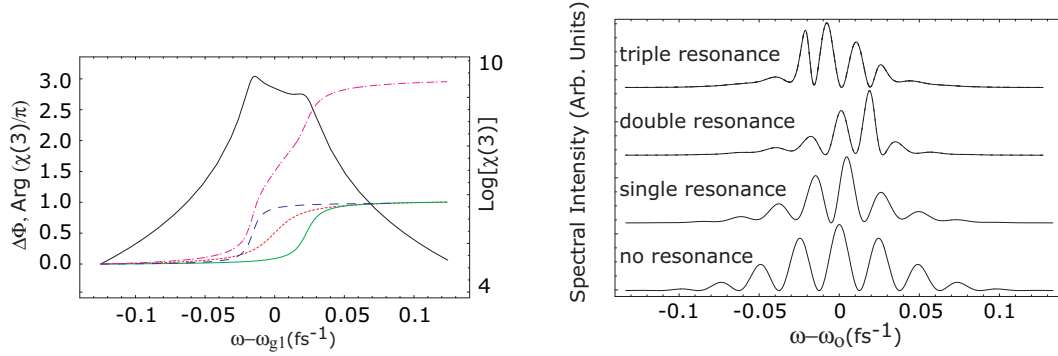
states on the nanoparticle and resonant states off of the nanoparticle are expected. The NdAlO_3 -Ag nanoparticle sample has a matrix resonance at the fundamental laser frequency ω_1 and the nanoparticle has a resonance at the two-photon frequency ω_2 . Excited matrix electrons at the edge of the nanoparticle may be further excited into the resonant two-photon state in the nanoparticle, and stimulate photons with a phase shift of π , relative to the fundamental field. Electrons that are isolated to either the nanoparticle or the NdAlO_3 will participate with only one or the other resonances, and will stimulate photons with a smaller phase shift of $\pi/2$ relative to the fundamental field. The latter case of a single resonance in NdAlO_3 was verified experimentally in Fig. 6.15. In that case, the observed TH spectrum of the bare substrate displays a different spectral phase compared to when the coated substrate. In heterogeneous samples, the overall spectral phase may be more complex. Decomposing the third-harmonic field into phase components may allow one to isolate coherent electronic transitions between states on the nanoparticles and the surrounding media from transitions based on isolated electrons.

The concept of resonance superposition can be extended further for more complex nanomaterials. If the material contains an additional partial concentration of nanoparticles with a resonance at ω_3 at the third harmonic frequency (such would be the case of an AlN core nanoparticle inside of a silver shell), an electron which participates with all three of these will stimulate a photon which is further phase shifted by $\pi/2$. A simulation of the interferometric response of such a material is shown in Fig. 6.16.

The model for the material analyzed in Fig. 6.16 does not include material absorption, which will reduce the overall signal by depleting the input field as well as the radiated field. (The nanostructured films discussed in this chapter are so thin that the aforementioned assumption is valid.) Fundamental field depletion due to significant energy conversion is also neglected, because conversion efficiency is



(a) We modeled the nonlinear response of an idealized unit cell of a material nanostructure with 3 resonances. In it, a Nd^{3+} :glass matrix is in intimate contact with large band gap nanoparticles (AlN/GaN), encapsulated by a silver shell.



(b) The magnitude of Eq. 6.7 was evaluated for all material components in resonance, given realistic values for the line-widths. The corresponding spectral phase is also plotted for the individual resonances, and for the case of the triply resonant case.

(c) The interferometric signal gives a stronger contrast for each of the cases. The spectral phase in Fig. 6.16(b) is encoded in the fringe locations.

Figure 6.16: In addition to large nonlinear susceptibilities, unique spectral signatures are predicted to generate from resonant nanostructures.

$\ll 1$. In addition, energy level symmetries determine the oscillator strengths of each transition. In the NdAlO_3 -Ag material, an electron initially in the f-level of the neodymium ion can make a transition through the quadrupolar plasmon polariton level, or to an unpopulated d-bands state. Nanostructure has a large influence on the level symmetry. Though nanoparticles below 10 nm are excited primarily like dipoles, a spherical harmonic expansion of the polarization of the larger 50- to 100-nm particles in our samples will contain significant quadrupolar terms. Furthermore, the random material structure and shape of the actual silver materials described in chapter 1 also requires quadrupolar and even higher-order terms to describe the angular momentum of the local electric fields. Given the surface roughness and larger size of our particles, our samples have a strong potential for coupling the neodymium atomic resonances with the silver plasmon.

6.6 Conclusions

Based on the measurements of SHG and THG in Ag nanoparticle and coated nanocomposites, we identified an intensity-dependence of local field excitation. The mechanism underlying the intensity-dependent enhancement is a consequence of the increased population of conduction band electrons, which occurs only on ultrafast time-scales. In bare samples, there is a cross-over to saturation which we expect is governed by collisions with the surrounding dielectric, though without further analysis it is unknown whether collisions are of a ballistic or thermal nature [43].

What is clear from our experiments is that matrix materials influence the intensity-dependent optical response of nanoparticles, though participation with the surface electrons and surface collision processes. Sapphire-coated materials exhibited less low intensity enhancement, but saturated at high intensities like the bare Ag samples. However, using a resonant matrix lowered enhancement at low in-

tensities, but prevented the onset of saturation at high intensities. Because both effects are derived from wall collisions in the nanoparticle, the conclusion is that the neodymium matrix acts as a damping mechanism for collisions, either by cooling the nanoparticles, or by absorbing collisional energy by exciting atomic transitions in the neodymium ion.

As a final note, it is worth comparing the greatest observed TH enhancement at 10^{11} W/cm² to the TH response of another medium, indium tin oxide (ITO). Transparent conductors such as ITO and ZnO (zinc oxide) have recently been subjected to investigation, because of their observed, large conversion efficiencies [67]. The samples analyzed in this chapter were compared to an ITO thin film (nominally 300-nm-thick), and the results are plotted in Fig. 6.17. The order-of-magnitude

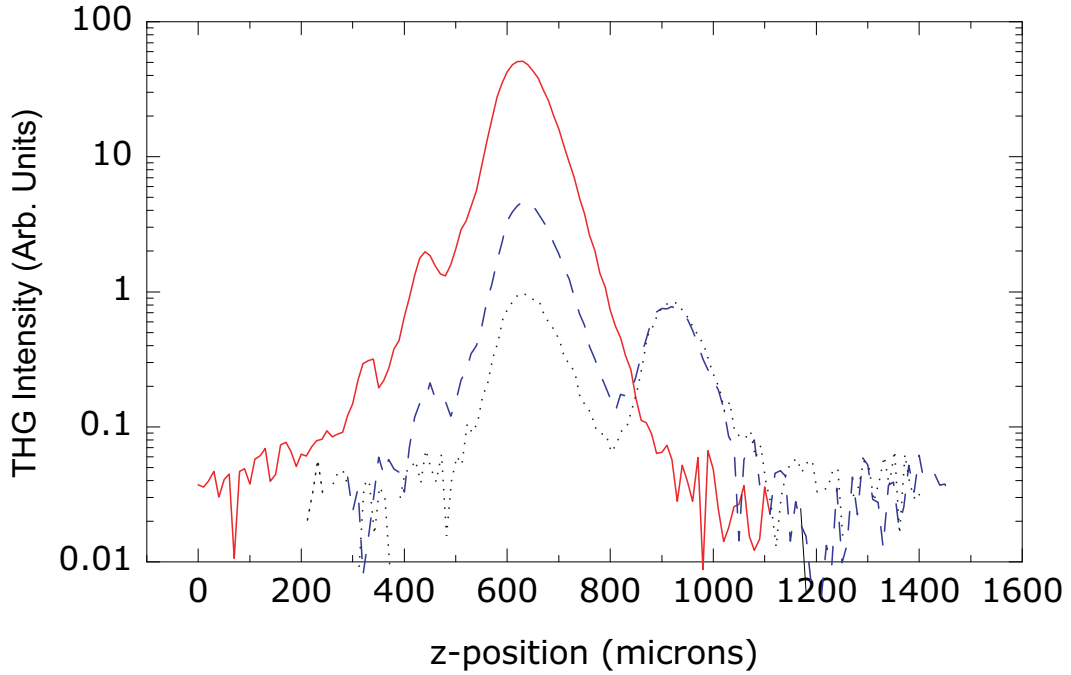


Figure 6.17: Comparison of the maximum observed TH signal from NdAlO₃ (dashed) to ITO (solid), and a bare sapphire substrate (dotted).

greater response of the ITO makes a compelling argument that field enhancement

is not the best approach for enhancing third-harmonic generation. However, the active thickness of the nanocomposites is a factor of 3 thinner. After considering that the nonlinear response of thin materials grows like the square of the material thickness, one determines that the material susceptibility of the field-enhanced resonant nanocomposite is comparable to ITO.

Appendix A

Operation Manual for the Femtosoftware FROG Apparatus

A.1 Introduction

This appendix is meant to serve as a short guide for using Femtosoftware Technologies' implementation of the FROG (frequency-resolved optical gating) algorithm to retrieve the amplitude and phase of a femtosecond laser pulse. The data collection is achieved through a LabView program "ak_spectrographfrog.vi" developed in Professor Keto's laboratory by Kay Hoffmann, John McDowell, and myself. The goal of the guide is to familiarize a new user with the relevant software and the files which are created for loading into the FROG subroutine, or that are produced after the routine has completed.

A.2 Collecting data with ak_spectrographfrog.vi

In principle, ak_spectrographfrog.vi can be run in a 'stand alone' mode. Following the recording of a frequency-resolved autocorrelation of a laser pulse, the .vi auto-

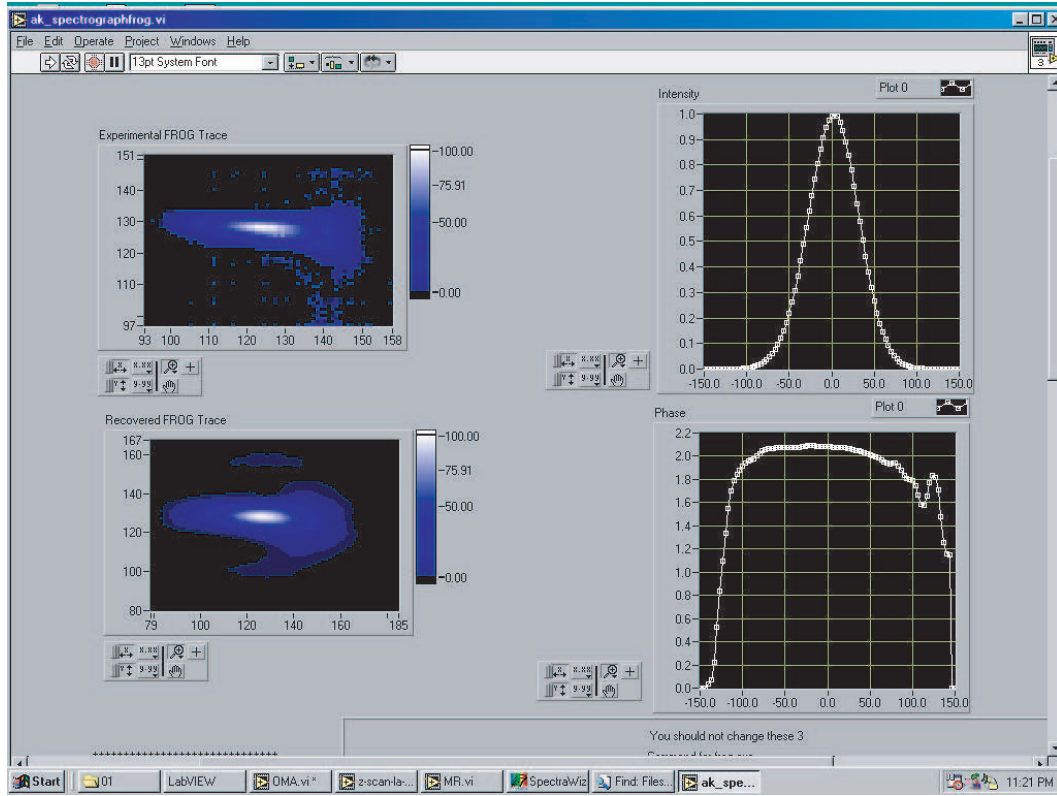


Figure A.1:

matically transforms the data along with important input parameters into a file of the form, "FROGTRACE_#_.dat". The FROGTRACE file contains a parameter header which is read by the Femtosoft frog executable, "Frog3.exe". After reading the FROGTRACE file, Frog3.exe performs an iterative loop that (following suitable convergence) returns several files. One of them, Ek.dat, contains the fitted E-field amplitude and E-field phase data. Another file, arecon.dat, contains the Frog Trace data (the 2-D contour data one often sees), albeit in a somewhat garbled form. The .vi then takes the arecon.dat file, and produces two intensity plots, 'aformat.dat' and 'areconfo.dat' which are the experimental and recovered frog traces, respectively. These latter two files are easily plotted using any commercially available

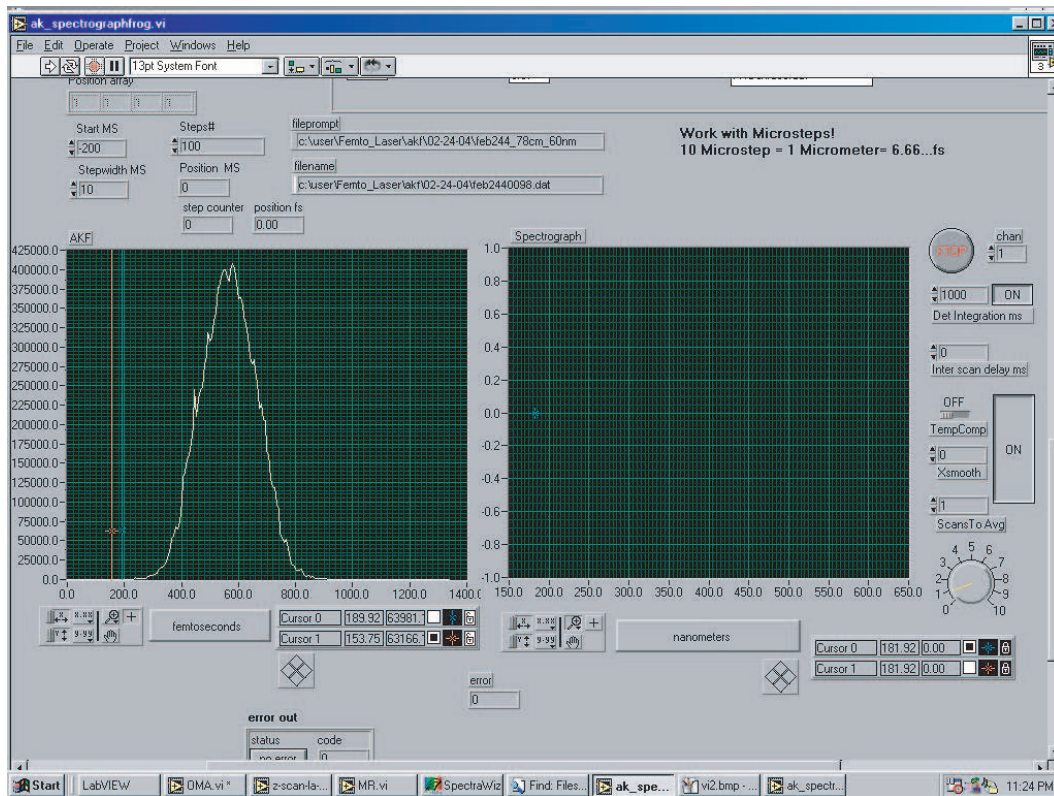


Figure A.2:

plotting software.

Fig. A.1 shows a screen shot of the upper half of `ak_spectrographfrog.vi`, where the frogtrace data are displayed following a successful execution of `Frog3.exe`. On the right hand side, the squared amplitude and the phase data from `Ek.dat` are plotted. Both the experimental and recovered frog traces are shown to the left. One can immediately see how they resemble one-another, an indication of a successful fit.

The lower portion of the `.vi` is shown in Fig. A.2. On the left is a typical autocorrelation of a Ti:sapphire oscillator pulse. The autocorrelation is a plot of the integrated second-harmonic spectrum as a function of delay. The delay is plotted in

femtoseconds, though in actuality the delay is obtained by microstepping the delay arm of a Michelson interferometer. This point is emphasized on the .vi by mentioning that 10 microsteps=1 micron =6.667 fs. Though not shown in Fig. A.2, while the .vi is acquiring data the background free second-harmonic spectrum for a fixed delay will be shown to the right of the in-progress autocorrelation. The knobs to the right of the empty plot are used to control the data acquisition mode of Spectrawiz spectrograph(Stellarnet Inc.). It is imperative that ak_spectrographfrog.vi be located in the same directory as the spectrawiz dynamic link library sw.dll, or several function calls will improperly link when opening the .vi.

A.3 Managing the Frog routine through the Femtosoft executable

Though ak_spectrographfrog.vi will automatically generate a data file and read it into the Femtosoft software, it is possible to load a previously-generated FROG-TRACE-#-.dat file by hand. It is highly recommended that one try this to gain familiarity of the software's several utilities and tweaks. Knowing what the Frog3.exe does can make the analysis take just a few seconds as compared to a few hours!

The Frog3.exe file is located in the ./femtosoft_frog subdirectory on the C-drive of Ketopc2. Double click on it. After it opens, one sees the modest grey window with a menu. Select RUN→Frog from the RUN drop down menu. After selecting 'RUN', the input window will appear. The grid size is selectable within the left-hand column. For most applications, 256x256 is sufficient. Selecting 1024x1024 will cause the algorithm to take a very long time, so avoid that grid value (grids are also selectable on the front panel of ak_spectrographfrog.vi.). As shown in Fig. A.3, select SHG in the NLO section, and selecting 'Experimental Frog Trace' causes a new window on the right to appear. This is the window where the experimental

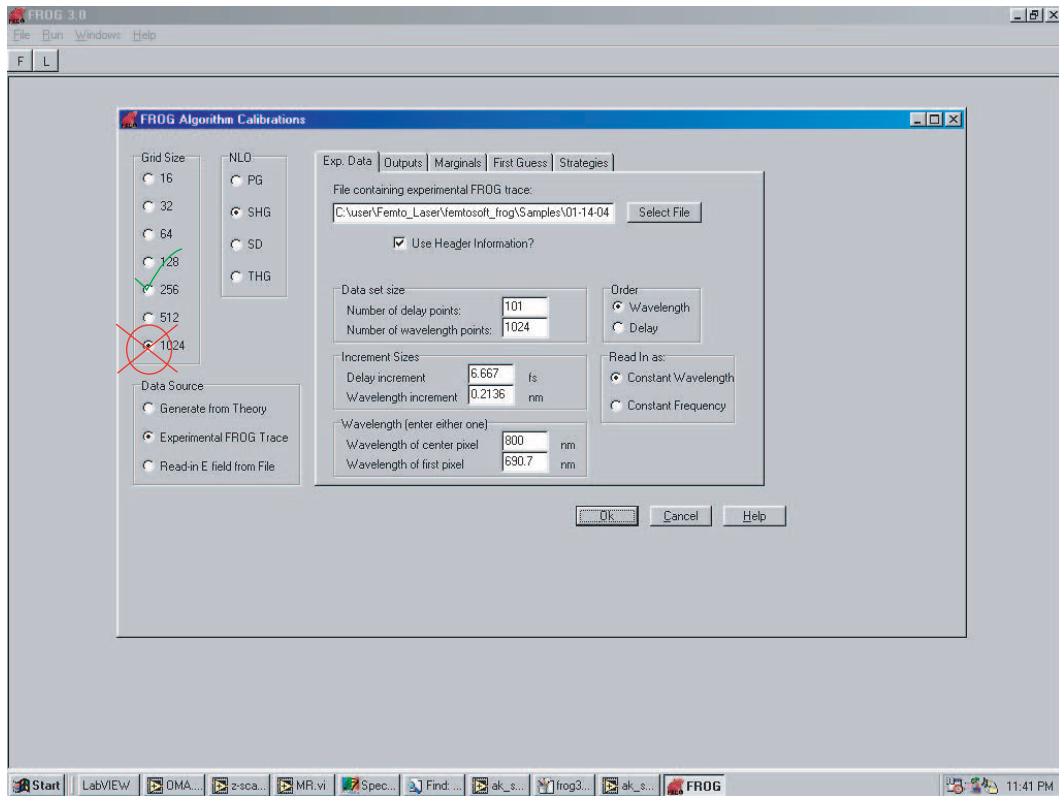
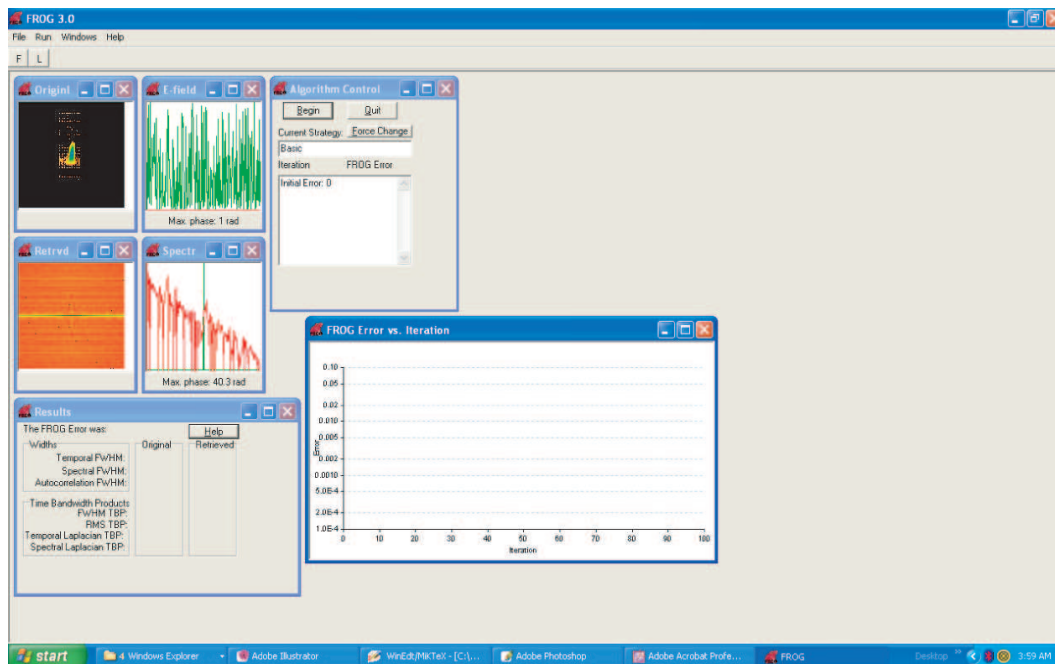


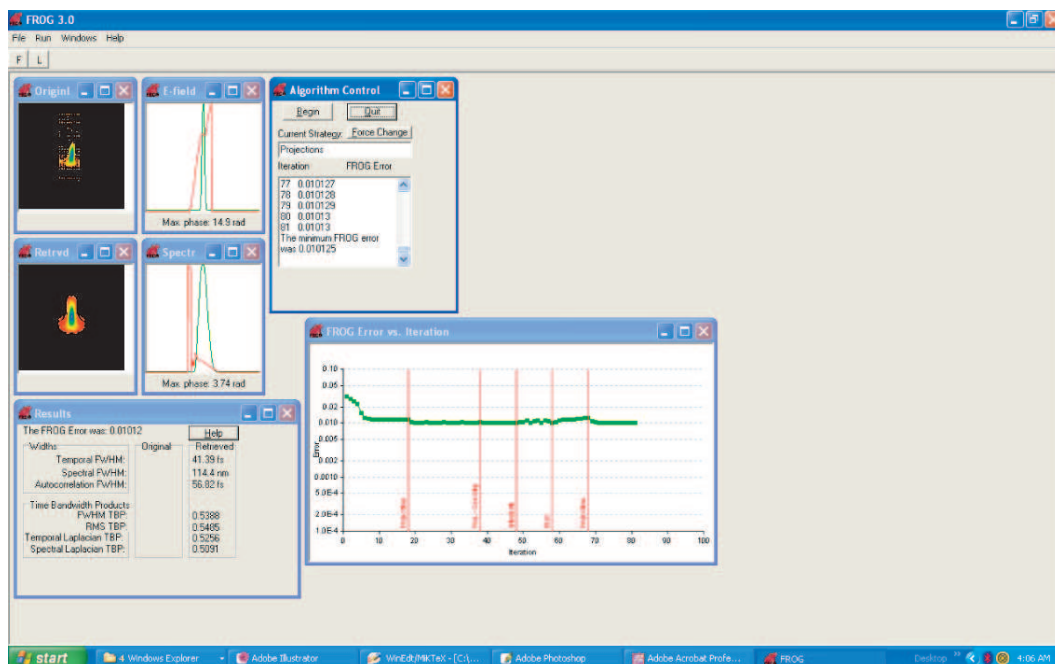
Figure A.3:

FROGTRACE data is selected. Under the 'Marginals' tab, you may also select the same FROGTRACE file under 'Autocorrelation'. Select the directory where the output files will be placed (again, this is automatically done in the .vi). There are many other features which may be turned on and off, but just leave them as default for the time being. After selecting the desired variables, click the 'read from header' box, and the 'OK' button should darken. You are almost ready to start the routine.

After clicking 'OK' you are presented with a small window showing the experimental Frogtrace data. In this window, you may apply a FFT filter or resample the time-domain. Clicking 'Grid Data' will bring transform the screen to what is



(a) Frog3.exe after pressing 'Grid Data'



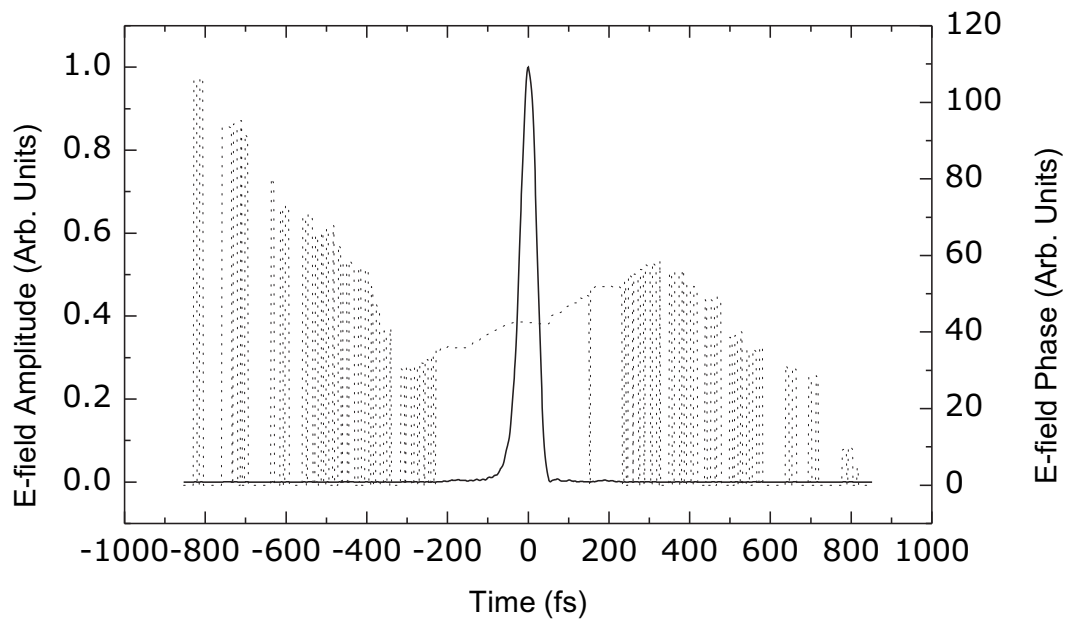
(b) Frog3.exe after halting FROG routine

Figure A.4:

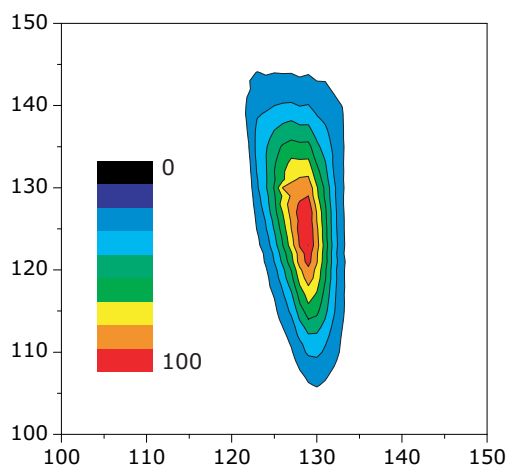
shown in Fig. A.4(a). At this point, clicking the 'Begin' button in the algorithm control window will start the FROG routine. A series of iterations will decrease the Error shown in the 'Frog Error vs. Iteration' window. It is up to the user to decide when to stop the routing. Stopping is accomplished by pressing 'Stop' in the 'Algorithm Control' window. The after a few (milli)seconds, the results of the routing are summarized in the 'Results' window, as shown in Fig. A.4(b).

A.4 Manipulating the Frog3.exe output

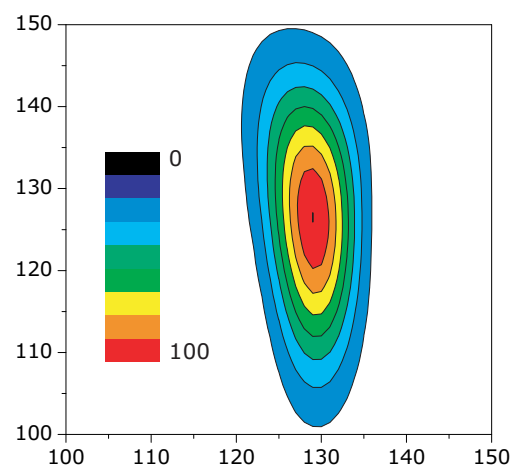
The temporal amplitude and phase output of the Frog3.exe program is shown in Fig. A.5(a), which was produced directly by plotting the second (amplitude) and third (phase) columns of the Ek.dat file found in the selected output directory. However, for some reason one might want to make a contour plot of the experimental and retrieved Frog traces (perhaps to hang in the local coffee shop). To this end, Frog3.exe doesn't quite live up to its expectations. However, with the help a a simple helper LabView program called 'convert.areconfo.vi', one can produce two files, 'aformat.dat' (exp. Frog Trace) and 'areconfo.dat' (recovered Frog Trace), which may be plotted with any contour plotting utility. Using convert.areconfo.vi on the Frog3.exe output arecon.dat produces contour plots like the ones shown in Fig. A.5. The latter Frog Traces in Figs. A.5(b) and A.5(c) are similar to the data shown in the Chapter 4 of this dissertation.



(a) Ek.dat



(b) Experimental Frog trace



(c) Recovered Frog Trace

Figure A.5:

Appendix B

CAD Drawings of the Pyrolytic Boron Nitride Vacuum Furnace Assembly

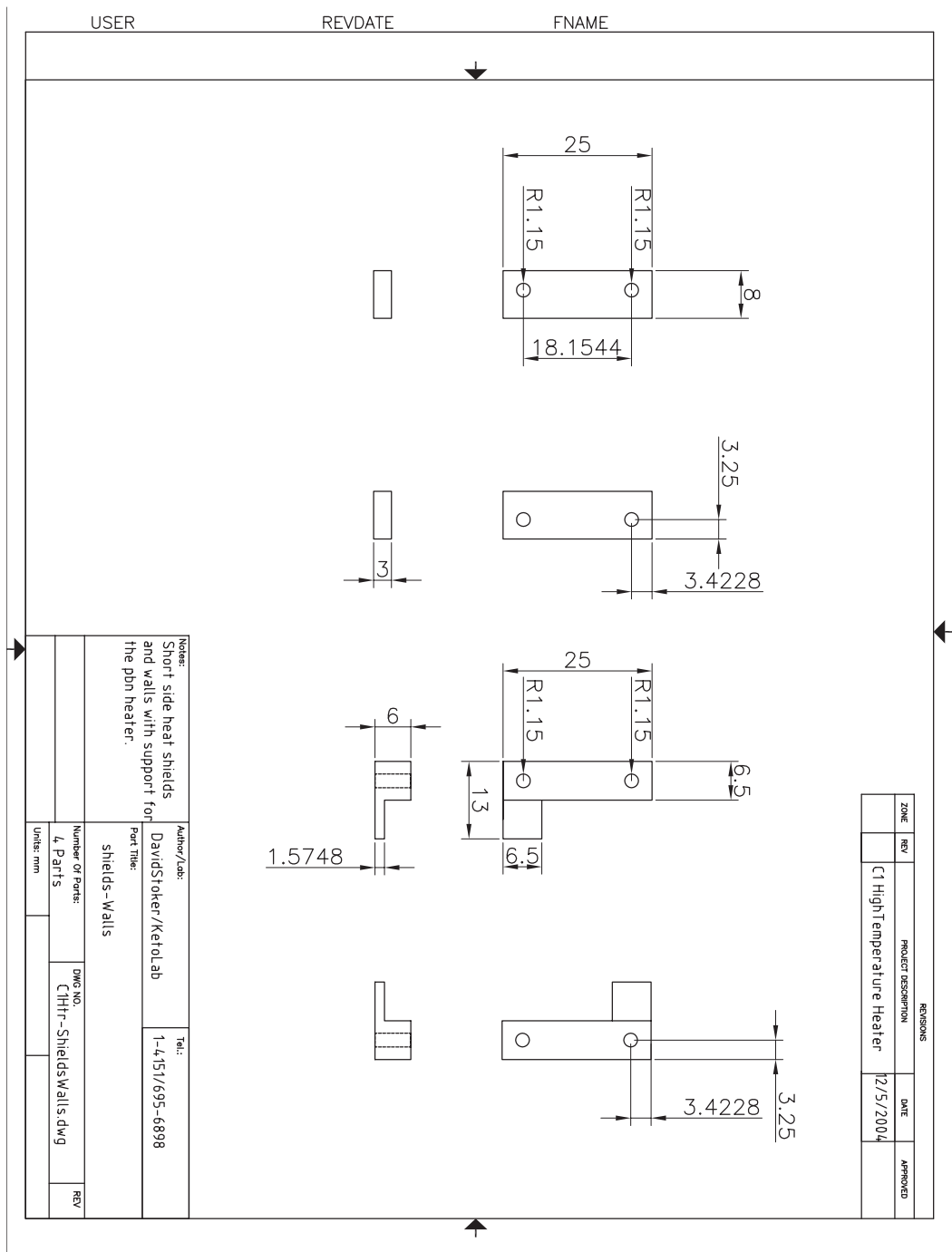


Figure B.1:

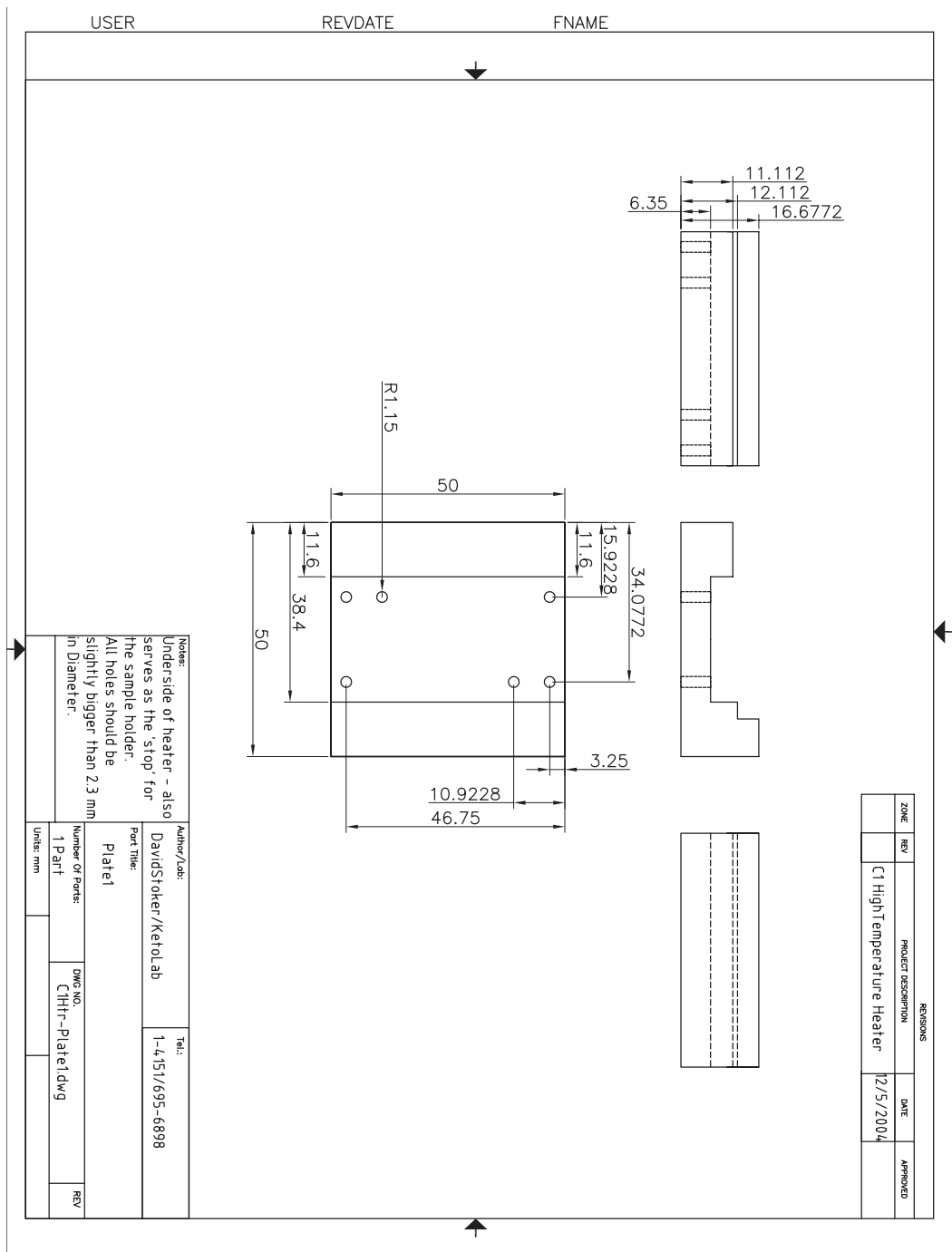


Figure B.2:

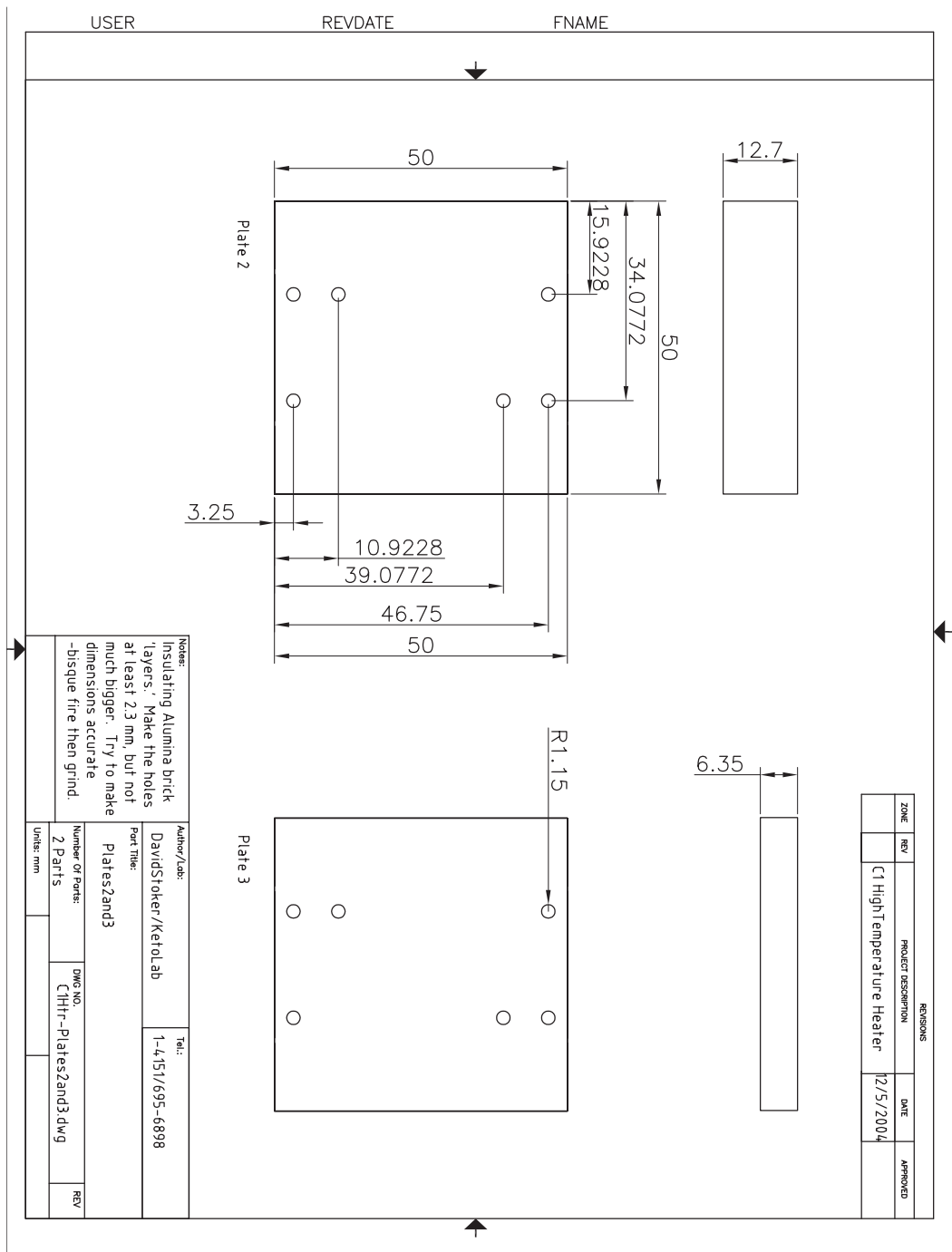


Figure B.3:

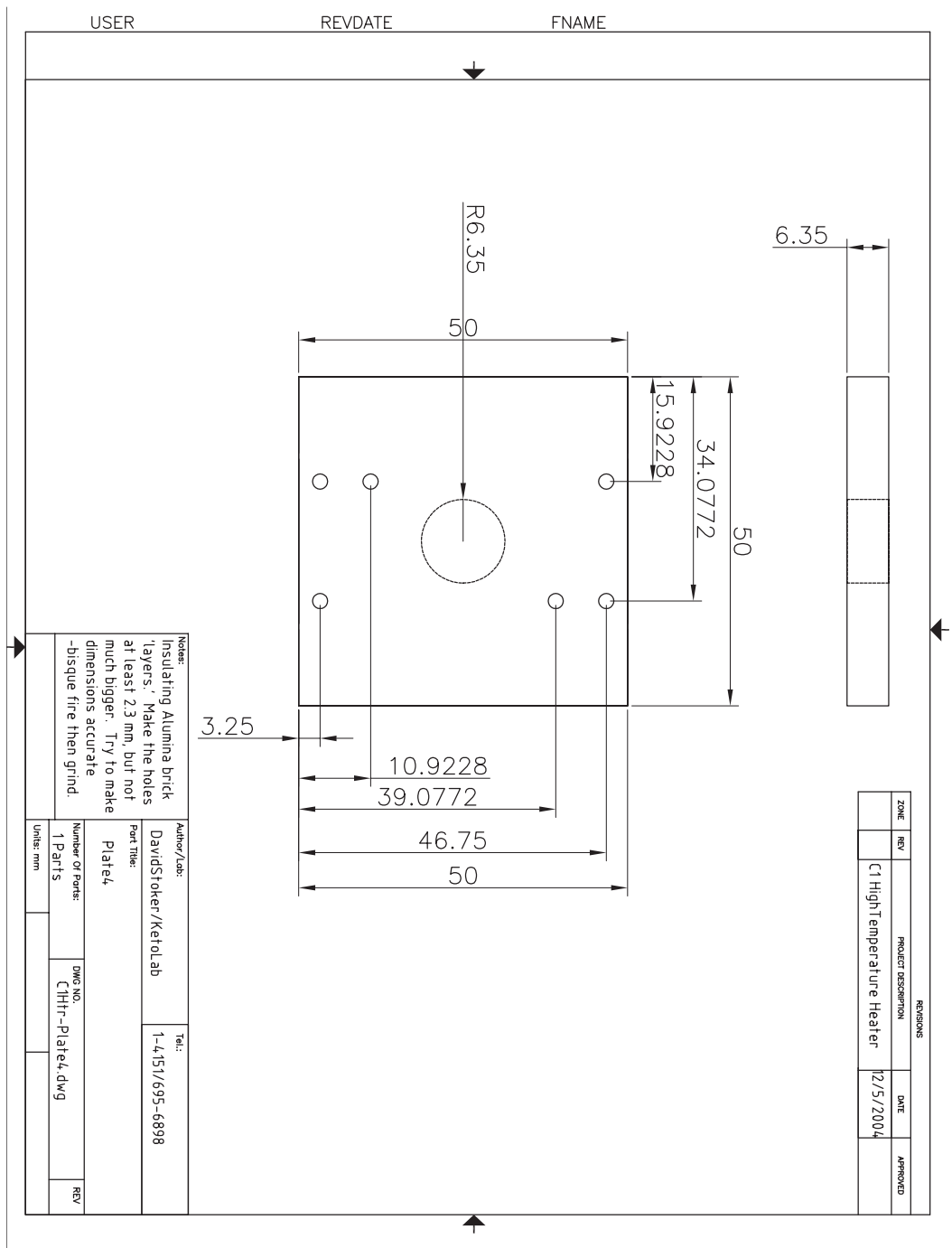


Figure B.4:

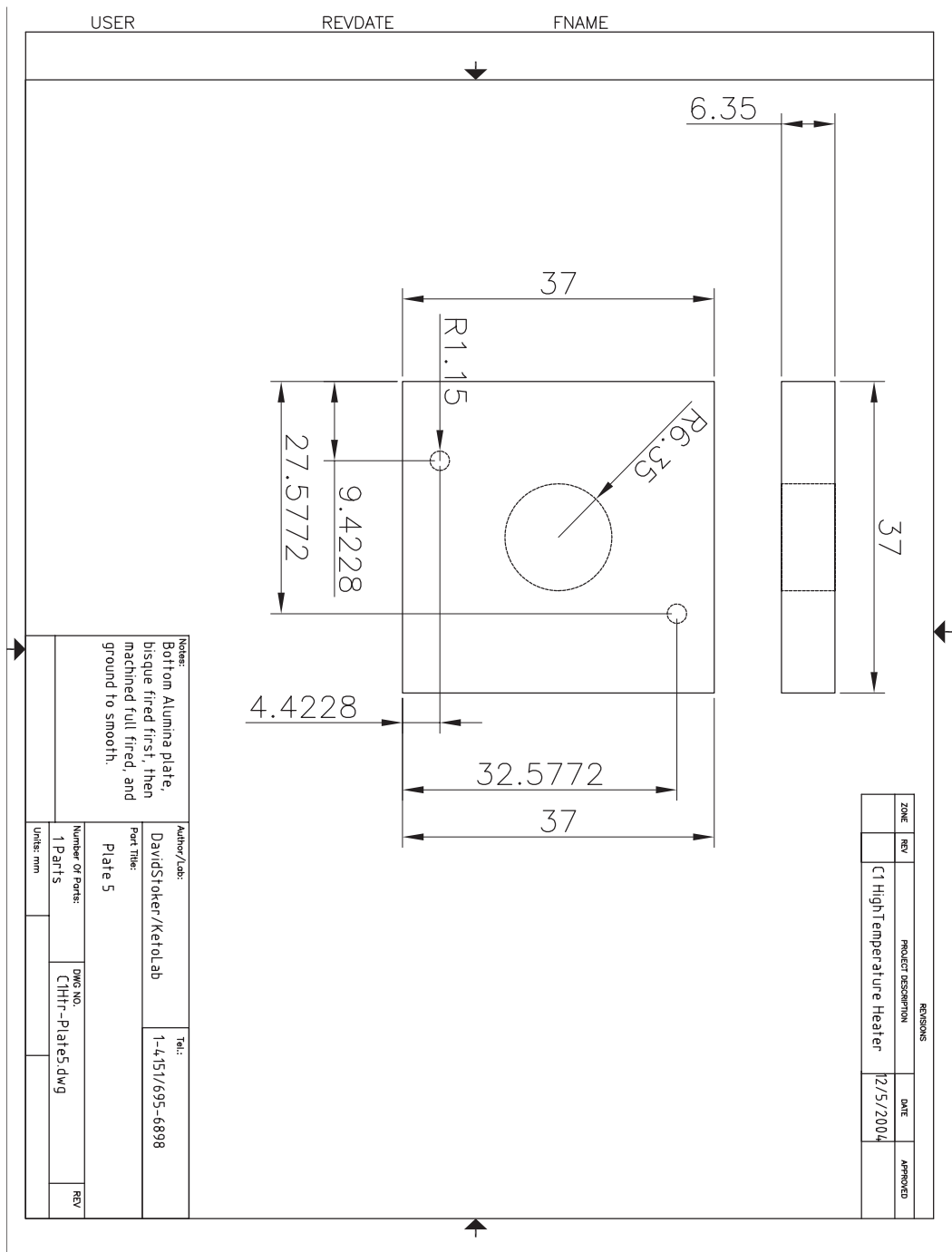


Figure B.5:

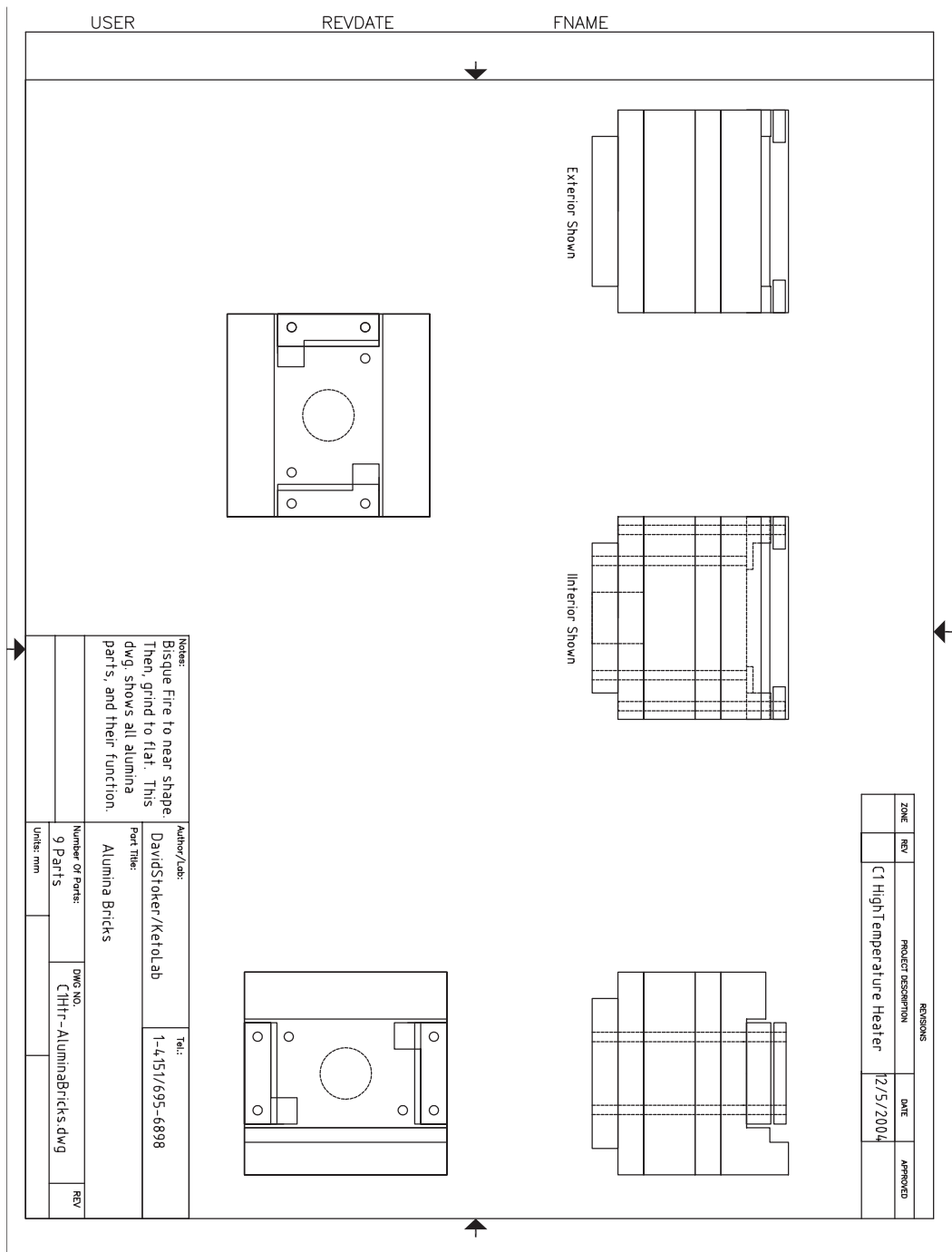


Figure B.6:

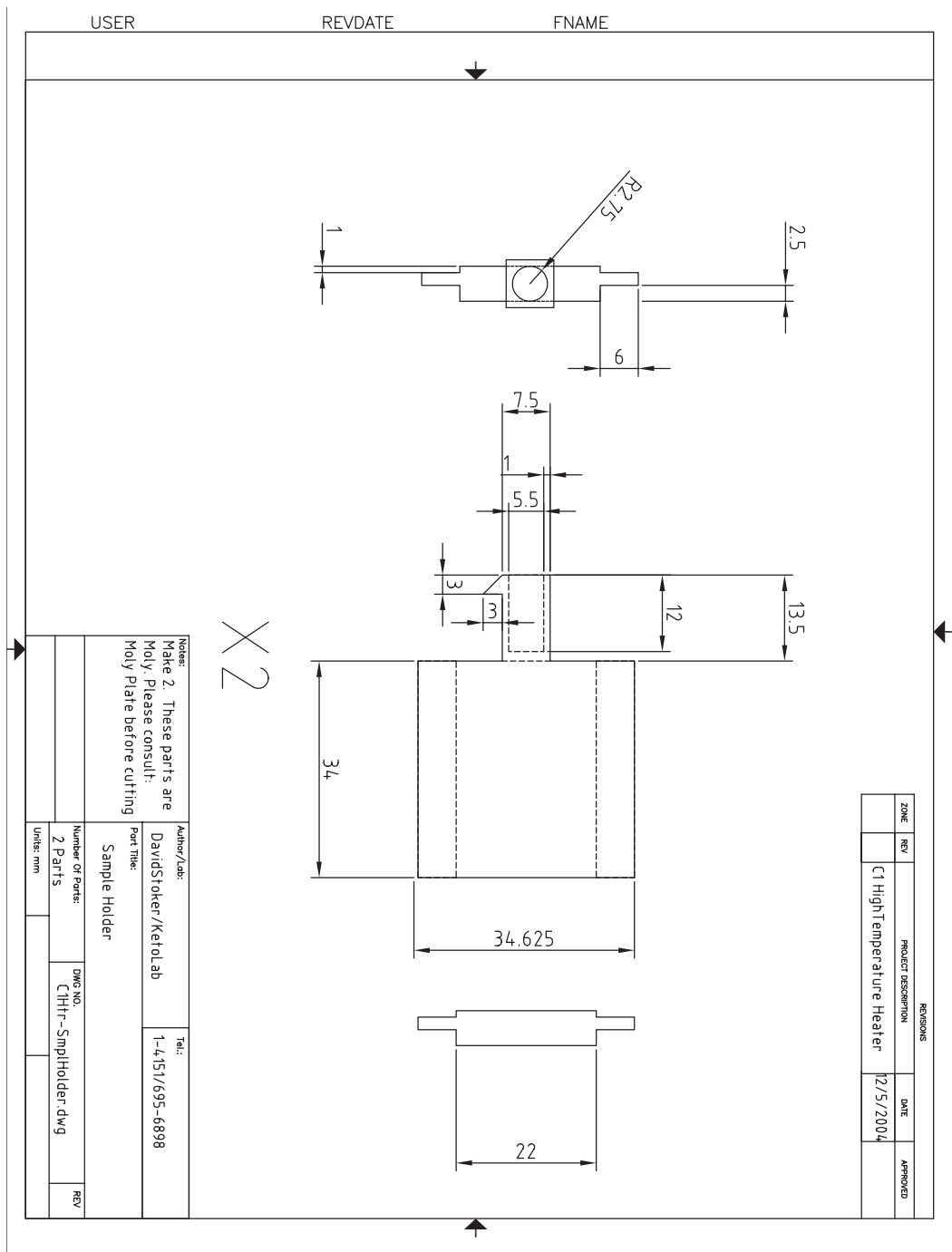


Figure B.7:

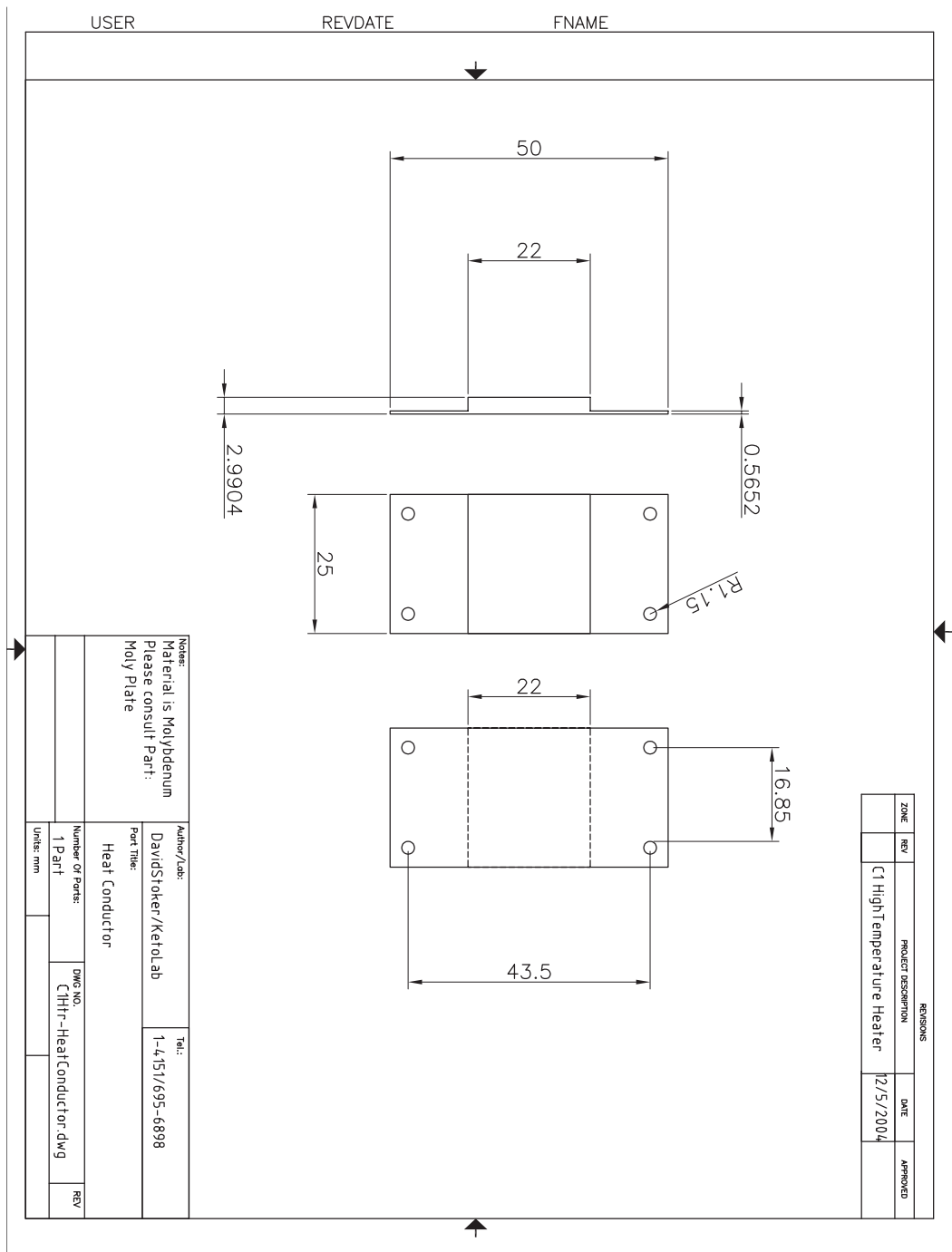


Figure B.8:

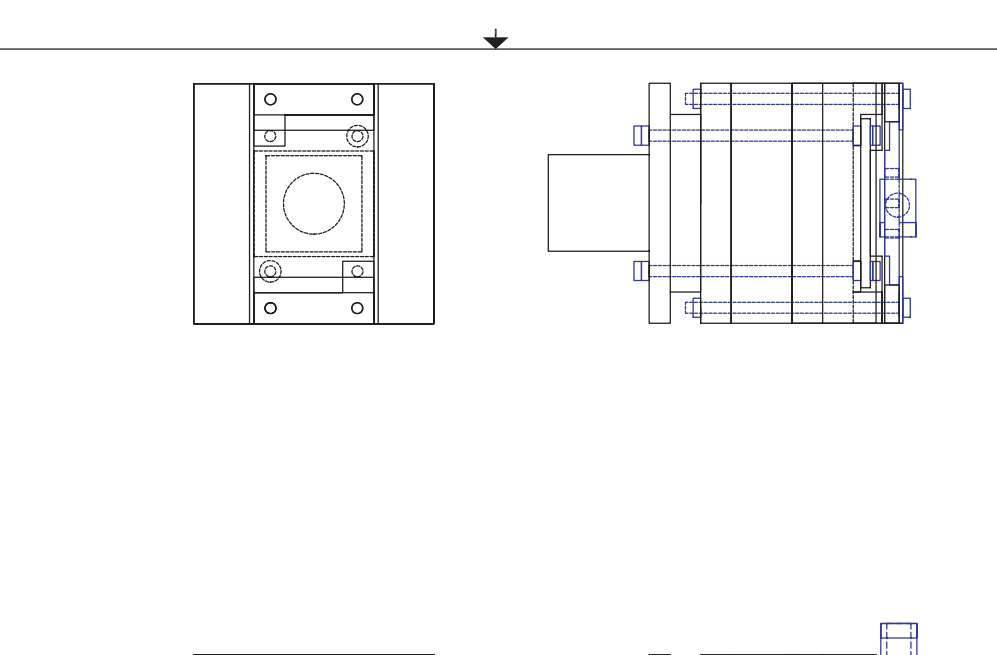
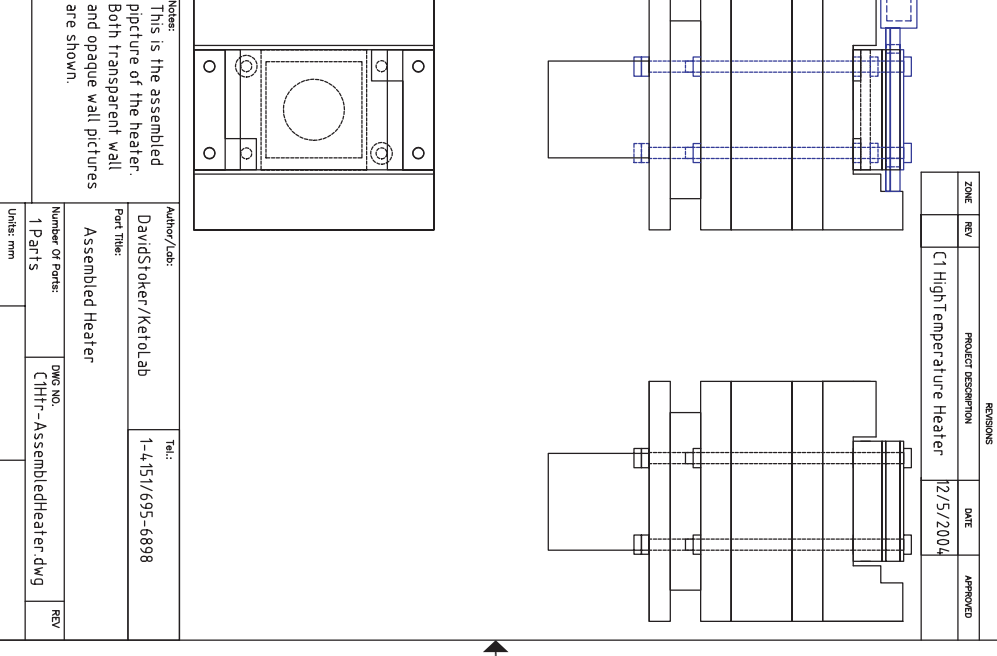
| USER | | REVDATE | | FNAME | | | | | | | | | | | | | | | | | | | | | | | | | | | | | | | | | | | | | | | | | | | |
|--|-----|----------------------------|-----------|---------------------------|--|-----------|--|-------------|--|-------|-----|--|------|---------------------|--|-----------------|----------------------------|-----------|--|-------------|--|--|--|--|--|------------------|--|--|--|--|--|------------------|--|---------|--|--|--|---------|--|---------------------------|--|--|--|-----------|--|-----|--|
|  | | | | | | | | | | | | | | | | | | | | | | | | | | | | | | | | | | | | | | | | | | | | | | | |
|  | | | | | | | | | | | | | | | | | | | | | | | | | | | | | | | | | | | | | | | | | | | | | | | |
| <table border="1"> <thead> <tr> <th colspan="4">REVISIONS</th> </tr> <tr> <th>ZONE</th> <th>REV</th> <th>PROJECT DESCRIPTION</th> <th>DATE</th> <th>APPROVED</th> </tr> </thead> <tbody> <tr> <td></td> <td></td> <td>C1 High Temperature Heater</td> <td>12/5/2004</td> <td></td> </tr> </tbody> </table> | | | | | | REVISIONS | | | | ZONE | REV | PROJECT DESCRIPTION | DATE | APPROVED | | | C1 High Temperature Heater | 12/5/2004 | | | | | | | | | | | | | | | | | | | | | | | | | | | | | |
| REVISIONS | | | | | | | | | | | | | | | | | | | | | | | | | | | | | | | | | | | | | | | | | | | | | | | |
| ZONE | REV | PROJECT DESCRIPTION | DATE | APPROVED | | | | | | | | | | | | | | | | | | | | | | | | | | | | | | | | | | | | | | | | | | | |
| | | C1 High Temperature Heater | 12/5/2004 | | | | | | | | | | | | | | | | | | | | | | | | | | | | | | | | | | | | | | | | | | | | |
| <table border="1"> <tr> <td colspan="2">Notes:</td> <td colspan="2">Author/Lab:</td> <td colspan="2">Tel.:</td> </tr> <tr> <td colspan="2">This is the assembled picture of the heater. Both transparent wall and opaque wall pictures are shown.</td> <td colspan="2">DavidStoker/Ketolab</td> <td colspan="2">1-4151/695-6898</td> </tr> <tr> <td colspan="2"></td> <td colspan="2">Part Title:</td> <td colspan="2"></td> </tr> <tr> <td colspan="2"></td> <td colspan="2">Assembled Heater</td> <td colspan="2"></td> </tr> <tr> <td colspan="2"></td> <td colspan="2">Number Of Parts:</td> <td colspan="2">DWG NO.</td> </tr> <tr> <td colspan="2"></td> <td colspan="2">1 Parts</td> <td colspan="2">C1Htr-AssembledHeater.dwg</td> </tr> <tr> <td colspan="2"></td> <td colspan="2">Units: mm</td> <td colspan="2">REV</td> </tr> </table> | | | | | | Notes: | | Author/Lab: | | Tel.: | | This is the assembled picture of the heater. Both transparent wall and opaque wall pictures are shown. | | DavidStoker/Ketolab | | 1-4151/695-6898 | | | | Part Title: | | | | | | Assembled Heater | | | | | | Number Of Parts: | | DWG NO. | | | | 1 Parts | | C1Htr-AssembledHeater.dwg | | | | Units: mm | | REV | |
| Notes: | | Author/Lab: | | Tel.: | | | | | | | | | | | | | | | | | | | | | | | | | | | | | | | | | | | | | | | | | | | |
| This is the assembled picture of the heater. Both transparent wall and opaque wall pictures are shown. | | DavidStoker/Ketolab | | 1-4151/695-6898 | | | | | | | | | | | | | | | | | | | | | | | | | | | | | | | | | | | | | | | | | | | |
| | | Part Title: | | | | | | | | | | | | | | | | | | | | | | | | | | | | | | | | | | | | | | | | | | | | | |
| | | Assembled Heater | | | | | | | | | | | | | | | | | | | | | | | | | | | | | | | | | | | | | | | | | | | | | |
| | | Number Of Parts: | | DWG NO. | | | | | | | | | | | | | | | | | | | | | | | | | | | | | | | | | | | | | | | | | | | |
| | | 1 Parts | | C1Htr-AssembledHeater.dwg | | | | | | | | | | | | | | | | | | | | | | | | | | | | | | | | | | | | | | | | | | | |
| | | Units: mm | | REV | | | | | | | | | | | | | | | | | | | | | | | | | | | | | | | | | | | | | | | | | | | |

Figure B.9:

Bibliography

- [1] W. Nichols *et al.*, Appl. Phys. Lett **78**, 1128 (2001).
- [2] M. F. Becker, (unpublished) .
- [3] A. Iwata, J. Akedo, and M. Lebedev, J. Am. Ceram. Soc. **88**, 1067 (2005).
- [4] J. Akedo and M. Lebedev, Journal of Crystal Growth **275**, 1301 (2005).
- [5] W. Nichols, Ph.D. thesis, The University of Texas at Austin, 2003.
- [6] G. Scherer and T. Garino, J. Am. Ceram. Soc. **68**, (1985).
- [7] G. W. Scherer, J. Sol-Gel Sci. Technol. **8**, (1997).
- [8] T. Garino and H. Bowen, J. Chem. Phys. **70**, 315 (1987).
- [9] G. Scherer, J. Am. Ceram. Soc. **70**, (1987).
- [10] J. Baek, Ph.D. thesis, The University of Texas at Austin, 2006.
- [11] J. Baek, D. Kovar, J. W. Keto, and M. F. Becker, Journ. Appl. Phys. (**in press**), (2005).
- [12] R. C. Powell, Physics of Solid-State Laser Materials (Springer-Verlag, New York, 1998).
- [13] J. Maxwell-Garnett, Phil. Trans. R. Soc. London **203**, 385 (1904).

- [14] J. Maxwell-Garnett, Phil. Trans. R. Soc. London **205**, 237 (1906).
- [15] M. Yamane and Y. Asahara, Glasses for Photonics (Cambridge University Press, Cambridge, 2000).
- [16] R. H. Ritchie, Surf. Sci. **34**, 1 (1973).
- [17] H. J. Simon, D. E. Mitchell, and J. G. Watson, Phys. Rev. Lett. **33**, 1531 (1985).
- [18] R. H. Ritchie, Phys. Rev. **106**, 874 (1957).
- [19] R. H. Ritchie, E. T. Arakawa, J. J. Cowan, and R. N. Hamm, Phys. Rev. Lett. **21**, 1530 (1968).
- [20] Y. Teng and E. A. Stern, Phys. Rev. Lett. **19**, 511 (1967).
- [21] M. Muskovits, Rev. Mod. Phys. **57**, 783 (1985).
- [22] D. Hennecke *et al.*, J. Chem. Phys. **119**, 6802 (2003).
- [23] G. T. Boyd, T. Rasing, J. R. R. Leite, and Y. R. Shen, Phys. Rev. B **30**, 519 (1984).
- [24] J. Gersten and A. Nitzan, J. Chem. Phys. **73**, 3023 (1980).
- [25] R. Greenler, D. R. Snider, D. Witt, and R. S. Sorbello, Surf. Sci. **118**, 415 (1982).
- [26] R. W. Boyd, Nonlinear Optics (Academic Press, San Diego, 1992).
- [27] W. E. Angerer *et al.*, Phys. Rev. B **59**, 2932 (1999).
- [28] Y. Q. An and S. Cudiff, Submitted to J. Appl. Physics **25**, (2005).
- [29] P. M. Lundquist *et al.*, Appl. Phys. Lett. **65**, 1085 (1994).

- [30] L. P. Wang *et al.*, J. Vac. Sci. Technol. **23**, 1284 (2005).
- [31] J. Baek, J. Keto, M. Becker, and D. Kovar, Thin Solid Films (submitted) (2005).
- [32] C. Ristoscu *et al.*, Appl. Phys. A **79**, 927 (2004).
- [33] J. Dadap, J. Shan, K. B. Eisenthal, and T. F. Heinz, Phys. Rev. Lett. **83**, 4045 (1999).
- [34] R. Lazzari and I. Simonsen, Thin Solid Films **419**, 124 (2002).
- [35] R. E. Hummel and P. Wißmann, Handbook of optical properties v.II (CRC Press, Boca Raton, 1997).
- [36] A. M. Michaels, M. Nirmal, and L. E. Brus, Journ. Am. Chem. Soc. **121**, 9932 (1999).
- [37] A. Mooradian, Phys. Rev. Lett. **22**, 185 (1969).
- [38] O. Varnavski *et al.*, J. Chem. Phys. **114**, 1962 (2001).
- [39] M. R. Beversluis, A. Bouhelier, and L. Novotny, Phys. Rev. B **68**, 115433 (2003).
- [40] O. P. Varnavski, T. G. III, M. B. Mohamed, and M. A. El-Sayed), Phys. Rev. B **72**, 235405 (2005).
- [41] P. Mühlischlegel *et al.*, Science **308**, 1607 (2005).
- [42] R. H. Ritchie and H. B. Eldridge, Phys. Rev. **126**, 1935 (1962).
- [43] R. Knorren, G. Bouzerar, and K. H. Bennemann, J. Phys.: Condens. Matter **14**, R739 (2002).
- [44] R. Trebino *et al.*, Rev. Sci. Instr. **68**, 3277 (1997).

- [45] A. E. Siegman, LASERS (University Science Books, Sausalito, 1986).
- [46] R. S. Tasgal and Y. B. Band, Phys. Rev. A. **70**, 053810 (2004).
- [47] R. C. Eckardt and J. Reintjes, IEEE J. of Quant. Elect. **QE-20**, 1178 (1984).
- [48] R. S. Tasgal, M. Trippenbach, M. Matuszewski, and Y. B. Band, Phys. Rev. A. **69**, 013809 (2004).
- [49] D. Stoker, M. C. Becker, and J. W. Keto, Phys. Rev. A: *Rapid Communication* **71**, (2005).
- [50] K. D. Moll, D. Homoelle, A. L. Gaeta, and R. W. Boyd, Phys. Rev. Lett. **88**, 153901 (2002).
- [51] Y. Barad, H. Eisenberg, M. Horowitz, and Y. Silberberg, Appl. Phys. Lett. **70**, 922 (1997).
- [52] T. Y. F. Tsang, Phys. Rev. A **52**, 4116 (1995).
- [53] R. Barille, L. Canioni, L. Sarger, and G. Rivoire, Phys. Rev. E **66**, 067602 (2002).
- [54] P. N. Saeta and N. A. Miller, Appl. Phys. Lett. **79**, 2704 (2001).
- [55] T. Tsang *et al.*, Opt. Lett. **52**, 1381 (1996).
- [56] J. F. Ward and G. H. C. New, Phys. Rev. **185**, 57 (1969).
- [57] G. C. Bjorklund, IEEE J. Quant. Elect. **QE-11**, 287 (1975).
- [58] A. M. Weiner, IEEE J. Quant. Elect. **QE-18**, 1276 (1983).
- [59] K. Hayata and M. Koshiba, Appl. Phys. Lett. **62**, 2188 (1993).
- [60] M. F. Becker, Y. C. Kim, S. Gautam, and E. J. Powers, IEEE J. Quant. Elect. **79**, 2704 (1982).

- [61] J.-C. Diels and W. Rudolph, Ultrashort Laser Pulse Phenomena (Academic Press, San Diego, 1996).
- [62] P. T. Wilson *et al.*, Opt. Lett. **24**, 496 (1999).
- [63] M. Sheik-Bahae, A. Said, and E. V. Stryland, Opt. Lett. **14**, 955 (1989).
- [64] J. xin Cheng, A. Volkmer, L. D. Book, and X. S. Xie, J. Ram. Spect. **34**, 642 (2003).
- [65] C.-K. Sun *et al.*, Appl. Phys. Lett. **77**, (2005).
- [66] D. Debarre, W. Supatto, and E. Beaurepaire, Opt. Lett. **30**, 2134 (2005).
- [67] G. Petrov *et al.*, Appl. Phys. Lett. **83**, 3993 (2003).
- [68] Y. R. Shen, Nature **337**, 519 (1989).
- [69] D. A. Kleinman and R. C. Miller, Phys. Rev. **148**, 302 (1966).
- [70] G. Banfi *et al.*, Phys. Rev. A **64**, 063812 (2001).
- [71] N. A. Sanford *et al.*, Journ. Appl. Phys. **97**, 053512 (2005).
- [72] W. . P. Lin *et al.*, Appl. Phys. Lett. **63**, 2875 (1993).
- [73] T. Suga *et al.*, Appl. Phys. Lett. **86**, 163113 (2005).
- [74] J. Miragliotta and D. K. Wickenden, Phys. Rev. B **50**, 14960 (1994).
- [75] W. K. Burns and N. Bloembergen, Phys. Rev. B **4**, 3437 (1971).
- [76] R. B. Miles and S. E. Harris, IEEE J. Quant. Elect. **9**, 470 (1973).
- [77] P. D. Maker, R. W. Terhune, M. Nisenoff, and C. M. Savage, Phys. Rev. Lett. **8**, 21 (1962).

- [78] M. D. Levenson, IEEE J. Quantum Electron. **QE-10**, 110 (1974).
- [79] G. E. Francois and A. E. Siegman, Phys. Rev. **139**, A4 (1965).
- [80] M. Asobe and *et al.*, IEEE Photonics Techn. Lett. **4**, (1992).
- [81] N. S. *et al.*, Opt. Lett. **21**, 1637 (1996).
- [82] B. L. J. R. K. A. Leitner and F. R. Aussenegg, Phys. Rev. Lett. **83**, 4421 (1999).
- [83] K. Uchida *et al.*, J. Opt. Soc. Am. B **11**, 1236 (1994).
- [84] G. T. Boyd, Z. H. Yu, and Y. R. Shen, Phys. Rev. B **33**, 7293 (1986).
- [85] R. C. Hart, W. R. Garrett, and M. G. Payne, Phys. Rev. A **46**, 4213 (1992).
- [86] H. SCHEINGRABER and C. R. VIDAL, **QE-19**, 1747 (1983).
- [87] H. Puell, H. Scheingraber, and C. R. Vidal, Phys. Rev. A. **22**, 1165 (1980).
- [88] N. D. Fatti, R. Bouffanaïs, F. Valle, and C. Flytzanis, Phys. Rev. Lett. **81**, 922 (1998).
- [89] N. W. Ashcroft and N. D. Mermin, Solid State Physics (Harcourt College Publishing, Tokyo, 1976).
- [90] E. Tokunaga, A. Terasaki, and T. Kobayashi, Opt. Lett. **17**, 1131 (1992).
- [91] J. P. Geindre *et al.*, Opt. Lett. **19**, 1997 (1994).

Vita

David Stevens Stoker was born November 23, 1976 to Michael D. Stoker and Catherine A. Stoker, in Arcata, California. Two years later his family moved to Ohio, where he attended parochial schools, and played baseball in the summertime. After graduating from St. Xavier High School in Cincinnati in 1994, David enrolled at The Ohio State University. There, he conducted numerous experiments in soft condensed matter physics with Dr. Maarten Rutgers, receiving an Alphas W. and Adah B. Smith Research Scholarship for “Pressure profiles in fluidized sand”. After completing his Bachelors of Science in 2000, with majors in mathematics and physics, he moved to Texas for graduate study at the University of Texas at Austin. David continues to live in Austin with his wife, Irina.

Permanent Address: 710 W. 34th St. #204
Austin, Tx 78705-1224

This dissertation was typeset with $\text{\LaTeX 2}_{\epsilon}$ ¹ by the author.

¹ $\text{\LaTeX 2}_{\epsilon}$ is an extension of \LaTeX . \LaTeX is a collection of macros for \TeX . \TeX is a trademark of the American Mathematical Society. The macros used in formatting this dissertation were written by Dinesh Das, Department of Computer Sciences, The University of Texas at Austin, and extended by Bert Kay, James A. Bednar, and Ayman El-Khashab.